High Reynolds turbulence : Study of the inertial intermittency in axisymmetric jet and von Kármán cryogenic flows

Swapnil Prabhakar Kharche

Université Grenoble Alpes

THÈSE

Pour obtenir le grade de

DOCTEUR DE L'UNIVERSITÉ GRENOBLE ALPES

Spécialité : MEP : Mécanique des fluides, Energétique, Procédés

Arrêté ministériel : 25 mai 2016

Présentée par

Swapnil KHARCHE

Thèse dirigée par **Christophe BAUDET**,
préparée au sein du **Département des Systèmes Basses Températures**
dans **l'École Doctorale I-MEP2**

Turbulence à Haut Reynolds : Etude de l'intermittence inertielle dans un jet axisymétrique et un écoulement de von Kármán cryogéniques

High Reynolds turbulence: Study of the inertial intermittency in axisymmetric jet and von Kármán cryogenic flows

Thèse soutenue publiquement le **15 Décembre 2021**,
devant le jury composé de :

M. Joachim PEINKE
Professeur, Carl von Ossietzky Universität Oldenburg, Président
M. Sébastien AUMAITRE
Ingénieur HDR, CEA Saclay, Rapporteur
M. Nicolas MAZELLIER
Professeur des Universités, Université d'Orléans, Rapporteur
Mme. Léonie CANET
Professeur des Universités, Université Grenoble Alpes, Examinatrice
M. Christophe BAUDET
Professeur des Universités, Université Grenoble Alpes, Directeur
M. Alain GIRARD
Ingénieur Chercheur, CEA Grenoble, Invité

ACKNOWLEDGEMENTS

This thesis would not have been possible without the help and support from many people. First of all, I would like to thank my PhD supervisor Dr. Alain Girard for his continuous support and encouragement during this thesis. I really appreciate his great enthusiasm and incredible patience towards me in the scientific as well as in the personal context. I would also like to thank my PhD director Prof. Christophe Baudet for allowing and believing in me to work on this exciting field of turbulence. I really appreciate his timely guidance during this thesis. I feel thankful to get to work with both the experienced experimentalists Dr. Alain Girard and Prof. Christophe Baudet. Because of their very subtle and kind approach, I was able to write the best version of my PhD manuscript.

I would like to thank all the jury members of my thesis for accepting the invitation to evaluate my PhD work. I would especially like to thank the reviewers of my thesis, Dr. Sébastien Aumaître and Prof. Nicolas Mazellier for reviewing such a long PhD manuscript carefully. I am also grateful to Prof. Joachim Peinke and Prof. Léonie Canet for examining my PhD work.

This was an experimental thesis which needed the help and support from many technicians and engineers. In this respect, first of all, I would like to thank Mr. Jean-Paul Moro for sharing his skills and expertise with us to fabricate numerous hot-wire sensors. The success of this thesis was only possible because of these hot-wire sensors. Special thanks to Mr. Jérôme Chartier for helping me with installation and operation of various experimental facilities. I am also thankful to him for making some hot-wire sensors that are used in this thesis. I am extremely thankful to both Mr. Michel Bon-Mardion and Mr. Jérôme Chartier for teaching me various experimental techniques specially related to the cryogenic environment. Special thanks to the electronics team at DSBT including Christophe, Jeremy, Thomas, Anthony and Patrick.

A big thanks to the program of Chair of Excellence by LANEF with which we had an opportunity to collaborate with Prof. Joachim Peinke and his laboratory. I had very fruitful discussions with Prof. Joachim Peinke during his visits to CEA-Grenoble and also in Oldenburg. Thanks to this funding, I had opportunities to visit the University of Oldenburg and discuss various research topics with other PhD students and researchers. I specially would like to thank Mr. André Fuchs for having very long discussions and clearing my doubts from time to time. I really appreciate his warm welcoming gesture and the very fun moments I had during my stay in Germany.

I am very grateful to the people in DSBT especially working at 10.01 for their very welcoming and lively gesture all the time. I am thankful to all of them for being very patient towards my French communication skills. I am especially thankful to the jogging sessions organized by Michel every week during which we had a lot of fun. Also, thanks to Michel for organizing Repas de Noël and BBQ each year. I would like to thank Arbi for helping me with various experiments and also for the fun discussions we had together. I would like to thank Bernard and Pantxo for helping me with various experimental activities along with numerous technical discussions. Thanks to Herve, Christophe, Didier and Pierre for having regular fun discussions at the workplace. I would also like to thank Christine, Jean-Marc, Pascal, Frederic, Sulayman, Pierre and Julien for their continuous support and help. Last but not least, I thank everyone who brought French croissants and chocolates in 10.01, I enjoyed eating them a lot, haha!

Contents

List of Figures v

List of Tables xiv

I INTRODUCTION 1
I.1 Navier-Stokes equation 2
I.2 Global picture of turbulence 2
I.3 Literature survey 5
I.3.1 Intermittency 5
I.3.2 Von Kármán flow 7
I.3.3 Cryogenic jet flows 7
I.3.4 Turbulence in superfluid 8
I.4 Why Helium? 8
I.5 Challenges, motivations and objectives of the thesis 11
I.6 Statistical quantities of turbulence 13
I.6.1 Velocity of the flow 13
I.6.2 Taylor hypothesis 14
I.6.3 The power spectrum 15
I.6.4 Turbulence intensity of the flow 16
I.6.5 Autocorrelation coefficient 17
I.6.6 Structure functions 18
I.6.7 Energy budget within turbulent cascade 19
I.6.8 Length scales in turbulence 23
I.6.8.1 Integral length scale 23
I.6.8.2 Taylor microscale 24
I.6.8.3 Kolmogorov length scale 24
I.6.9 Reynolds number 25
I.6.10 Probability density function 25
I.7 Organization of the thesis 26

II HOT-WIRE ANEMOMETRY 29
II.1 Constant current anemometry (CCA) 31
II.2 Constant temperature anemometry (CTA) 33
II.3 Constant voltage anemometry (CVA) 34
II.4 Resistance dependence on temperature 36
II.4.1 Micro-fabricated hot-wire 36
II.4.2 Pt-Rh Wollaston hot-wire 37

II.5 Sensitivity of the hot-wire during different calibrations in the SHREK experiment . . . 39
II.6 Hot-wire calibration in the ECOUTURB experiment . . . 41
II.7 Time constant measurement in CCA mode . . . 42
II.7.1 SHREK experiment . . . 44
II.7.2 ECOUTURB experiment . . . 45
II.7.3 HECAL experiment . . . 46
II.8 Correction of the hot-wire signal based on its time constant . . . 47
II.9 Conclusion . . . 48

III HECAL EXPERIMENT . . . 51
III.1 Introduction . . . 51
III.2 Experimental set-up . . . 52
III.2.1 Hot-wire support . . . 53
III.2.2 Instrumentation for precise calibration of hot-wires . . . 54
III.3 Results . . . 55
III.3.1 Calibration of hot-wire at ambient temperature . . . 56
III.3.2 Calibration of hot-wire in HeI . . . 57
III.3.3 Calibration of hot-wire in HeII . . . 62
III.3.4 Repeatability and sensitivity . . . 65
III.3.5 Application in the SHREK/ECOUTURB experiment . . . 67
III.3.6 Power spectrum at null velocity in HeI and HeII . . . 68
III.4 Conclusion . . . 72

IV HEJET EXPERIMENT . . . 75
IV.1 Experimental set-up . . . 75
IV.1.1 The new centrifugal pump . . . 78
IV.1.2 Dimensions of the nozzle and the grid position . . . 82
IV.1.3 Temperature sensors . . . 83
IV.1.4 Pressure sensors . . . 84
IV.1.5 Helium level indicator . . . 85
IV.1.6 The hot-wire support . . . 86
IV.2 Procedure to cool-down . . . 87
IV.3 Results . . . 88
IV.3.1 Macroscopic characteristics of the HEJET facility: the pump, mass flow rate and the energy balance . . . 88
IV.3.1.1 The pressure change across the venturi, nozzle and the centrifugal pump . . . 88
IV.3.1.2 The flow rate . . . 89
IV.3.1.3 Electrical power consumption of the motor . . . 90
IV.3.1.4 Mechanical power output of the centrifugal pump . . . 92
IV.3.1.5 Estimation of heat losses from evaporation . . . 93
IV.3.1.6 Estimation of flow rate based on power balance in HeI . . . 94
IV.3.1.7 Efficiency of the centrifugal pump . . . 96
IV.3.1.8 Vibration analysis . . . 97
IV.3.2 Calibration of the hot-wire . . . 99
IV.3.3 PDF and compensated PSD . . . 100
IV.3.4 Empirical mode decomposition . . . 103
IV.3.5 Statistical analysis of the turbulent jet flow . . . 107

IV.3.6 Intermittency . . . 111
IV.3.7 Observations in HeII . . . 115
IV.3.8 Importance of thermal stability . . . 117
IV.4 Conclusion . . . 119

V SHREK EXPERIMENT . . . 121
V.1 Experimental set-up . . . 121
V.1.1 von Kármán cell and hot-wire position . . . 121
V.1.2 Different types of turbines . . . 123
V.1.3 Conventions of rotation of turbine . . . 123
V.1.4 Classification of experimental data . . . 126
V.2 PSD of velocity signal . . . 126
V.3 PDF of velocity signal . . . 127
V.4 Effects of forcing on dissipation and Kolmogorov scale . . . 129
V.5 Dimensionless dissipated power per unit mass . . . 131
V.6 Effects of forcing on Re_λ . . . 132
V.7 Scaling laws . . . 133
V.7.1 $\frac{\lambda}{\eta} \propto Re^{\frac{1}{4}}$ . . . 133
V.7.2 $\frac{\eta}{L} \propto Re^{-\frac{3}{4}}$ . . . 134
V.7.3 $\frac{u_\eta}{u_{rms}} \propto Re^{-\frac{1}{4}}$ . . . 135
V.8 Re_λ effect on $\frac{L}{\lambda}$ . . . 136
V.9 Intermittency . . . 137
V.9.1 Flatness and skewness of PDFs of velocity increments . . . 138
V.9.2 Dependence of flatness and skewness of PDFs of velocity increments on Re_λ . . . 141
V.9.3 Dependence of scaling exponent ζ_p on Re_λ . . . 143
V.10 Observations in HeII . . . 151
V.10.1 PSD of hot-wire signal . . . 151
V.10.2 Calibration of the hot-wire . . . 153
V.10.3 Statistical analysis of velocity signal . . . 154
V.10.4 Study of intermittency . . . 156
V.10.5 Structure functions and scaling exponents . . . 156
V.11 Conclusion . . . 158

VI DESCRIPTION OF TURBULENT CASCADE USING FOKKER-PLANCK EQUATION IN THE SHREK EXPERIMENT . . . 161
VI.1 The turbulent cascade as a Markov process . . . 161
VI.1.1 Markov process . . . 161
VI.1.2 Historical approach: Chapman-Kolmogorov equation . . . 162
VI.1.3 Further tests of the Markovian property . . . 163
VI.1.3.1 Wilcoxson test . . . 164
VI.1.3.2 Single conditioned and double conditioned PDF . . . 165
VI.2 Description of the turbulent cascade through a Fokker-Planck equation . . . 167
VI.2.1 Kramers-Moyal expansion of the evolution of the conditional PDF in scale . . . 167
VI.2.1.1 Fokker-Planck equation . . . 168
VI.2.1.2 Estimation of the Kramers-Moyal coefficients . . . 168
VI.2.1.2.1 Conditional moment of first and second order . . . 168

VI.2.1.2.2 Dependence of $D^{(1)}$ and $D^{(2)}$ on scale and velocity increments . . . 169
VI.2.1.3 Langevin formulation . . . 172
VI.2.2 Assessment of the Fokker-Planck description of the turbulent cascade . . . 172
VI.2.2.1 Reconstruction of PDFs of velocity increment using drift and diffusion coefficient . . . 172
VI.2.2.2 Integral fluctuation theorem verification . . . 177
VI.3 Discussion on the drift and diffusion coefficients . . . 183
VI.3.1 Interpretation of some coefficients linked with K41 and K62 . . . 183
VI.3.2 Dependence of parameters d_{11}, d_{20} and d_{22} on scale . . . 184
VI.3.3 Dependence of parameters d_{11}, d_{20} and d_{22} on Re_λ . . . 185
VI.4 Application of FPE and IFT in HeII . . . 193
VI.5 Conclusion . . . 195

VII CONCLUSION AND PERSPECTIVES . . . 197
VII.1 Future works . . . 198

Bibliography . . . 201

List of Figures

Figure I.1 Phase diagram of ^{4}He [The phase diagram is constructed using the data obtained from HEPAK (computer program to estimate thermophysical properties of helium)] . . . 9

Figure I.2 Normalized density (density fraction) of superfluid $\left(\frac{\rho_s}{\rho}\right)$ and normal helium $\left(\frac{\rho_n}{\rho}\right)$ below T = 2.17K (source: HEPAK) . . . 11

Figure I.3 Raw hot-wire signal before and after the calibration using CCA mode in the SHREK facility using straight blades for the co-rotation configuration at 1.2Hz . . . 13

Figure I.4 Comparison of classical and corrected Taylor hypothesis on the SHREK experimental data of contra configuration: +1.0(H) - 1.0(B) . . . 14

Figure I.5 Different representations of power and dissipation spectrum on a log-log scale in the frequency f and wavenumber k domain for the contra configuration: +1.0(H) - 1.0(B) in the SHREK facility . . . 16

Figure I.6 Variation of u_{rms} and $\mathcal{I}$ with respect to turbine frequency $\mathcal{F}_1$ or $\mathcal{F}_2$ in the SHREK experiment using curved blades . . . 17

Figure I.7 Autocorrelation coefficient for the co-rotation configuration in the SHREK experiment performed with radial blades at $\mathcal{F}_1 = \mathcal{F}_2 = 1.2$Hz [Hot-wire position: close to the top turbine (15cm away from the equatorial plane)] 18

Figure I.8 p^{th} order structure function with respect to scale r for the co-rotation configuration in the SHREK experiment at $\mathcal{F}_1 = \mathcal{F}_2 = 1.2$Hz [for clarity the structure functions are arbitrarily shifted in the vertical direction and for better representation odd order structure functions are estimated using absolute values of the velocity increments given by: $T_p(r) = \langle |u_r|^p \rangle = \langle |u(x+r) - u(r)|^p \rangle$] . . . 19

Figure I.9 Estimation of energy transfer rate (dissipation rate) from the compensated 3^{rd} order structure function along with the effects of the correction term . . . 21

Figure I.10 Estimation of energy dissipation rate by different methods for contra configuration: -0.24(H) + 0.36(B) . . . 22

Figure I.11 Cumulative integral of R_{uu} showing the estimation of $L \approx 0.03m$ [shown by dashed line] for the co-rotation configuration in the SHREK experiment at $\mathcal{F}_1 = \mathcal{F}_2 = 1.2$Hz . . . 24

Figure I.12 Probability density function (PDF) of instantaneous velocity in the SHREK experiment . . . 25

Figure II.1 Typical home-made hot-wire of $d_w = 1.27\mu m$, $l_w = 300\mu m$ and Resistance = 43Ω at 300K . . . 30
Figure II.2 Experimental data points and the calibration curve using King's Law of calibration for CCA in the SHREK facility in HeI at T = 2.2K ($d_w = 1.27\mu m$ and $l_w = 300\mu m$)[$y(x)$ is the hot-wire voltage where x is the velocity]. . . . 33
Figure II.3 Experimental data points and the calibration curve using the King's law of calibration in HeI at T = 2.2K in the SHREK facility using curved blades ($d_w = 1.27\mu m$ and $l_w = 300\mu m$) . . . 34
Figure II.4 Experimental data points and the calibration curve using Kings law of calibration (commercial hot-wire: $d_w = 5\mu$m, $l_w = 1$mm) . . . 36
Figure II.5 Micro-fabricated hot-wire resistance with respect to temperature using pulse tube cryocooler . . . 37
Figure II.6 Change in hot-wire resistance with respect to temperature from 300K to 78K . . . 38
Figure II.7 Change in hot-wire resistance with respect to temperature from 70K to 4.2K . . . 38
Figure II.8 Different hot-wire calibrations in CCA mode performed in the SHREK experiment using straight blades in HeI at T = 2.2K ($d_w = 1.27\mu m$ and $l_w = 300\mu m$) . . . 39
Figure II.9 Different hot-wire calibrations in CTA mode performed in the SHREK experiment using curved blades in HeI at T = 2.2K . . . 40
Figure II.10 Multiple hot-wire calibrations performed over different duration in the SHREK experiment using straight blades in HeI at T = 2.2K [$d_w = 1.27\mu m$ and $l_w = 300\mu m$; hot-wire position: 4cm above the equatorial plane] . . . 41
Figure II.11 Hot-wire calibration in the ECOUTURB experiment in HeI at T = 2.2K 42
Figure II.12 Procedure to find the time constant of the hot-wire in CCA mode . . . 44
Figure II.13 Measured time constant of the hot-wire in the SHREK experiment using straight blades in HeI and HeII ($d_w = 1.27\mu m$ and $l_w = 300\mu m$) . . . 45
Figure II.14 Time constant at different velocities and its experimental fit according to equation II.9 . . . 45
Figure II.15 Measured time-constant of the hot-wire in the ECOUTURB experiment in HeI and HeII ($d_w = 1.27\mu m$ and $l_w = 300\mu m$) . . . 46
Figure II.16 Time constant measurement in the HECAL experiment . . . 47
Figure II.17 Effect of the correction of the raw hot-wire signal based on the time constant for +1.0Hz co-rotation configuration in the SHREK facility using straight blades [$L = 0.06$m, $\lambda = 700\mu m$] . . . 48
Figure III.1 Schematic and actual experimental set-up of the HECAL facility (not to scale) . . . 52
Figure III.2 Motor with reductor at bottom end and tachogenerator at top end . . . 53

Figure III.3 Hot-wire signal within one rotation of arm with respect to velocity using the motor with reductor (in CCA mode) . . . 53
Figure III.4 Hot-wires mounted on the rotational arm [Right figure: At the center of the rotating arm assembly we can see the 9 pin DIN connector] . . . 54
Figure III.5 Mounting of the rotational arm to the motor shaft in the pressurized helium bath (Bottom view) . . . 54
Figure III.6 Simplified block diagram of the HECAL experimental set-up . . . 55
Figure III.7 Theoretical estimation of time (ramp time) required to achieve the maximum desired velocity after one rotation . . . 55
Figure III.8 Raw signal of hot-wire (in CCA mode) and tachogenerator along with its calibration at 300K ($r = 69mm, d_w = 1.27\mu m$ and $l_w = 1mm$) . . . 56
Figure III.9 Comparison of measured velocity using tachogenerator and the calibrated hot-wire over two consecutive rotations of the arm . . . 57
Figure III.10 Details of the hot-wire calibration performed in HeI at T = 2.4K ($r = 57mm$, $d_w = 1.27\mu m$ and $l_w = 1mm$) . . . 58
Figure III.11 Hot-wire calibration curve using King's law in HeI at T = 2.4K ($r = 57mm$, $d_w = 1.27\mu m$ and $l_w = 1mm$) . . . 59
Figure III.12 Change in hot-wire response with respect to the rotating arm over time in HeI at T = 2.35K ($r = 45mm$, $d_w = 1.27\mu m$ and $l_w = 300\mu m$) . . . 60
Figure III.13 Hot-wire calibration and power spectrum density at T = 2.35K ($r = 45mm$, $d_w = 1.27\mu m$ and $l_w = 300\mu m$) . . . 61
Figure III.14 Effect of the vibration of the rotating arm at the beginning of rotation on the hot-wire signal in HeI [zoomed view of figure III.12 within Time = 5 - 6 secs; blue arrow: Time = 180msec; red arrow: Time = 230msec and magenta arrow: Time = 320msec] . . . 62
Figure III.15 Details of the hot-wire calibration performed in HeII at T = 2.0K ($r = 57mm$, $d_w = 1.27\mu m$ and $l_w = 1mm$) . . . 63
Figure III.16 Hot-wire calibration curve using King's law in HeII at T = 2.0K ($r = 57mm$, $d_w = 1.27\mu m$ and $l_w = 1mm$) . . . 63
Figure III.17 Effect of the vibration of the rotating arm at the beginning of rotation on the hot-wire signal in HeII at T = 2.0K [blue arrow: Time = 180msec; red arrow: Time = 280msec; orange arrow: Time = 350msec and magenta arrow: Time = 360msec] . . . 65
Figure III.18 Two calibrations of the same hot-wire showing repeatability of the HECAL experiment in HeI at T = 2.35K . . . 66
Figure III.19 Sensitivity of hot-wire using multiple calibrations for different overheating in HeI at T = 2.35K ($r = 45mm$, $d_w = 1.27\mu m$ and $l_w = 300\mu m$) . . . 67
Figure III.20 Application of the hot-wire calibration performed in the HECAL experiment to the ECOUTURB experiment in HeI at T = 2.3K ($d_w = 1.27\mu m$ and $l_w = 300\mu m$) . . . 68
Figure III.21 Raw hot-wire signal at null velocity; top: T = 2.4K (HeI); middle: T = 2.0K (HeII); bottom: T = 1.9K (HeII) ($d_w = 1.27\mu m$ and $l_w = 300\mu m$) . . . 70

Figure III.22 PSD of the raw hot-wire signal at null velocity using different overheating in CCA mode [$d_w = 1.27\mu m$ and $l_w = 300\mu m$; the temperature T indicates the temperature surrounding the hot-wire in the pressurized helium bath; I denotes the operating current of the hot-wire (with the percentage of overheating in the bracket)] 71

Figure IV.1 Description of the HEJET facility (not to scale, original figure from Duri [2012] modified here). 1. DC Motor 2. Saturated bath pressure sensor 3. Throttle valve (to regulate the saturated bath pressure) 4. Pumping of saturated bath 5. Motor/Pump shaft assembly 6. Turbine of centrifugal pump 7. Grid for jet stability 8. Experimental section 9. Venturimeter 10. Nozzle 11. Honeycomb 12. Helicoidal heat exchanger 13. Communication valve between pressurized and saturated He bath 14. Outer cylinder of liquid nitrogen bath 15. Inner cylinder of saturated helium bath 16. Radiation shields 17. Valve for pressurization [blue star: hot-wire location at $\frac{z}{d} = 50$ with $d =$ nozzle diameter, z is the axial direction whereas r is the radial direction of the jet; h is the level of helium in the saturated He bath; red filled circles: Temperature sensors; blue filled circles: differential pressure measurement locations ($(\Delta P)_{pump} = P_2 - P_1$, $(\Delta P)_{venturi} = P_3 - P_4$, $(\Delta P)_{nozzle} = P_5 - P_6$)] 77

Figure IV.2 Phase diagram of ^{4}He [The phase diagram is constructed using the data obtained from HEPAK (computer program to estimate thermophysical properties of helium)] 78

Figure IV.3 The new centrifugal pump characteristics $(\Delta P)_{pump}$ along with the system characteristics $(\Delta P)_{nozzle}$ [This plot is provided by the pump designer] 80

Figure IV.4 Turbine of the newly designed centrifugal pump [provided by the pump designer; sense: anti-clockwise rotation] 81

Figure IV.5 The hub and housing of the turbine [provided by the pump designer] . . 81

Figure IV.6 Different components of the centrifugal pump showing the turbine assembly [red arrow shows the flow of the fluid and yellow arrow shows the sense of rotation of the turbine in the centrifugal pump] 82

Figure IV.7 Experimental section showing temperature sensors and the nozzle of $d =$ 5mm 83

Figure IV.8 Calibration of differential pressure sensors at T = 300K 85

Figure IV.9 Actual view of the HEJET experimental facility [h denotes the level of helium in the saturated helium bath measured by the sensor of superconductor and R1 to R6 denotes the position (level) of 6 different resistances installed in the saturated helium bath] 86

Figure IV.10 Hot wires mounted on the support which is fixed at $z = 50d$ in the experimental region [$d = 5$mm] 87

Figure IV.11 The dependence of measured ΔP on $\mathcal{F}_t$ given by, $\Delta P \propto \mathcal{F}_t^2$ for the venturi, nozzle and the pump [the experimental fit is expressed by $y(x) = ax^2 + b$ where $y(x)$ is the pressure change in mbar and x is the turbine frequency in Hz] 89

Figure IV.12 Volumetric flow rate estimated from the venturimeter as a function of turbine frequency; the inset represents the mass flow rate expressed in $\frac{g}{s}$ [the experimental fit is expressed by $y(x) = ax + b$ where $y(x)$ is the flow rate in $\frac{m^3}{s}$ or $\frac{g}{s}$ and x is the turbine frequency in Hz] 90

Figure IV.13 Electrical power consumption of the DC motor as a function of the turbine frequency [the experimental fit is expressed by $y(x) = ax^3 + bx$ where $y(x)$ is the electrical motor power in W and x is the turbine frequency in Hz; $a = 0$ at T = 300K] 92

Figure IV.14 Mechanical power output of the centrifugal pump as a function of turbine frequency [the experimental fit is expressed by $y(x) = ax^3 + b$ where $y(x)$ is the pump mechanical power in W and x is the turbine frequency in Hz] 93

Figure IV.15 Heat losses from evaporation as a function of turbine frequency [the experimental fit is expressed by $y(x) = ax^3 + b$ where $y(x)$ is P_{roots} in W and x is the turbine frequency in Hz] 94

Figure IV.16 Pressure head across the pump and efficiency of the centrifugal pump with respect to mass flow rate at T = 1.8 - 2.4K 97

Figure IV.17 PSD of the accelerometer signal on lin-lin scale 98

Figure IV.18 PSD of the accelerometer signal on lin-log scale at $\mathcal{F}_t = 0$ 98

Figure IV.19 Hot-wire calibration in HeI at T = 2.4K using King's law fit in CCA mode (Hot-wire location: $\frac{z}{d} = 50$, $d = 5mm$, $d_w = 1.27\mu m$ and $l_w = 300\mu m$) . . 100

Figure IV.20 PDF of the raw hot-wire voltage in HeI at T = 2.4K (A dashed curve in each PDF shows a Gaussian distribution; HW voltage: hot-wire voltage; $\mathcal{F}_t$: turbine frequency) 102

Figure IV.21 PSD of the velocity signal at different turbine frequency $\mathcal{F}_t = 8$ up to 25Hz 103

Figure IV.22 Cumulative integral of the auto-correlation coefficient of the velocity signal at $\mathcal{F}_t$ = 25Hz 104

Figure IV.23 Intrinsic mode functions along with the residual of velocity signal with respect to time [out of 15 only 4 IMFs are shown here along with the residual] 105

Figure IV.24 PSD showing the application of EMD on the velocity signal $\left[\sum_{i=1}^{n} \text{IMF}_i\right.$, for $n = 1$ to 15 from bottom to top; red dashed line shows the slope of $f^{-\frac{5}{3}}\left.\right]$ 106

Figure IV.25 Cumulative integral of the auto-correlation coefficient with respect to scale r using EMD $\left[\sum_{i=1}^{n} \text{IMF}_i\right.$, from $n = 15$ to 1 from top to bottom$\left.\right]$ . . 107

Figure IV.26 PDF of the hot-wire voltage and the calibrated velocity after performing EMD on the hot-wire signal using $\sum_{i=1}^{n=7} \text{IMF}_i + R$ [From top to bottom: $\mathcal{F}_t$ = 25, 20 and 15Hz; F specify the flatness of the PDF; the dashed-line shows the Gaussian distribution in each plot] 108

Figure IV.27 Estimation of the dissipation rate from the compensated third order structure function in the HEJET experiment 110

Figure IV.28 Demonstration of the phenomenon of intermittency in the HEJET experiment using the PDFs of velocity increments at different scales for $Re_\lambda = 2860$ (the curves are arbitrarily shifted for the better visualization) 112

Figure IV.29 Quantification of intermittency using flatness and skewness of the PDFs of velocity increment at $\mathcal{F}_t = 15, 20$ and 25Hz 113

Figure IV.30 Structure functions and its scaling exponents up to order p = 8 in the HEJET experiment 114

Figure IV.31 Compensated structure functions with respect to scale r [For clarity the compensated structure functions are arbitrarily shifted in the vertical direction] 115

Figure IV.32 PSD of the raw hot-wire signal at different turbine frequency in the HEJET facility at various pressurized bath temperature using CCA mode [$d_w = 1.27\mu m$ and $l_w = 300\mu m$] 117

Figure IV.33 Change in the hot-wire resistance with respect to the increasing pressurized helium bath temperature in the HEJET facility at null velocity [$d_w = 1.27\mu m$ and $l_w = 300\mu m$; the hot-wire is operated at 35% overheating] 118

Figure V.1 Detailed sketch of SHREK facility; Left: Dimensions of various parts in the SHREK experiment; Right: von Kármán cell with the turbines with curved blades 122

Figure V.2 Bottom view of the von Kármán cell along with the hot-wire 122

Figure V.3 Different types of turbine blades used in the SHREK experiment 123

Figure V.4 Sign conventions used in the SHREK experiment: co-rotation, contra and anti-contra configuration 125

Figure V.5 PSD of the velocity signal in the SHREK experiment for anti-contra configuration at $\mathcal{F}_1 = \mathcal{F}_2 = 0.6$Hz 127

Figure V.6 Probability density function (PDF) of the velocity signal in the SHREK experiment with curved blades for the co-rotation configuration [black circles show the PDF of experimental data and the dashed-line shows the Gaussian distribution in each plot; the hot-wire is operated in the CTA mode with 0.7% overheating] 128

Figure V.7 Probability density function (PDF) of the velocity signal in the SHREK experiment with radial blades for the co-rotation configuration [black circles show the PDF of experimental data and the dashed-line shows the Gaussian distribution in each plot; the hot-wire is operated in the CCA mode with 18% overheating] 129

Figure V.8 Estimation of local dissipation rate in the SHREK experiment from third order structure function [Co-Rotation: $Re_\lambda = 4410$; Contra: $Re_\lambda = 6180$; Anti-Contra: $Re_\lambda = 8100$] 130

Figure V.9 Variation of dissipation and Kolmogorov scale with applied forcing for different configurations of the von Kármán flow 131

Figure V.10 Dimensionless dissipated power per unit mass as a function of $Re = \frac{\pi(\mathcal{F}_1+\mathcal{F}_2)R^2}{\nu}$ 132

Figure V.11 Variation of Re_λ with applied forcing . . . 133
Figure V.12 Scaling of $\frac{\lambda}{\eta}$ with Re . . . 134
Figure V.13 Scaling of $\frac{\eta}{L}$ with Re . . . 135
Figure V.14 Scaling of $\frac{u_\eta}{u_{rms}}$ with Re . . . 136
Figure V.15 The evolution of ratio of integral scale to Taylor microscale with respect to Re_λ . . . 137
Figure V.16 PDFs of velocity increment at different scale on lin-log plot [for better clarity the curves are arbitrarily shifted in vertical direction] . . . 138
Figure V.17 Flatness of PDFs of velocity increment as a function of scale $\ln\left(\frac{r}{L}\right)$ [ln stands for natural logarithm] . . . 140
Figure V.18 Skewness of PDFs of velocity increment as a function of scale $\ln\left(\frac{r}{L}\right)$ . . . 141
Figure V.19 The dependence of flatness of PDFs of velocity increment on Re_λ for different flow configurations mentioned in table 6 . . . 142
Figure V.20 The dependence of skewness of PDFs of velocity increment on Re_λ for different flow configurations mentioned in table 6 . . . 143
Figure V.21 Structure functions of order $p = 2$ to 8 as a function of scale r for the contra configuration: + 1.0(H) - 1.0(B) in the SHREK experiment performed with straight blades [For clarity the structure functions are shifted arbitrarily in the vertical direction] . . . 144
Figure V.22 Statistical convergence test . . . 145
Figure V.23 p^{th} order structure function $\ln(T_p)$ with respect to $\ln(T_3)$ for the scales ranging from L down to λ for the contra configuration: + 1.0 (H) - 1.0 (B) in the SHREK experiment with radial blades [black-dashed line is the linear fit for the corresponding structure function] . . . 146
Figure V.24 Compensated structure functions $\left(\text{i.e. } \frac{T_p}{r^{\zeta_p}}\right)$ with respect to scale r [For clarity the structure functions are arbitrarily shifted in the vertical direction]. . . . 147
Figure V.25 Different intermittency models showing the scaling exponents ζ_p for each of the lower and higher Re_λ flows of data set A to G mentioned in table 6 (SHREK experiment with turbine with curved blades) . . . 149
Figure V.26 Different intermittency models showing the scaling exponents ζ_p for each of the lower and higher Re_λ flows of data set E' and G' mentioned in table 6 (data set E' and G' belongs to the SHREK experiment with turbine with radial blades) . . . 149
Figure V.27 Estimation of K62 intermittency parameter μ from the scaling exponents ζ_p estimated using ESS for the anti-contra configuration: + 0.6 (H) - 0.6 (B) in the SHREK experiment with curved blades . . . 150
Figure V.28 K62 intermittency parameter μ with respect to Re_λ for the data sets A to G, E' and G' are the data sets using straight blades . . . 151

Figure V.29 PSD of the raw hot-wire signal in the anti-contra configurations of the SHREK experiment in HeII at T = 2.0K [$d_w = 1.27\mu m$ and $l_w = 300\mu m$; $\mathcal{F}_1$ and $\mathcal{F}_2$ denotes the frequency of top and bottom turbine respectively (see data set G in table 6 where $\mathcal{F}_1 = \mathcal{F}_1$)] 152

Figure V.30 Calibration of the hot-wire and PSD in HeII at T = 2.0K in the SHREK experiment with straight blades for von Kármán flow configuration: +1.0(H) -1.0(B) [$d_w = 1.27\mu m$ and $l_w = 300\mu m$] 154

Figure V.31 Third order structure function S_3 compensated by the scale r with respect to the scale $\frac{r}{L}$ for HeI and HeII in the SHREK experiment performed with straight blades for the anti-contra flow configuration: + 1.0(H) - 1.0(B) [A vertical black-dashed line indicates the spatial filter of the hot-wire at $l_w \approx 300\mu m$]. 155

Figure V.32 Phenomenon of intermittency in superfluid at T = 2.0K 156

Figure V.33 p^{th} order structure function T_p for order p = 2 to 7 in HeII at T = 2.0K [For clarity the structure functions are shifted arbitrarily in the vertical direction] 157

Figure V.34 Estimation of scaling exponents ζ_p based on ESS in HeI and HeII and its comparison with other intermittency models 158

Figure VI.1 Fulfillment of Chapman-Kolmogorv equation (i.e. Markov property) for the SHREK experimental data [$\lambda \approx 400\mu m$, $r_1 = \lambda$ and $\delta = \lambda$] 163

Figure VI.2 Estimation of Einstein–Markov length based on the Wilcoxson test for the +0.8Hz co-rotation configuration of the SHREK experiment with curved blades [$l_{EM} \approx 442\mu m$ and $\lambda \approx 468\mu m$] 165

Figure VI.3 Markovian process at $\delta \approx 400\mu m$ [$r_1 = \lambda$] 166

Figure VI.4 Non-Markovian process at $\delta \approx 100\mu m$ 167

Figure VI.5 Conditional moments of first and second order with respect to scale separation δ at scale $r_2 = \frac{L}{2}$ and for velocity increment $u_{r_2} = 0 \pm 0.1$ 169

Figure VI.6 Drift and diffusion coefficient for +1.2Hz co-rotation configuration in the SHREK experiment with turbine with radial blades 171

Figure VI.7 Contour plots showing experimental and reconstructed conditional PDFs using short time propagator 173

Figure VI.8 Comparison of experimental ($p_{exp}(u_{r_1})$) and reconstructed ($p_{calc}(u_{r_1})$) PDF of velocity increment at various scales r_1 using the first scenario; From top to bottom $r_1 = \lambda$, 5λ, 10λ, 50λ, 100λ and $175\lambda \approx L$ where $\lambda = 450\mu m$ and $L = 0.08m$ [For better visualization, the PDFs at various scales are shifted in the vertical direction] 174

Figure VI.9 Comparison of experimental ($p_{exp}(u_{r_1})$) and reconstructed ($p_{calc}(u_{r_1})$) PDF of velocity increment at various scales r_1 using the second scenario; From top to bottom $r_1 = \lambda$, 5λ, 10λ, 50λ, 100λ and $175\lambda \approx L$ where $\lambda = 450\mu m$ and $L = 0.08m$ [For better visualization, the PDFs at various scales are shifted in the vertical direction] 175

Figure VI.10 The parameter d_{20} and d_{22} with and without the contribution of d_{21} . . 176

Figure VI.11 Comparison of experimental ($p_{exp}(u_{r_1})$) and reconstructed ($p_{calc}(u_{r_1})$) PDFs of velocity increment at various scales r_1 using the first scenario explained in section VI.2.2.1 while using $d_{21} = 0$; From top to bottom r_1 = λ, 5λ, 10λ, 50λ, 100λ and 175$\lambda \approx L$ where $\lambda = 450\mu m$ and $L = 0.08m$ [For better visualization, the PDFs at various scales are shifted in the vertical direction] 177

Figure VI.12 A "probable" trajectory of the evolution of velocity increment $|u_r|$ with respect to scale $\frac{r}{\lambda}$ 178

Figure VI.13 A "rare" trajectory of the evolution of velocity increment $|u_r|$ with respect to scale $\frac{r}{\lambda}$ 179

Figure VI.14 Evolution of $\langle e^{-\Delta S_{tot}} \rangle_N$ as a function of number of independent trajectories N on log-lin scale for the co-rotation configuration in the SHREK experiment [The horizontal blue-dashed line indicates the fulfillment of IFT i.e. $\langle e^{-\Delta S_{tot}} \rangle_N = 1$] 181

Figure VI.15 Evolution of $\langle e^{-\Delta S_{tot}} \rangle_N$ for various contra configurations 182

Figure VI.16 Validity of integral fluctuation theorem with and without the parameter d_{21} [The horizontal black-dashed line indicates the fulfillment of IFT i.e. $\langle e^{-\Delta S_{tot}} \rangle_N = 1$] 183

Figure VI.17 The parameters d_{11}, d_{20} and d_{22} as a function of $\frac{r}{\lambda}$ for the drift and diffusion coefficients plotted in figure VI.6 185

Figure VI.18 The parameters d_{11}, d_{20} and d_{22} as a function of scale $\frac{r}{\lambda}$ for various Re_λ corresponding to different configurations of flow as mentioned in table 6 . 188

Figure VI.19 Power law exponents of parameter d_{11} and d_{22} with respect to Re_λ for all the flow configurations shown in figure VI.18 189

Figure VI.20 Parameter d_{11} as a function of Re_λ for data sets A to G 190

Figure VI.21 Prefactor $\mathcal{P}_1$ in equation VI.23 with respect to Re_λ for data sets A to G 190

Figure VI.22 Parameter d_{20} as a function of Re_λ for data sets A to G 191

Figure VI.23 Parameter d_{22} as a function of Re_λ for data sets A to G 192

Figure VI.24 Prefactor $\mathcal{P}_2$ in equation VI.23 with respect to Re_λ for data sets A to G 192

Figure VI.25 Drift and diffusion coefficients in superfluid at T = 2.0K and its comparison with normal helium for +1.0(H) - 1.0(B) anti-contra configuration in the SHREK experiment with turbine with radial blades 194

Figure VI.26 Evolution of $\langle e^{-\Delta S_{tot}} \rangle_N$ with respect to independent number of trajectories N in HeI and HeII showing the validity of integral fluctuation theorem 195

List of Tables

Table 1 Dimensions of von Kármán cell in different experiments [H is the height and D is the diameter of von Kármán cell] . . . 7

Table 2 Dimensions of the cryogenic jet flow facilities in different experiments [H is the height and D is the diameter of experimental chamber; d is the nozzle diameter and z is the axial distance at which measurements were performed] . . . 8

Table 3 Reynolds number dependence on the choice of working fluid for the turbulent flow characterized by $U = 1\frac{m}{s}$ and $L = 0.5$m . . . 10

Table 4 Estimation of the mass flow rate in the HEJET facility based on different methods at $\mathcal{F}_t = 25$Hz in HeI at T = 2.4K . . . 95

Table 5 Statistical quantities of the turbulent jet flow in HeI at T = 2.4K and P = 2.5bar . . . 109

Table 6 Details of the configurations of the von Kármán flow, $\mathcal{F}_1$ & $\mathcal{F}_2$ are the frequencies of top and bottom propellers respectively . . . 126

Table 7 Various intermittency models for the scaling exponent ζ_p . . . 145

Table 8 Summary of the statistical quantities in HeI and HeII for the anti-contra configuration: +1.0(H) - 1.0(B) in the SHREK experiment performed with straight blades . . . 155

High Reynolds turbulence: Study of the inertial intermittency in axisymmetric jet and von Kármán cryogenic flows

Abstract: In this experimental thesis, we study very high Reynolds number (Re_λ) turbulent flows with emphasis on the understanding of inertial scale dynamics and intermittency. Thanks to the low kinematic viscosity of helium at low temperatures (T = 1.8 - 2.4K) we were able to study jet and von Kármán flows for Re_λ varying in a vast range between 1000 and 13000. The turbulent fluctuations of the velocity are measured thanks to home-made Wollaston hot-wires. The high values of Reynolds numbers reached in our experiments push the dissipative scales to the micron range, which unfortunately could not be resolved by our anemometers ($300\mu m$ in length), so that we limit our study to the inertial intermittency. A dedicated cryostat (HECAL) has been built and operated to calibrate the hot wires, based on the flying hot-wire technique. In order to study well established turbulent flows, we have modified the HEJET experiment already built in a previous thesis, in order to reduce the instability of the jet, by installing a new turbine better adapted to the HEJET flow. We have fully characterized this new turbine, and verified that its performance is in a good agreement with its design characteristics. However, the new turbine does not allow to solve the issue of the instability of the jet, which exhibits unusual characteristics: in particular, the fluctuations of the velocity are not Markovian, probably due to the instability of the jet induced by the lateral confinement. Most of the measurements presented in this thesis are therefore obtained in the SHREK von Kármán experiment with different kinds of flows. We verify that these very high Reynolds number flows fulfill usual scaling laws. From the study of inertial intermittency, it seems that intermittency tends to reduce as the Reynolds number increases. In order to move a step further, we apply a Fokker-Planck approach to investigate the evolution in scale of the whole PDF of the velocity increments. Indeed, this approach is valid in the SHREK flows, and the drift and diffusion coefficients derived are presented and analyzed. The Integral Fluctuation theorem (IFT) is fulfilled with a good accuracy. Our study confirms that the diffusion coefficient, strongly connected to intermittency, decreases as the Reynolds number increases, which tends to prove that K41 is a model well adapted to infinite Reynolds number flows.

Key-words: Turbulence, von Kármán flow, axisymmetric jet flow and intermittency

Turbulence à Haut Reynolds: Etude de l'intermittence inertielle dans un jet axisymétrique et un écoulement de von Kármán cryogéniques

Résumé: Dans cette thèse expérimentale, nous étudions des écoulements à très grand nombre de Reynolds (Re_λ), en nous intéressant plus particulièrement à la dynamique de la cascade turbulente et à l'intermittence. Du fait de la très faible viscosité de l'hélium aux basses températures (T = 1.8 - 2.4K), nous avons pu générer et étudier des écoulements de jet et de von Kármán dans une vaste gamme de Reynolds (Re_λ varie entre 1000 et 13000). Nous mesurons les fluctuations de vitesse avec des anémomètres à fil chaud de Wollaston qui sont fabriqués au laboratoire. Les grands Reynolds générés entrainent des échelles dissipatives dans le domaine du micron, ce qui n'est pas malheureusement accessible à nos anémomètres (de longueur typiquement $300\mu m$), de sorte que nous limitons notre étude à l'intermittence inertielle. Un cryostat (HECAL) a été construit et exploité pour calibrer les fils chauds en déplaçant ceux-ci dans un fluide initialement au repos. Afin d'étudier un écoulement bien établi, nous avons modifié l'expérience HEJET qui avait été construite dans le cadre d'une thèse antérieure. Dans le but de réduire l'instabilité du jet, nous avons installé une nouvelle turbine mieux adaptée à l'écoulement. Nous avons ainsi caractérisé cette turbine, et vérifié que ses performances sont conformes à celles attendues à sa conception. Cependant cette nouvelle turbine ne permet pas de résoudre l'instabilité du jet que nous attribuons désormais essentiellement au confinement radial de celui-ci. Ce confinement induit des phénomènes inhabituels, au nombre desquels le caractère non Markovien des fluctuations de vitesse. La plupart des mesures présentées dans ce travail sont donc obtenues dans l'expérience de von Kármán (SHREK) dans laquelle nous avons réalisé différents types d'écoulements. Nous y avons vérifié que les écoulements étudiés, de très hauts nombres de Reynolds, vérifient les habituelles lois d'échelle. Pour ce qui est de l'intermittence, il semble que celle-ci a tendance à diminuer lorsque le Reynolds augmente. Afin d'approfondir ce point, nous utilisons une approche de Fokker-Planck pour étudier l'évolution suivant les échelles des PDF des incréments de vitesse. Nous avons calculé les termes de dérive et de diffusion, et comparé les coefficients pour différents types d'écoulement. Le Théorème des Fluctuations Intégrales (IFT) est vérifié avec une grande précision. Notre étude confirme que le coefficient de diffusion, directement lié à l'intermittence, décroit lorsque le nombre de Reynolds augmente, ce qui tendrait à prouver que K41 pourrait être un modèle bien adapté pour décrire les écoulements à Reynolds infini.

Mots-clé: Turbulence, écoulement de von Kármán, écoulement de jet axisymétrique et intermittence

I INTRODUCTION

Turbulent flows are so ubiquitous in nature that one can hardly escape from experiencing them in the daily routine. Different types of flows exist in our surroundings. Out of which some flows are orderly and smooth while other flows are disordered and chaotic. Typically, the flow of a very high viscosity fluid such as engine oil at very low velocities is laminar. Laminar flows are generated when the size of object is small, the speed of flow is low or if the fluid viscosity is large. On the other hand, the fluid motion becomes highly disordered with random velocity fluctuations at very high velocities which is characterized as turbulent. Turbulent flows are generated when the size of the object is large, the flow velocity is high or if the fluid viscosity is small. The flow which alters between laminar and turbulent is called transitional flow. Thanks to the celebrated work of Osborne Reynolds in the 1880s, using his experiments we were able to establish these three basic categories of the flow namely, laminar, transitional and turbulent flow. These flows were categorized based on the Reynolds number which measures the relative importance of the inertial forces to the viscous forces. Overall, turbulence is highly irregular in space and time with a huge number of degrees of freedom which is a consequence of the non-linear feature of the Navier-Stokes equation governing the flow variables.

Our surroundings are mostly filled with different types of fluids such as air and water. A strong movement of any fluid instigated by the external forces can create turbulent flows. Because of the low viscosity of air, at high velocities we encounter turbulent flows in our surroundings. Turbulence has a very broad spectrum of occurrences in nature from everyday life to industry. Some of the examples of the turbulent flow include atmospheric flows, stratified flows, jet flows, flows in rivers and oceans and to the vast extent of the plasma, geophysical and astrophysical flows. Turbulent flows are everywhere. We face it simply while riding a bicycle and to a greater extent due to the violent and sudden motion of an airplane encountering turbulence in the atmosphere. The devastating events in the atmosphere such as cyclones and tornadoes are turbulent. Most of the flows encountered in engineering practice are turbulent. For example, in car engine the turbulent mixing of fuel-air mixture plays an important role during combustion. The efficiency of heat exchangers in various applications can be enhanced by turbulent heat transfer. The pressure drops in pipes are deeply influenced by turbulent momentum transfer. Therefore, looking at all these examples we can realize the importance of thorough understanding of turbulent flows.

Turbulence is a challenging and at the same time an exciting topic for both fundamental and applied research. It is evident that a better understanding of the phenomenon of turbulence could help us to forecast weather and climate, to design cars, airplanes and ships, to predict the performance of fusion devices like Tokamaks and ITER. A full understanding of turbulence could help us to design better models to predict the flow behavior. So, why is the turbulence so complicated? The main reason is that with increase in Reynolds number, the flow becomes so complicated on various length scales, that it is difficult to predict completely using simple analytical and theoretical skills. Therefore, we use the computational, experimental and the statistical tools to understand the phenomenon of turbulence in a more compact manner. Fundamentally, the study of turbulent flows is inspired by the tough question which says, whether there exists an universal description of turbulent flows or not? If so, what is it? If not, it suggests that different kinds of turbulent flows have different fingerprints in terms of their flow behavior and predictability which makes the study even more difficult for researchers. Since last century until today, huge amount of efforts are being put to answer this question. To unravel this unsolved puzzle we as physicists and scientists are working continuously using the analytical, computational and experimental approaches.

I.1 Navier-Stokes equation

The Navier-Stokes equation is the cornerstone of fluid mechanics which describes the motion of a fluid at position $\boldsymbol{x}$ in the flow field and at time t given by [Landau and Lifshitz, 1987; Frisch, 1995]:

$$\rho\left[\frac{\partial \boldsymbol{u}}{\partial t} + (\boldsymbol{u}\cdot\nabla)\boldsymbol{u}\right] = -\nabla P + \mu\nabla^2\boldsymbol{u}, \tag{I.1}$$

where ρ is the fluid density, $\boldsymbol{u}$ is the flow velocity vector field, ∇ is the gradient operator, P is the pressure, μ is the dynamic viscosity of the fluid and ∇^2 is the Laplacian operator. The Navier-Stokes equation is a time dependent, non-linear, second-order partial differential equation. The analytical solutions for the Navier-Stokes equation are unobtainable except for very simple flow fields. We see that equation I.1 has four unknowns namely three velocity components and pressure, yet it represents only three equations (each equation for each component). The fourth equation is the continuity equation for the incompressible fluid flow given by:

$$\nabla\cdot\boldsymbol{u} = 0. \tag{I.2}$$

Let us introduce a characteristic velocity U and length scale L of the fluid flow. In equation I.1, the term $(\boldsymbol{u}\cdot\nabla)\boldsymbol{u}$ signifies the effects of inertia by means of advection for which the time scale corresponds to $\tau_{iner} \sim \frac{L}{U}$. The term $\mu\nabla^2\boldsymbol{u}$ describes the diffusion of momentum (i.e. viscous/frictional effects) as a consequence of finite viscosity of the fluid for which the time scale corresponds to $\tau_{visc} \sim \frac{L^2\rho}{\mu}$. Using the inertial and viscous time scales, to characterize a fluid flow we define a dimensionless parameter called Reynolds number Re given by:

$$\frac{1}{Re} \sim \frac{\tau_{iner}}{\tau_{visc}} \sim \frac{\mu}{\rho UL} \sim \frac{\nu}{UL}, \tag{I.3}$$

where $\nu = \frac{\mu}{\rho}$ is the kinematic viscosity of the fluid.

The non-linearity in the Navier-Stokes equation is due to the convective acceleration. This makes the Navier-Stokes equation difficult to solve. For very low Reynolds number flows the nonlinear terms are negligible which results into a laminar flow. However, an increase in the Reynolds number results into a chaotic motion of fluid called Turbulence which leads to large number of bifurcations and instabilities in the flow. To find the solution of Navier-Stokes equation is considered as one of the seven millennium problems proclaimed by the Clay Mathematics Institute [Clay, 2000]. The Navier-Stokes equation is very sensitive to the initial/boundary conditions (butterfly effect) such as vanishing tangential velocity at confining walls. Because of this it is non predictable and non deterministic. The diffusion term in the Navier-Stokes equation induces irreversibility. As turbulence is only predictable in a statistical sense, such randomness in the Navier-Stokes equation provokes to introduce a statistical description of turbulence.

I.2 Global picture of turbulence

The turbulence phenomenon is known to humankind from many centuries which was first depicted by the famous paintings of Leonardo da Vinci in the early sixteenth century. But, later it took centuries to establish the simplest theoretical models of turbulence mainly because of the necessary statistical probabilistic description. In 1922 Richardson [1922] proposed one of the best and meaningful definition of turbulence. This description considers that the turbulent flow is composed of eddies/scales of different sizes r. The Richardson cascade reflects the idea that at steady state when the energy is injected into the fluid at large scales ($r \approx L$) it is transferred towards smaller scales until the dissipation takes place at the molecular scales. Let us consider

a turbulent flow of characteristic velocity U and characteristic length scale L. From the dimensional analysis it follows that the rate of injection of energy $E_I \approx \frac{U^3}{L}$. The Richardson cascade states that this rate of injection of energy must be equal to the rate of transfer of energy across scales which is eventually equal to the mean dissipation rate $\langle\epsilon\rangle$ at molecular scales, where $\langle\cdot\rangle$ denotes the ensemble average of the desired quantity. Therefore the Richardson cascade implies that $\langle\epsilon\rangle \approx \frac{U^3}{L}$.

In the 1930s Taylor [1935] introduced the statistical tools for the analysis of homogeneous isotropic turbulence for the first time which served as a promising pathway to unravel turbulence. In 1941 Kolmogorov [1941] (K41) proposed three hypotheses which depict a theoretical description of statistically stationary and homogeneous turbulence. These hypotheses are based on turbulent flows with very high Reynolds number as previously defined as $Re = \frac{UL}{\nu}$.

Kolmogorov's hypothesis of local isotropy states that in a turbulent flow of sufficiently high Reynolds number the small scale turbulent eddies ($r \ll L$) show statistical isotropic behavior. Kolmogorov's first similarity hypothesis states that the statistics of these small scales is determined uniquely based on the mean dissipation rate and the kinematic viscosity of the fluid. Based on these two parameters $\langle\epsilon\rangle$ and ν, the following Kolmogorov quantities are defined [Pope, 2001]:

$$\eta = \left[\frac{\nu^3}{\langle\epsilon\rangle}\right]^{1/4}, \tag{I.4}$$

$$u_\eta = [\langle\epsilon\rangle\nu]^{1/4}, \tag{I.5}$$

$$\tau_\eta = \left[\frac{\nu}{\langle\epsilon\rangle}\right]^{1/2}, \tag{I.6}$$

where η, τ_η and u_η are the Kolmogorov scales corresponding to the space, time and velocity respectively. These are the smallest dissipation scales in the turbulent flow. For each scale r in the turbulent cascade we can attribute a local Reynolds number such as: $Re_r = \frac{U_r r}{\nu}$, where U_r is the characteristic velocity of scale r. Using the characteristic length and velocity from equation I.4 and equation I.5 we obtain the local Reynolds number of unity. This signifies that the energy cascade continues until the smallest scale at which the local Reynolds number (i.e. $Re_\eta = \frac{u_\eta \eta}{\nu}$) is unity (i.e. inertial forces are equal to viscous forces) where the viscous dissipation is totally dominant.

Kolmogorov's second similarity hypothesis states that in a turbulent flow of high Reynolds number the statistics of scale r in the range $\eta \ll r \ll L$ have universal form independent of viscosity which is only determined from $\langle\epsilon\rangle$. Based on these hypotheses we can establish the common notion of scales in the turbulent flow. The energy is injected into the flow at large scales say up to $r \approx L$. The transfer of energy occurs in the range of scales $\eta \ll r \ll L$ which is referred as the inertial range because of the dominant inertial effects of the large eddies. After the inertial range, the energy cascade continues in the dissipation range where the viscous effects are dominant at small scales. By definition, the averaged dissipation rate is determined by:

$$\langle\epsilon\rangle = \frac{\nu}{2}\sum_{i,j=1}^{3}\left\langle\left(\frac{\partial u_i}{\partial x_j} + \frac{\partial u_j}{\partial x_i}\right)^2\right\rangle, \tag{I.7}$$

where u is the fluctuating component of velocity (see section I.6.1). Expanding the above equation for the case of homogeneous isotropic turbulence, the average dissipation rate is given

by [Pope, 2001]:

$$\langle \epsilon \rangle = 15\nu \left\langle \left(\frac{\partial u}{\partial x} \right)^2 \right\rangle. \tag{I.8}$$

Let us define the longitudinal velocity increment at scale r which is given by: $u_r = u(x+r) - u(x)$. The structure function of order p is defined as $S_p(r) = \langle u_r^p \rangle$. From the Kolmogorov's second similarity hypothesis it follows that:

$$S_2(r) \propto \langle \epsilon \rangle^{\frac{2}{3}} r^{\frac{2}{3}}, \tag{I.9}$$

where the equality can be imposed using the universal constant $C_2 = 2.0$ - 2.4 [Sreenivasan, 1995]. From the second similarity hypothesis of Kolmogorov, it follows that the energy spectrum in the inertial range is given by:

$$E(k) = C\langle \epsilon \rangle^{\frac{2}{3}} k^{-\frac{2}{3}-1} = C\langle \epsilon \rangle^{\frac{2}{3}} k^{-\frac{5}{3}}, \tag{I.10}$$

where $k = \frac{2\pi}{r}$ is the wavenumber in the longitudinal direction and $C = 0.25C_2$ is the universal constant [Frisch, 1995]. The above equation is a mere consequence of the Fourier transform of equation I.9. Applying the same phenomenology of Kolmogorov to higher order structure functions gives:

$$S_p(r) = C_p(\langle \epsilon \rangle \cdot r)^{\frac{p}{3}} \sim r^{\zeta_p}, \tag{I.11}$$

where C_p depends on the nature of turbulent flow [Frisch, 1995] and ζ_p is the scaling exponent associated with p^{th} order structure function. When the structure functions behave according to equation I.11, we refer it as a scale invariance property of the flow. Equation I.11 implies that the distribution of velocity increments at a scale r in the inertial range has the same form i.e. self-similar $\left[\left\langle \left(\frac{u_r}{(\langle \epsilon \rangle \cdot r)^{\frac{1}{3}}} \right)^p \right\rangle = C_p \right]$. The Kolmogorov's hypothesis suggests that ζ_p varies linearly with respect to p such that:

$$\zeta_p = \frac{p}{3}. \tag{I.12}$$

According to K41 model given by the above equation it implies that the higher order moments of the distribution of velocity increments such as the flatness remains constant across scales. To have a more accurate estimation of ζ_p, a large inertial range needs to exist where the power law holds i.e. $\frac{L}{\eta} >> 1$.

In the turbulent flow, the dissipation is non-uniformly distributed in space and scale. Typically, in experiments we measure the statistics of turbulent flow at a single point. Thus, we use Taylor hypothesis (see section I.6.2) to calculate the structure functions in order to estimate the dissipation rate in the homogeneous isotropic turbulence. Karman and Howarth [1938] worked out the derivation of the mean dissipation rate from the structure function given by:

$$S_3(r) = -\frac{4}{5}\langle \epsilon \rangle r + 6\nu \frac{dS_2(r)}{dr}. \tag{I.13}$$

The negative sign in the above equation is the consequence of the transfer of average energy mainly (or predominantly) towards the smallest scales i.e. an irreversible process. Because of the negligible viscous effects in the inertial range the contribution of the term $6\nu \frac{dS_2(r)}{dr}$ may be neglected. Therefore, neglecting the viscous contribution in equation I.13 we get [Kolmogorov, 1941]:

$$S_3(r) \approx -\frac{4}{5}\langle \epsilon \rangle r. \tag{I.14}$$

Equation I.14 is known as Kolmogorov four-fifths law (where $C_3 = -\frac{4}{5}$) which is one of the most important and exact result and it requires stationarity, homogeneity and isotropy of the underlying flow*.

I.3 Literature survey

The study presented in this thesis is related to complex topics in different types of turbulent flows. Turbulent flows studied in this thesis involve cryogenic von Kármán flows and jet flows. This thesis include the study of scaling laws, intermittency, application of Fokker-Planck equation, integral fluctuation theorem and understanding of turbulent superfluid flows. For each of these topics vast amount of literature is available for different kinds of turbulent flows. Some of the most relevant and important work aligned with this thesis will be presented in this section.

I.3.1 Intermittency

Theory of K41 is based on the self-similarity of the structures of different sizes and do not exhibit any intermittent features. The numerical simulations of the Navier-Stokes equation in parallel with the extent of experimental analysis of turbulent flows show deviations from the K41 prediction. To study these deviations it is sufficient to examine the evolution of flatness of the distribution of velocity increments across scales. For example, Batchelor et al. [1949] had found strong intermittent events from the velocity signal measured by a hot-wire in a wind tunnel. More recently, based on the experimental observations Anselmet et al. [1984] had found that equation I.12 is not accurate, which prompted physicists to introduce intermittency corrections i.e. modifications to K41 predictions. Since then, various models of intermittency are proposed by numerous researchers. Some of the models used in the present work are mentioned here.

Landau took an objection on the universal formulation of K41 theory. He invoked that the energy transfer rate and the dissipation rate are random variables which are linked to the fluctuations in the rate of energy injection. This fact has not been taken into account in K41. This simply suggests that $\langle\epsilon\rangle^{\frac{p}{3}} \neq \langle\epsilon^{\frac{p}{3}}\rangle$. To take into account the random nature of dissipation rate, in 1962 Kolmogorov [1962] (K62) proposed the refined similarity hypothesis in which the mean dissipation rate is replaced by the local average of the dissipation rate over a sphere of radius r and volume V given by:

$$\epsilon_r = \frac{1}{V}\int_r \epsilon \, dV. \tag{I.15}$$

Kolmogorov [1962] proposed a log-normal distribution of ϵ_r (i.e. the probability density function of ln (ϵ_r) is Gaussian) which takes into account the multiplicative properties of the turbulence cascade in the inertial range (i.e. log-additive) for which the variance $(\sigma^2_{\ln \epsilon_r})$ of ln (ϵ_r) is given by:

$$\sigma^2_{\ln \epsilon_r} = A + \mu \ln\left[\frac{L}{r}\right], \tag{I.16}$$

where additive constant A depends on the macrostructure of the flow and μ is the intermittency parameter which is found to be equal to 0.2 by Anselmet et al. [1984]. In other words, equation I.16 means that the variance of ln (ϵ_r) evolves towards small scales with a power law given by: $\sigma^2_{\ln \epsilon_r} \propto r^{-\mu}$. According to K62, the intermittency model expressing the scaling exponent of the p^{th} order structure function is given by:

$$\zeta_p = \frac{p}{3} - \frac{\mu p(p-3)}{18}. \tag{I.17}$$

*For simplicity, the use of symbol $\langle\cdot\rangle$ for the mean dissipation rate is dropped for further discussion.

A dynamical version of the intermittency model proposed by Novikov [1964] is introduced by Frisch et al. [1978]. This model is based on the idea that the volume occupied by the smaller eddies decreases by a factor β as compared to the larger eddies. In this model factor β is an adjustable parameter which can vary within 0 to 1. According to this model the scaling exponents are given by:

$$\zeta_p = \frac{p}{3} + (d - D)\left(1 - \frac{p}{3}\right), \tag{I.18}$$

where D can be interpreted as fractal dimension [Mandelbrot, 1977] and d depends on the number of dimensions in the space under consideration. The quantity $d - D = \frac{\ln(\beta)}{\ln(r)}$ is referred as the codimension of the turbulent structures/scales which is exactly equal to μ in 3D space [Frisch, 1995]. By assuming $\mu = 0$ we can recover K41 model from K62 and β-model. Linked with the vortex filaments She and Leveque [1994] proposed an intermittency model based on the hierarchy of turbulent structures which leads to:

$$\zeta_p = \frac{p}{9} + 2 - 2\left(\frac{2}{3}\right)^{\frac{p}{3}}. \tag{I.19}$$

Detailed overview of all these intermittency models along with fractal and multifractal models can be found in Frisch [1995] and Anselmet et al. [1984].

The understanding of intermittency from the experiments has been put forward using different approaches in the past. So far, many researchers have studied the phenomenon of intermittency for various kinds of flows. Among all, a selection of these methods are mentioned here. Castaing et al. [1990] and Benzi et al. [1993] studied the probability density functions (PDFs) of the velocity increments at different scale separation lengths and showed the evolution of these PDFs towards small scales. Tabeling et al. [1996] studied the intermittency in high Reynolds number flows using the flatness and skewness of the probability density functions of the velocity increments. Castaing et al. [1990, 1993] and Kahalerras et al. [1998] studied the intermittency using the parameter so called "depth of the cascade". Using similar approach they introduced an intermittency dependent estimator β and showed its dependence on Reynolds number [Castaing et al., 1990, 1993; Malécot et al., 2000]. Chanal et al. [2000] studied the intermittency from the structure functions of higher orders with the help of extended self-similarity (ESS). Praskovsky and Oncley [1997] studied the dependence of K62 intermittency parameter μ and estimator β over a very large range of Reynolds number achieved in the atmospheric surface layer measurements. Chevillard et al. [2005] studied the intermittency by estimating the flatness of probability density functions of velocity increments at different scales. In this study, universal features in the inertial range has been observed independent of the Reynolds number. Later Chevillard et al. [2012] also extended these observations towards Eulerian as well as Lagrangian velocity fluctuations in turbulent flows using experimental and numerical approach. Saw et al. [2018] studied the intermittency using the estimation of exponents of structure functions up to 9^{th} order.

The use of structure functions to study the intermittency in the turbulent cascade implies the assumption of power laws in the inertial range. Numerous studies have been performed in the past to describe turbulent cascade by using an alternative approach of the Fokker-Planck equation (FPE). In fact, the Fokker-Planck equation is a model to characterize the turbulent cascade without any assumption about the power laws in the inertial range. Friedrich and Peinke [1997a] described the turbulent cascade by FPE using an experimental data set of a turbulent free jet. The validity of Chapman-Kolmogorov relation was established by Friedrich and Peinke [1997b]. Naert et al. [1997] performed the similar analysis for a low temperature helium jet. Castaing [1997] showed a link between cumulants approach and the Fokker-Planck approach by

assuming a linear drift coefficient and a quadratic diffusion coefficient with respect to velocity increments. Friedrich, R. et al. [1998] showed the fulfillment of Chapman-Kolmogorov equation for the scale separation larger than Einstein-Markov length. A very detailed discussion of Markov properties and its implications while using FPE was done using experimental data of a turbulent round jet by Renner et al. [2001]. Renner et al. [2002] performed the Fokker-Planck analysis up to the Re_λ of 1200 yet seeking the need for high Re_λ flows to establish a better understanding of the intermittent behavior of scales in the inertial range. Reinke et al. [2018] carried out such analysis for Re_λ = 153 - 996 for flows such as grid flows, jet flows and cylinder wake flows and found that each flow has its own fingerprints in terms of drift and diffusion coefficients. Ali et al. [2019] conducted a similar analysis in the wake of the wind turbine. Recently Fuchs et al. [2021c] also studied the application of FPE to the Lagrangian particles in turbulence. Seifert [2005] addressed the validity of the application of FPE using the integral fluctuation theorem. Reinke et al. [2018] and Fuchs et al. [2020] showed the validity of the integral fluctuation theorem (IFT) for various kinds of turbulent flows. For a quick and simple overview of FPE and IFT an annual review article by Peinke et al. [2019] is recommended.

I.3.2 Von Kármán flow

A flow generated with the help of rotation of two coaxial disks/turbines in a closed cylinder is called von Kármán flow. This kind of flow geometry can produce a very high level of velocity fluctuations. At the same time, using the fluid medium of very little kinematic viscosity, we can achieve a very high Reynolds number turbulent flow. This explains the interest of numerous studies of von Kármán flow in different sizes. Some of the von Kármán flow experiments with their cell size is mentioned in table 1.

Table 1: Dimensions of von Kármán cell in different experiments [H is the height and D is the diameter of von Kármán cell]

Reference	H (cm)	D (cm)	Working fluid
Douady et al. [1991]	15.6	10	water
Fauve et al. [1993]	3.2, 6, 8	10, 17.5	water
J.-F. Pinton and R. Labbé [1994]	25	20	air
Maurer et al. [1994]	4.8	6.4	helium gas
Cadot et al. [1997]	7.2, 13.5	16, 30	water/glycerol solution
Maurer and Tabeling [1998]	20	8	liquid helium/superfluid
Bourgoin et al. [2002]	40	40	sodium
Ravelet [2005]	18	18.5	water
Rousset et al. [2014]	70	78	liquid helium/superfluid

The von Kármán flows studied in this thesis belong to the SHREK experiment described in Rousset et al. [2014]. From the above table we can see that the SHREK experiment is largest in size compared to other von Kármán flow facilities. In addition to that, the lower kinematic viscosity of normal helium/superfluid allows to study very high Reynolds number flows in the laboratory environment (see section I.4).

I.3.3 Cryogenic jet flows

In this thesis, study of round axisymmetric cryogenic jet flows is presented. Similar jet flows were studied in the past to study statistics and intermittency at cryogenic temperatures. Cryogenic jet flow facilities are basically built to mimic free turbulent jet flows. But, because of the limited

size of the cryostat used in the cryogenic jet flow facilities these jet flows are intrinsically confined jet flows. Table 2 summarizes the dimensions of the different cryogenic jet flow facilities.

Table 2: Dimensions of the cryogenic jet flow facilities in different experiments [H is the height and D is the diameter of experimental chamber; d is the nozzle diameter and z is the axial distance at which measurements were performed]

Reference	H (cm)	D (cm)	d (mm)	$\frac{z}{d}$	Working fluid
Chabaud [1992] Naert et al. [1997] Chanal [1998] [CRTBT]	35	14	2	40-50	helium gas
Pietropinto et al. [2002] [GReC]	250	110	25	50	helium gas
Duri [2012] [HEJET]	45	20	5	60	liquid helium/superfluid
present study [HEJET]	45	20	5	50	liquid helium/superfluid

I.3.4 Turbulence in superfluid

Below the temperature T = 2.17K at saturated vapor pressure, liquid helium exhibits physical properties which can only be expressed by using a full quantum mechanical model (quantification of vorticity). Such state which shows the quantum features of helium is referred as superfluid (see section I.4 for more details). In this thesis, high turbulent intensity superfluid flows are studied with the help of the SHREK and HEJET facilities using local hot-wire measurements. The turbulence in superfluid is investigated in order to address the validity of theories of K41 and K62 for the limiting case of very high Reynolds number flows. The first experimental energy spectra in turbulent superfluid flows were reported by Maurer and Tabeling [1998] where they measured local pressure fluctuations in the von Kármán flow at T = 1.4K. From these measurements they found the existence of a Kolmogorov spectrum in the inertial range of turbulent superfluid flow. Salort et al. [2010] measured turbulent velocity fluctuations in superfluid down to T = 1.55K using stagnation pressure probes in grid and wake flows. In this study they observed classical energy spectrum in turbulent superfluid flow. Barenghi et al. [2014] also observed classical Kolmogorov spectrum in superfluid wind tunnel at T = 1.56K. Recently Durì et al. [2015] also reported Kolmogorov-like spectra in superfluid jet flows at temperatures down to T = 1.76K. Very recently Diribarne et al. [2021b] also reported Kolmogorov spectrum in the low intensity turbulent grid flow at T = 2.13K.

I.4 Why Helium?

Helium is the first noble gas in the periodic table and it has very interesting properties. Two isotopes of helium are commonly used in the laboratory: ^{3}He and ^{4}He. ^{4}He is more abundant in nature and less expensive than ^{3}He. Because of this reason, its use in the laboratory is very common for a wide range of applications. Helium is the only element which stays in liquid state until the absolute zero temperature at atmospheric pressure. The superfluid transition in ^{4}He occurs at T = 2.17K whereas in ^{3}He it occurs at around T = 2.6mK. In the present work, only ^{4}He is used as the cryogenic working fluid in the experiments. Figure I.1 shows the pressure-temperature phase diagram of ^{4}He. From the phase diagram we can distinguish four different phases of helium. Contrary to other common liquids there is no triple point in

the phase diagram of helium. Helium exhibits two different liquid phases. Normal helium or liquid helium typically denoted by 'HeI' is characterized by the properties of typical classical liquids which follow Navier-Stokes equation. Another liquid phase of helium is called Superfluid typically denoted by 'HeII', which has very exceptional properties described by microscopic quantum effects. At saturated vapor pressure of about 50mbar and T = 2.17K lambda point exists. The line separating normal helium from the superfluid helium is called the lambda line. The transition temperature decreases while increasing the pressure as shown by lambda line in figure I.1. Saturated HeI line separates normal liquid from helium gas whereas saturated HeII line separates superfluid from helium gas. The solid phase of helium can only be attained by applying an external pressure more than 25bar. The critical point of helium is at T = 5.2K and P = 2.2bar. Above this pressure helium is in single phase which is referred as supercritical helium. At ambient pressure of 1bar normal helium boils at T = 4.2K. Typically, all the experiments in this thesis are performed at an absolute P = 2.5 - 3.0bar and T = 1.7 - 2.4K. In this work, hot-wires are used as the primary tools for turbulence flow measurements. From figure I.1 it is evident that in liquid helium and at P < 2.2bar a heated hot-wire is exposed to the risk of cavitation because of the phase transition. As the hot-wires are very fragile this could result in the breaking of the hot-wire. Moreover, in this case the heat transfer is no longer based on single phase convection. Therefore, to avoid this, the hot-wire measurements are always performed at an absolute P = 2.5 - 3.0bar where the hot-wire operates in the supercritical region.

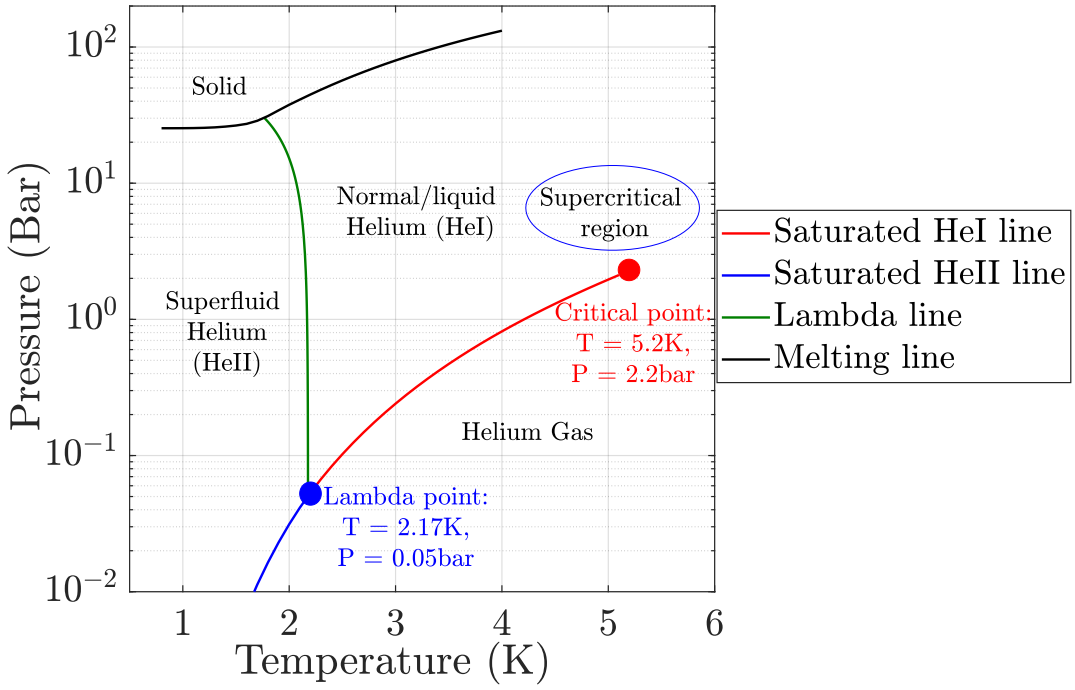

Figure I.1: Phase diagram of ^{4}He [The phase diagram is constructed using the data obtained from HEPAK (computer program to estimate thermophysical properties of helium)]

Below the transition temperature T = 2.17K, helium shows some unusual properties. Indeed, HeII can behave as an inviscid fluid, where heat conduction itself cannot be described in terms of a bulk thermal conductivity. These two unique properties (viscosity and heat transfer) give rise to spectacular effects, like the fountain effect. The existence of quantized vortices in ^{4}He (similar to other Bose-Einstein condensates) is another illustration of quantum effects in ^{4}He. Below T

= 2.17K helium can be modeled as a mixture of normal fluid and superfluid having the density of ρ_n and ρ_s respectively [Tisza, 1938]. In this model, normal helium carries the entropy whereas superfluid does not. Normal helium has a finite viscosity whereas superfluid has no viscosity. The total density of superfluid helium is expressed by $\rho = \rho_s + \rho_n$. Figure I.2 shows the superfluid density fraction $\left(\frac{\rho_s}{\rho}\right)$ and normal helium density fraction $\left(\frac{\rho_n}{\rho}\right)$ below T = 2.17K. This figure shows that at T = 2.17K the total density $\rho = \rho_n$ whereas at T = 1.0K the total density $\rho \approx 0.99\rho_s + 0.01\rho_n$ and at T $\approx$ 0K the total density becomes $\rho \approx \rho_s$ [Van Sciver, 2012]. The heat transfer in HeII is fundamentally different from other conventional fluids. Indeed, heat is transported by the normal component flowing in opposite direction to the superfluid component. The Fourier's law of heat transfer applicable in classical fluids (such as HeI) is not valid in HeII (for more details see equation 6.73 in Van Sciver [2012]). The "effective" thermal conductivity of superfluid depends on the length and cross-sectional area of the duct. Typically, for a duct of cross-sectional area 1cm^2 with a length of 10cm the effective thermal conductivity at T = 2.0K is $2\frac{kW}{m \cdot K}$ which is an order of magnitude greater than for pure copper at low temperatures. This is why superfluid can be used to transport a large amount of heat [Claudet, 1981]. For example, superfluid is used to evacuate a large amount of heat to maintain the superconducting magnets at T = 1.9K at CERN.

Let us consider a turbulent flow on a laboratory scale characterized by the flow velocity of $U = 1\frac{m}{s}$ and energy injection scale of L = 50cm. Table 3 provides the Reynolds number attained using different working fluids in the experiments. In case of SF_6 higher pressure is required to lower the kinematic viscosity significantly. This table shows that we can increase Re from $\mathcal{O}(10^4)$ to $\mathcal{O}(10^7)$ simply by changing the working fluid from air to helium. We can imagine that to produce Re $\approx \mathcal{O}(10^7)$ using air as a working fluid, we would need a very high flow velocity in a very big size experiment. Building such kind of bulky experimental facilities is very difficult in the perspective of design, construction, cost and power consumption. On the other hand, we can construct experimental facilities on a laboratory scale which can operate using helium as a working fluid, so that we could study turbulent flows at Re $\approx \mathcal{O}(10^7)$ or even more.

Table 3: Reynolds number dependence on the choice of working fluid for the turbulent flow characterized by $U = 1\frac{m}{s}$ and L = 0.5m

Working fluid	Temperature (K)	Pressure (Bar)	Kinematic viscosity $(\frac{m^2}{s})$	Re = $\frac{UL}{\nu}$
Air	293	1	1.5×10^{-5}	3.0×10^4
Water	293	1	1.0×10^{-6}	5.0×10^5
SF_6	273	10	1.8×10^{-7}	2.7×10^6
Helium gas	4.5	1	0.9×10^{-7}	5.5×10^6
Liquid helium (HeI)	2.2	1	2.1×10^{-8}	2.3×10^7
Superfluid helium (HeII)	1.8	1	9.6×10^{-9}	5.2×10^7

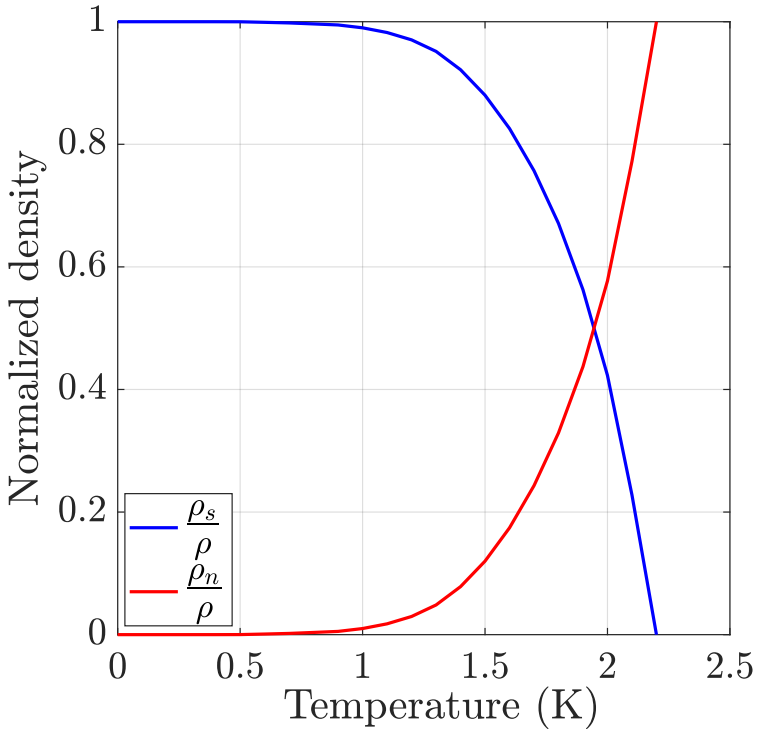

Figure I.2: Normalized density (density fraction) of superfluid $\left(\frac{\rho_s}{\rho}\right)$ and normal helium $\left(\frac{\rho_n}{\rho}\right)$ below T = 2.17K (source: HEPAK)

I.5 Challenges, motivations and objectives of the thesis

Theories such as K41 and K62 are derived for turbulent flows in the limit of very large Reynolds numbers. The assumption of homogeneous isotropic turbulence also simplifies the analysis by great extent. Such renowned theories assume the local isotropy of small scales in the turbulent flow. Experiments help to demonstrate the validity of such theories. The main motivation of this thesis is to address the validity of such theories at very high Reynolds number flows using laboratory scale experiments. As of today, the numerical simulations of high Reynolds number turbulent flows is very difficult because the number of degrees of freedom in turbulent flow grows very fast with respect to Reynolds number. In fact, it can be shown that in 3D turbulent flows the number of degrees of freedom $\sim \left(\frac{L}{\eta}\right)^3 \sim Re^{\frac{9}{4}}$ [Frisch, 1995]. This explains the motivation of building laboratory scale cryogenic facilities to study high Reynolds number turbulent flows.

All experiments in this thesis are conducted at cryogenic temperatures of T = 1.7K to 2.4K. Performing successful experiments at cryogenic temperatures is both exciting and challenging at the same time. The topics studied in this thesis are very broad, which offers the possibility to dive into many different directions. In what follows, we present a brief outline and motivations behind each objective of this thesis.

To achieve the objectives of this thesis the first and foremost requirement is the fabrication of home-made hot-wires (HW). This is because of the non availability of commercial sensors which can measure turbulent velocity fluctuations at cryogenic temperatures. Typically, the spatial resolution of the home-made hot-wires is of $300\mu m$ having a diameter of $1.27\mu m$. Manufacturing such a small-sized hot-wire sensor merely by using hand skills is a very challenging task. Therefore, to fabricate each hot-wire successfully, multiple attempts are required. These hot-wires are extremely fragile and even little vibrations/shocks can result into breaking of the hot-wire.

Because of their extreme delicacy, mounting and demounting of hot-wires in the experimental set-up is a very challenging task. To withstand the contraction forces during cool down process is one of the critical phase for the home-made hot-wires. Typically, in each experiment only 1 out of 4 hot-wires survives during the cool-down process. Possible reasons for breaking of the hot-wires include vibrations, shocks, inadequate soldering of hot-wire on to the prongs, non-uniform bending of hot-wire, excessive and differential contraction forces during cool-down process. This reveals the complexity and challenge of the cryogenic experiments in this thesis. To measure the turbulent statistics at very high Reynolds number flows, the spatial and temporal resolution of the hot-wire must be as high as possible. Hence to determine the frequency response (time constant) of home-made hot-wires, their characterization is done in the SHREK and HECAL experiments.

The objective of the HECAL cryostat is to perform precise and accurate hot-wire calibration at cryogenic temperatures. In this thesis a significant amount of time is devoted to the optimization of the instrumentation in the HECAL facility. For the first time, a successful calibration of the hot-wire in the HECAL facility is obtained. The idea is to use the HECAL facility to calibrate the hot-wire at cryogenic temperatures and install the same hot-wire in the HEJET and SHREK facilities. In this way, very precise and accurate hot-wire calibrations can be used to study the statistics of von Kármán and jet flows.

In the SHREK experiment the von Kármán flow is generated using turbines equipped with blades, whereas in the ECOUTURB experiment, the von Kármán flow is generated using smooth disks (turbine without any blades) focusing on torque measurements. Successful execution of the SHREK, ECOUTURB and HEJET experiments along with the local velocity measurements using the home-made hot-wires is one of the objectives of this thesis. The HEJET experiment is a closed circuit wind tunnel facility to generate turbulent jet flows at cryogenic temperatures. All cryogenic experiments performed in this thesis are complex, which needs much advanced planning. These experiments cannot be performed on a day-to-day basis. To have successful measurements from the SHREK/ECOUTURB experiment we need at least 3 - 4 months, whereas for the HEJET/HECAL experiment we need at least 3 - 4 weeks of advanced planning. The SHREK experiment allows to study turbulent flows of Re_λ =1000 - 13000 whereas the HEJET experiment allows to study turbulent jet flows of Re_λ =2000 - 3000 (see section I.6.9 for the definition of Re_λ). The uniqueness of the SHREK and HEJET facilities lies in their capability to generate very high Reynolds number turbulent flows in the laboratory.

To maintain a constant flow rate in the wind tunnel of the HEJET facility a centrifugal pump is used. The novelty of the HEJET experiment in this thesis is the design, manufacturing and testing of the new turbine of the centrifugal pump. Indeed, a new turbine in the HEJET facility is manufactured to improve the stability of the turbulent jet flow. Multiple HEJET experiments are performed in order to ensure the precise installation of the new turbine. The characterization of this newly designed centrifugal pump is an important aspect of this thesis. The scaling laws and intermittency phenomenon studied for the classical turbulence are addressed for very high Reynolds number turbulent flows using the SHREK and HEJET experiments.

The final objective of this thesis is to study the statistical intermittency of turbulent flows using a Fokker-Planck modelization and to address the validity of integral fluctuation theorem at very high Reynolds number flows. This is the first time the intermittency in turbulent flows is studied at such high Re_λ of $\mathcal{O}(10^4)$ using laboratory scale experiments.

This thesis is mainly dedicated to study turbulent flows in classical fluids such as normal helium (HeI). During each experiment of HECAL/HEJET/SHREK, there is always a possibility to acquire and explore the measurements in superfluid. Although, study of superfluid turbulent flows is not the goal of this thesis, an attempt is made to better understand the hot-wire response in superfluid turbulent flows. With this spirit, numerous experimental observations are made

in each of the HECAL, HEJET and SHREK experiments. These observations are put forward using the hot-wire calibration, power spectral density, investigation of intermittency, validity of Fokker-Planck equation and integral fluctuation theorem in superfluid turbulent flows.

I.6 Statistical quantities of turbulence

Different kinds of turbulent flows occur in nature as well as in engineering industries. Statistics is the tool which helps to differentiate and classify various kinds of turbulent flows. In this section, the methods used for the estimation of statistical quantities of turbulence will be discussed in detail with examples. The aim of this section is simply to introduce the basic terminologies used in this entire work, their interpretation and to show the procedure to estimate those quantities.

I.6.1 Velocity of the flow

A turbulent flow is characterized by its mean velocity and velocity fluctuations. Figure I.3 shows the raw signal of the hot-wire voltage in the top part and the corresponding velocity signal in the bottom part during a period of 1s with an acquisition frequency of 50kHz. The hot-wire is operated in the mode of constant current anemometry (CCA). In CCA mode the voltage across the hot-wire decreases with increase in velocity. In the turbulent flow assumed to be statistically stationary, the velocity is a random variable carrying fluctuations. A statistically stationary turbulent flow is the one in which the statistics of the flow remains constant with respect to time. From figure I.3, we see that the turbulent velocity fluctuates around mean flow, which is a typical signature of statistically stationary turbulent flow. From a visual inspection, we see that the flow contains structures of varying scales. The velocity in figure I.3 can be expressed as:

$$U = \langle U \rangle + u, \tag{I.20}$$

where $\langle \cdot \rangle$ stands for an ensemble average, U is the instantaneous velocity, $\langle U \rangle$ is the mean velocity and u is the fluctuating velocity component of the flow.

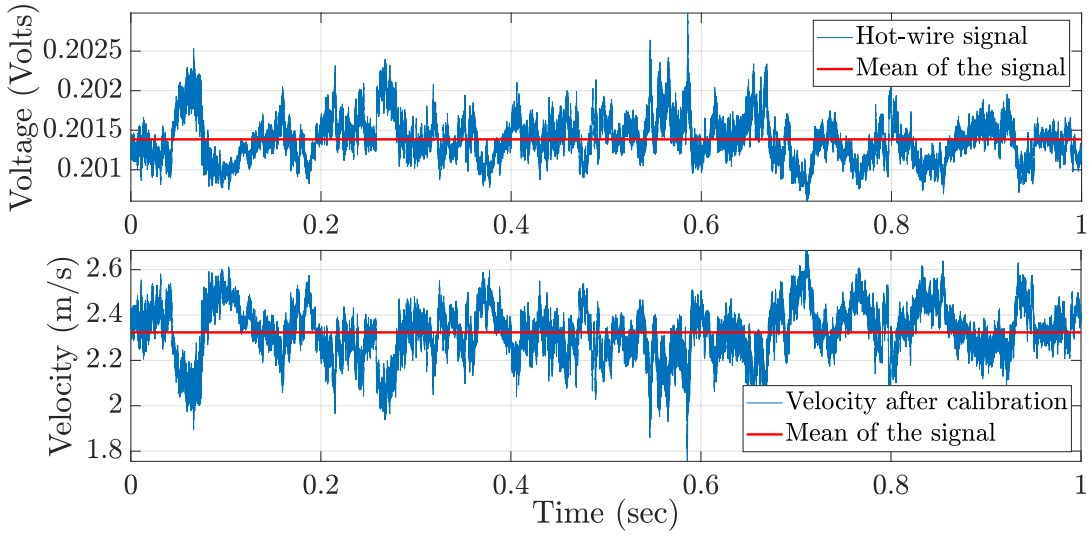

Figure I.3: Raw hot-wire signal before and after the calibration using CCA mode in the SHREK facility using straight blades for the co-rotation configuration at 1.2Hz

I.6.2 Taylor hypothesis

The hot-wire temporal signal, such as discussed in section I.6.1 is measured at a fixed location in space. But, in order to estimate the structure functions and auto-correlation at scale r, we need the velocity data at different locations in space separated by a distance r. Ideally, this can be done by moving the hot-wire in the direction of the flow, but in experiments most of the times this is not possible. Hence, in turbulent flow measurements, it is a common practice to convert temporal velocity series into spatial series using the Taylor hypothesis of frozen turbulence [Taylor, 1938]. This hypothesis tells us that the fluctuations can be considered to be advected to the hot-wire sensor with the mean velocity of the flow, in the direction of the flow. Therefore, a temporal dimension τ can be simply converted into the spatial dimension r using the relation $r = -\langle U \rangle \tau$. This hypothesis is most accurately applicable for the turbulent flows with less than 10% of turbulent intensity. As advection is the basic assumption of this hypothesis, the turbulent flow must have a sufficient mean velocity, which is always true for the experimental data considered in this work.

This hypothesis needs a special attention when the velocity fluctuations are comparable to the mean velocity of the flow. This is the case in the SHREK and HEJET experiments, where the turbulent intensity can reach up to 40%. Hence, in such cases a correction to the Taylor hypothesis has been introduced by J.-F. Pinton and R. Labbé [1994]. A detailed algorithm to convert the temporal velocity series into equally spaced velocity series has been discussed by Kahalerras et al. [1998], the same algorithm is used here for the demonstration. Basically, this method is based on the use of instantaneous velocity for advection rather than the mean velocity of the flow. The corrected Taylor hypothesis is applied to the contra configuration +1.0(H) - 1.0(B) of the SHREK experimental data having 38% of turbulent intensity to see its effects. +1.0(H) represents the frequency of the top turbine whereas -1.0(B) represents the frequency of bottom turbine in Hz in the SHREK facility (see section V.1.3 for more details of the flow configurations).

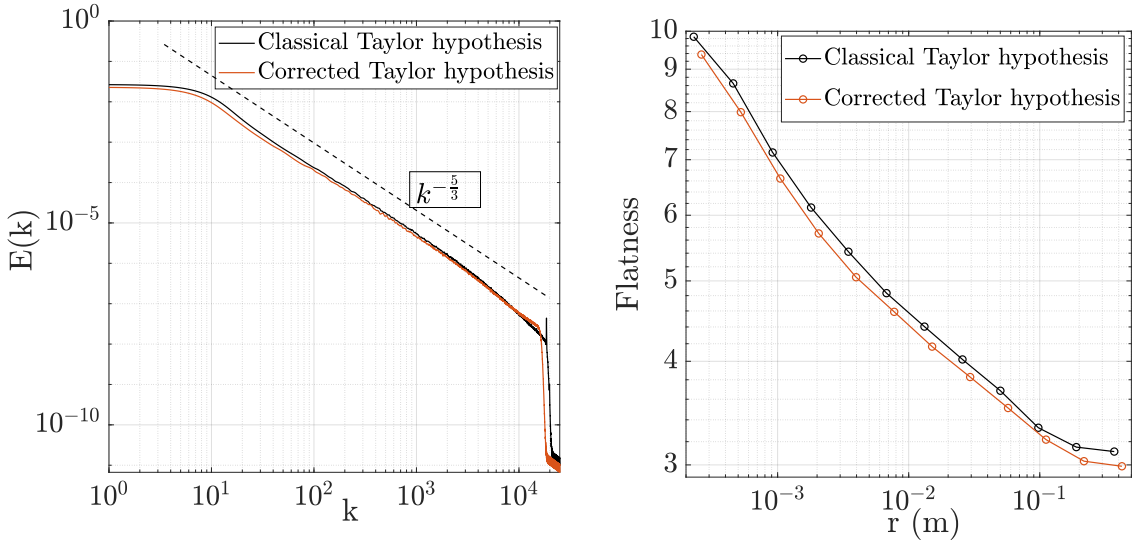

(a) Power spectrum with respect to wavenumber on log-log scale

(b) Flatness of PDFs of velocity increment with respect to scale r on the log-log scale

Figure I.4: Comparison of classical and corrected Taylor hypothesis on the SHREK experimental data of contra configuration: +1.0(H) - 1.0(B)

In figure I.4 the power spectrum is plotted in the wavenumber domain on a log-log[†] representation which shows the effect of corrected Taylor hypothesis over the classical Taylor hypothesis. The first observation is that the slope of $k^{-\frac{5}{3}}$ is maintained within the inertial range with or without the correction. At very high wavenumbers, a slight change in the spectrum can be observed. This particular behavior after applying the corrected Taylor hypothesis has also been observed by J.-F. Pinton and R. Labbé [1994] and Kahalerras et al. [1998]. To investigate the effects of corrected Taylor hypothesis on the intermittency, the flatness of probability density functions (PDFs) of velocity increment at different scales is estimated[‡]. Figure I.4b shows the flatness of PDFs of the velocity increments with respect to the scale r in the inertial range. From this figure, we see that the corrected Taylor hypothesis tends to drive the statistics towards Gaussian distribution. Interestingly, the difference of flatness using these two methods from integral scale L ($\approx 0.2m$) down to the Taylor microscale λ ($\approx 300\mu m$) is constant, which is about 5%. This means that a constant error of 5% is attributed to the use of classical over corrected Taylor hypothesis. On the other hand, it has been found that this error grows towards smaller scales in the dissipation range [Kahalerras et al., 1998]. This thesis mainly addresses the intermittency in the inertial range, hence the use of corrected Taylor hypothesis has not been implemented on the data. The single hot-wire temporal measurements are therefore devoted to access longitudinal statistics of the stream wise component of the velocity field using classical Taylor hypothesis.

I.6.3 The power spectrum

An information from the hot-wire signal or velocity signal can be deduced from the power spectrum. Figure I.5 shows different representations of the power spectrum with respect to frequency f and wavenumber k on a log-log plot. The top-left corner shows the power spectral density (PSD) with respect to frequency with the well known slope of $f^{-\frac{5}{3}}$. A very large inertial range over a span of 3 decades can be observed in figure I.5 which belongs to the contra configuration (+1.0(H) - 1.0(B)) in the SHREK facility. We see that the power spectrum shows peaks at high frequencies. The exact origin of these high frequency peaks is still unknown, but it could be associated with the vibrations in the experimental assembly or the vibrations of the hot-wire prongs themselves [Duri, 2012].

Figure I.5 shows the power spectrum before and after applying a low-pass digital filter on the velocity signal. The data is acquired using the system from National Instruments composed of a controller NI PXIe-8820 within a chassis of NI PXIe-1071. Either NI PXIe-4464 or PXI-4462 data acquisition cards are used to record the signal, in which the anti-aliasing filter has been enabled by default. Most commonly, a sampling frequency of 50kHz is used for the data acquisition. A low-pass filter at about 5kHz is applied after the anti-aliasing filter to remove the high frequency peaks present in the signal using a 4^{th} order butterworth filter in MATLAB. Moreover, we note that the cut-off frequency associated with the thermal time constant (temporal filter) of the hot-wire ranges within 5 - 13kHz depending on the mean velocity of the flow (see section II.7 for more details). The temporal filter causes the attenuation of the velocity fluctuations at frequencies higher than the cut-off frequency.

The power spectrum in the wavenumber domain is given by $E(k) = \frac{E(f)\langle U\rangle}{2\pi}$. The top-right corner represents the power spectrum in wavenumber $k(m^{-1}) = \frac{2\pi f}{\langle U\rangle}$ domain which also shows the famous $k^{-\frac{5}{3}}$ slope predicted by Kolmogorov (see Equation I.10). In top-right figure, the vertical black-dashed line represents the spatial filter of the hot-wire of length $l_w \approx 300\mu m$ at the

[†]Throughout this thesis the power spectrum and other figures on the log-log or semi-log scale are plotted using the base 10 logarithmic function, unless otherwise stated.

[‡]The notion of intermittency and flatness are introduced in detail in section V.9

wavenumber $k_w = \frac{2\pi}{l_w}$. The finite probe length acts as a spatial filter (low-pass) for the velocity fluctuations on the scale comparable to the hot-wire length. The dissipation spectrum is given by $E(k) \cdot k^2$. The bottom figure shows the dissipation spectrum with respect to wavenumber. From the dissipation spectrum, we see that the dissipation increases towards high wavenumbers i.e. smaller scales until the cut-off frequency. The dissipation spectrum can be used to estimate the mean dissipation rate in the turbulent flow (see section I.6.7).

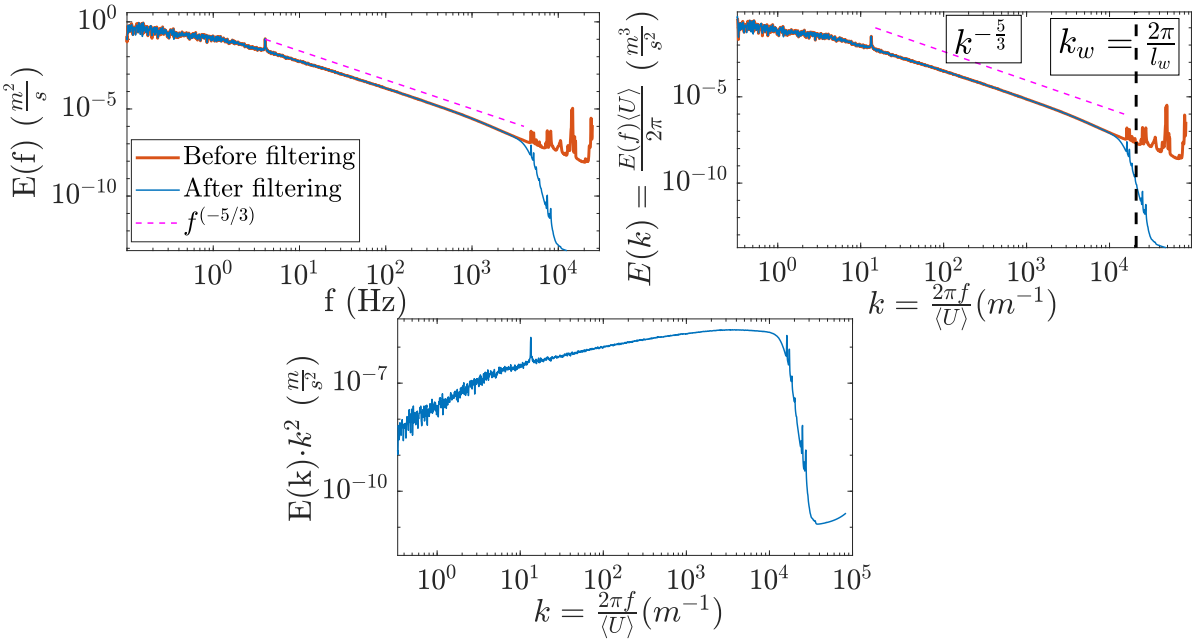

Figure I.5: Different representations of power and dissipation spectrum on a log-log scale in the frequency f and wavenumber k domain for the contra configuration: +1.0(H) - 1.0(B) in the SHREK facility

I.6.4 Turbulence intensity of the flow

The turbulent intensity of the flow ($\mathcal{I}$) is defined as the ratio of the root mean square velocity of fluctuations (u_{rms}) or the standard deviation of instantaneous velocity (U_{std}) over the mean velocity of the flow expressed as:

$$\mathcal{I} = \frac{u_{rms}}{\langle U \rangle}. \tag{I.21}$$

Turbulence intensity quantifies the importance of velocity fluctuations as compared to the mean flow. Figure I.6a shows the root mean square velocity of fluctuations, u_{rms} for different flows while increasing the turbine frequency in the SHREK experiment. $\mathcal{F}_1$ denotes the frequency of the top turbine whereas $\mathcal{F}_2$ denotes the frequency of the bottom turbine in Hz. We see that the u_{rms} increases with respect to increase in the turbine frequency for any kind of flow configuration. This figure shows that for the same amount of forcing the anti-contra configuration ($+\mathcal{F}_1$(H) - $\mathcal{F}_2$(B)) has highest u_{rms} and it is smallest for the co-rotation configuration of flows.

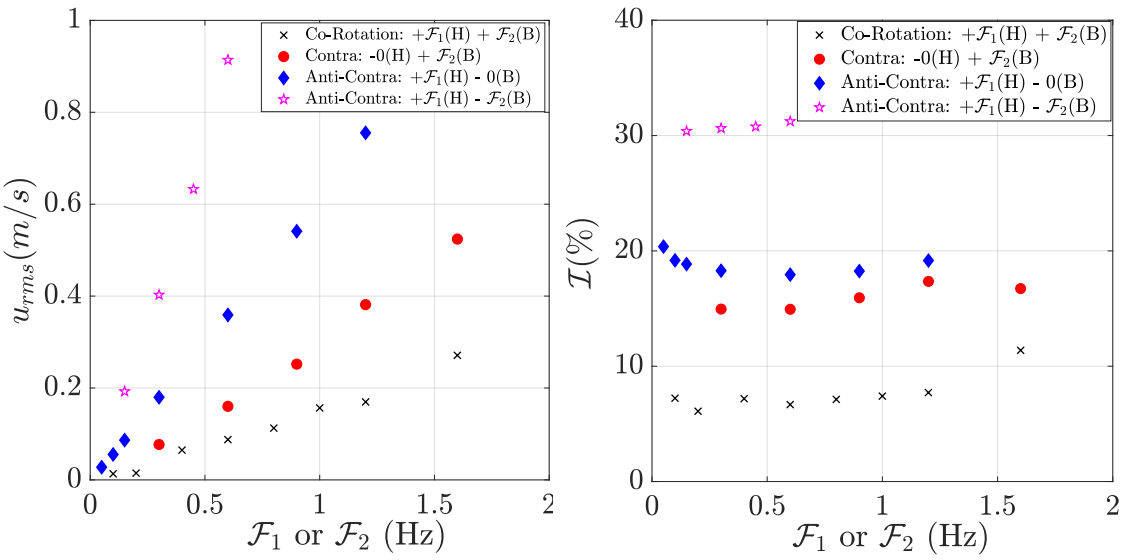

(a) RMS velocity of fluctuations with respect to applied forcing

(b) Turbulence intensity with respect to applied forcing

Figure I.6: Variation of u_{rms} and $\mathcal{I}$ with respect to turbine frequency $\mathcal{F}_1$ or $\mathcal{F}_2$ in the SHREK experiment using curved blades

Figure I.6b shows the turbulent intensity for different configurations of the von Kármán flow in the SHREK experiment with respect to turbine frequency. The turbulent intensity does not show any strong dependence on the Reynolds number i.e. applied forcing through the turbine frequency, although it shows strong dependence on the configuration of the von Kármán flow. From this figure, we see that the turbulent intensity is smallest for co-rotation configuration. The maximum of the turbulent intensity is observed in the "anti-contra" configuration. Overall, in the SHREK facility depending on the flow configuration a turbulent intensity of 5 - 40% is observed which is in accordance with the previous studies carried out for the von Kármán flows [N. Mordant et al., 1997].

I.6.5 Autocorrelation coefficient

The autocorrelation coefficient R_{uu} is defined as:

$$R_{uu}(r) = \frac{\langle u(x)u(x+r)\rangle}{\langle (u(x))^2\rangle}, \tag{I.22}$$

where u is the fluctuating component of velocity and r is the distance between two points in which the correlation is estimated. To obtain the spatial velocity at $u(x)$ we apply Taylor hypothesis of frozen turbulence. A typical autocorrelation coefficient plot for one of the configurations of the von Kármán flow is shown in figure I.7.

This autocorrelation coefficient belongs to the co-rotation configuration at $\mathcal{F}_1 = \mathcal{F}_2 = 1.2$Hz in the SHREK experiment. We see that the autocorrelation coefficient does not converge to zero at large scales: at large scales it oscillates in a periodic manner with a distance between two peaks of ≈ 0.6m. In this experiment each of the top and bottom turbine is equipped with 4 radial blades. Thus, the circumferential distance between two adjacent blades is also ≈ 0.6m (see figure V.1). In the time domain, the periodic oscillations in the autocorrelation coefficient occurs at a time difference of ≈ 0.2s while operating the SHREK experiment at $\mathcal{F}_1 = \mathcal{F}_2 =$

1.2Hz ($\langle U \rangle = 2.52\frac{m}{s}$ at the hot-wire location). And, 0.2s corresponds to the periodicity of each of the blades of the turbine i.e. $\frac{(1/1.2Hz)}{4} \approx 0.2$s. Therefore, the periodicity at large scales in figure I.7 is rather the consequence of the temporal oscillations measured by the hot-wire in the SHREK experiment. In fact, this represents the modulation of the injection of energy in the von Kármán cell by each of the blades of the turbine. Similar observations are also reported by Moisy [2000].

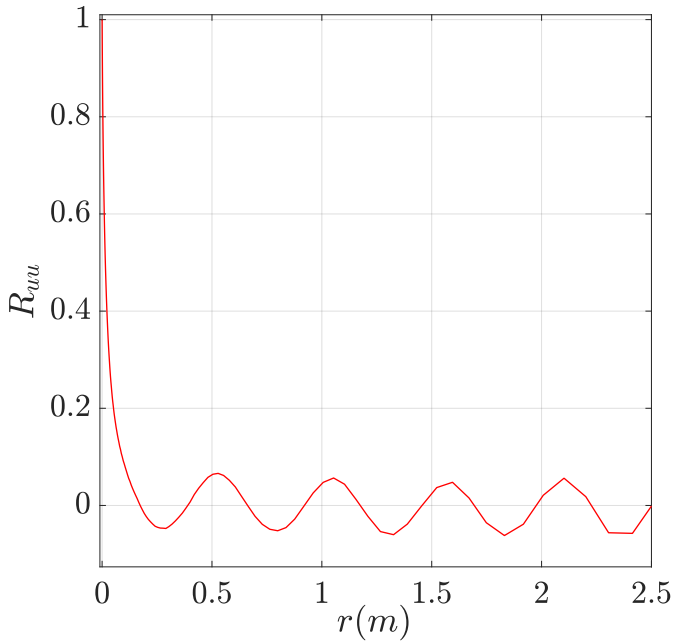

Figure I.7: Autocorrelation coefficient for the co-rotation configuration in the SHREK experiment performed with radial blades at $\mathcal{F}_1 = \mathcal{F}_2 = 1.2$Hz [Hot-wire position: close to the top turbine (15cm away from the equatorial plane)]

I.6.6 Structure functions

We know that the turbulent flow consists of eddies of different sizes r. The velocity increments between two spatial points (one scale) in the flow give information about the structures at that scale. Typically, in the experiments the longitudinal measurements are performed at a fixed spatial location. In this case, the Taylor hypothesis of frozen turbulence allows to estimate moments of the velocity increments at different scales representing the structures within the turbulent flow. The p^{th} order structure function is defined as:

$$S_p(r) = \langle (u_r)^p \rangle = \langle (u(x+r) - u(x))^p \rangle, \tag{I.23}$$

where u is the fluctuating velocity component and r is the distance separating two points on which the structure function is defined. The structure functions S_1, S_2, S_3 and S_4 represent the mean, standard deviation, skewness and flatness of the distribution of velocity increments at scale r respectively. From equation I.22 and equation I.23, one can establish a relationship between the autocorrelation coefficient and the second order structure function:

$$R_{uu}(r) = 1 - \left[\frac{S_2(r)}{2u_{rms}^2}\right]. \tag{I.24}$$

In this way the autocorrelation coefficient can be directly calculated from the structure function with the help of equation I.24. Figure I.8 shows the structure functions with respect to scale r from order $p = 2$ up to $p = 7$. This figure shows that at large scales the structure functions saturate at a constant value. Structure functions are usually characterized by a slope of p in the dissipation range, however not accessible to our measurements because of the limited spatial resolution of the home-made hot-wire. In figure I.8 a vertical black-dashed line represents the spatial filter of the hot-wire at $r \approx 300\mu m$. According to the theory of K41 the structure functions with respect to scale r in the inertial range are characterized by a slope of $\frac{p}{3}$ in the log-log coordinates. But the experimental observations suggest corrections to the theory of K41, which are referred as intermittency corrections. The scaling exponents that depart from the K41 scaling are called anomalous scaling exponents and thus the structure functions in the inertial range are anomalous.

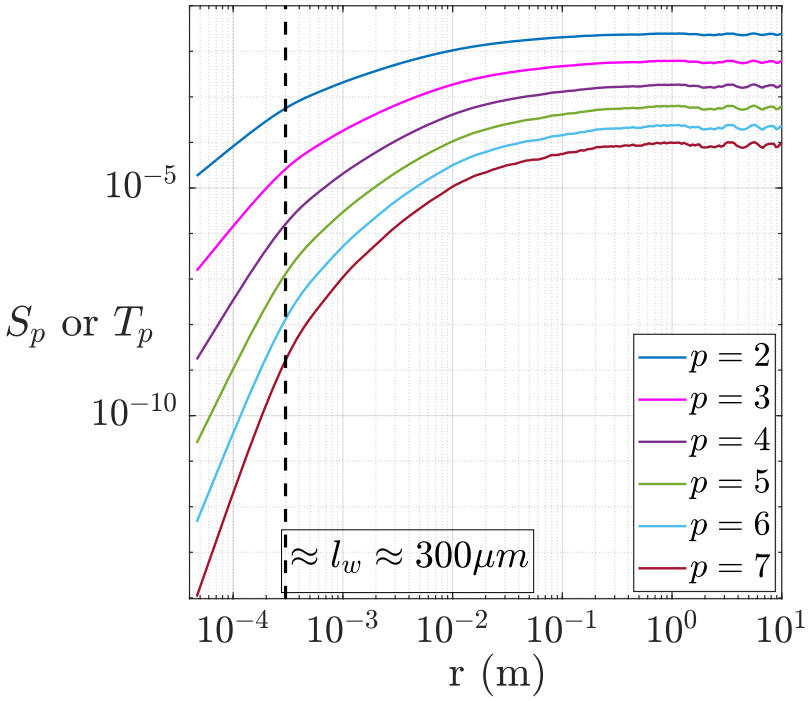

Figure I.8: p^{th} order structure function with respect to scale r for the co-rotation configuration in the SHREK experiment at $\mathcal{F}_1 = \mathcal{F}_2 = 1.2$Hz [for clarity the structure functions are arbitrarily shifted in the vertical direction and for better representation odd order structure functions are estimated using absolute values of the velocity increments given by: $T_p(r) = \langle |u_r|^p \rangle = \langle |u(x+r) - u(r)|^p \rangle$]

I.6.7 Energy budget within turbulent cascade

Basically, the energy transfer mechanism in the turbulent cascade happens in three different ways. First, the rate of injection of energy in any turbulent flow is characterized by $\frac{u_{rms}^3}{L}$ at the integral length scale L. The global energy injection rate can be directly estimated from the parameters of the experiments such as the torque and the angular velocity of the turbines in the von Kármán flow. Secondly, the injected energy up to the integral length scale transfers across the scales within the inertial range down to the scale at which viscous effects start being significant. Thirdly, the transferred energy across the inertial scales starts to dissipate into

heat because of the dominant effects of viscosity over scales of the dissipation range. From the conservation of energy principle, it follows that in steady state the rate of injection of energy at scale L, the energy transfer rate across inertial scales and the energy dissipation rate at small scales in the dissipation range must be equal.

From the velocity signal there are many ways one can estimate the rate of viscous dissipation. Based on the simple dimensional arguments of space and time, Kolmogorov [1941] proposed the estimation of dissipation from the second order structure function, introducing a universal constant C_2. The energy transfer rate and consequently the energy dissipation rate can be estimated from the second order or third order structure function in the inertial range using the following mathematical relations [Pope, 2001]:

$$\epsilon_{S_2}(r) = \frac{1}{r}\left[\frac{S_2(r)}{C_2}\right]^{3/2}, \tag{I.25}$$

$$\epsilon_{S_3}(r) = -\frac{5}{4}\frac{S_3(r)}{r}, \tag{I.26}$$

where ϵ_{S_2} and ϵ_{S_3} is the dissipation rate estimated from S_2 and S_3 respectively. C_2 is a constant within 2.0 - 2.4 [Frisch, 1995]. A proper tuning of constant C_2 leads to almost same estimate of ϵ_{S_2} and ϵ_{S_3}. We note that the dissipation rate has the units of $\frac{m^2}{s^3}$ or $\frac{W}{kg}$, hence for a known amount of fluid mass in a control volume one can estimate the power in Watts, assuming that the flow is homogeneous. Figure I.9 shows the compensated S_3 as a function of scale r for two different contra configurations of the von Kármán flow on a log-log scale. The dissipation rate is then calculated by taking the average of the energy transfer rate in the central inertial range. Therefore, from figure I.9 we estimate the dissipation rate of $0.002\frac{m^2}{s^3}$ for -0.12(H) + 0.18(B) and $0.014\frac{m^2}{s^3}$ for -0.24(H) + 0.36(B) contra flow configuration. As expected, higher forcing (i.e. higher frequency of the turbines) leads to higher dissipation rate. This figure also shows the contribution of the correction term $6\nu\frac{dS_2(r)}{dr}$ (see equation I.13) in the compensated S_3 shown by dashed line. It shows the effect of the correction term at small scales where the effects of viscosity are dominant. We see that the correction term is important typically at scales smaller than l_w (a vertical dashed-dotted line represents the spatial filter of the hot-wire at $r \approx 300\mu m$). Nevertheless, as expected we see no effect of the correction term in the inertial range and at very large scales. Hence, the correction term does not alter the estimation of the dissipation rate from the inertial range. Overall, we see that the correction term tends to drive the compensated S_3 to reach an asymptotic plateau.

In figure I.9 the two configuations of the von Kármán flow have $Re_\lambda = 2980$ and 4280 (see section I.6.9 for the definition of Re_λ). And, even at such high Reynolds numbers we do not notice a clear plateau over a range of scales in the inertial range. Such forms of the compensated third order structure functions without a clear plateau are also reported by Salort [2011] at $Re_\lambda = 1960 - 2280$. At sufficiently high Reynolds number flows we would expect a clear (and wider) plateau in figure I.9 as there is no intermittency correction associated with S_3 because of the exact Karman-Howarth relation (see equation I.14). The use of the Karman-Howarth relation implies homogeneity and stationarity of the turbulent flow. The lack of isotropy in the turbulent flow does not alter the appearance of the plateau in the compensated third order structure function. In fact, the lack of isotropy only changes the prefactor in the Karman-Howarth relation (i.e. C_3). We do not see any reason for the non stationarity in the von Kármán flow. We only know the source of non stationarity in the SHREK experiment which is related to the temporal oscillations of the injection of energy at large scales (see section I.6.5). We believe that the homogeneity may have been compromised because the hot-wire is installed quite close to the wall (40mm from the wall) of the von Kármán cell. Thus, the lack of

homogeneity might be the primary reason for the inadequacy of the plateau in the compensated third order structure function in all flow configurations of the SHREK experiment. Secondly, this range of scales in which we see a plateau-like behavior of the compensated S_3 in figure I.9 is smaller also because of the limited spatial resolution of the hot-wire sensor.

The energy dissipation at small scales is caused by the viscous friction of eddies in the dissipation range. Hence, in its most fundamental form, the energy dissipation rate in a homogeneous isotropic turbulent flow can be estimated from the velocity gradient given by [Tennekes, 1972]:

$$\epsilon = 15\nu\left\langle\left(\frac{du}{dx}\right)^2\right\rangle, \tag{I.27}$$

where ν is the kinematic viscosity of the fluid. To use the above relation, the assumption of isotropic turbulence at small scales applies, which holds for sufficiently high Reynolds number turbulent flows. A dissipation spectrum can also be used to estimate the energy dissipation rate at small scales, which can be calculated mathematically from the following expression [Tennekes, 1972]:

$$\epsilon = 15\nu\int_0^\infty k^2 E(k)dk. \tag{I.28}$$

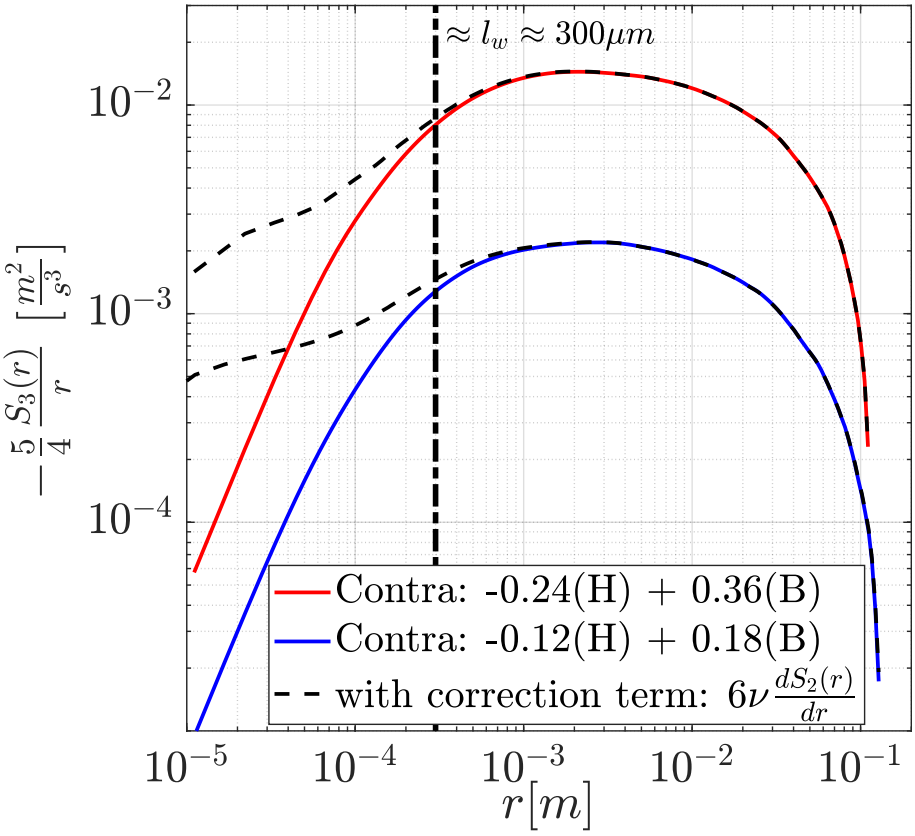

Figure I.9: Estimation of energy transfer rate (dissipation rate) from the compensated 3^{rd} order structure function along with the effects of the correction term

Filtering of the signal using low-pass filter plays an important role while estimating the dissipation rate using different methods as it directly cuts the amount of energy present in the spectrum possibly resulting in an under-estimation of the energy dissipation rate. A higher cut-off frequency means, more energy is taken into consideration towards energy dissipation

estimation. While using dissipation spectrum or velocity derivative to estimate the dissipation rate, it is required that all the scales in the flow are resolved by the measurement sensor. To use equation I.27 the spatial resolution of the hot-wire sensor must be less than the smallest scale of the turbulent flow i.e. Kolmogorov scale, in order to estimate the velocity gradient precisely. Otherwise equation I.27 gives an underestimated value of the dissipation rate [Sadeghi et al., 2018]. All the methods mentioned above are tested in order to estimate energy transfer/dissipation rate precisely on the biggest data set available of $\mathcal{O}(10^9)$ number of samples. The energy dissipation rate estimated by different methods is shown in figure I.10 as a function of normalized cut-off frequency.

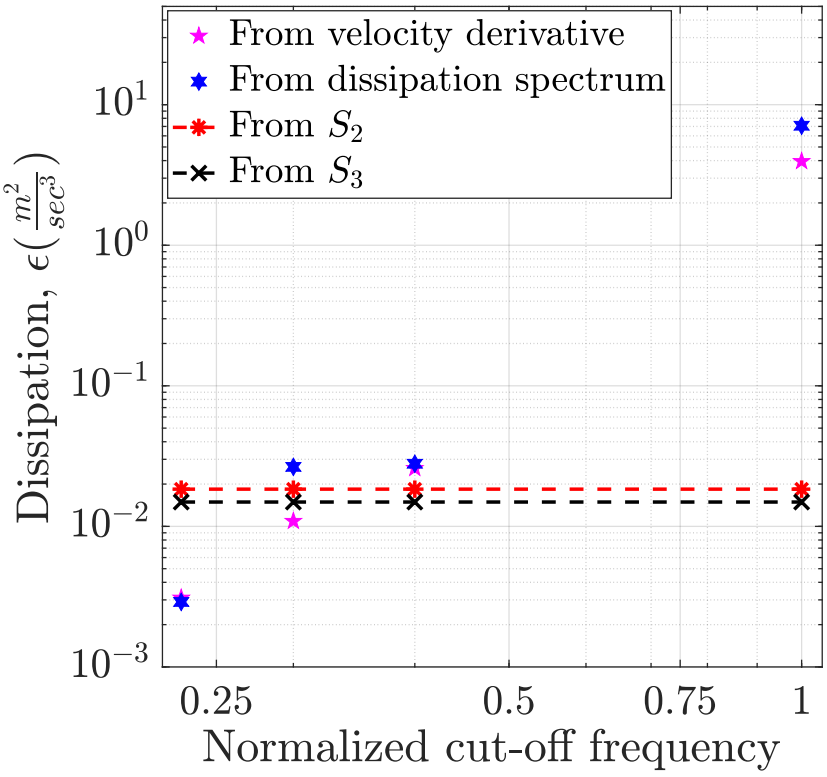

Figure I.10: Estimation of energy dissipation rate by different methods for contra configuration: -0.24(H) + 0.36(B)

In figure I.10 the normalized cut-off frequency is the ratio of the cut-off frequency over half of the acquisition frequency. For example, a normalized cut-off frequency of 0.3 corresponds to a cut-off frequency of 7.5kHz, when a sampling frequency $F_s = 50$kHz is used i.e. $\frac{7500}{(F_s/2)} = 0.3$. In this figure, the data points corresponding to S_2 and S_3 are calculated after applying the low-pass filter on the velocity data as explained in section I.6.3. As the energy dissipation rate estimated from S_2 and S_3 represents the energy transfer rate within the inertial range, the dissipation rate estimated using these methods has no dependence on the normalized cut-off frequencies as mentioned in figure I.10. From figure I.10 we see that there is a slight difference between the values of dissipation while using S_2 and S_3. This is because of the discrepancy in the value of constant C_2 (2.0 - 2.4). In the present calculation $C_2 = 2.1$ is used. Putting $C_2 = 2.2$ we get the same estimate of dissipation rate using S_2 or S_3. We see that at normalized cut-off frequency = 0.23, the dissipation rate estimated using equation I.27 and equation I.28 is less than the dissipation estimated using S_2 and S_3. This is because of the poorer spatial resolution of the hot-wire than the dissipation scales [Sadeghi et al., 2018]. Also, we see that the higher cut-off

frequency results into higher dissipation rate. Based on the analysis done in this figure, it is decided to use the value of dissipation rate estimated using the cut-off frequency slightly less than the typical frequency peaks at $\approx 5 - 6$kHz (see figure I.5) using S_3.

I.6.8 Length scales in turbulence

The turbulent cascade is composed of different sizes of eddies. In the turbulent cascade, there exists some particular size of the eddies i.e. scales which are important to describe the nature of turbulence. Typically, the turbulent cascade is expressed in terms of three different length scales as mentioned below.

I.6.8.1 Integral length scale

Integral length scale L is the scale up to which the energy is injected into the flow. This is the largest scale of the flow from which the energy cascade begins, hence the starting of the inertial range. Integral length scale for a particular experiment is defined by its size. For example, in grid turbulence it is of the order of mesh size, in jet flow it is of the order of jet diameter, in von Kármán flow it is of the order of radius of the impeller. Statistically, there are different ways to estimate the integral length scale. The most common estimate of L from the autocorrelation coefficient (see figure I.7) is given by:

$$L = \int_0^\infty R_{uu}(r)dr. \tag{I.29}$$

The quantity L can be clearly identified after plotting the cumulative integral given by $\int_0^r R_{uu}(r)dr$ with respect to scale r as shown in figure I.11 in the log-log scale. From this figure, we see that after $r \approx 0.1m$ the cumulative integral of R_{uu} has an asymptotic value, which can be taken as the measure of the integral length scale L [Bourgoin et al., 2018].

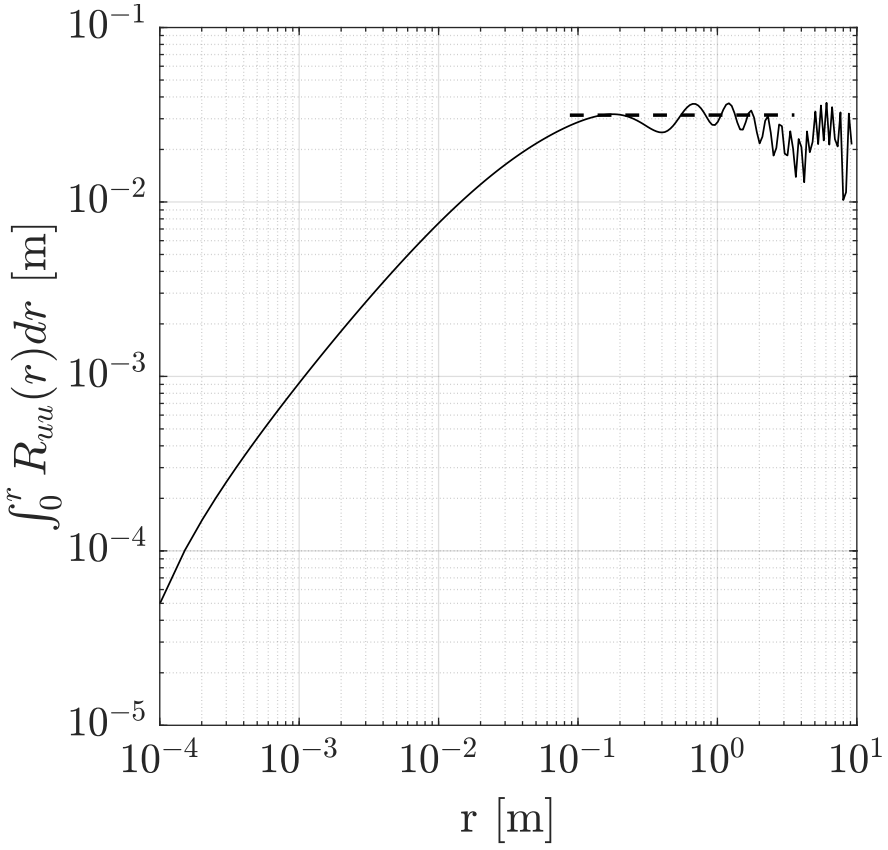

Figure I.11: Cumulative integral of R_{uu} showing the estimation of $L \approx 0.03m$ [shown by dashed line] for the co-rotation configuration in the SHREK experiment at $\mathcal{F}_1 = \mathcal{F}_2 = 1.2$Hz

I.6.8.2 Taylor microscale

In the inertial range, the injected energy in the turbulent flow at scale L cascades down to smaller scales without any significant effect of fluid viscosity. From the statistical point of view there exists an intermediate scale within the energy cascade called Taylor microscale (also referred as Taylor scale) which can be calculated using the analytical formula developed for homogeneous isotropic turbulence and is given by [Taylor, 1935; Pope, 2001]:

$$\lambda = \sqrt{\frac{15\nu u_{rms}^2}{\epsilon}}. \tag{I.30}$$

I.6.8.3 Kolmogorov length scale

The injected energy in the forcing range cascades down in the dissipation range. Starting from the Taylor microscale, the damping of eddies continues in the dissipation range until the smallest scale. The effects of fluid viscosity are so dominant on such a small scale, that the entire energy is directly converted into heat. The smallest scale in the turbulent flow at which the local Reynolds number (≈ 1) is small enough for fluid viscosity to be very effective is called Kolmogorov length scale η which is given by:

$$\eta = \left[\frac{\nu^3}{\epsilon}\right]^{1/4}. \tag{I.31}$$

I.6.9 Reynolds number

Reynolds number of a flow is associated with its characteristic velocity, its characteristic length scale and the fluid kinematic viscosity, ν. Thus, based on the velocity and scale used, the definition of Reynolds number differs. In the most general form of turbulent flows and also in this entire work following definition of Reynolds number is used:

$$Re_\lambda = \frac{u_{rms}\lambda}{\nu}, \tag{I.32}$$

where Re_λ is the Reynolds number based on Taylor microscale. Taylor microscale Reynolds number allows to compare different turbulent flows irrespective of their large scale features. The Reynolds number based on the integral length scale is given by:

$$Re = \frac{u_{rms}L}{\nu}. \tag{I.33}$$

I.6.10 Probability density function

The instantaneous velocity of a turbulent flow is a random variable. The probability density function (PDF) of a random variable shows a likelihood of a particular value of that random variable. A PDF of instantaneous velocity is shown in figure I.12. In homogeneous isotropic turbulence a Gaussian PDF of a random variable like velocity is expected due to the central limit theorem. In many numerical simulations and experiments we have also witnessed the Gaussian distribution of instantaneous velocity. For each set of standard deviation and mean velocity, a Gaussian distribution can be constructed having a skewness of 0 and flatness of 3. In figure I.12 we have compared the PDF of velocity with its Gaussian distribution and we see that these two distributions are in fact very similar.

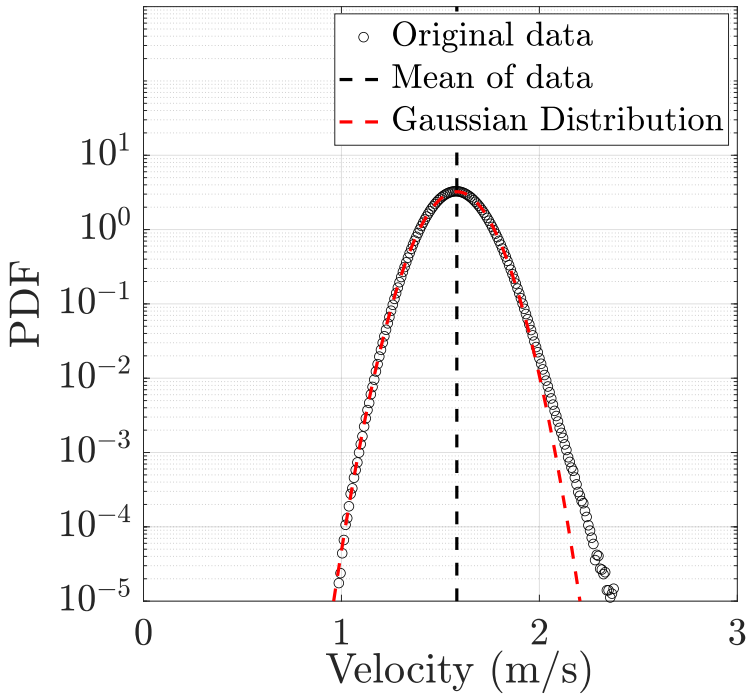

Figure I.12: Probability density function (PDF) of instantaneous velocity in the SHREK experiment

I.7 Organization of the thesis

The working principle of hot-wire anemometry is explained in Chapter II. Different modes of operation of hot-wire anemometry are explained along with calibration process. Hot-wire calibration in the SHREK and ECOUTURB experiments are presented. The procedure to measure the time constant of the home-made hot-wires is demonstrated and the subsequent analysis is performed in the SHREK, ECOUTURB and HECAL experiments. Based on the estimated time constant of the hot-wire the possibility of correcting the raw hot-wire signal is explored.

Chapter III presents the design, operation and functioning of the HECAL experiment. This chapter presents the experimental set-up along with the modified instrumentation to carry out the precise hot-wire calibration. In this chapter, first results ever obtained from the HECAL experiment are shown. A successful hot-wire calibration curve obtained in air and normal helium is presented. The repeatability and sensitivity of the hot-wire calibration is addressed in normal helium. The effect of overheating of the hot-wire is presented to interpret its counterflow turbulence in superfluid. A hot-wire calibration in superfluid is demonstrated with partial interpretation.

The wind tunnel called HEJET facility is presented in Chapter IV. The experimental set-up is explained in detail along with the procedure to cool-down. The design, assembly and installation of the new turbine of the centrifugal pump is shown. The macroscopic characteristics of the centrifugal pump in the HEJET facility are presented. The analysis of turbulent jet flow in normal helium is performed using the local hot-wire measurements. The method of empirical mode decomposition is presented for the post-processing of hot-wire signal in order to reduce the effects of jet instability. Accordingly, the statistical analysis of the jet flow in normal helium is performed along with the discussion on intermittency. The observations in superfluid turbulent jet flow are presented based on the power spectral density of the hot-wire signal.

In Chapter V a brief description of the SHREK facility is presented along with different types of turbines used to generate von Kármán flows. Effects of forcing on different statistical quantities of turbulence are studied for various von Kármán flow configurations. The scaling laws of classical turbulence are demonstrated for the SHREK experimental data up to the Reynolds number of $\mathcal{O}(10^7)$. The phenomenon of intermittency is studied using the flatness and skewness of probability density functions of velocity increments along with the scaling exponents of the structure functions. The estimated scaling exponents are compared with K41 and other well known intermittency models. The intermittency correction provided by K62 is addressed up to the $Re_\lambda = 13000$. The observations about the evolution of power spectral density in superfluid von Kármán flows are shown. The calibration of hot-wire is performed in superfluid and the statistical analysis of the superfluid von Kármán flow is done. In addition, the investigation of the phenomenon of intermittency is performed for turbulent superfluid von Kármán flow.

Chapter VI presents the turbulent cascade using the Fokker-Planck equation which describes the evolution of PDFs of velocity increments, and accordingly the study of the intermittency phenomenon in the SHREK experiment is addressed. This chapter delivers a main message of this thesis in perspective of intermittency in turbulent flows at very high Reynolds numbers. The fulfillment of Markovian property within the energy cascade is shown. A detailed procedure to estimate the drift and diffusion coefficients of the Fokker-Planck equation is shown. Dependence of the drift and diffusion coefficients on the type of von Kármán flows and Reynolds number is discussed. The link of diffusion coefficient in the Fokker-Planck equation with the K62 intermittency parameter μ is shown. Experimentally, the dependence of all these intermittency parameters with respect to Re_λ up to 13000 is shown. The reliability of the estimated drift and diffusion coefficients is addressed by reconstructing the conditional PDFs and using the integral fluctuation theorem. In addition, the application of Fokker-Planck equation and

integral fluctuation theorem is investigated for turbulent superfluid flow having very high level of velocity fluctuations. Finally, in Chapter VII the conclusions of this thesis are summarized and recommendations for the future work are presented.

II HOT-WIRE ANEMOMETRY

The turbulence generated by a fluid flow can be measured using many different experimental techniques such as hot-wire anemometry (HWA), laser doppler velocimetry (LDV), particle image velocimetry (PIV), particle tracking velocimetry (PTV), pitot tube and cantilever. Out of all these techniques the most popular and widely used method is the HWA. Also, to make the turbulence measurements in an Eulerian frame of reference at temperatures as low as 1.6K, only certain techniques are feasible such as HWA, pitot tube and cantilever. HWA promises to resolve high frequency content of the fluid flow fluctuations at very high Reynolds number. The work presented in this thesis is particularly dedicated to the use of technique of HWA at low temperatures to study the turbulent characteristics of the flow.

The hot-wire anemometer is a device to measure velocity of the flow and its fluctuations induced by turbulence at a fixed point in space (i.e. in the Eulerian context). The available commercial hot-wires made by Dantec Dynamics are of the diameter $d_w = 5\mu m$ with a length l_w = 1.25mm. For very high Reynolds number flows, we need hot-wires of a few hundreds of microns in length or even smaller. To achieve this, in our laboratory, we have been continuously trying to reduce the sensitive length of the hot-wire. The smallest length of the hot-wire is important for the following two reasons. Firstly, a large aspect ratio $\frac{l_w}{d_w}$ >200 is required to measure only one component of the velocity namely the one parallel to the mean velocity [Bruun, 1995]. This is mainly important because we are interested in the statistics of the longitudinal spatial velocity increment. Secondly, the smallest the diameter of the hot-wire, the higher is the cut-off frequency and time resolution of the measurement. This is important because we want to probe a large range of the inertial range.

Let us consider that $\boldsymbol{U}$ is the velocity vector of the given velocity field then the voltage output of the hot-wire anemometer E is proportional to the modulus of the velocity given by $U_e = \sqrt{U_x^2 + U_y^2 + U_z^2}$, where U_x, U_y and U_z are the components of velocity in x, y and z direction respectively [Bruun, 1995]. U_x and U_y are the component of velocity perpendicular to the hot-wire whereas U_z is parallel to the hot-wire. Given that the mean velocity along the x-direction (i.e. parallel to mean flow) is large compared to other components, U_e becomes:

$$\begin{aligned} U_e &= \sqrt{(\langle U_x \rangle + u_x)^2 + u_y^2 + u_z^2}, \\ &= |U_x| \sqrt{1 + 2\frac{u_x}{\langle U_x \rangle} + \frac{u_x^2 + u_y^2 + u_z^2}{\langle U_x \rangle^2}}, \\ &\approx |U_x| + u_x + \mathcal{O}\left(\frac{u_x^2}{\langle U_x \rangle^2}, \frac{u_y^2}{\langle U_x \rangle^2}, \frac{u_z^2}{\langle U_x \rangle^2} \right), \end{aligned} \tag{II.1}$$

where $\langle U_x \rangle$ is the mean velocity, $|U_x|$ is the absolute velocity in the x-direction and u_x, u_y, u_z are the velocity fluctuations in the x, y and z direction respectively. Neglecting the higher order terms in the above equation we see that the hot-wire is sensible to the modulus of the velocity at first order [Bruun, 1995; Moisy, 2000].

All the hot-wires used in this work are home-made using a Wollaston wire of Platinum-Rhodium ($90\% - 10\%$) alloy with a silver coating of diameter $50\mu m$. The Pt-Rh Wollaston wire is used instead of Pt wires because of its lower thermal conductivity $\left(0.4 \text{ instead of } 0.7 \frac{W}{\text{cm K}}\right)$, which helps to reduce the heat conductive end losses, because of its higher resistivity (19 instead of 9.8 $\mu\Omega cm$) and also because of its mechanical robustness. The tensile strengh of Platinum-Iridium Wollaston wire is superior but because of its brittle nature the attempts to make a hot-wire by this technique were not fruitful. The silver coating is removed using chemical

etching to create and define the sensitive length of the hot-wire. In order to compensate for the thermal contraction of the hot-wire during the cool-down process, the hot-wires are slightly bent.

Many hot-wires have been fabricated during this work. The diameter of the hot-wire could be of $d_w = 5\mu m$, $2.5\mu m$, $1.27\mu m$, $0.65\mu m$, $0.5\mu m$ or $0.3\mu m$. Typically, the sensitive length of the home-made hot-wires is of $l_w = 200$ - $400\mu m$. Therefore, maintaining $\frac{l_w}{d_w} \geq 200$, the end conduction effects are very negligible [Paranthoen et al., 1982; Klewicki and Falco, 1990]. The $l_w >> d_w$ also ensures that the hot-wire measures only one component of incoming velocity. In this work, hot-wires of different lengths and diameters are used. The specifications of each hot-wire will be mentioned accordingly with results in the following chapters. A typical hot-wire fabricated in the laboratory which is made up of Pt-Rh Wollaston wire is shown in figure II.1 [Moro, 2010].

For turbulent flow measurements, a hot-wire can be operated in different modes such as constant temperature anemometry (CTA), constant voltage anemometry (CVA) and constant current anemometry (CCA) [Bruun, 1995]. Each of these different modes of operation have their pros and cons. The main aim of this chapter is to describe briefly the different modes of operation of the hot-wire with an example showing its calibration. In the current work, all the hot-wires are home-made in order to make them sustain the lowest temperatures. Typically, the Pt-Rh home-made hot-wires are of the $d_w = 1.27\mu m$ and $l_w = 300\mu m$. As such hot-wires are not commercially available, their performance characteristics is not readily available. In order to rely on their performance, their characterization is necessary. In this chapter, the operating principle, the performance characteristics of the hot-wires in terms of their working temperature dependence, time constant (i.e. frequency response) and sensitivity to different calibrations is discussed in the subsequent sections.

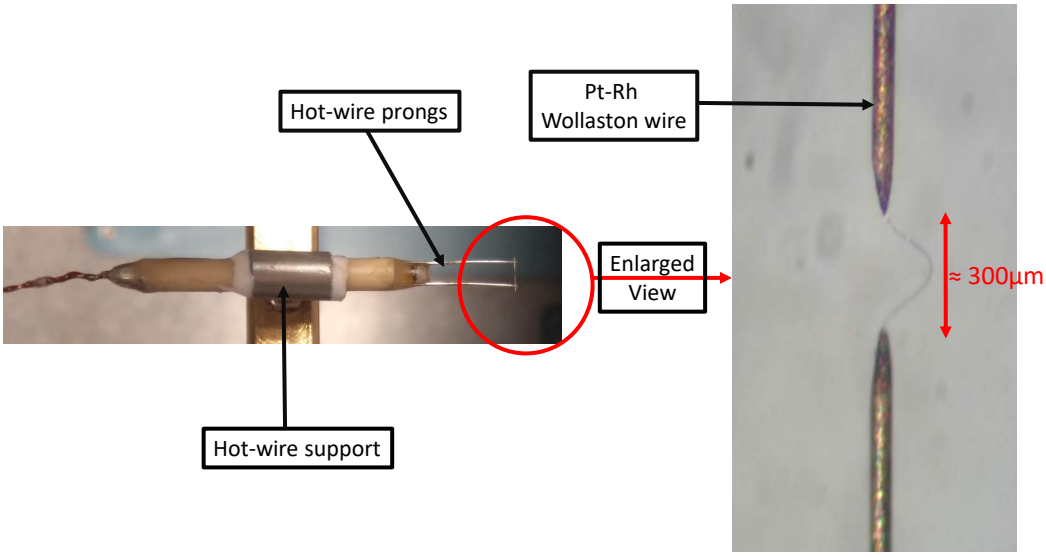

Figure II.1: Typical home-made hot-wire of $d_w = 1.27\mu m$, $l_w = 300\mu m$ and Resistance = 43Ω at 300K

The operating principle of hot-wire is simply based on the convective heat transfer from the hot-wire to the cold moving fluid. Consider a hot-wire of diameter d_w, length l_w, mass m, heat capacity C_w $\left(\frac{J}{K}\right)$ with resistance R_w at temperature T_w. Consider this hot-wire is heated by a current I, in a fluid at temperature $T_a < T_w$ with thermal conductivity k_f, kinematic viscosity

ν_f moving with a velocity U ($\frac{m}{s}$) around the hot-wire. For the home-made hot-wire $l_w >> d_w$ thus we can neglect the heat transfer by conduction at the ends of hot-wire which indicates that the temperature of the hot-wire along the sensitive length remains constant. Neglecting the radiative heat transfer, the heat balance across the hot-wire is given by [Comte-Bellot, 1976; Bruun, 1995]:

$$C_w \frac{dT_w}{dt} = R_w I^2 - \pi l_w k_f (T_w - T_a) Nu, \tag{II.2}$$

where $Nu = \frac{h d_w}{k_f}$ is the Nusselt number which represents the enhancement of the convective heat transfer characterized by the heat transfer coefficient h relative to the conduction heat transfer. In equation II.2 $R_w I^2$ is the heat supplied to the hot-wire sensor by Joule effect and the second term on the right hand side is the rate of heat loss due to forced convection across the thermal boundary layer developing in the fluid around the hot-wire. The first term in equation II.2 is the rate of change of energy stored in the hot-wire which, in steady state condition, is assumed to be negligible. King and Barnes [1914] proposed a square root empirical law for the Nusselt versus Reynolds number define by $Re_w = \frac{U d_w}{\nu_f}$. The King's Law in its generalized form is given by:

$$Nu = A + B Re_w^{0.5}, \tag{II.3}$$

where A and B are the constants for given calibration. The convective heat transfer from the hot-wire is controlled by its viscous and thermal boundary layer. The thickness of both the viscous and thermal boundary layers around the hot-wire accounts for the $Re_w^{0.5}$ dependence in equation II.3. The resistance of the hot-wire is given by $R_w = \chi l_w / A_w$, where χ is the resistivity of the hot-wire material defined by the resistance per unit length per unit cross-sectional area. A_w is the cross-sectional area of the hot-wire. So, for a given length of the hot-wire the resistance increases with decreasing its diameter and for a given diameter of the hot-wire the resistance increases with increasing length of the hot-wire. The operating resistance R_w of the hot-wire at temperature T_w is given by:

$$R_w = R_a[1 + \alpha(T_w - T_a)], \tag{II.4}$$

where R_a is the hot-wire resistance at reference temperature, T_a and α is the temperature coefficient of resistance at T_a defined by $\alpha = \frac{1}{R}\frac{dR}{dT}$. Replacing T_w, $(T_w - T_a)$ and Nu in equation II.2 using equation II.3 and equation II.4 we get the following differential equation:

$$\frac{C_w}{\alpha R_a (a' - I^2 + b' U^n)} \frac{dR_w}{dt} + R_w = \frac{a' + b' U^n}{(a' - I^2 + b' U^n)} R_a, \tag{II.5}$$

where $a' = \frac{\pi l_w k_f}{\alpha R_a} A$, $b' = \frac{\pi l_w k_f}{\alpha R_a} \left(\frac{d_w}{\nu_f}\right)^n B$ and $n \approx 0.5$.

II.1 Constant current anemometry (CCA)

In constant current anemometry the current across the hot-wire is kept constant. In this mode, the velocity fluctuations in the turbulent flow are measured by virtue of the fluctuation of the convective heat transfer which leads to the fluctuations of the temperature of the hot-wire. Thus, the resistance of the hot-wire fluctuates and hence we can measure the fluctuating voltage across the hot-wire. Compared to CVA and CTA, in CCA the hot-wire instrumentation is very simple. This is the most common mode of operation of the hot-wire in the present work. As the temperature of the hot-wire is not constant, in this mode temperature fluctuations experienced by the hot-wire are expected to be damped due to thermal inertia of the hot-wire (whose temperature fluctuates). In equation II.5, considering a steady state condition we can

neglect the time derivative and then multiplying with current I leads to the following equation which is the King's law of calibration while using CCA [Bruun, 1995]:

$$\begin{aligned} V_w = IR_w &= \frac{a' + b'U^n}{(a' - I^2 + b'U^n)} R_a I, \\ V_w = IR_w &= \frac{c(1 + aU^n)}{(1 - b + aU^n)}, \end{aligned} \tag{II.6}$$

where V_w is the voltage across hot-wire and U is the reference mean velocity for performing calibration. $a = \left(\frac{d_w}{\nu_f}\right)^n \frac{B}{A}$, $b = \frac{I^2 \alpha R_a}{\pi l k_f A}$ and $c = R_a I$ are the constant of calibration for CCA. Typically, for a hot-wire of $d_w = 1.27\mu m$ and length $l_w = 300\mu m$ a current of 8 - 10mA is required to operate the hot-wire with overheating of 35 - 40% in HeI at T = 2.2K. In this thesis, the term "overheating" is used in the following context. Let us assume that at T = 2.2K in HeI the hot-wire resistance is 20Ω in still fluid. Using CCA, the current across the hot-wire is adjusted for the targeted resistance of say 30Ω. In this case the hot-wire is operated at overheating of 50% (similarly, if the targeted resistance is 28Ω the hot-wire is operated at overheating of 40%). In CCA, we can significantly improve the signal to noise ratio with increased overheating but optimum overheating must be used in order to prevent the risk of burning (melting) of the hot-wire. Optimum overheating of the hot-wire is also important to avoid the spurious effect of natural convection over the hot-wire particularly at low flow velocities. Minimum overheating of the hot-wire helps to measure low velocities in the flow.

Figure II.2 shows a typical hot-wire calibration performed in the SHREK facility in CCA mode. This hot-wire calibration is performed over a duration of 6 hours. The least squares method is used to obtain all the calibration fits in this work. To construct the calibration fit the velocity exponent n in equation II.6 is assumed equal to 0.5. From the calibration curve we see that the experimental data points follow quite well the fit defined by equation II.6. We note that the uncertainty of the calibration constants a, b and c shown in figure II.2 accounts to less than ±1%. This calibration is performed in the SHREK facility using co-rotation configuration of the von Kármán flow using straight/radial blades (see section V.1.3 for the details of the configurations). This hot-wire is installed 4cm above the equatorial plane and 4cm away from the wall of the von Kármán cell. The hot-wire is installed in such a way that it can measure either the azimuthal, vertical or the mixed component of these velocities. To perform the calibration, the reference mean velocity in the SHREK facility (figure II.2) is estimated assuming the solid body rotation attained in the stationary co-rotation configuration. Therefore, the azimuthal component of velocity is chosen to perform the hot-wire calibration. This velocity is given by, Velocity $\left(\frac{m}{s}\right) = \mathcal{R} \times \omega = \mathcal{R} \times 2\pi f$, where $\mathcal{R} = 0.35m$ is the distance of the hot-wire from the axis of the von Kármán cell, $\omega = 2\pi f$ is the angular velocity in $\frac{rad}{s}$ and f is the frequency of rotation of turbines in Hz which is measured using a home-made optic instrumentation which has 0.1% of accuracy. All the hot-wire calibrations in the SHREK experiment are performed using this method.

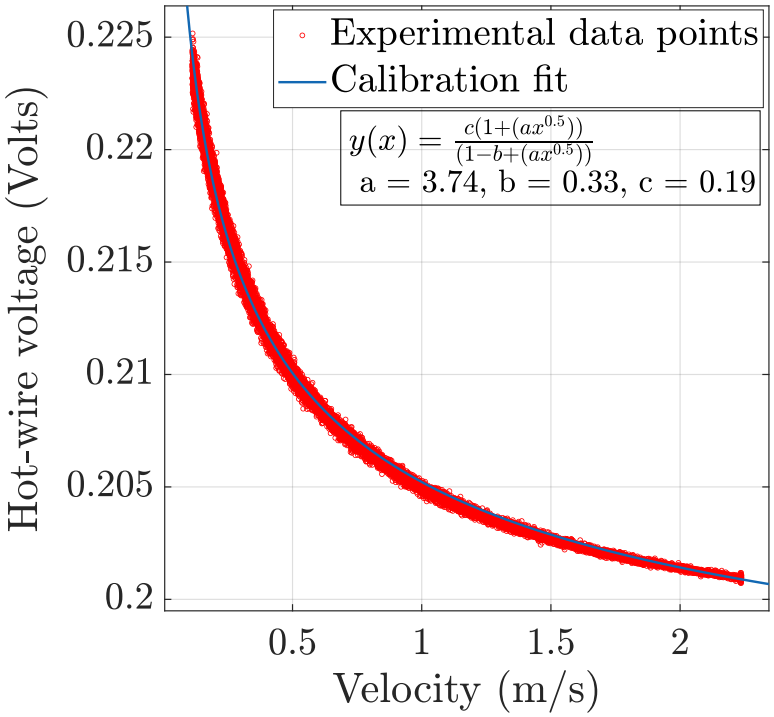

Figure II.2: Experimental data points and the calibration curve using King's Law of calibration for CCA in the SHREK facility in HeI at T = 2.2K ($d_w = 1.27\mu m$ and $l_w = 300\mu m$)[$y(x)$ is the hot-wire voltage where x is the velocity].

II.2 Constant temperature anemometry (CTA)

In this mode of operation, the hot-wire is operated at a constant temperature (i.e. at constant resistance). The constant temperature mode of operation of the hot-wire is achieved by feeding the overheating current to the hot-wire through a wheatstone bridge and adding a feedback circuit to correct for the unbalance of the bridge resulting from the fluctuations of the incoming turbulent flow velocity. Exposed to the incoming turbulent flow velocity the current across the hot-wire fluctuates and hence the voltage output of the CTA module fluctuates. This hot-wire calibration has been performed in the SHREK facility using curved blades. As the hot-wire is operated at constant temperature, it is less prone to thermal inertia effects (practically, one is only limited by the finite bandwidth of the feedback circuit). A typical calibration of the hot-wire in CTA mode is shown in figure II.3. This hot-wire calibration is performed over a duration of 12 hours. The hot-wire is operated using the commercial system of DISA 55M10 CTA standard bridge. Once having the reference mean velocity estimate, the hot-wire calibration is performed using King's Law [King and Barnes, 1914; Bruun, 1995] which establishes the relation between the measured voltage E across the hot-wire and the local incoming flow velocity U. Mathematically, in CTA mode this relation is written as:

$$E^2 = AU^n + B, \tag{II.7}$$

where A and B are calibration constants for a given sensor. E is the measured hot-wire voltage in volts and U is the velocity in $\frac{m}{s}$. In practice, the values of constants A and B change for each hot-wire sensor and it is therefore necessary to calibrate each sensor individually and to do this calibration frequently (due to possible aging effects of the hot-wire alloy). In CTA mode, the hot-wire is operated at a temperature of about 20-24K which corresponds to a typical

overheating of 0.7%. In CTA mode, the hot-wire is exposed to the risk of breaking in case of possible spurious electrical oscillations of the feedback system. This is specially important for the home-made hot-wires because of their fragility. To operate the hot-wire at high overheating using the system DISA, the hot-wire is at very high risk of burning, therefore, limiting the signal to noise ratio which necessitates the use of an amplifier. On the contrary, the tuning of current across the hot-wire can be easily done in CCA mode for the desired overheating to improve the signal to noise ratio at the expense of a bandwidth smaller than in constant temperature and constant voltage anemometry due to thermal inertial of the hot-wire. In the case of low temperature measurements one could expect that this thermal inertia is strongly reduced due to the small thermal capacity of the hot-wire at low temperatures.

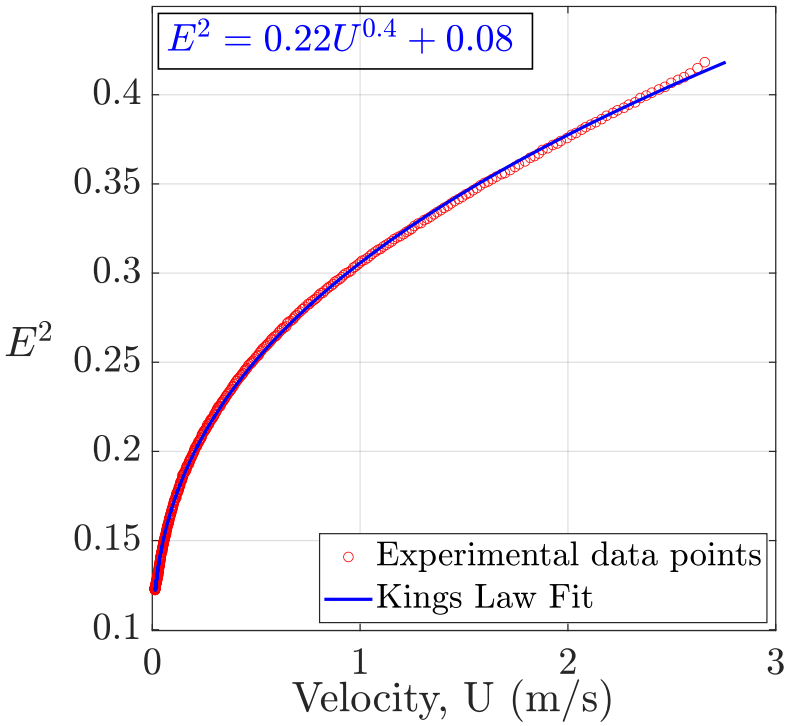

Figure II.3: Experimental data points and the calibration curve using the King's law of calibration in HeI at T = 2.2K in the SHREK facility using curved blades ($d_w = 1.27\mu m$ and $l_w = 300\mu m$)

II.3 Constant voltage anemometry (CVA)

As the name implies, in constant voltage anemometry the voltage across the hot-wire is kept constant (using a simple constant voltage feedback loop made with an operational amplifier) during the measurement while measuring the current passing through it. In CVA we impose a constant voltage across the hot-wire. Thus, a current flows through the hot-wire resulting in its heating by Joule law. For a constant incoming flow velocity the balance between the Joule heating and the convective heat transfer across the boundary layer of the hot-wire results in a hot-wire temperature higher than the fluid temperature (hence an increase in the resistance of the hot-wire). If the flow velocity fluctuates, the convective heat transfer fluctuates and thus the temperature of the hot-wire, resulting in fluctuations of the current flowing through the wire maintained at constant voltage. To operate the hot-wire in CVA mode, we have used the commercial CVA Model "4-600CVA" manufactured by Tao Systems [Sarma, 1998]. As the

temperature of the hot-wire is fluctuating, CVA is affected by the thermal inertia of the hot-wire. This thermal inertia can be compensated once the time constant of the system is known. And, one can measure the time constant using the module provided with this system using the square wave response. Using the time constant estimation we can correct the raw signal in order to compensate for the effects of thermal inertia. So far, this module has been used with the hot-wires of diameter $d_w \geq 2.5\mu m$ [Mohammed-Taifour et al., 2015; Comte-Bellot and Sarma, 2001; Berson et al., 2010] for which the expected time constant is of the order of 0.1ms or more. The use of CVA for the hot-wire of $d_w = 2.5\mu m$ has been investigated by Comte-Bellot and Sarma [2001] for the maximum $Re_w = 20$. The Re_w for the home-made hot-wires of $d_w = 1.27\mu m$ at cryogenic temperature lies within 100 - 150. Hence, the sensitivity of the time constant measured using CVA over such high range of Re_w for the home-made hot-wire of $d_w = 1.27\mu m$ is questionable and needs to be addressed. Also with this module the time constant compensation settings are available for minimum of 0.1ms to maximum of 0.3ms. The hot-wires used in the present work are of diameter $1.27\mu m$ for which the estimated time constant lies within the orders of few tens of microseconds (see section II.7). The main advantage of the CVA is the elimination of cable capacitance effects as compared to CTA and CCA [Sarma, 1993]. Thus, using CVA, one can use long cable length without making a compromise between frequency response and stability [Sarma, 1998]. CVA provides large bandwidth with high signal to noise ratio as compared to CTA and CCA. For the hot-wire of $d_w = 2.5\mu m$, Comte-Bellot and Sarma [2001] found that in CVA mode the time constant of the hot-wire is smaller than in CCA mode. Thus, we expect that the time constant of the hot-wire in CVA mode is smaller than in the CCA mode [Sarma, 1993]. In this thesis, we have not explored the use of CVA at low temperatures. A typical calibration of the commercial hot-wire using CVA is shown in figure II.4, which is carried out using the hot-wire calibrator at LEGI at ambient temperature. The hot-wire calibration is performed using King's law of calibration [Comte-Bellot, 1976] given by:

$$V_s = AU^n + B, \tag{II.8}$$

where A and B are the constants for given sensor. V_s is the CVA output voltage.

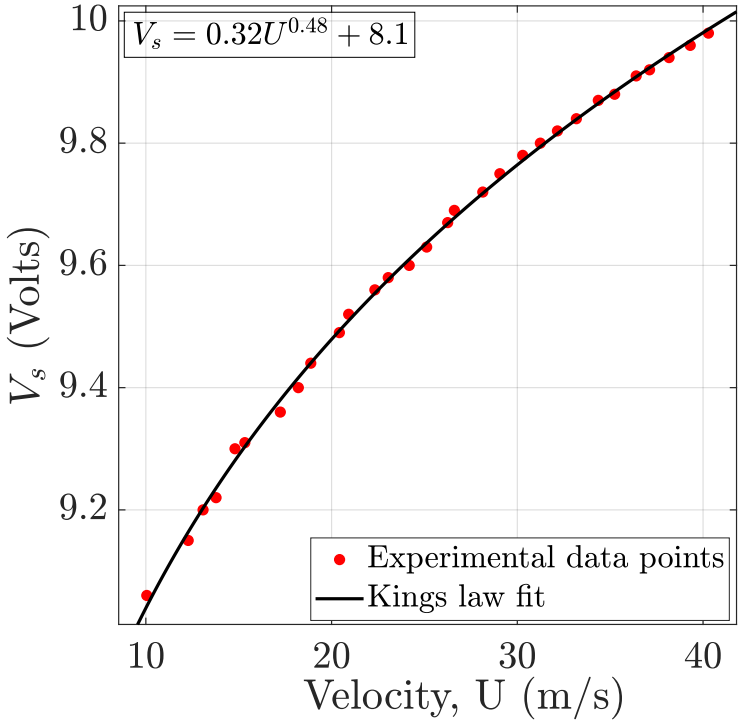

Figure II.4: Experimental data points and the calibration curve using Kings law of calibration (commercial hot-wire: $d_w = 5\mu$m, $l_w = 1$mm)

II.4 Resistance dependence on temperature

Because of the rapid velocity fluctuations in the turbulent flow, the resistance of the hot-wire changes in CCA mode. But, it is then necessary that a significant change in the resistance of hot-wire is induced by even the smallest flow fluctuations. To achieve this, it is important to know the resistance of the hot-wire with respect to temperature, so that we can tune the current to operate the hot-wire at the desired temperature. Also, it is crucial to operate the hot-wire within the temperature range at which the temperature coefficient of resistivity remains significant.

II.4.1 Micro-fabricated hot-wire

The micro-fabricated hot-wires were first fabricated by Vallikivi and Smits [2014] which are known as nanoscale thermal anemometry probe (NSTAP). Because of its smallest dimensions of $l_w \approx 50\mu m$, these hot-wires have been found to have a better performance to capture the statistics at smaller scales. Motivated by the spatial resolution of these hot-wires, we have made micro-fabricated hot-wires in the laboratory to explore the possibility of its use at cryogenic temperatures. The performance of such micro-fabricated hot-wires with respect to temperature is studied using the pulse tube cryocooler over many experiments. Figure II.5 shows the change in resistance of the micro-fabricated hot-wires with respect to temperature. Unfortunately, the micro-fabricated hot-wires never survived during the cool-down process in the SHREK experiment hence no measurements were obtained using them. Therefore, efforts are still in progress to make the Wollaston Pt-Rh home-made hot-wires having the smallest spatial resolution possible.

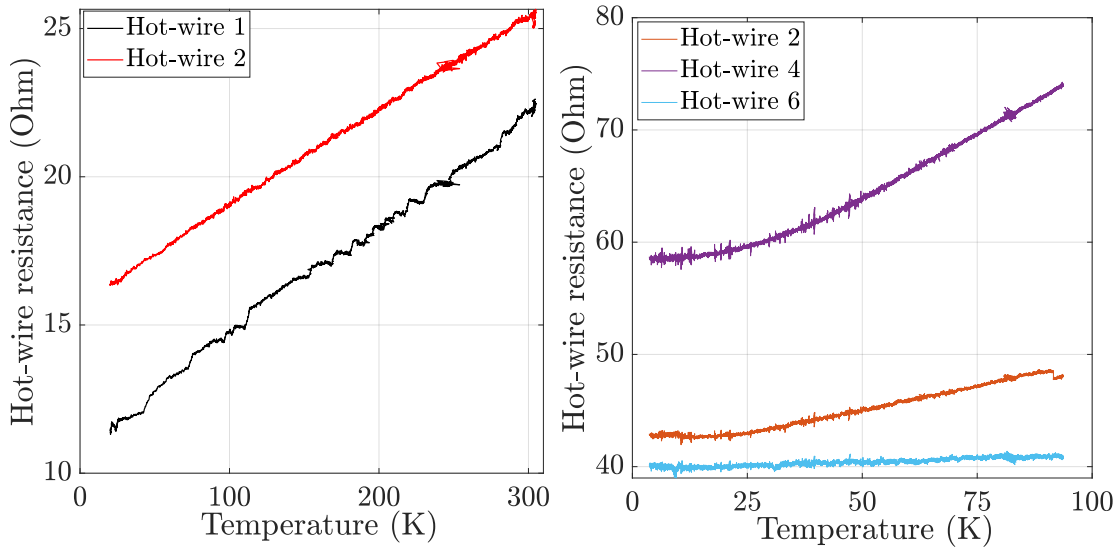

(a) Hot-wires made of Au

(b) Hot-wires made of Pt

Figure II.5: Micro-fabricated hot-wire resistance with respect to temperature using pulse tube cryocooler

II.4.2 Pt-Rh Wollaston hot-wire

During the cool-down operation in the HEJET/HECAL experiment there are mainly two steps. Firstly, the cool-down from 300K to 78K using liquid nitrogen in the outer casing of cryostat (liquid nitrogen bath) which takes around 36 - 48 hours and then secondly, the cool-down from 78K to 4.2K while filling with liquid helium in the saturated and pressurized bath which takes around 2 - 3hours. To record the resistance of the hot-wires during cool-down process, they are connected in a circuit using a very small current of 0.1mA for the hot-wire of $d_w = 0.5\mu m$ and of 1mA for the hot-wire of $d_w = 1.27\mu m$. Figure II.6 shows the measurements of the change in resistance of the hot-wire during the first stage of the cool-down process performed in the HEJET experiment. This figure shows the linear dependence of the hot-wire resistance on the temperature. Typically, hot-wire measurements are performed at 35% overheating in CCA mode which corresponds to the operating temperature of the hot-wire around 110 - 120K with $\alpha = 0.0017K^{-1}$ estimated based on the entire temperature range from figure II.6 [Bruun, 1995]. In fact, based on this figure we observed that the local α may vary within $0.001 - 0.003K^{-1}$.

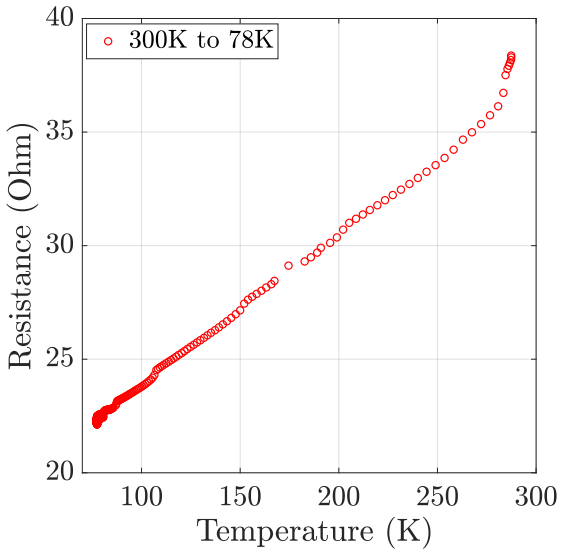

(a) Hot-wire of $d_w = 1.27\mu m$ and $l_w \approx 200\mu m$

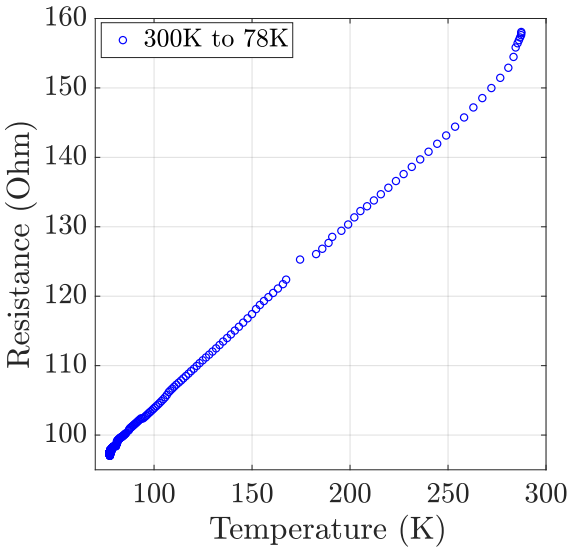

(b) Hot-wire of $d_w = 0.5\mu m$ and $l_w \approx 200\mu m$

Figure II.6: Change in hot-wire resistance with respect to temperature from 300K to 78K

Figure II.7 shows the change in hot-wire resistance during the second stage of cool-down process down to 4.2K while filling liquid helium in the saturated and pressurized bath. From this figure we confirm that the resistance of the hot-wire decreases linearly with respect to temperature until $\approx$ 20K showing a constant temperature coefficient of resistance α. The important thing to note from figure II.7 is that the resistance of these hot-wires do not change below 20K. Therefore, in any operating mode (CCA/CTA/CVA) the temperature of the hot-wire must be maintained above 20K so that it is sensitive enough to the velocity fluctuations.

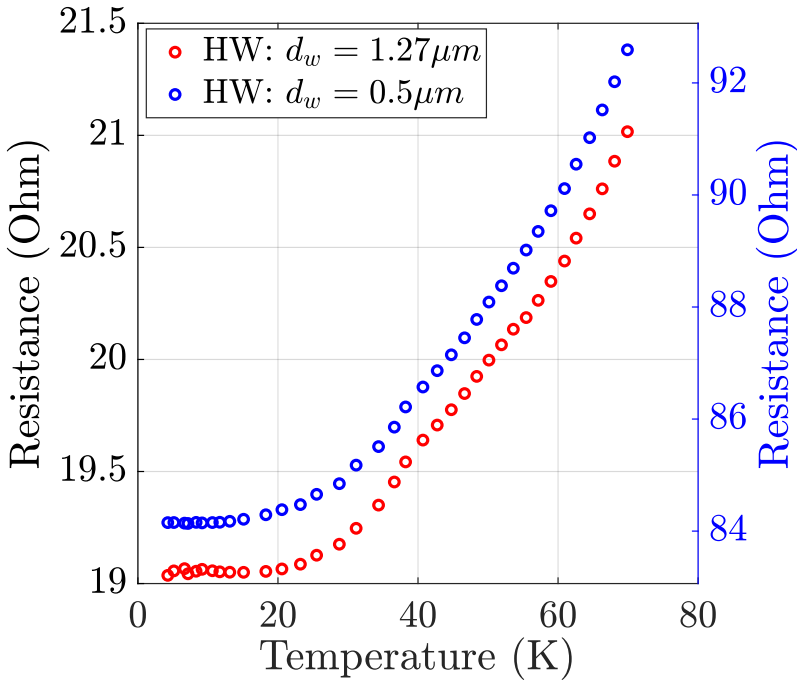

Figure II.7: Change in hot-wire resistance with respect to temperature from 70K to 4.2K

II.5 Sensitivity of the hot-wire during different calibrations in the SHREK experiment

The SHREK experiment is typically performed over a period of 3 - 4 weeks and hence, multiple calibrations of the hot-wire are performed to check the stability of the dynamic response of the hot-wire during the entire experiment. Figure II.8 shows four such different calibrations performed in the SHREK experiment using the straight blades turbine configuration with the hot-wire operated in CCA mode. The four calibrations shown in the figure are performed successively over a period of 3 - 4 weeks. The hot-wire in figure II.8a is installed at the equatorial plane while the hot-wire in figure II.8b is installed close to the top turbine which is 15cm away from the equatorial plane. From these two figures, we see that at small velocities the calibration of the hot-wire does not change, whereas for velocities larger than $0.25\frac{m}{s}$ the calibration of the hot-wire slightly changes. The most probable reason for this difference in calibration is the following. After the demounting of hot-wires from the SHREK experiment we found that the hot-wires are slightly covered with small particles of Molybdenum disulfide (lubricant), which is likely to change the resistance of the hot-wire a bit. Hence, the last hot-wire calibration which is performed over 6 hours tends to lower the hot-wire voltage with respect to velocity. The same behavior of the hot-wire has also been observed while using CTA in the SHREK experiment using curved blades as shown in figure II.9. From this figure, we see that to compensate for the reduced resistance of the hot-wire, the current in the hot-wire needs to be increased. And hence for the same velocity higher hot-wire voltage is recorded in the final calibration compared to the initial hot-wire calibration.

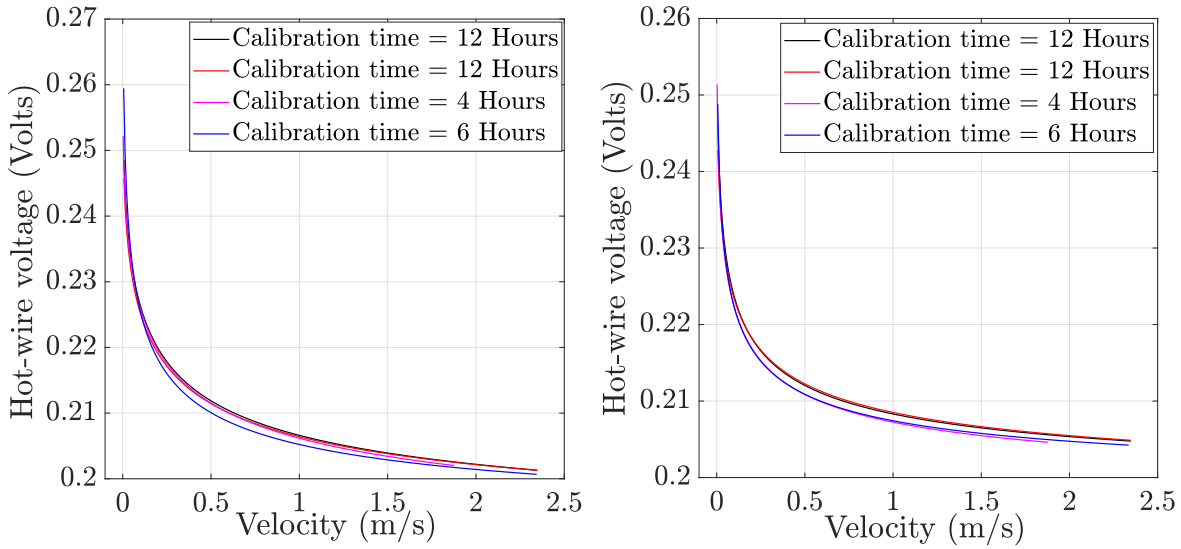

(a) Hot-wire position: 4cm above the equatorial plane

(b) Hot-wire position: close to top turbine (15cm away from the equatorial plane)

Figure II.8: Different hot-wire calibrations in CCA mode performed in the SHREK experiment using straight blades in HeI at T = 2.2K ($d_w = 1.27\mu m$ and $l_w = 300\mu m$)

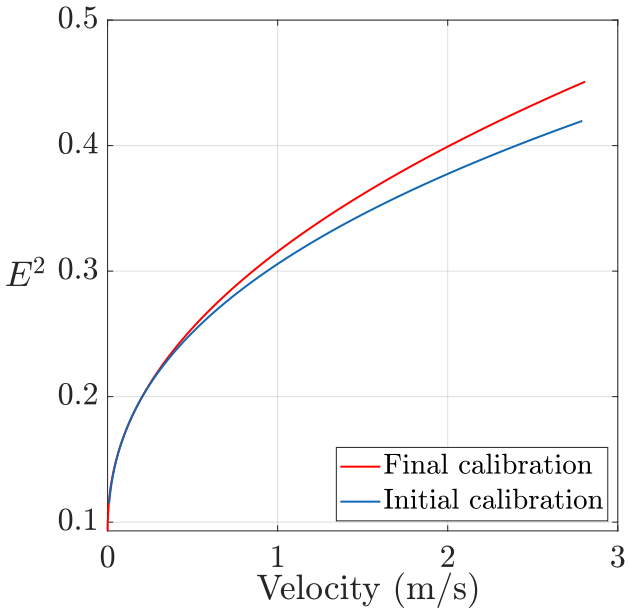

Figure II.9: Different hot-wire calibrations in CTA mode performed in the SHREK experiment using curved blades in HeI at T = 2.2K

Multiple hot-wire calibrations are performed in the SHREK experiment in a single day to study the effects of the varying duration of the calibration. These calibrations are performed over 15 mins, 30 mins, 2 hours and 4 hours respectively either by decreasing the turbine frequency from 1Hz to 0Hz or by increasing it from 0Hz to 1Hz simultaneously. The purpose of performing such calibrations is also to know the time required to stabilize the von Kármán flow after imparting a particular turbine frequency. Figure II.10 shows such 8 different hot-wire calibrations performed in the CCA mode. From this figure, we observe no significant differences in the calibration for turbine frequencies more than 0.125Hz ($\approx 0.27\frac{m}{s}$). This ensures the consistency of calibration over various duration of calibration for higher velocities. However, the hot-wire is very sensitive to the effects of its own natural convection at smaller turbine frequencies in the range from 0 to 0.125Hz. At smaller velocities, we observed that when the calibration is performed while decreasing the turbine frequency from 1Hz to 0Hz the hot-wire shows lower voltage as compared to the calibration performed while increasing the turbine frequency from 0Hz to 1Hz. This is because it takes longer time to stabilize the von Kármán flow while decreasing the turbine frequency from 1Hz to 0Hz as compared to increasing the turbine frequency from 0Hz to 1Hz. This can also be explained with the help of following example. Let us consider that we want to perform the SHREK experiment at 0.5Hz in co-rotation configuration. Let t_1 be the time to reach steady state at 0.5Hz starting from 0Hz. And, let t_2 be the time to reach steady state at 0.5Hz starting from 1Hz. In this case, t_2 will be higher than t_1 because of the additional inertia of the moving fluid already present at 1Hz. Therefore, because of the low viscosity of helium we should wait long time so that the flow reaches steady state. Hence, the hot-wire calibration performed over 4 hours of duration (over longest duration) is the most accurate calibration at all velocities.

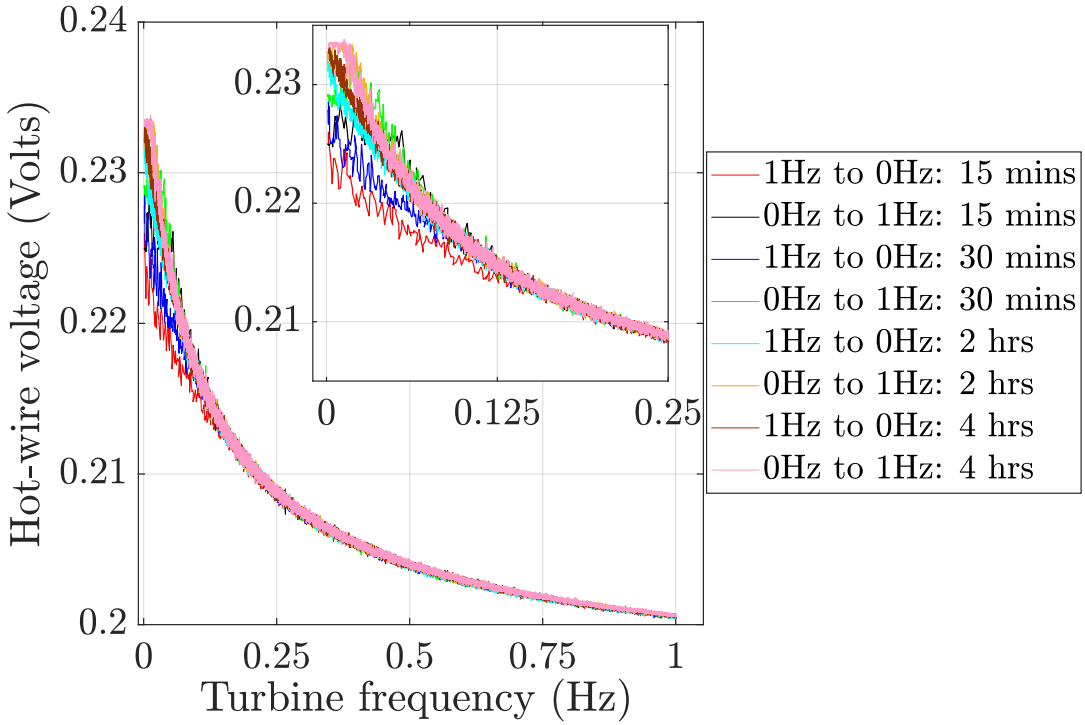

Figure II.10: Multiple hot-wire calibrations performed over different duration in the SHREK experiment using straight blades in HeI at T = 2.2K [$d_w = 1.27\mu m$ and $l_w = 300\mu m$; hot-wire position: 4cm above the equatorial plane]

II.6 Hot-wire calibration in the ECOUTURB experiment

The ECOUTURB experiment is in fact the SHREK experiment but using smooth disks instead of turbines with blades. The ECOUTURB experiment is performed mainly to study the scaling laws of torque (mean and fluctuations) measured in HeI and HeII. As explained earlier, the reference mean velocity in the hot-wire calibration performed in the SHREK experiment is calculated based on the assumption of solid body rotation achieved in co-rotation configuration of flow. But, this is very less likely to be true when the turbine with blades are replaced by the smooth disks. This velocity is then given by, Velocity (m/s) $= \mathcal{A} \times \mathcal{R} \times \omega = \mathcal{A} \times \mathcal{R} \times 2\pi f$, where $\mathcal{R} = 0.35m$, $\omega = 2\pi f$ is the angular velocity in $\frac{rad}{s}$, f is the frequency of rotation of turbines in Hz and $\mathcal{A}$ is the prefactor while estimating the reference velocity. The prefactor $\mathcal{A} = 1$ is assumed in case of turbine with blades but for smooth disks it is found to be equal to 0.2 at the equatorial plane from the numerical analysis (G. Balarac et al., not yet published). Figure II.11 shows the hot-wire calibrations performed in the ECOUTURB experiment using two hot-wires of $d_w = 1.27\mu m$ and $d_w = 0.5\mu m$. From figure II.2 and figure II.11a, we see that the dynamic range of the hot-wire voltage is bigger for the SHREK experiment than the ECOUTURB experiment for the same range of velocities. We have also confirmed that the prefactor $\mathcal{A}$ is far less in the ECOUTURB as compared to the SHREK experiment by performing a precise hot-wire calibration in the HECAL experiment (see section III.3.5 for more details).

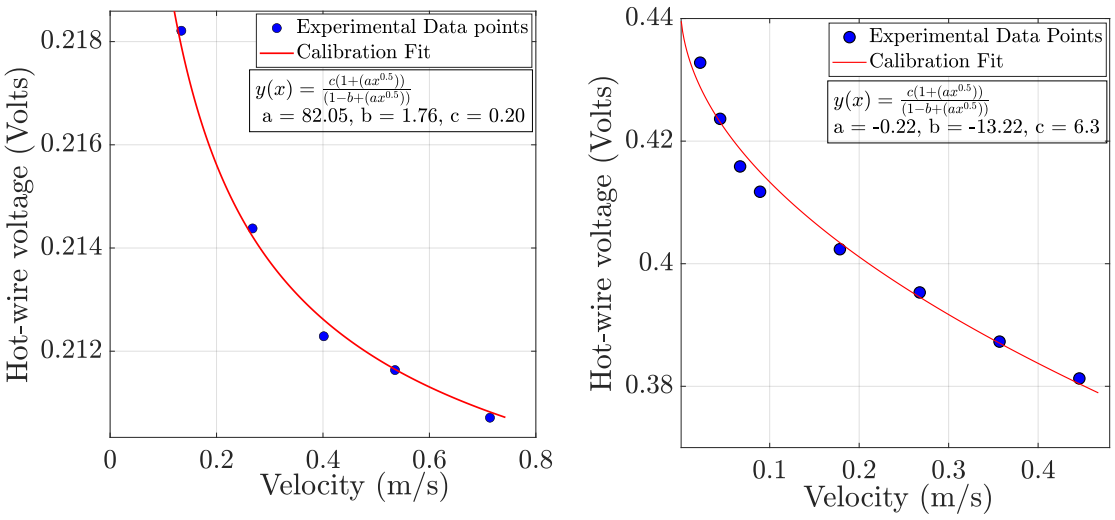

(a) Hot-wire position: At equatorial plane with $d_w = 1.27\mu m$ and $l_w = 300\mu m$

(b) Hot-wire position: At equatorial plane with $d_w = 0.5\mu m$ and $l_w = 300\mu m$

Figure II.11: Hot-wire calibration in the ECOUTURB experiment in HeI at T = 2.2K

II.7 Time constant measurement in CCA mode

The problem of thermal inertia of the hot-wire is associated with the inability to respond instantaneously to the flow velocity fluctuations. In the CCA mode (and also in the CVA mode) the temperature of the hot-wire does not remain constant, which necessitates to take into account the finite thermal capacity of the hot-wire (see equation II.12). The time constant of the hot-wire must therefore be estimated. The higher value of the volumetric heat capacity $\left(\frac{J}{m^3 \cdot K}\right)$ of the hot-wire means a longer time for the hot-wire to reach thermal equilibrium. The smaller the thermal inertia of the hot-wire (i.e. volumetric heat capacity), the smaller will be its time constant and *vice versa*. The time constant τ signifies that the hot-wire is able to measure velocity fluctuations of frequency $< \frac{1}{2\pi\tau}$ with no signal damping [Bruun, 1995]. Beyond frequencies $> \frac{1}{2\pi\tau}$ the hot-wire response attenuates which leads to decrease in the signal to noise ratio. This also means that the response of the hot-wire is flat until the frequency $f \approx \frac{1}{2\pi\tau}$. The differential equation expressed by equation II.5 leads to the following expression for the time constant given by [Bruun, 1995]:

$$\tau = \frac{C_w}{\alpha R_a (a' - I^2 + b' U^n)}. \tag{II.9}$$

Considering the rate of change of energy stored in the hot-wire as negligible, the energy balance of the hot-wire can be expressed by:

$$\frac{I^2 R_w}{R_w - R_a} = a' + b' U^n. \tag{II.10}$$

Inserting the thermal capacity, $C_w = \rho_w A_w l_w c_w$, where c_w is the specific heat capacity $(\frac{J}{kg \cdot K})$ and $\chi_0 = R_a A_w / l_w$ along with equation II.10 in equation II.9, the time constant can be expressed by:

$$\tau = \frac{\rho_w A_w^2 c_w (R_w - R_a)}{\alpha \chi_0 I^2 R_a}. \tag{II.11}$$

From the above equation, we see that the time constant of the hot-wire is independent of its length, but depends strongly on its diameter [Comte-Bellot, 1976] (see equation 2.51 in Bruun

[1995] for more details). This equation reflects that the time constant of the hot-wire increases with the overheating ratio and decreases with increasing velocity of the flow. Thus, the time constant of the hot-wire operated at high temperature (say $\approx$ 100K) is higher than the hot-wire operated at low temperature (say $\approx$ 25K) because of the increased thermal capacity of the hot-wire at high temperatures. The time constant of the hot-wire also depends on its material properties and on the properties of the fluid. From equation II.11 we see that the response time of the hot-wire in CCA mode depends on the mean flow velocity (change in R_w). This is because of the thickness of the thermal boundary layer which controls the convective heat flux from the hot-wire to the fluid which scales like U^n with $n \approx 0.5$. Thus, we have to estimate the time constant "in place" in the presence of the external flow. But, in this case the turbulent velocity fluctuations are superimposed on the hot-wire response to the pulse (or square) wave. A way to get rid of the velocity fluctuations is to perform a coherent average (phase locked to the pulse wave frequency) over the different cycles of the pulse wave.

We decided to measure the time constant of the hot-wire using its step response to a pulse wave generated using a Tektronix function generator AFG3102. A pulse wave of frequency 30Hz with the width of 5ms (i.e. a duty cycle of 15%) is used over a total duration of 68 seconds, which ensured the total number of cycles to be more than 2000. An offset which corresponds to 15% overheating of the hot-wire is chosen for the pulse wave. The rise time (leading edge) and fall time (trailing edge) of the pulse wave is set to 100ns. It must be ensured that the rise time (or fall time) is much smaller than (say $\approx$ 10 times) the expected time constant of the hot-wire. The data acquisition is done with the help of a PXI-5922 National Instruments acquisition card which has the maximum sampling rate of 15MHz. A sampling rate of 1MHz is used which ensured the precise measurement of the time constant of the hot-wire. Figure II.12 shows the hot-wire response averaged over 2032 cycles. An averaging over a large number of cycles is required to obtain a clean response of the hot-wire. Note that this is also the case for the CVA measurements (not shown here). The time constant measurement shown in figure II.12 is performed in the co-rotation configuration of the SHREK experiment at turbine frequency of 1Hz in HeI at T = 2.2K. Figure II.12a shows various stages of the hot-wire during pulse wave response. Initially, the voltage across the hot-wire is $V = RI$, which then increases suddenly by a factor of $dV1 = R(di)$ because of the instantaneous increase in current. And then, the hot-wire voltage increases exponentially with $dV2 = (dR)I$ while heating the hot-wire which determines the time constant. This increase ($dV2$) in voltage is mainly because of the increase in the resistance (i.e. temperature) of the hot-wire. The same is also true while cooling the hot-wire. Hence, we can estimate the time constant of the hot-wire during either heating-up or cooling-down of the hot-wire without significant difference. The time constant τ is then given by the time taken to reach $63\%\Delta V$ from the peak value as shown in figure II.12b [Bruun, 1995; Jiang, 1997; Russo, 2011].

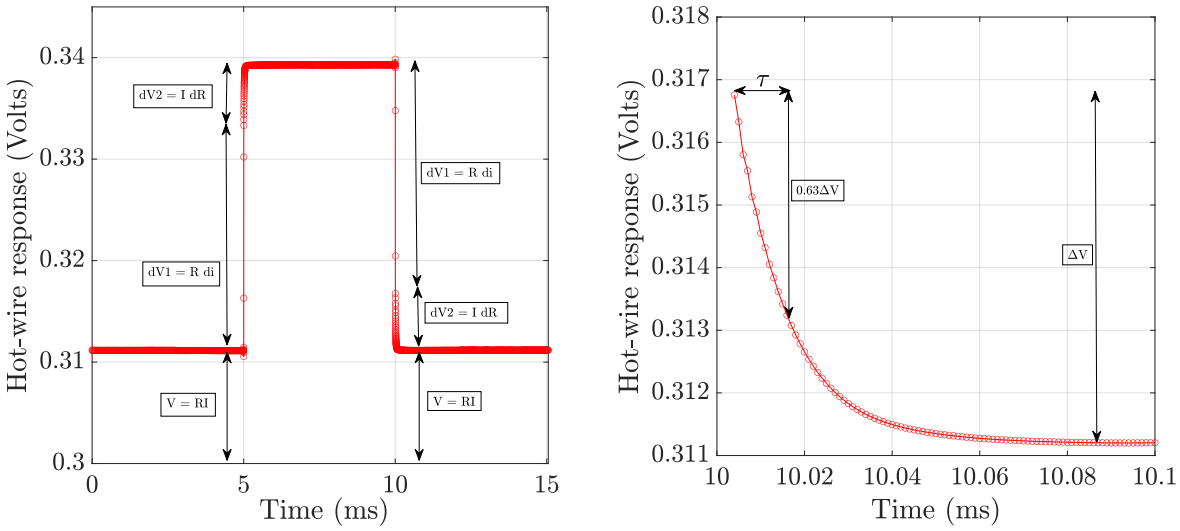

(a) Pulse wave response of the hot-wire averaged over 2032 cycles

(b) Zoomed view of pulse wave response of the hot-wire during cooling, $\tau = 13\mu s$

Figure II.12: Procedure to find the time constant of the hot-wire in CCA mode

II.7.1 SHREK experiment

The time constant of the hot-wire is measured in the SHREK experiment in the co-rotation configuration of flow for different frequency of turbines. Figure II.13 shows the time constant of the hot-wire in normal helium at T = 2.2K and in superfluid helium at T = 2.0K. This figure shows that the measured time constant of the hot-wire decreases as the velocity increases, which is consistent with equation II.9 [Comte-Bellot and Sarma, 2001; Sarma and Lankes, 1999; Mohammed-Taifour et al., 2015]. From this figure, we see that the time constants measured during heating-up and cooling-down of the hot-wire are in good agreement. The hot-wire is operated at the same overheating current in both HeI and HeII ($\approx 18\%$). We found that the time constant in HeII is smaller than in HeI, which confirms better cooling of the hot-wire in HeII. A better cooling of the hot-wire in superfluid is expected because of its higher effective thermal conductivity compared to HeI. According to equation II.9 a fit is constructed to verify the dependence of time constant with respect to velocity. Figure II.14a shows that the experimental data points follow the fit very nicely for normal helium. But, in case of superfluid as shown in figure II.14b, the fit does not follow the experimental data points very nicely, although the dependence on the velocity can be clearly seen. The heat transfer mechanism in superfluid helium is different than in classical fluids which may explain the inadequate fit of the time constant in HeII [Castaing, 2016; Diribarne et al., 2021b,a].

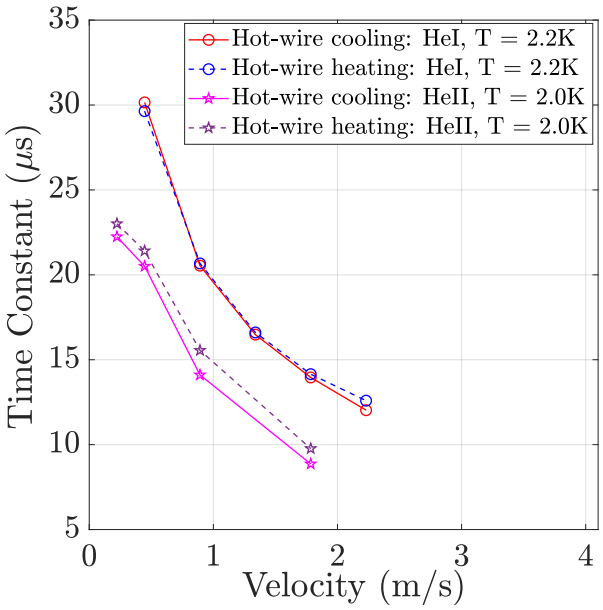

Figure II.13: Measured time constant of the hot-wire in the SHREK experiment using straight blades in HeI and HeII ($d_w = 1.27\mu m$ and $l_w = 300\mu m$)

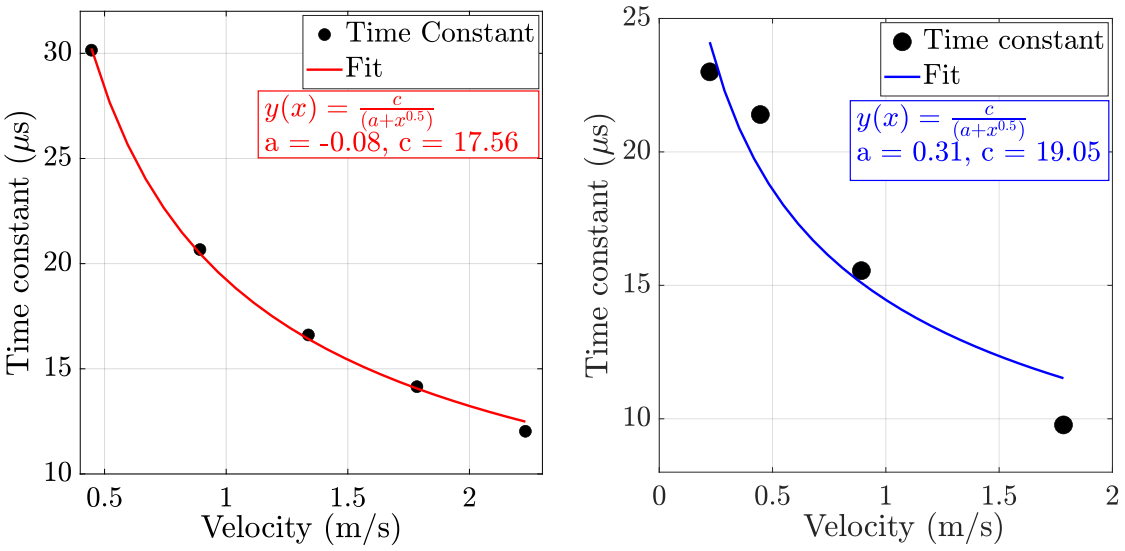

(a) Time constant in HeI with fit

(b) Time constant in HeII with fit

Figure II.14: Time constant at different velocities and its experimental fit according to equation II.9

II.7.2 ECOUTURB experiment

In the SHREK experiment, the turbines are equipped with blades, and the maximum mean velocity attained in the von Kármán cell in the co-rotation configuration is about $2.5\frac{m}{s}$ (see figure II.13). On the other hand, in the ECOUTURB experiment, as the turbines are replaced with smooth disks, the maximum mean velocity attained is about $1\frac{m}{s}$. Therefore, the time constant of the hot-wire in the ECOUTURB experiment is measured at the maximum velocity of $1\frac{m}{s}$ (see figure II.11a). The time constant is measured at three different medium temperature of T =

2.2, 2.0 and 1.86K with higher overheating of the hot-wire in superfluid than in normal helium. The heat transfer from the hot-wire is more efficient in HeII than in HeI. Therefore, higher overheating in HeII is used to operate the hot-wire at the same resistance (i.e. temperature) as in HeI. Different but similar hot-wires are used in the SHREK and ECOUTURB experiments. Figure II.15 shows the time constant of the hot-wire in the ECOUTURB experiment with respect to velocity in the co-rotation configuration of flow. This figure shows that the time constant decreases with respect to increasing velocity for all the medium temperatures. As the same overheating (same current) of the hot-wire is maintained at T = 2.0K and T = 1.86K, the effect of superfluid temperature on the time constant can be seen from this figure. The time constant of the hot-wire is found to be smaller for lower superfluid temperatures, suggesting the better cooling of the hot-wire. According to equation II.9, at U = 0 the hot-wire has the maximum time constant as compared to U > 0. At T = 1.86K, the maximum time constant of the hot-wire is found to be $13.63\mu s$ at null velocity which is consistent with equation II.9.

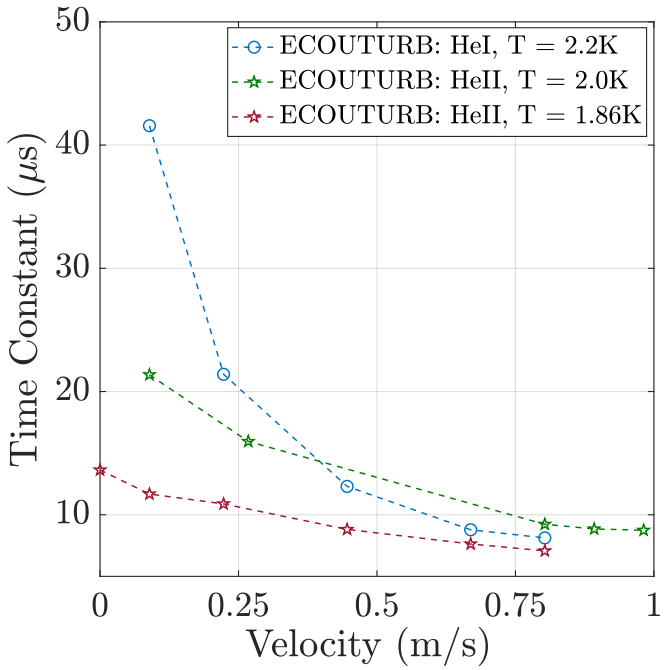

Figure II.15: Measured time-constant of the hot-wire in the ECOUTURB experiment in HeI and HeII ($d_w = 1.27\mu m$ and $l_w = 300\mu m$)

II.7.3 HECAL experiment

The functioning and operation of the HECAL experiment will be discussed in detail in Chapter III. Figure II.16 shows the time constant of the hot-wire measured in the HECAL experiment. Compared to the SHREK and ECOUTURB experiments, from figure II.16 we see that in the HECAL experiment, the time constant of the hot-wire is estimated for a higher range of velocities (i.e. $> 3\frac{m}{s}$ in HeI and HeII). We note that the velocity plotted in figure II.16 is the velocity of the rotational arm i.e. the hot-wire. But, in fact, at constant frequency of the rotational arm the hot-wire measures its relative velocity with respect to the moving fluid i.e. wake flow (more details in Chapter III). Thus, the estimated time constant corresponds to the relative velocity rather than the velocity of hot-wire itself which is shown in figure II.16. Two different hot-wires of $d_w = 1.27\mu m$ and $d_w = 5\mu m$ having a $l_w = 1mm$ (i.e. much longer than in other experiments) are used. Figure II.16a shows the time constant of the hot-wire with $d_w = 1.27\mu m$ and $l_w =$

$1mm$ which is comparable to the time constants estimated in the SHREK and ECOUTURB experiments. From figure II.13 and figure II.16a, it is verified that the time constant of the hot-wire does not depend on its length (see equation II.11). In the HECAL experiment higher overheating (current) is used for HeII than in HeI to target the same resistance of the hot-wire after heating-up (i.e. after leading edge of the pulse wave). Hence, the time constants for this hot-wire in superfluid are observed to be higher than in normal helium. From figure II.16a it appears that the time constant is yet sensitive to higher velocities in HeII, however, it seems to be non sensitive in HeI (i.e. $> 4.5\frac{m}{s}$). Figure II.16b shows the time constant for hot-wire of $d_w = 5\mu m$ in HeII at T = 2.0K. As $\tau \propto d_w^2$, the time constant of the hot-wire of $d_w = 5\mu m$ is at least 10 times that of the hot-wire with $d_w = 1.27\mu m$ [Comte-Bellot, 1976]. Hence, the time constant of the hot-wire with $d_w = 5\mu m$ within the range of 100 - $250\mu s$ is consistent. Figure II.16c shows the time constant of the hot-wire of $d_w = 5\mu m$ at ambient temperature using He gas. Overall, the time constant of the hot-wire of $d_w = 5\mu m$ varies within 460 - $510\mu s$ at ambient temperatures. This is typically the time constant of commercially available hot-wires of $d_w = 5\mu m$ and $l_w = 1mm$ at ambient temperatures. From figure II.16b and figure II.16c, we also see that the time constant of hot-wire of $d_w = 5\mu m$ in superfluid at T = 2.0K is less than at ambient temperature.

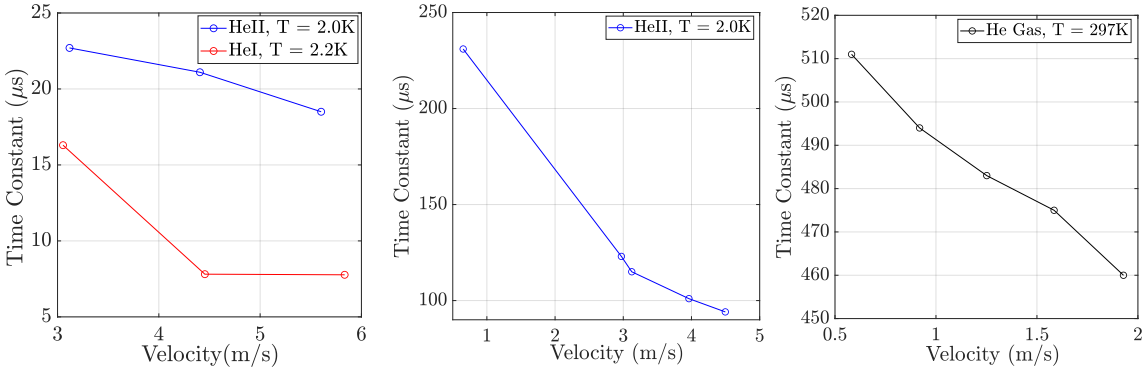

(a) Time constant of hot-wire of $d_w = 1.27\mu m$ & $l_w = 1mm$ in HeI & HeII

(b) Time constant of hot-wire of $d_w = 5\mu m$ & $l_w = 1mm$ in HeII

(c) Time constant of hot-wire of $d_w = 5\mu m$ & $l_w = 1mm$ in He gas at ambient temperature

Figure II.16: Time constant measurement in the HECAL experiment

II.8 Correction of the hot-wire signal based on its time constant

After estimating the time constant of the hot-wire in the CCA mode, using the thermal lag compensation, we can improve the raw signal of the hot-wire. A time constant of τ means that the velocity fluctuations measured by the hot-wire are attenuated above the frequency of $f_w \approx \frac{1}{2\pi\tau}$ [Bruun, 1995]. Using equation II.5, the signal can be corrected above the frequencies of f_w Hz using the following relation given by [Dryden, 1929; Comte-Bellot, 1976]:

$$\tau \frac{dR_w}{dt} + R_w = R_w^*, \tag{II.12}$$

where R_w^* is the resistance fluctuation of the ideal hot-wire. Typically, in the SHREK experiment in the PSD of the hot-wire spurious frequency peaks are observed beyond 5 - 6kHz where the low-pass filter is used for the data post-processing. The range of hot-wire time constant which lies within 12 - $30\mu s$ corresponds to f_w of 13 - 5kHz. Figure II.17 shows the effect of the correction of the raw hot-wire signal using thermal lag compensation. Figure II.17a shows the power

spectrum density of the raw hot-wire signal before (original) and after applying the thermal lag compensation (corrected) according to equation II.12. A slight improvement of the original signal could be achieved at higher frequencies which seems to extend the $f^{-\frac{5}{3}}$ dependence. Applying the thermal lag compensation to the original signal, a higher range of velocities (i.e. wider PDF) is observed in the corrected signal. It is also confirmed that there is no significant change in the statistical quantities of turbulence such as $\langle U \rangle$, u_{rms}, dissipation rate and turbulence scales before and after applying the thermal lag compensation. Figure II.17b shows the compensated third order structure function with respect to scale r for the original and corrected velocity signal based on the estimated time constant. A vertical black-dashed line in this figure shows the spatial filtering of the hot-wire at $l_w \approx 300\mu m$. From this figure we see no significant change in the compensated third order structure function in the inertial range.

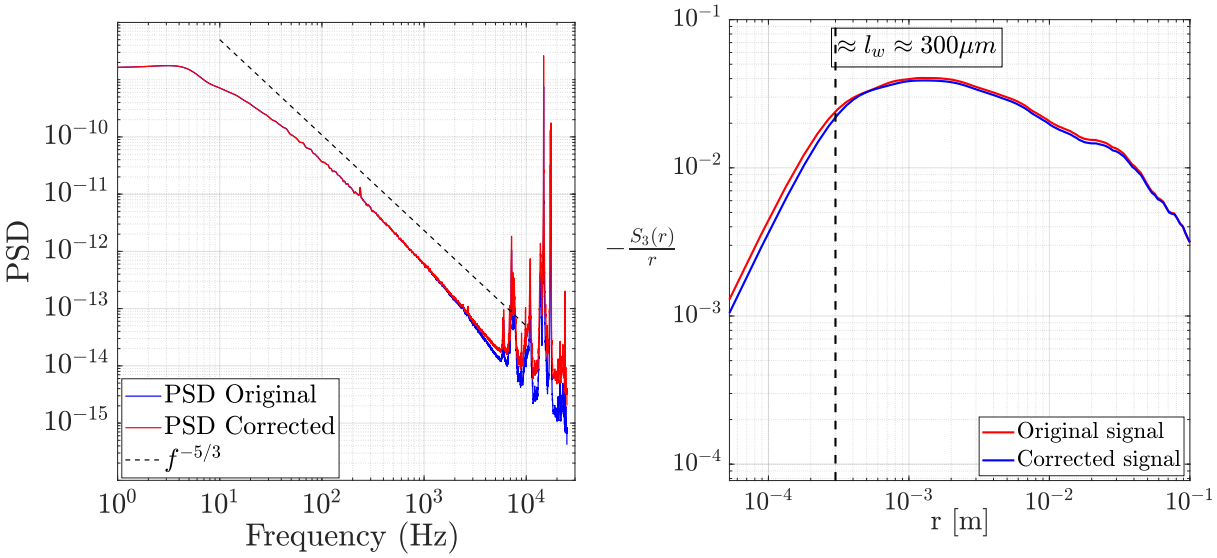

(a) PSD of the original and corrected hot-wire signal

(b) The compensated third order structure function estimated from the original and corrected velocity signal based on the time constant

Figure II.17: Effect of the correction of the raw hot-wire signal based on the time constant for +1.0Hz co-rotation configuration in the SHREK facility using straight blades [$L = 0.06$m, $\lambda = 700\mu m$]

II.9 Conclusion

In this chapter, the basic principle of operation of the hot-wire is explained. A brief procedure to fabricate the hot-wire made of Pt-Rh Wollaston wire is demonstrated. Typically, the home-made hot-wires of $d_w = 1.27\mu m$ and $l_w = 300\mu m$ are used in this work. The different modes of operation of hot-wire are discussed with pros and cons. The heat transfer relationship is established leading to the usual King's law of calibration. In CTA mode a feedback electronics is used which might lead to some instabilities. The oscillations in the feedback loop expose the hot-wire to the risk of burning. The preferred choice of operating the hot-wire in CCA mode is supported by its simple instrumentation (without feedback loop and hence more stable) and easy manipulation towards higher overheating with less risk associated with burning of the hot-wire. A satisfactory signal to noise ratio can be achieved in the CCA mode together with safer operation as compared to the CTA mode.

The characterization of home-made hot-wires of different diameters and lengths is performed. The dependence of resistance of the hot-wires with respect to temperature from ambient down to 2K is explored. Based on those curves, the value of temperature coefficient of resistance, α for the hot-wires is found. The sensitivity of the hot-wires for different calibrations carried out during the SHREK experiment are explored in CCA and CTA mode. We found that the calibrations of hot-wire performed over 3 - 4 weeks in the SHREK experiment do not change significantly. To have the precise hot-wire calibration, it is recommended to perform the calibration over a very long duration such as over 12 hours, so that the flow has enough time to reach steady state. The hot-wire calibration performed in the ECOUTURB experiment is shown which covers a relatively small range of velocity and hence a comparatively small range of hot-wire voltage as compared to the SHREK experiment. The hot-wire calibrations performed using CCA mode in HeI follow the King's law of calibration very nicely.

The time constant of different home-made hot-wires are measured in the experiments of SHREK, ECOUTURB and HECAL using its response to the pulse wave. In all cases, the time constant of hot-wires is found to be decreasing for increasing velocity. For the same overheating of hot-wire, the time constant in HeII is found to be smaller than in HeI. It is found that the dependence of the time constant on the velocity follows the calibration fit nicely. The time constant of the hot-wire is explored for two different superfluid temperatures and we found that the time constant of the hot-wire decreases with lowering the superfluid temperature. The time constant found in the HECAL experiment are comparatively similar to those in the SHREK and ECOUTURB experiments without any dependence on the length of hot-wires. Based on $\tau \propto d_w^2$, the time constant of hot-wire of $d_w = 5\mu m$ is experimentally found to be at least 10 times the hot-wire of $d_w = 1.27\mu m$. A method to correct the hot-wire signal using time constant for thermal lag compensation is demonstrated. Based on the power spectrum it is shown that a slight improvement of the raw hot-wire signal is possible using thermal lag compensation beyond the cutoff frequency f_w.

In this thesis many hot-wires of $d_w = 0.3$ to $5\mu m$ are tested at low temperatures. The best hot-wire to use in cryogenic turbulent flows would be of $d_w = 0.3\mu m$ or even less, with l_w comparable to the Kolmogorov scale (say $\approx 50\mu m$). But, we noticed that the hot-wires of $d_w = 0.3$ and $0.5\mu m$ are very susceptible to break because of the vibration/shocks and differential contraction forces during cool-down process. Therefore, we hardly succeeded to obtain velocity measurements using the hot-wire of $d_w = 0.3$ or $0.5\mu m$. In this scenario, the home-made hot-wire of $d_w = 1.27\mu m$ and $l_w = 300\mu m$ promises to be the best candidate to work at cryogenic temperatures, whose spatial resolution is at least enough to resolve the scales in the inertial range.

III HECAL EXPERIMENT

HECAL is the experimental facility which is developed to perform the hot-wire calibration at low temperatures in HeI and HeII. HECAL stands for the hot-wire **CAL**ibration in **HE**lium. The HECAL cryostat is based on the HEJET experiment. Hence its cryogenic operation is very similar, so that only the difference between the HECAL and HEJET experiment are emphasized here. For the HECAL experiment mainly the pressurized helium bath of the HEJET experiment is modified. The details of the HEJET experiment are described in Chapter IV along with a full description of the cool-down process, which is the same as for the HEJET and HECAL experiment. The objective of this chapter is to demonstrate the methodology towards precise calibration of the hot-wire and to modify the instrumentation accordingly. The whole purpose of the HECAL experiment is to perform precise calibration of the hot-wire, and install the same hot-wire in the SHREK and HEJET facilities. In this way, the experimental measurements in the SHREK and HEJET can be performed using the pre-calibrated hot-wires.

III.1 Introduction

In the SHREK experiment, the hot-wire calibration is performed using the assumption of solid body rotation attained in the co-rotation configuration of the von Kármán flow. Whereas in the HEJET experiment, the hot-wire calibration is performed using the established experimental relationship (see equation IV.8) between the velocity at an axial distance of 50d (d = nozzle diameter) and the nozzle exit velocity. These calibrations of the hot-wires performed in the SHREK and HEJET facilities are not absolutely precise and accurate. Hence, a small error in the hot-wire calibrations can cause uncertainty in the results. Therefore, to obtain an accurate and precise hot-wire calibration, the experiment of HECAL has been designed.

Traditionally, the hot-wire calibration is performed using the reference of an incoming constant flow velocity measured with the help of various techniques such as pitot tube, venturimeter, cup anemometer or a hot-wire calibrator using a free jet. But, on the other hand, moving the hot-wire itself in a still environment with a known velocity allows to eliminate any uncertainty associated with the previous methods, where the hot-wire stays fixed in a moving fluid [Bruun, 1995]. In other words, the hot-wire calibration can be performed either by placing a hot-wire in an incoming flow or by moving the hot-wire itself with a known velocity in a still fluid. In this work, the latter approach of flying/moving hot-wire is implemented. From figure II.2 we see that in the SHREK experiment the range of velocity for the hot-wire calibration lies within 0 - 2.5$\frac{m}{s}$. From figure IV.3.2 we see that in the HEJET experiment the range of velocity for the hot-wire calibration lies within 0 - 1.8$\frac{m}{s}$.

An accurate hot-wire calibration is required in the experiments or in the practical scenarios, where the maximum velocity is less than 1$\frac{m}{s}$. Multiple attempts have been made in the past to perform the calibration of hot-wires at low velocities in ambient air. Sattarzadeh et al. [2013] and Lee and Budwig [1991] used a vortex shedding method for the calibration of hot-wire at low velocities. They could calibrate the hot-wire at the velocity of as low as 0.15$\frac{m}{s}$. Guellouz and Tavoularis [1995] used a pendulum technique to perform the hot-wire calibration over low velocity range. They could calibrate the hot-wire at the lowest velocity of 50$\frac{mm}{s}$. Bruun et al. [1989] used a swinging arm calibration method for the hot-wire probe calibration with which they could calibrate the hot-wire lowest up to 1$\frac{m}{s}$. Ozahi et al. [2010] proposed a calibration method using a simple laminar pipe flow set-up, with which they could calibrate the hot-wire over a range of 29$\frac{mm}{s}$ to 1.79$\frac{m}{s}$. They also proposed a rotating disc method of calibration to perform the hot-wire calibration over a range of 50$\frac{mm}{s}$ to 1.05$\frac{m}{s}$. Recently, Ozkan [2019] performed the low speed hot-wire calibration in water using the rotating arm over a range of 0 - 0.6$\frac{m}{s}$. But this calibration has not been performed during one rotation of the arm, rather the

arm has been rotated at constant angular velocity, in which the contribution of the wake flow appears. Considering all these techniques available in the literature, in this chapter a similar technique of the hot-wire calibration using CCA mode, over a velocity range of $20\frac{mm}{s}$ to $5\frac{m}{s}$ for multiple hot-wires, performed within one rotation of the arm is proposed.

III.2 Experimental set-up

The HEJET and HECAL experiments consist of many common parts, whose details are explained in Chapter IV. Nevertheless, the description of the HECAL experiment presented in this section is enough to follow this chapter without discontinuity. Figure III.1 shows the schematic and actual experimental set-up of the HECAL facility.

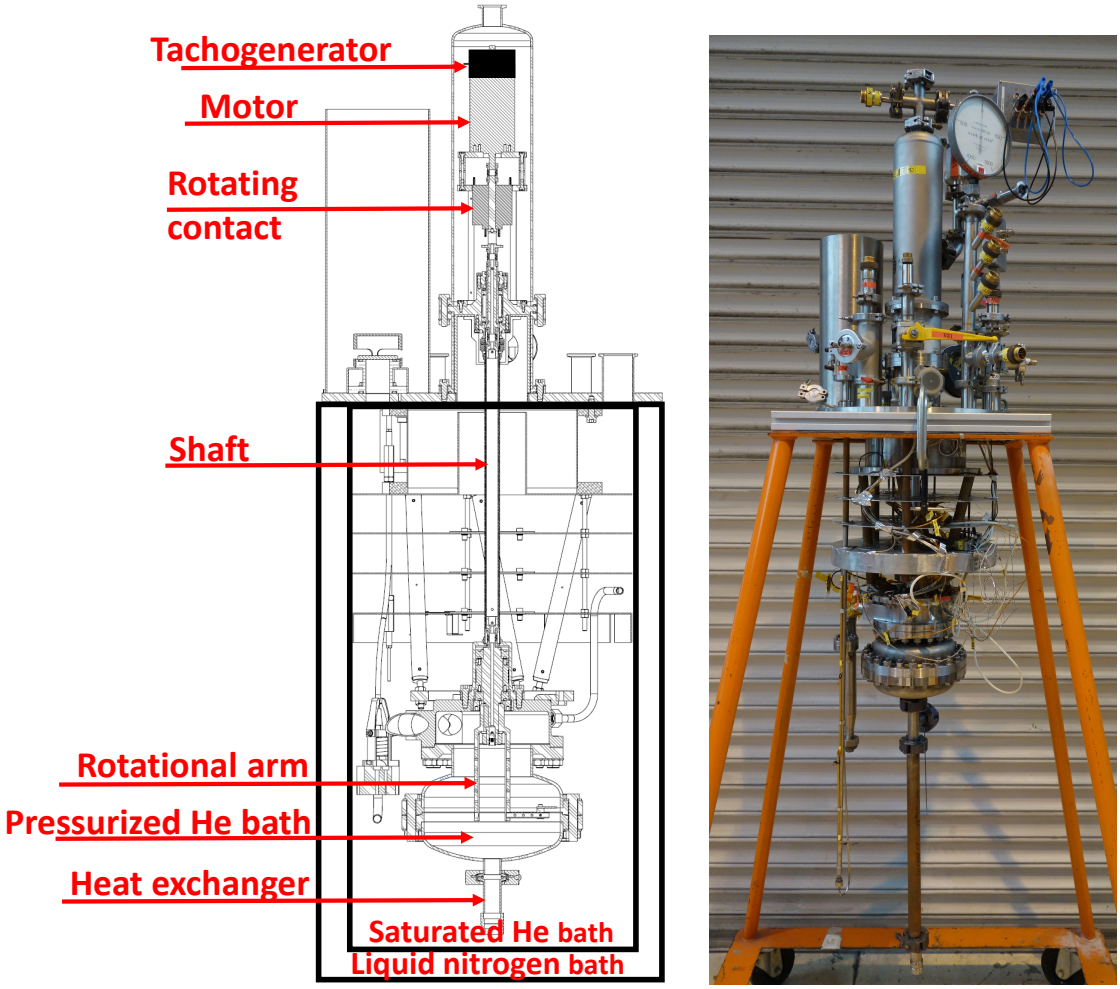

Figure III.1: Schematic and actual experimental set-up of the HECAL facility (not to scale)

Mainly, the HECAL facility consists of a DC motor with tachogenerator, shaft assembly with rotating contact and the rotational arm on which the hot-wires are mounted. Similar to other cryogenic facilities, the HECAL facility is composed of a pressurized helium bath, where the hot-wires are installed; the pressurized bath is thermalized in a saturated helium bath, whose temperature is controlled. A liquid nitrogen bath provides thermal shielding of the saturated helium bath. To construct the experimental set-up of HECAL, the turbine, volute and the

labyrinth of the HEJET facility are removed. At the place of turbine, the hot-wire support along with the rotational arm is mounted at the end of the rotating shaft. The pressurized helium bath also incorporates one vertical copper tube, which acts as a heat exchanger to evacuate the heat into the saturated helium bath. This copper tube is most efficient in HeII.

We have two different DC motors of the same type which can be used to rotate the shaft in the HECAL/HEJET experiment. Out of these two, one DC motor is coupled with a reductor (PLG52) of reduction ratio 4.5:1. At temperatures as low as 2K, because of the contraction of the entire shaft assembly and the joints, a high starting torque is needed to overcome static solid friction. In that case, it is fruitful to use the motor with reductor, because it generates higher torque as compared to the motor without reductor. But, on the other hand, the rotational motion imparted by the shaft of the motor with reductor is found to be non uniform because of the mechanical limitations associated with the gear box. This suggested that the rotary motion transmitted within the reductor is not uniform. As the tachogenerator is mounted with the DC motor at top end, and the reductor is coupled with the motor shaft at the bottom end, the effects of the non-uniform transmission of rotary motion cannot be observed in the tachogenerator signal. Therefore, in the case of motor with reductor the velocity of the rotational arm measured by the tachogenerator is not accurate. This malfunctioning in the rotary motion can be seen in the signal of the hot-wire as shown in figure III.3. This hot-wire calibration is performed using the micro-fabricated hot-wire at ambient temperature. From this figure, we can clearly see that the rotational arm is moving in steps within one rotation, which causes delay in the rotary motion. For this reason, the use of motor with reductor has been discarded.

Figure III.2: Motor with reductor at bottom end and tachogenerator at top end

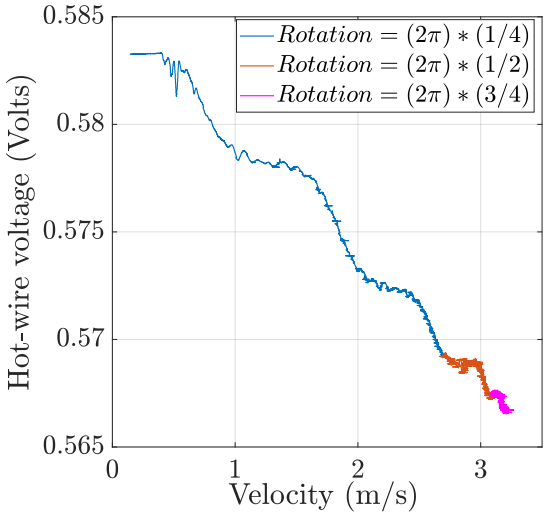

Figure III.3: Hot-wire signal within one rotation of arm with respect to velocity using the motor with reductor (in CCA mode)

III.2.1 Hot-wire support

Figure III.4 shows the hot-wire support which consists of the rotational arm on which hot-wires are installed. Each hot-wire can be operated independently using a separate battery. The 4 hot-wires can be mounted at once on the rotational arm each at a radius of $r = 33, 45, 57$ and 69 mm.

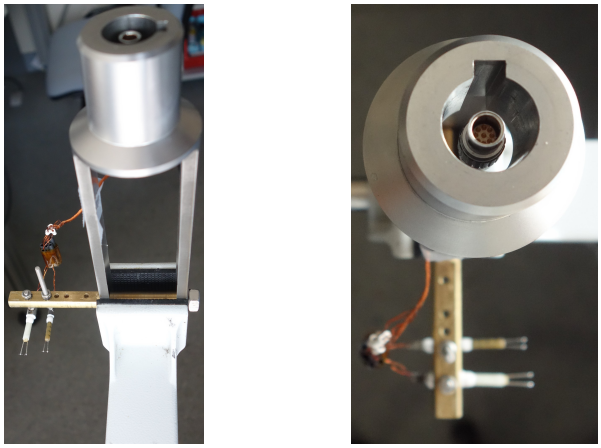

Figure III.4: Hot-wires mounted on the rotational arm [Right figure: At the center of the rotating arm assembly we can see the 9 pin DIN connector]

Figure ?? shows the rotational arm mounted in the pressurized helium bath of the HECAL facility. The hot-wire connecting wires are passed through the bottom end of the shaft using the 9 pin DIN connector as shown in figure III.4. These hot-wire connecting wires are then connected to the rotating contact at the top end of the shaft as shown in figure III.1. This figure shows two different ways of installing the hot-wire on the rotational arm. The hot-wires can be installed either above or below the rotational arm. In either way, the hot-wires are installed to measure the azimuthal (θ) component of velocity which is perpendicular to the hot-wire itself.

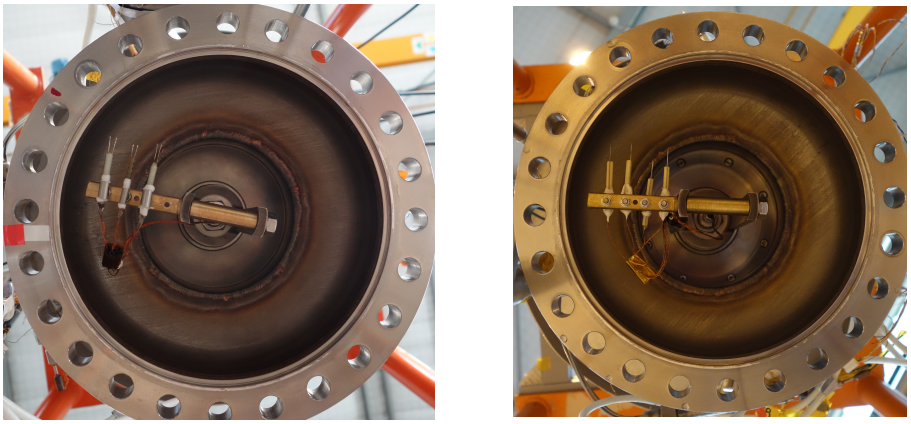

Figure III.5: Mounting of the rotational arm to the motor shaft in the pressurized helium bath (Bottom view)

III.2.2 Instrumentation for precise calibration of hot-wires

Figure III.6 shows the simplified block diagram of the entire experimental set-up with hot-wires mounted on the rotational arm. A brushed Dunkermotoren DC motor GR63X55 is used, whose speed is controlled by the function generator through controller and simultaneously measured by the tachogenerator mounted on the motor as shown in the figure III.6. The function generator AFG 3102 is used along with the ESCON 70/10 servo controller. The Baumer tachogenerator of type GT5.05L/407 is used which generates $7\frac{mV}{RPM}$ linearly until 21V at 50Hz from which the instantaneous angular velocity of the rotational arm is estimated.

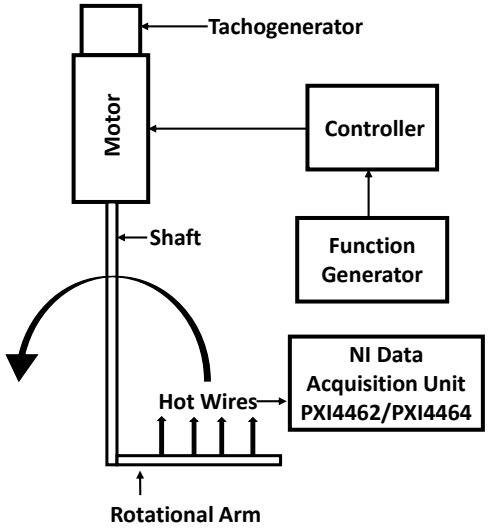

Figure III.6: Simplified block diagram of the HECAL experimental set-up

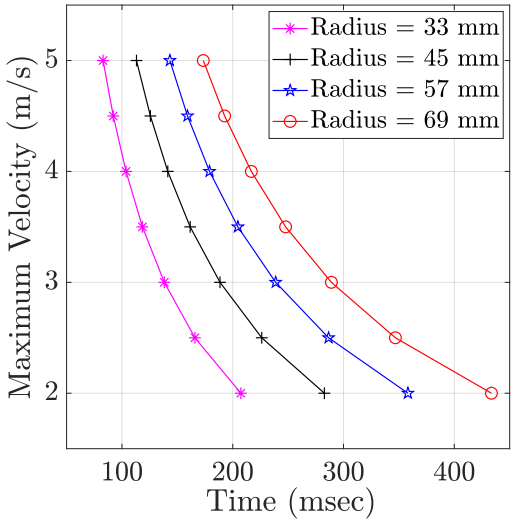

Figure III.7: Theoretical estimation of time (ramp time) required to achieve the maximum desired velocity after one rotation

To perform the calibration of the hot-wire accurately and precisely using this rotational arm assembly, the following strategies are used. In order to get rid of the flow perturbations, the calibration of the hot-wire is performed within only one rotation of the arm. The maximum desired velocity for the hot-wire calibration must be reached before the end of one complete rotation of the rotational arm. To estimate the time required to reach the maximum velocity, we impose a constant angular acceleration on the rotational arm. Applying this condition, it is therefore possible to estimate the duration of the linear ramp required to reach the maximum desired velocity using the relation of tangential velocity given by, $V = r \times \Omega = r \times 2\pi f$, where V is the maximum desired velocity for calibration, r is the radius at which the hot-wire is mounted on the rotational arm, f is the instantaneous frequency of the rotational arm in Hz measured using tachogenerator and Ω is the angular velocity of the arm in $\frac{rad}{s}$.

With the reference of an estimated ramp time, we can construct a linear ramp using a function generator, and use it as an input to the motor through a controller. Such kind of ramps can be designed according to the time required to reach a desired maximum velocity at the end of one rotation of arm, for hot-wires located at different radii, as plotted in figure III.7. For example, if we need to perform the calibration of a hot-wire located at $r = 69mm$ with a maximum velocity of $4.5\frac{m}{s}$, then as an input to the controller we can program a linear ramp from 0V to 4V spanning over a period of 200msec. Typically, in this experiment half a second is enough to perform the hot-wire calibration. In such a way, multiple hot-wire calibrations can be performed using different linear ramps of variable duration corresponding to the maximum desired velocity of calibration.

III.3 Results

For the reasons discussed earlier, all the hot-wire calibrations are performed using the motor without reductor. The reference velocity with which the hot-wire calibration can be performed is measured using the tachogenerator. The hot-wires are calibrated for the tangential component of the velocity during the rotation. Typically, for the home-made hot-wires the thermal time constant is of the order of few hundreds of microseconds at ambient temperatures and few tens of microseconds at lower temperatures. The characteristic time scale for the change of velocity

$\left(\frac{dv}{(dv/dt)} \approx \mathcal{O}(10^2)msec\right)$ during the hot-wire calibration in the HECAL experiment is of the orders of few hundreds of milliseconds, which is far more than the time constant of the hot-wire. This guarantees that the hot-wire is in thermal equilibrium and hence avoids the problem of thermal lag over a time scale of more than a millisecond [Comte-Bellot, 1976].

III.3.1 Calibration of hot-wire at ambient temperature

Before performing the actual hot-wire calibration at cryogenic temperatures, we have performed numerous tests at ambient temperatures. Many calibrations of the hot-wire are carried out at ambient temperature. Figure III.8a shows one such calibration. This figure shows the hot-wire voltage and the angular velocity of the rotational arm with respect to time during two consecutive rotations of the arm. The hot-wire is operated in CCA mode with 40% of overheating (at r = 69mm). Each color in this figure represents a change of $\frac{\pi}{2}$ radians, except the last one (green) which represents a rotation of 2π radians. From this figure we see that after one complete rotation of the arm, the hot-wire is sensitive to the perturbations caused by the wakes of the rotational arm. So, in order to perform the calibration of the hot-wire only the data up to the end of one rotation i.e. up to 330msec are used. Figure III.8b shows the calibration fit along with the experimental data points (see equation II.6 and figure II.2 for more details). This figure shows that the experimental data points follow the King's law fit very well.

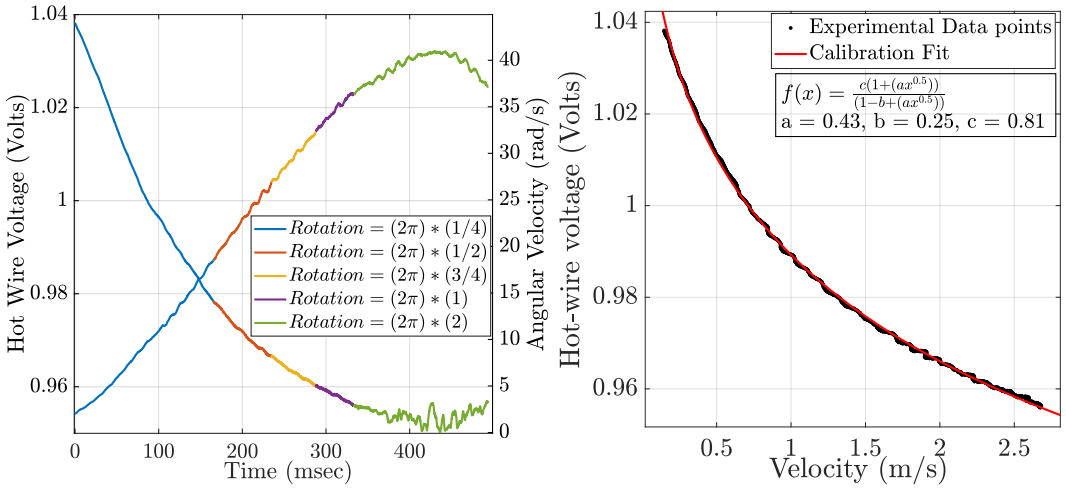

(a) Change of the hot-wire voltage and arm angular velocity over two rotations [1^{st} rotation: blue + orange + yellow + maroon color; 2^{nd} rotation: green color]

(b) Hot-wire calibration using King's law fit

Figure III.8: Raw signal of hot-wire (in CCA mode) and tachogenerator along with its calibration at 300K ($r = 69mm, d_w = 1.27\mu m$ and $l_w = 1mm$)

The consistency of this hot-wire calibration at ambient temperature is addressed in the following way. First, the reference estimate of the velocity of the rotational arm is measured from the tachogenerator. Once the hot-wire calibration is performed, we can use this calibration itself on the raw hot-wire signal to measure the velocity of the rotational arm. Figure III.9 shows the comparison of the velocity calculated from tachogenerator and the estimated velocity using the hot-wire after calibration during two consecutive rotations of the arm. This figure shows that after calibration the hot-wire follows the tachogenerator very precisely during the

first rotation of the arm. During the second rotation of the arm, we see that the hot-wire is sensitive to the perturbations caused by the wakes of the arm.

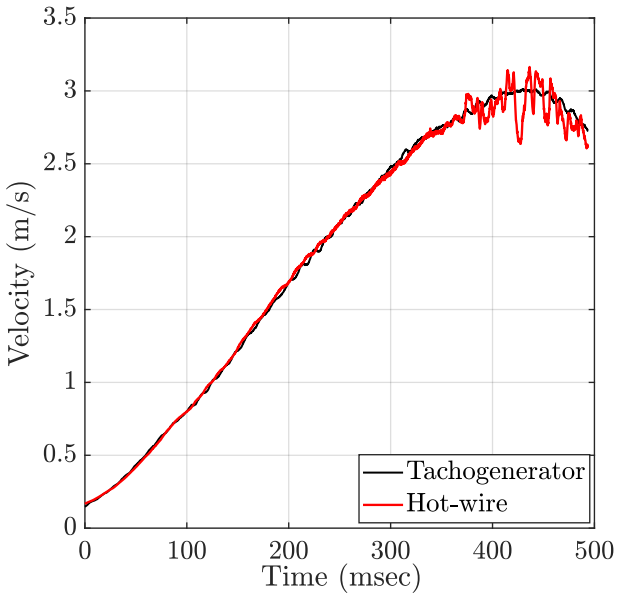

Figure III.9: Comparison of measured velocity using tachogenerator and the calibrated hot-wire over two consecutive rotations of the arm

III.3.2 Calibration of hot-wire in HeI

At extremely low velocities, proper care needs to be taken in order to ensure that the electrical response of the hot-wire is dominated by forced convection and not by free thermal convection. A theoretical estimate of critical velocity can be defined based on the Richardson number Ri, which defines the ratio of free convection to the forced convection, at which the effects of free convection can be neglected. For the hot-wire of $d_w = 1.27\mu m$, this critical velocity corresponds to about 20 mm/s [Hultmark and Smits, 2010]. This critical velocity increases with overheating of the hot-wire. The higher the overheating of the hot-wire, the higher is the critical velocity and thus the smaller will be the range of velocity calibration.

Figure III.10 shows the raw signal of hot-wire and tachogenerator at T = 2.4K in HeI. Unfortunately, the hot-wire which had been mounted at $r = 69mm$ did not survive during the cool-down process. Following figure shows the calibration of the hot-wire which had been mounted at $r = 57mm$. This hot-wire is operated at an overheating of 35%. Figure III.10a shows the response of the hot-wire and tachogenerator as soon as the rotating arm starts to move. This figure shows that starting from time = 0sec, the hot-wire voltage (the temperature and hence the resistance) starts to drop as a consequence of increased forced convection. This continues until the rotating arm accelerates to the maximum rotating speed. The maximum instantaneous rotating frequency of 23.8Hz is reached at time = 1.1sec, which corresponds to 10V of tachogenerator voltage. After one rotation i.e. after time = 275msec, the response of the hot-wire is affected by the flow fluctuations generated by the wakes of the rotating arm. After time = 1.1sec, the rotating arm starts decelerating, while the hot-wire voltage increases, which shows that the relative velocity between the flow and the hot-wire itself starts to decrease. This continues until time = 1.7sec. At time = 1.7sec, we see that the hot-wire voltage starts to decrease again. This is because the relative velocity starts to increase as the hot-wire velocity decreases to zero, while the fluid has reached its maximum velocity.

Figure III.10b shows the hot-wire signal and the angular velocity of the rotating arm for two consecutive rotations attained over a duration of 380msec. Each color in this figure represents a change of $\frac{\pi}{2}$ radians, except the last one (green) which represents a rotation of 2π radians. This figure shows that the constant acceleration of the rotating arm is maintained over two rotations of the arm. From this figure we see that the rotating arm and the hot-wire completes one rotation in about 275msec. Therefore, the hot-wire calibration is performed using the experimental data points until time=275msec. Figure III.11 shows the experimental data points along with the calibration fit using King's law. From this figure we see that the experimental data points follow the King's law fit very nicely in normal helium. This figure shows an almost asymptotic behavior towards higher velocities ($> 3\frac{m}{s}$). From the calibration fit in this figure, at higher velocities we can expect $y(x) \simeq c$. In other words, the lowest hot-wire voltage in figure III.11 is not far from the value of constant c.

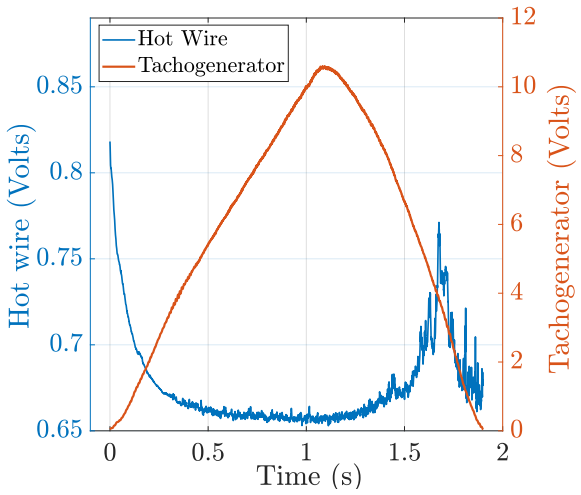

(a) Raw signal of the hot-wire voltage and tachogenerator voltage

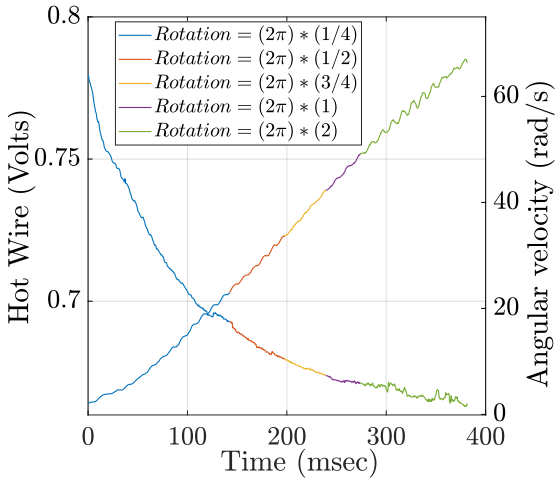

(b) Hot-wire voltage and angular velocity of rotational arm with respect to time over two consecutive rotations [1^{st} rotation: blue + orange + yellow + maroon color; 2^{nd} rotation: green color]

Figure III.10: Details of the hot-wire calibration performed in HeI at T = 2.4K ($r = 57mm$, $d_w = 1.27\mu m$ and $l_w = 1mm$)

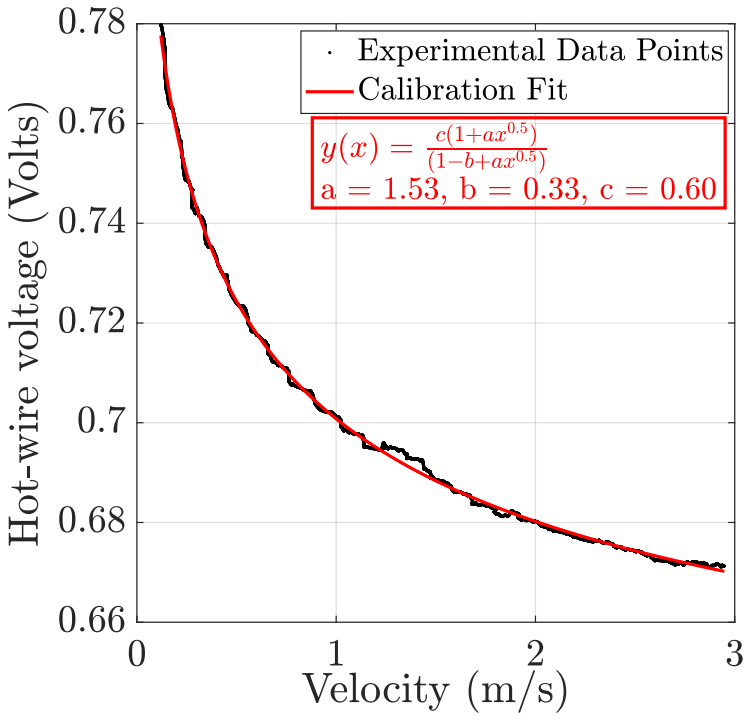

Figure III.11: Hot-wire calibration curve using King's law in HeI at T = 2.4K ($r = 57mm$, $d_w = 1.27\mu m$ and $l_w = 1mm$)

Another HECAL experiment is conducted to perform the calibration of a hot-wire having $d_w = 1.27\mu m$ and $l_w = 300\mu m$. This time, the only hot-wire which had survived the cool-down process had been mounted at $r = 45mm$. Unlike before, while performing this calibration, the rotating arm is kept in rotation after reaching the maximum desired velocity, for over 15 seconds. Figure III.12 shows how the hot-wire response evolves, if the rotating arm is kept in motion for a few seconds, and then stopped. We see that from time = 0sec to about 5sec, the hot-wire response is related to its natural convection in normal helium. As explained earlier, the hot-wire calibration is performed within time = 5 - 6sec. From time = 6sec, we see that the relative velocity between the hot-wire and the wakes generated by the rotating arm evolves until time = 10sec, after which the relative velocity becomes constant up to about time = 23sec. From time = 23 - 24sec, the rotating arm is brought to zero velocity, which results in to sudden high hot-wire voltage because of the reduced relative velocity. After time = 24sec, the hot-wire response is purely based on the damping of the wake flow, which keeps coming from the back side of the hot-wire. Over the span of few seconds, the wake flow decelerates and hence the hot-wire voltage rises gradually until it reaches initial value at time = 0sec (the data acquisition has been done only over time = 45sec). Therefore, to eliminate the effects of the wake during the calibration procedure, after performing each hot-wire calibration a pause of 4 - 5 minutes is recommended and has been implemented at all times.

Figure III.13a shows the calibration curve using King's law fit for the experimental data points shown in figure III.12 from time = 5 - 6sec. Using this calibration, the raw hot-wire signal is converted into the velocity signal. Figure III.13b shows the PSD of the velocity signal corresponding to the time = 10 - 23sec in figure III.12. From time = 10 - 23sec the hot-wire signal shows no drift. Hence, we can imagine that the wake flow is stabilized. The main observation about this figure is that the PSD of the velocity signal shows a peak at about 8Hz whereas the rotating frequency of the arm is 10 Hz. The wake flow is generated by the rotating arm, hence the rotating arm acts as a driver, while the wakes always lags behind the rotating arm. So, in

this process, the rotational frequency of the rotating arm is always higher than the rotational frequency of the wakes. This is confirmed by the peak in the PSD at 8Hz which represents the relative frequency between the rotating arm and the wakes generated by itself. Such a peak is also observed in HeII. We can also observe two different peaks in the spectrum each at about 590Hz and 2320Hz, which possibly indicates the frequency of vibration of the motor shaft assembly (see section IV.3.1.8). Although, the objective of the present work is not to examine the wake flows, interesting enough, the PSD shows $f^{-\frac{5}{3}}$ (red dashed line) dependence over the frequencies higher than 2.5kHz.

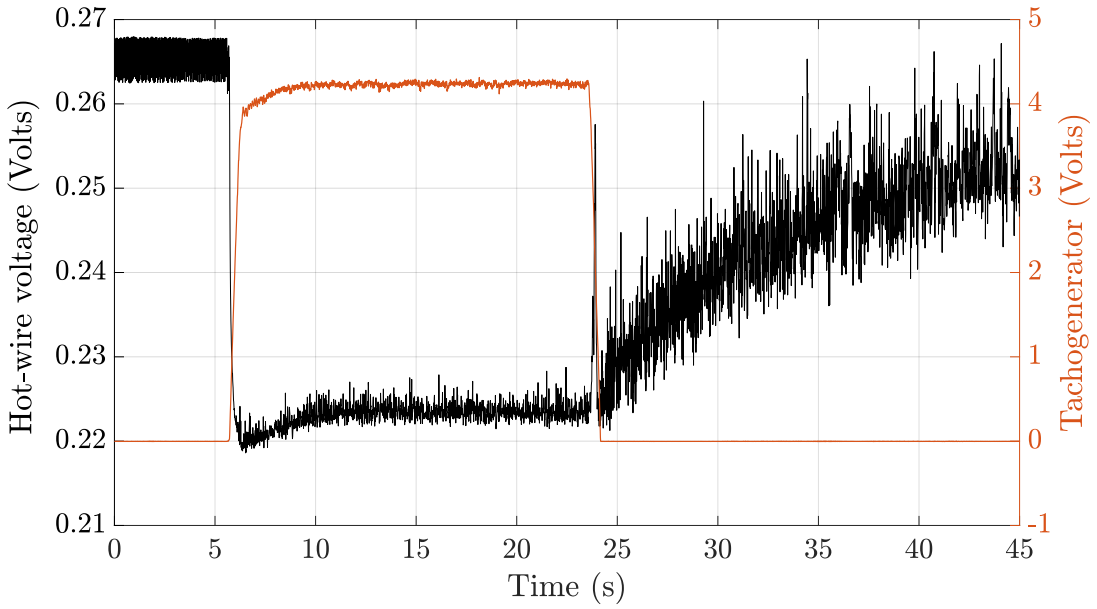

Figure III.12: Change in hot-wire response with respect to the rotating arm over time in HeI at T = 2.35K ($r = 45mm$, $d_w = 1.27\mu m$ and $l_w = 300\mu m$)

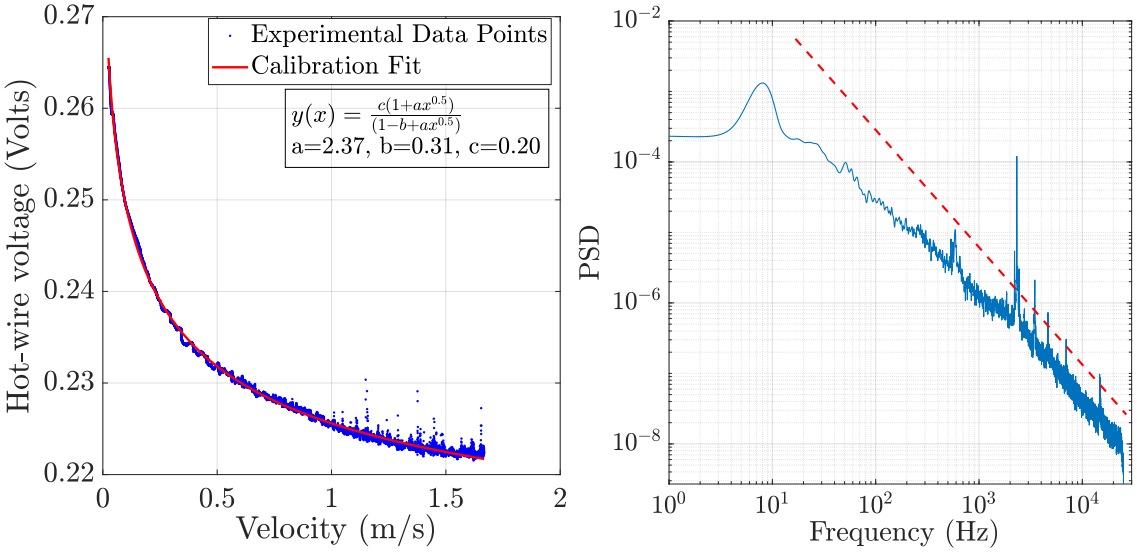

(a) Calibration curve using King's law fit for CCA

(b) PSD of the velocity signal from time = 10 to 20sec (red dashed line corresponds to $f^{-\frac{5}{3}}$)

Figure III.13: Hot-wire calibration and power spectrum density at T = 2.35K ($r = 45mm$, $d_w = 1.27\mu m$ and $l_w = 300\mu m$)

There is something peculiar about the hot-wire signal just before the rotating arm is put in motion. To see this effect precisely let's zoom the hot-wire signal from Time = 5 - 6 sec in figure III.12. This zoomed view is presented in figure III.14. Figure III.14a shows the hot-wire signal and the current supplied to the motor with respect to the time. The current supplied to the motor is measured using a current clamp (Model E3N from Chauvin Arnoux) which measures 100mV/A. Figure III.14b shows the hot-wire signal and the tachogenerator signal with respect to the time. The following discussion is based on the simultaneous observation of these two figures.

At very low velocities, the response of the hot-wire is dominated by natural convection in HeI. This hot-wire is operated at overheating of 25% in CCA mode. From time = 0 - 180msec (until blue arrow), when the rotating arm is at rest, the response of the hot-wire is stable, which is governed by the natural convection in HeI. At time = 180msec, a command (through signal generator) is passed to the motor to start the rotation. But, it is found that the motor slightly vibrates before actually starting the rotation of the arm. The motor does not start instantaneously. In fact, it takes a little time to magnetize the motor. Although the command to the motor is passed at time = 180msec, the rotating arm starts to move at about time = 320msec (magenta arrow), hence a delay of 140msec is associated from the command to the actual beginning of rotation of the arm. During this period (time = 180 - 320msec) the current in the motor keeps increasing without any movement of the rotating arm. Meanwhile, because of the vibration caused by the motor, the hot-wire is displaced from its initial position. The hot-wire cools because of this slight displacement and hence its voltage reduces until time = 230msec (red arrow). From time = 230 - 320msec, the hot-wire regains its thermal equilibrium until the rotating arm starts moving at time = 320msec. From time = 320msec onwards, the hot-wire voltage drops as the rotating arm starts to move because of the increased forced convection and the hot-wire calibration is performed as previously shown in figure III.13a.

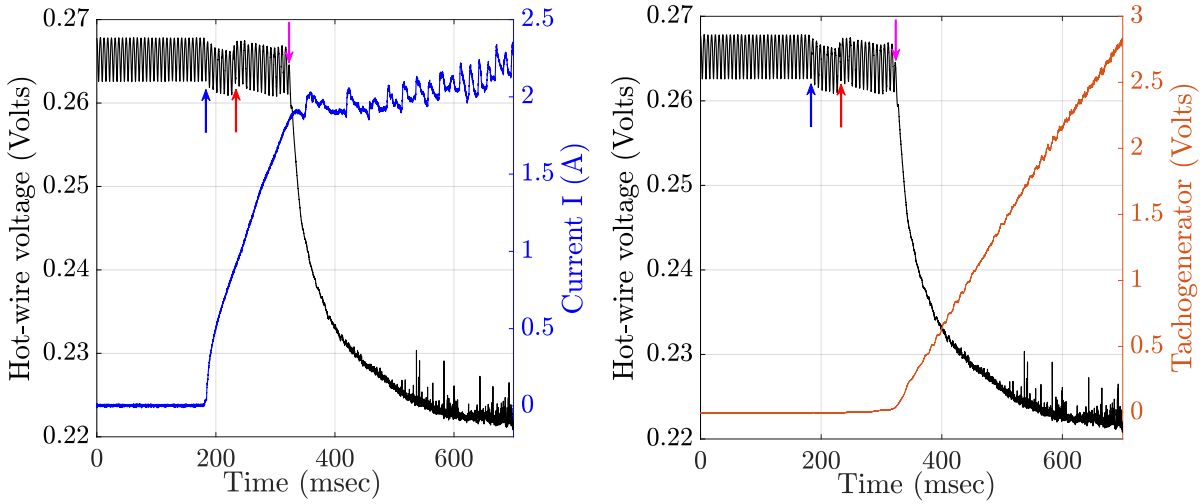

(a) Raw hot-wire signal and current in the motor with respect to time

(b) Raw hot-wire signal and tachogenerator signal with respect to time

Figure III.14: Effect of the vibration of the rotating arm at the beginning of rotation on the hot-wire signal in HeI [zoomed view of figure III.12 within Time = 5 - 6 secs; blue arrow: Time = 180msec; red arrow: Time = 230msec and magenta arrow: Time = 320msec]

A similar effect of the vibration of the rotating arm on the hot-wire signal is also observed in air. There is no significant effect of this vibration of the rotating arm which occurs at the beginning of rotation (time = 180 - 320msec) on the hot-wire calibration in HeI and air. But, it is found that it has significant effect in HeII which will be discussed in the next section.

III.3.3 Calibration of hot-wire in HeII

The hot-wire response in superfluid helium at T = 2.0K is similar to HeI which is discussed in figure III.10. Figure III.15 shows the time evolution of the hot-wire voltage and the tachogenerator voltage, once the rotating arm is put in rotation in the superfluid medium. From figure III.15a (HeII) and figure III.10a (HeI) we see that the hot-wire is more sensitive to smaller velocities in HeI compared to HeII and it is less sensitive to higher velocities in HeI compared to HeII. The effects of the wake flow can be seen clearly, also in superfluid helium, especially when the velocity of the hot-wire reaches close to zero. Figure III.15b shows the hot-wire response within two rotations of the arm with respect to time. Certainly, the mechanism of the heat transfer from the hot-wire in superfluid is not the same as in a classical fluid like normal helium. Therefore, the hot-wire response is not same in HeI and HeII. In fact, in superfluid the hot-wire shows more fluctuations than in normal helium.

To address the viability of the experimental data points in superfluid in view of the hot-wire calibration, a King's law fit is constructed as shown in figure III.16. This figure shows that the King's law is less satisfactory with the experimental data points in superfluid helium, although, we can see the dependence of the velocity on the hot-wire signal. In both HeI and HeII the hot-wire is operated at an overheating of 35%. Comparing the hot-wire calibration in HeII (figure III.16) with the one in HeI (figure III.11) we see that the sensitivity of the hot-wire signal over the range of 0 - 3 $\frac{m}{s}$ is 90mV in HeII and 110mV in HeI. From figure III.16 we can infer that even beyond $3\frac{m}{s}$ the hot-wire is sensitive to higher velocities. In other words, figure III.16 do not show the signs of asymptotic behavior until $3\frac{m}{s}$. Therefore, the value of the constant c in the calibration fit is far from the lowest hot-wire voltage in figure III.16

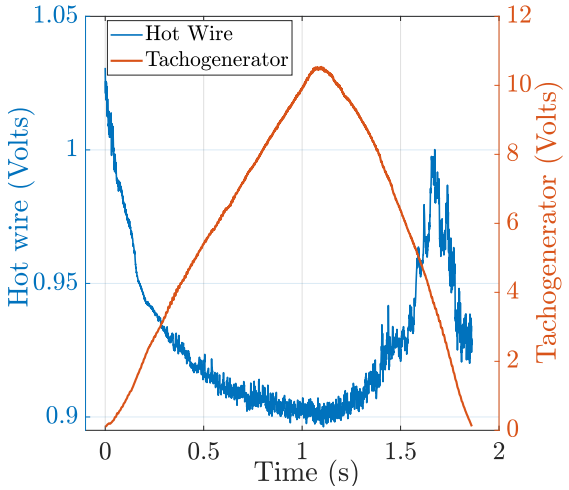

(a) Raw hot-wire signal and tachogenerator voltage

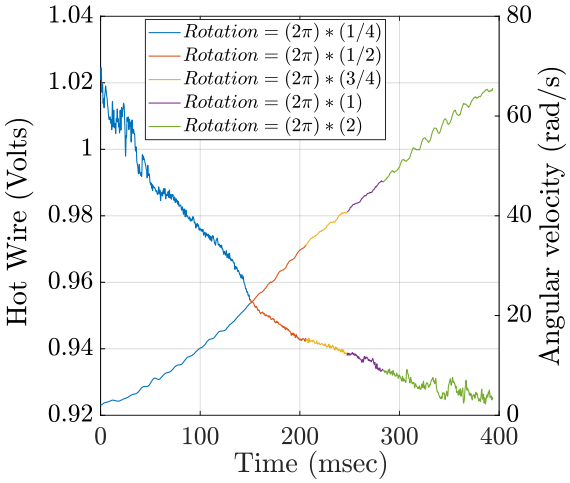

(b) Raw hot-wire signal and angular velocity of rotational arm with respect to time over two consecutive rotations [1^{st} rotation: blue + orange + yellow + maroon color; 2^{nd} rotation: green color]

Figure III.15: Details of the hot-wire calibration performed in HeII at T = 2.0K ($r = 57mm$, $d_w = 1.27\mu m$ and $l_w = 1mm$)

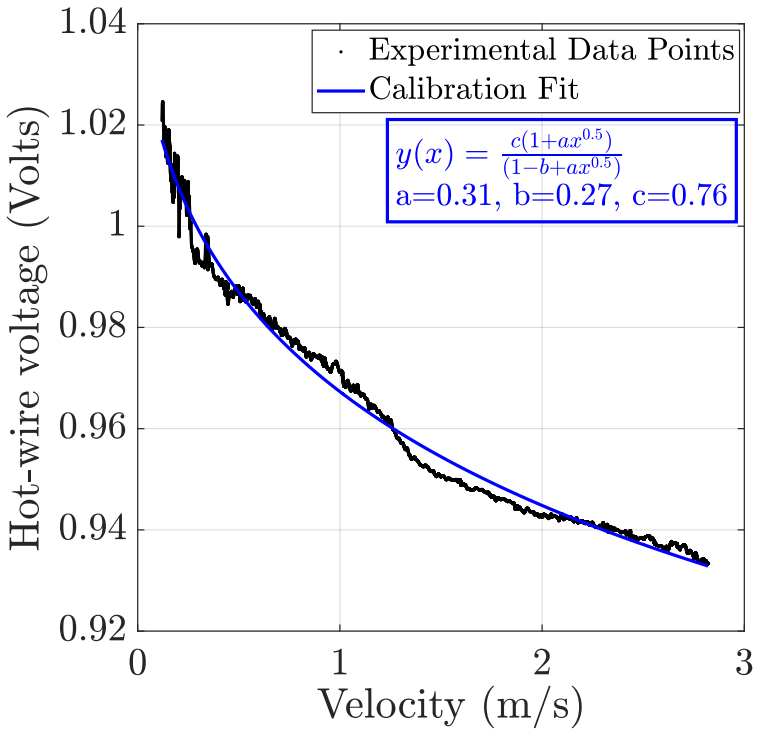

Figure III.16: Hot-wire calibration curve using King's law in HeII at T = 2.0K ($r = 57mm$, $d_w = 1.27\mu m$ and $l_w = 1mm$)

The precise and accurate calibration of the hot-wire in superfluid is not as simple as in normal helium. At very low velocities, the response of the hot-wire is dominated by its counterflow turbulence in HeII (for more details on counterflow turbulence see section III.3.6). Figure III.17 shows the effect of vibration of the rotating arm just before the first rotation on the hot-wire

signal in HeII at T = 2.0K. This figure shows the evolution of the hot-wire signal and tachogenerator voltage before and after the rotating arm is put in motion. This hot-wire is operated at overheating of 35% in CCA mode. Overall, we see that the effect of vibration of the rotating arm on the hot-wire signal is very different in HeII from that in HeI (comparison of figure III.14b and figure III.17). Unfortunately, during this experiment in HeII the measurement of the current in the motor was not available. But, similar behavior of the current in the motor is expected in HeII as observed in HeI (see figure III.14a).

In figure III.17 from time = 0 - 180msec (blue arrow), when the rotating arm is at rest, the response of the hot-wire is stable, which is governed by its counterflow turbulence in HeII. At time = 180msec, a command is passed to the motor to start the rotation. Although the command to the motor is passed at time = 180msec, the rotating arm starts to move at about time = 320msec, hence a delay of 140msec (same as in HeI) is associated from the command to the actual beginning of rotation of the arm. So, we can expect the increase of current in the motor from time = 180 - 320msec until the rotating arm starts to move. Meanwhile, because of the vibration caused by the motor, the hot-wire is displaced from its initial position at time = 180msec. It may be possible that this abrupt movement of the hot-wire occurs again and again until the start of actual uniform motion of the rotational arm. This causes a change in the boundary layer around the hot-wire which possibly leads to the poorer heat transfer from the hot-wire. Because of this, the hot-wire voltage starts to increase followed by a sudden decrease as the heat transfer starts to be efficient again. So, it seems like there is a characteristic time scale associated with the optimum heat transfer from the hot-wire, whenever the hot-wire is moved abruptly. This characteristic time scale depends on the extent by which the hot-wire is moved by the vibration effects of the rotating arm (see the time difference between blue-red arrow and red-orange arrow). In other words, this characteristic time scale reduces for successive vibrations of the rotating arm. From time = 180 - 280msec (red arrow), the hot-wire has recovered its original voltage. This increase and decrease of the hot-wire voltage continues again based on the successive vibrations of the rotating arm. From time = 280 - 350msec (orange arrow), the hot wire voltage increases and decreases again, possibly because of a second vibration of the rotating arm. At time = 350msec (magenta arrow), the hot-wire voltage increases possibly because of the third vibration of the rotating arm. From time = 360 onwards, the hot-wire voltage drops because of the increased forced convection as the rotating arm starts to move. But, this time the hot-wire signal contains lot of fluctuations (it is not as smooth as in HeI).

We may also expect that because of the counterflow turbulence of the hot-wire in superfluid it might take longer time to establish the boundary layer around the hot-wire than in normal helium. It is observed that the effect of the motor vibration on the hot-wire signal at the start is linked to the superfluid temperature. The effects of vibration of motor on the hot-wire signal in HeI are very negligible. But, the effects of vibration of motor on the hot-wire signal are more and more recognizable as the percentage of superfluid increases (i.e. below T_λ, at least down to T = 1.9K in the present work). Because of the vibration of the motor the maximum change in the hot-wire voltage (between blue and red arrow) of about 30mV is observed in HeII. This disturbs the entire dynamic range of the hot-wire calibration in HeII. Therefore, limiting to the present instrumentation in the HECAL facility, we found that as the temperature increases towards T_λ and beyond (from HeII to HeI), the experimental data points follows the King's law of calibration reasonably well.

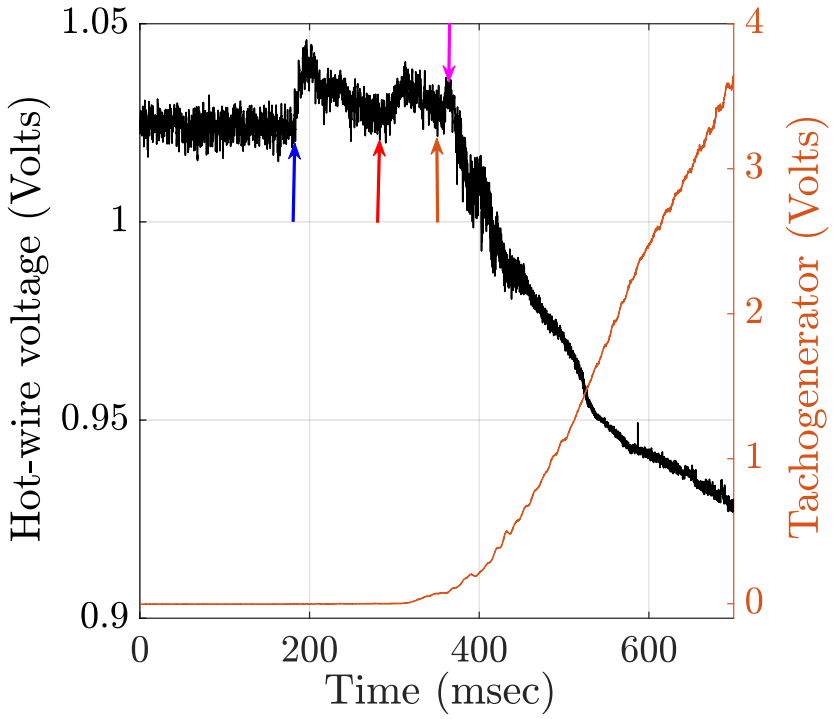

Figure III.17: Effect of the vibration of the rotating arm at the beginning of rotation on the hot-wire signal in HeII at T = 2.0K [blue arrow: Time = 180msec; red arrow: Time = 280msec; orange arrow: Time = 350msec and magenta arrow: Time = 360msec]

III.3.4 Repeatability and sensitivity

The consistency of any experiment depends on its repeatability. Figure III.18 shows the repeatability of the HECAL experimental set-up at T = 2.35K. The repeatability of the HECAL experiment is examined using two different hot-wires of $l_w = 300\mu m$ and $l_w = 1mm$ having $d_w = 1.27\mu m$. In figure III.18a, two calibrations of the same hot-wire ($l_w = 1mm$) are plotted for different desired maximum velocities, but the same time to complete one rotation of the arm. These two calibrations are performed over a period of 400msec each and for the same operating current through the hot-wire. Similarly, figure III.18b shows two calibrations of the same hot-wire ($l_w = 300\mu m$) attaining different maximum velocities at the end of one rotation of the arm, while operating at the same current. These two calibrations are performed over a period of 325msec. As the hot-wire in figure III.18a is mounted at $r = 57mm$, the velocity over which the calibration could be performed is maximum compared to the hot-wire in figure III.18b which is mounted at $r = 45mm$. Figure III.18 shows that different combinations of the linear ramps do not alter the hot-wire calibration. Figure III.18 confirms the repeatability of the HECAL experiment at low temperatures.

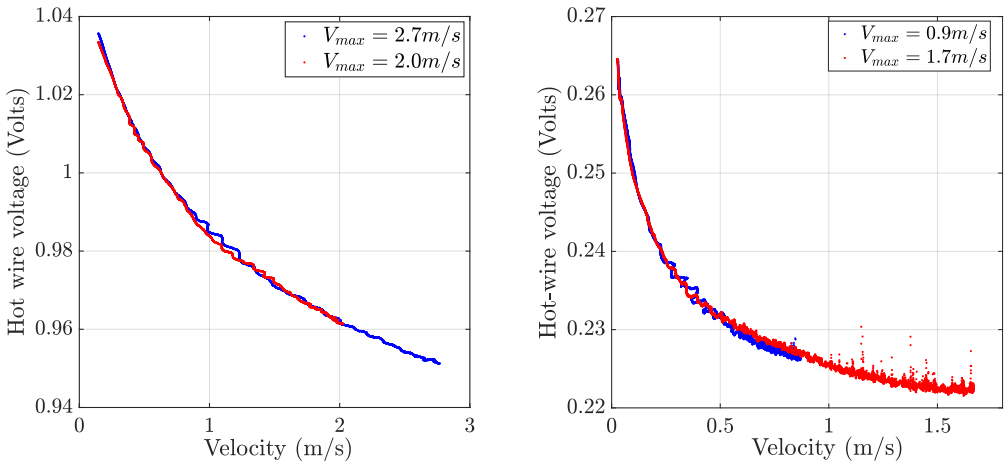

(a) Hot-wire details: $r = 57mm$, $d_w = 1.27\mu m$ and $l_w = 1mm$

(b) Hot-wire details: $r = 45mm$, $d_w = 1.27\mu m$ and $l_w = 300\mu m$

Figure III.18: Two calibrations of the same hot-wire showing repeatability of the HECAL experiment in HeI at T = 2.35K

The sensitivity of the hot-wire is defined as the relative change in hot-wire voltage with respect to the change in velocity. In turbulent flow, to capture the rapid flow fluctuations, the hot-wire having high sensitivity is always beneficial. In figure III.19, three calibrations of the same hot-wire are plotted for different operating currents. These three calibrations are performed for the different desired maximum velocity, while using different ramp times. The hot-wire operating current of I = 6.95, 8.91, 9.55mA corresponds to overheatings of 9%, 21% and 25% respectively. This figure shows that the hot-wire response is similar at three operating currents but with different dynamic range of the hot-wire voltage over the velocity. This can be quantified using the sensitivity of the hot-wire. It is found that the sensitivity of the hot-wire increases with respect to the increase in operating temperature of the hot-wire. The three calibration curves in this figure give the averaged sensitivity (defined as the ratio between the voltage excursion over the total velocity range) of 9.3, 20.1 and 25.2 $\frac{mV}{m/s}$. Hence, higher sensitivity of the hot-wire can be achieved using higher overheating.

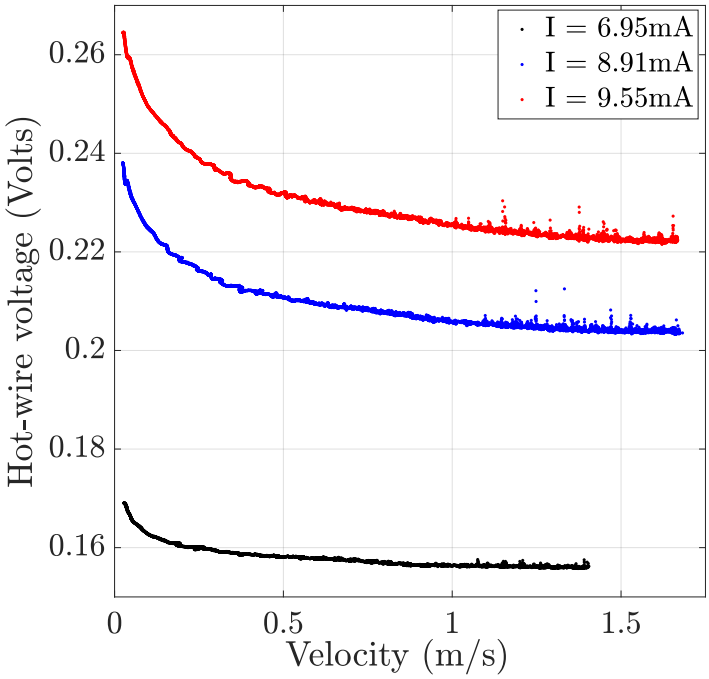

Figure III.19: Sensitivity of hot-wire using multiple calibrations for different overheating in HeI at T = 2.35K ($r = 45mm$, $d_w = 1.27\mu m$ and $l_w = 300\mu m$)

III.3.5 Application in the SHREK/ECOUTURB experiment

As mentioned earlier, the HECAL facility is designed to obtain a precise hot-wire calibration so that a pre-calibrated hot-wire can be installed in the SHREK/ECOUTURB experiment. For the first time, we have succeeded in this attempt to measure the velocity in the ECOUTURB experiment using the pre-calibrated hot-wire. Typically, in the SHREK experiment the reference velocity for the hot-wire calibration is estimated from the assumption of solid body rotation attained in the co-rotation configuration of the von Kármán flow (see section II.1). In this case the reference velocity is given by,

$$V = \mathcal{A} \times \mathcal{R} \times 2\pi f \tag{III.1}$$

where V is the reference velocity in $\frac{m}{s}$, $\mathcal{R}$ is the radial distance of the hot-wire from the axis of the von Kármán cell, f is the frequency of turbine in the co-rotation configuration and $\mathcal{A}$ is the prefactor assumed to be 1 in the SHREK experiment. Similarly, the hot-wire calibration is performed in the ECOUTURB experiment. This hot-wire calibration is then compared with the precise hot-wire calibration performed in the HECAL experiment in order to find the value of the prefactor $\mathcal{A}$ in the ECOUTURB experiment. In this experiment, the hot-wire is installed at 10mm away from the top disk and 4cm away from the wall of the von Kármán cell. The hot-wire is installed to measure the azimuthal component of velocity. Figure III.20 shows the comparison of the hot-wire calibration in the HECAL and ECOUTURB experiment. This calibration is performed in HeI at T = 2.3K. This hot-wire is operated at the same overheating (25%) in the HECAL as well as in the ECOUTURB experiment. In this figure the experimental data points (blue points) and King's law calibration fit (red curve) is obtained in the HECAL experiment (figure III.13a re-plotted here). The experimental data points in the ECOUTURB experiment are represented by green circles. These data points correspond to the co-rotation configuration at $f = 0, 0.5, 1.0, 1.5, 2.0$ Hz. Superposing the experimental data points from the ECOUTURB

experiment on to the precise hot-wire calibration in the HECAL experiment gives $\mathcal{A} = 0.37$ as shown in figure III.20 (The prefactor $\mathcal{A} = 0.33$ is also confirmed using the cantilever sensor in HeII).

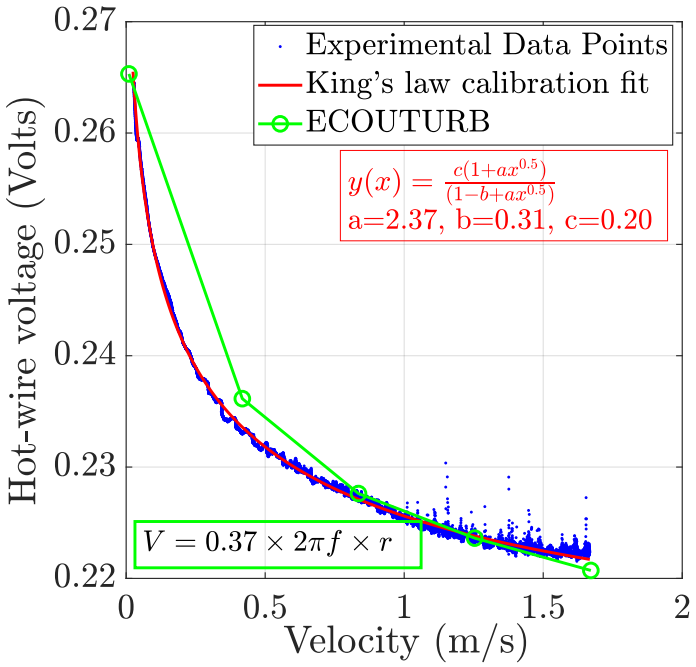

Figure III.20: Application of the hot-wire calibration performed in the HECAL experiment to the ECOUTURB experiment in HeI at T = 2.3K ($d_w = 1.27\mu m$ and $l_w = 300\mu m$)

III.3.6 Power spectrum at null velocity in HeI and HeII

In classical fluids the hot-wire response is purely due to forced convection after overcoming the effects of the natural convection. This situation is quite different in superfluid. Basically, the hot-wire can be thought as a very small sized heater installed in the experiment. While using hot-wire anemometry, the natural convection plays an important role in classical fluids at very low incoming velocities whereas in superfluid the hot-wire generates its own counterflow turbulence. Turbulent counterflow has a role in transfer of heat associated with the hot-wire which makes the heat transfer in superfluid very different compared to normal helium. Also, there is no classical analogy associated with counterflow turbulence in superfluid. In the present context of the hot-wire, the term "counterflow" needs a special description. Let us consider a very small sized resistance (such as the hot-wire) being heated in the surrounding medium of superfluid helium. In this situation, the normal component which carries the entropy moves away from the heater, and the superfluid component which does not carry any entropy moves towards the heater to conserve the mass. This movement of the normal and the superfluid component against each other (over the hot-wire) is called "counterflow". This counterflow does not necessarily have to be turbulent until the hot-wire is heated beyond a critical limit (associated with the heat flux). Therefore operating the hot-wire above the critical input power generates the counterflow turbulence around the hot-wire. Hence, first step towards understanding the incoming superfluid turbulence using the hot-wire anemometry would be to detect and quantify the counterflow turbulence of the hot-wire itself. In classical fluid, above a certain threshold velocity we can neglect the effects of natural convection of the hot-wire. The most challenging question here is, can we neglect the counterflow turbulence generated by the hot-wire above

some threshold velocity? If not, how does the counterflow turbulence of the hot-wire evolve with respect to the external superfluid turbulence? In superfluid, the counterflow turbulence of the hot-wire seems not to disappear as the velocity increases, on contrary to the natural convection in classical fluids. Therefore, in superfluid turbulence the response of the hot-wire is the superposition of external turbulent flow and counterflow turbulence generated by the hot-wire itself.

Figure III.21 shows the raw hot-wire signal at null velocity at three different helium bath temperatures of T = 2.4, 2.0 and 1.9K from top to bottom respectively. The hot-wire is operated in CCA mode at an overheating of 25%, 22% and 21% at helium bath temperatures of T = 2.4, 2.0 and 1.9K respectively. At T = 2.4K the hot-wire signal shows the response to natural convection. At null velocity the raw hot-wire signal in HeI is very different from the classical turbulent signal. It is interesting to note that at null velocity the raw hot-wire signal in HeI at temperatures 2.2 - 2.4K looks very similar to a sinusoidal wave, which is not the case in HeII or even air. From top part of figure III.21 we see that the frequency of natural convection corresponds to about 160Hz. The hot-wire signal in the middle and bottom part of figure III.21 shows the counterflow turbulence of the hot-wire itself in HeII. From visual inspection we see that at T = 2.0K the hot-wire signal shows repeated drifts whereas at T = 1.9K the hot-wire signal comparatively looks much stable. In order to understand thoroughly the counterflow turbulence generated by the hot-wire itself, the response of the hot-wire at null velocity is studied using the power spectrum.

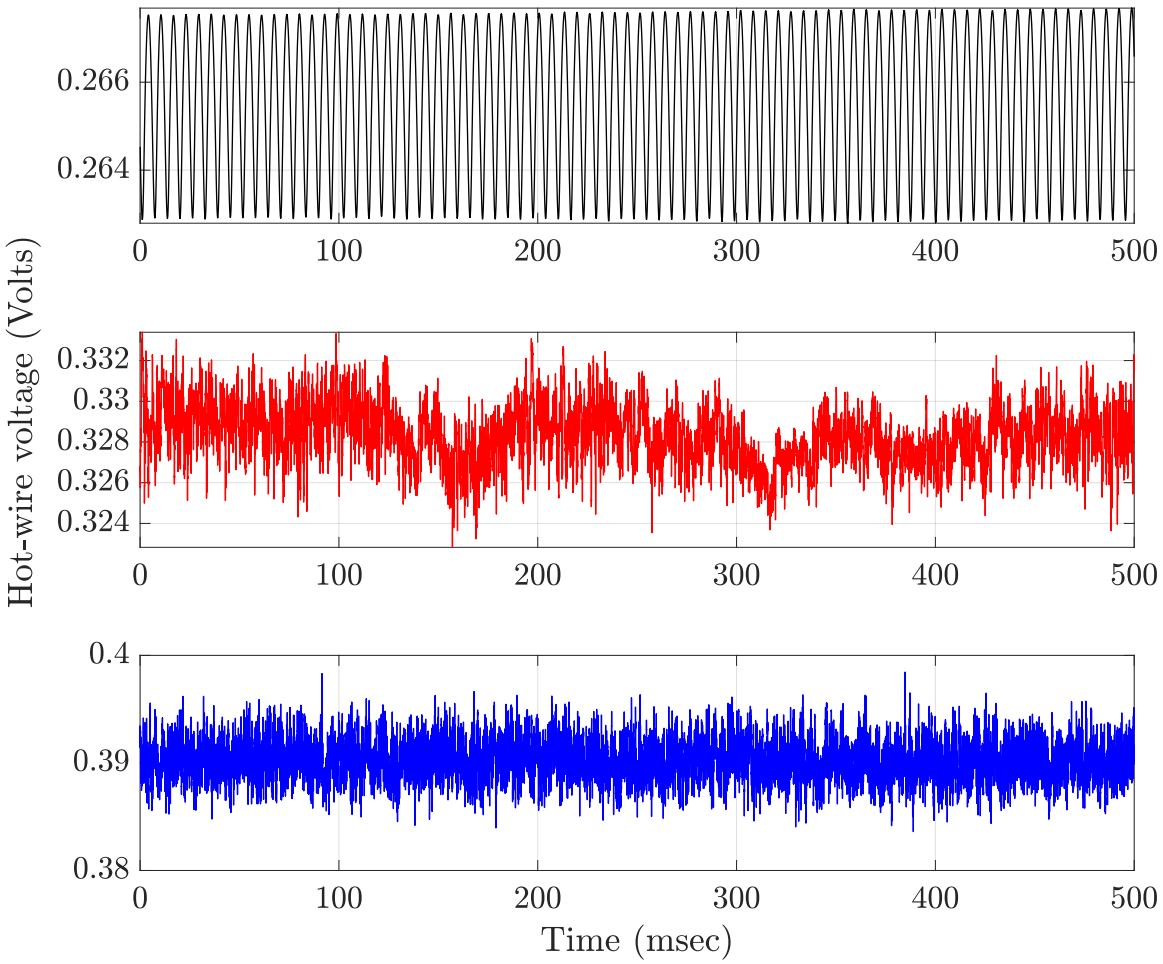

Figure III.21: Raw hot-wire signal at null velocity; top: T = 2.4K (HeI); middle: T = 2.0K (HeII); bottom: T = 1.9K (HeII) ($d_w = 1.27\mu m$ and $l_w = 300\mu m$)

Figure III.22 shows how the counterflow turbulence of the hot-wire evolves with respect to its increased overheating, at null velocity in CCA mode. Figure III.22a and figure III.22b show the PSD of the raw hot-wire signal for different overheating in the HECAL facility at T = 2.0K and T = 1.9K respectively at null velocity. Figure III.22a shows that even at 1.8% of overheating the hot-wire shows the effects of counterflow turbulence which gets modified further until the overheating of 22%. These observations are also similar to the spectrum shown in figure III.22b at T = 1.9K for the hot-wire overheating within the range of 3% to 21%. These figures show more fluctuations in the resistance of the hot-wire as a consequence of higher overheating of the hot-wire. From figure III.22a and figure III.22b we cannot establish a particular power law in the PSD based on the amount of overheating of the hot-wire. It's interesting to see the effects of overheating at null velocity in classical fluids such as HeI at which the hot-wire response is purely due to natural convection. Figure III.22c shows the effects of natural convection of the hot-wire in normal helium for overheating within the range of 2 - 25%. As expected, at very low overheating (of 2%) the hot-wire signal has very low fluctuations. But interestingly enough, on contrary to superfluid, the normal helium shows strikingly similar power spectrums

for the different overheating of the hot-wire over the range of 9-25%. We also find that in HeI at null velocity there exists a power law such that PSD $\propto f^{-2}$ within the frequency range $\approx$ 300Hz to 10kHz as shown by the black-dashed line in figure III.22c. For the hot-wire overheating over the range of 9-25%, the PSD curves shows a common peak at $\approx$ 160 Hz (wider for higher overheating) and its harmonics which are associated with the natural convection originated from the hot-wire. This shows how natural convection in HeI is very different from the counterflow turbulence in superfluid.

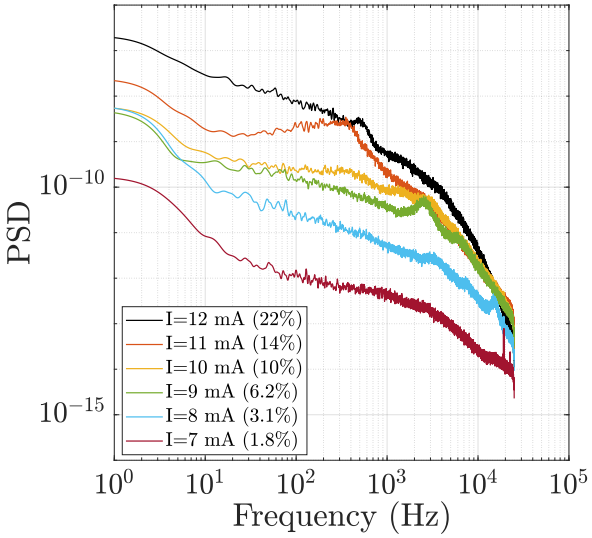

(a) At T=2.0K in the HECAL facility

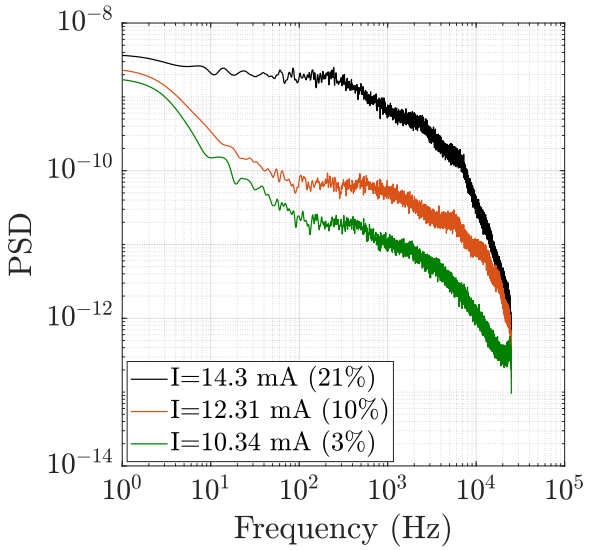

(b) At T=1.9K in the HECAL facility

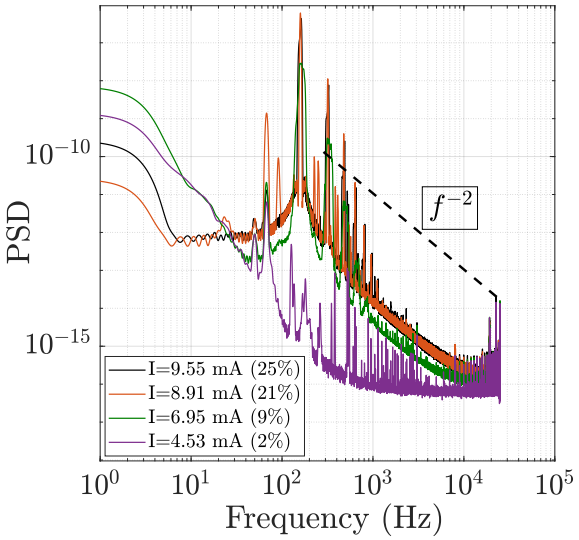

(c) At T=2.4K in the HECAL facility

Figure III.22: PSD of the raw hot-wire signal at null velocity using different overheating in CCA mode [$d_w = 1.27\mu m$ and $l_w = 300\mu m$; the temperature T indicates the temperature surrounding the hot-wire in the pressurized helium bath; I denotes the operating current of the hot-wire (with the percentage of overheating in the bracket)]

Overall, the main conclusion of figure III.22 is that the extent of counterflow turbulence depends on the degree of overheating of the hot-wire, which drives the resistance and hence the operating temperature of the hot-wire. In other words, different extent of counterflow turbulence can be observed by changing either the bath temperature ($T < T_\lambda$) surrounding the hot-wire or by varying the incoming turbulent flow over the heated hot-wire.

III.4 Conclusion

The experimental facility called HECAL is designed to obtain the calibration of hot-wires using flying/moving hot-wire technique. Using this facility, the hot-wire calibration can be performed within one rotation of the rotating arm which typically takes about less than half a second, while maintaining a constant angular acceleration. To conduct the precise and accurate hot-wire calibration, the instrumentation is modified to control the motor using a signal generator and a controller. At first, the modified instrumentation is tested at ambient temperatures to perform the hot-wire calibration, which ensured the proper functioning of the HECAL facility.

Two experiments of HECAL are conducted using the hot-wire of $l_w = 300\mu m$ and $l_w = 1mm$ having $d_w = 1.27\mu m$, at lower temperatures in HeI and HeII. The procedure to perform the hot-wire calibration in the HECAL facility is explained in detail, with the effects of wakes generated by the rotating arm. Multiple hot-wire calibrations are performed using different ramp times based on the maximum desired velocity for calibration. The calibration curves are found to be well in agreement with the King's law of calibration in normal helium. The King's law of calibration is found to be less satisfactory in superfluid helium, as the heat transfer mechanism in superfluid is different from the one in classical fluids such as normal helium, for which the King's law is defined. To use the HECAL facility to perform the hot-wire calibration in superfluid helium, a much deeper understanding of the counterflow turbulence is needed, which can be attained with the execution of numerous experiments. Certainly, a clear understanding of the counterflow turbulence is required to perform the satisfying hot-wire calibration in superfluid. The effect of vibration of the rotating arm at the beginning of rotation on the hot-wire signal is shown in HeI and HeII. This effect has no impact on the hot-wire calibration in HeI. But, it is found that this effect affects the hot-wire voltage significantly in HeII which may worsen the quality of the hot-wire calibration.

Multiple hot-wire calibrations are carried out, which show the repeatability of the HECAL experiment, even for attaining different maximum desired velocities for calibration using different ramp times. It is shown that the sensitivity of the hot-wire during calibration depends on the operating temperature of the hot-wire in CCA mode. The hot-wire must be operated at optimum temperature to gain higher sensitivity of the hot-wire with respect to the velocity during calibration. Overall, both at ambient and at low temperatures using HeI, HECAL promises to be the best and accurate hot-wire calibration tool. The pre-calibrated hot-wires can be readily installed in cryogenic experiments like HEJET and SHREK to perform the precise velocity measurements. The application of the pre-calibrated hot-wire in the ECOUTURB experiment is demonstrated. For the first time, we have succeeded to use a pre-calibrated hot-wire in the HECAL facility to measure the velocity in the ECOUTURB experiment. Comparing the hot-wire calibration in the HECAL and ECOUTURB experiment in HeI we found the calibration prefactor $\mathcal{A} = 0.37$.

An attempt is made to understand the hot-wire response in superfluid helium. To begin, the hot-wire response in superfluid is investigated at null velocity to examine the evolution of its counterflow turbulence. The raw hot-wire signal at null velocity shows different signatures according to the natural convection in HeI and counterflow turbulence in HeII. At first, as there is no classical analogue, the counterflow turbulence of the hot-wire itself is studied using different

overheating at various superfluid temperatures. From PSD it is observed that the counterflow turbulence depends on the overheating of the hot-wire. We confirmed that in HeII there is no particular power law in PSD at null velocity whereas in normal helium we find that the PSD $\propto f^{-2}$ within the frequency range of 300Hz to 10kHz.

IV HEJET EXPERIMENT

The HEJET experiment, which is a closed circuit jet flow facility has been designed to study turbulent jet flows at cryogenic temperatures using normal helium and superfluid helium. Using normal helium, we can study the classical turbulence generated from the jet flow at cryogenic temperatures as low as T = 2.2K. Using superfluid helium, we can study the quantum turbulence generated by the jet flow at temperatures as low as T = 1.8K. With the help of the HEJET experiment, we can compare the quantum turbulence with a typical classical turbulence generated by the jet flow. The main motivation of this experiment lies in the study of statistical intermittency in jet flows with the help of the experimental data acquired using the hot-wire anemometry. The SHREK experiment allows us to study the intermittency at high Reynolds number of $Re_\lambda \approx 1000 - 13000$ whereas the HEJET experiment allows us to study the intermittency in the range $Re_\lambda \approx 2000 - 3000$. In this aspect, it will be interesting to compare the intermittency coefficients depending on the flow generation mechanism.

In the HEJET facility, the old centrifugal pump was designed to deliver very high flow rate but was not well adapted to the piping circuit of the HEJET facility. An unstable behavior of the jet flow has been evidenced potentially related to the fact that the old pump was not working in nominal conditions. For this purpose, a new centrifugal pump has been designed based on the requirement of the flow rate and pressure head in the HEJET circuit. Therefore, based on the characteristics of the new pump and the HEJET circuit the operating point of the pump is determined. The experiments are then performed close to the optimal operating point of the pump (i.e. maximum mechanical efficiency), with much higher efficiency of the centrifugal pump compared to the old pump. To achieve this, and to ensure the steady flow of the helium in the closed circuit, it is of outmost importance to characterize the newly designed centrifugal pump. This is the main engineering aspect of the HEJET facility which is addressed in this work before actually studying the statistics of the turbulent jet flow.

IV.1 Experimental set-up

The schematic of the experimental set-up of the HEJET facility is shown in figure IV.1. The cryostat (No. 14) used in the HEJET/HECAL experiment has an external diameter of 60cm, internal diameter of 40cm with a height of 155cm. The vessels containing the liquid nitrogen (LN_2) and the helium (No. 15) are separated by vacuum. This facility is a closed circuit wind tunnel, within which the flow is maintained at a constant flow rate with the help of a centrifugal pump (No. 6), which is driven by the DC motor (No. 1) installed at the top end of the experiment as shown in figure IV.1. The pressure in the saturated helium bath (No. 15) is monitored using the pressure gauge manometer (No. 2) and also controlled by the throttle valve (No. 3). The pumping of the saturated helium bath is performed by a roots vacuum pump shown by No. 4. The valve indicated by No. 17 is used to pressurize the experimental section/region (No. 8). Multiple radiation shields are installed (No. 16) to prevent the room temperature radiations from heating the cold part of the HEJET facility. No. 5 shows the assembly of the motor shaft with the turbine of the centrifugal pump.

The detailed operation of the HEJET facility is described as follows. The dashed line (along with the arrow) in figure IV.1 shows the flow of the liquid helium inside the closed circuit wind tunnel i.e. inside the pressurized helium bath. The turbine of the centrifugal pump is rotated at the desired frequency with the use of the motor. This generates the fluid flow from experimental section towards the venturimeter (No. 9). The flow is then passed through the helicoidal heat exchanger (No. 12) which is made of copper. The flow is then passed through the honeycomb (No. 11), in order to improve the laminarity of the incoming flow upstream the jet nozzle. The fluid exits through the conical nozzle (No. 10) which generates the turbulent jet flow. The jet

develops from $z = 0$ at the nozzle exit in the vertical (axial) direction denoted by z. The hot-wire measurements are performed at the axial distance of $\frac{z}{d} = 50$ (blue star symbol), where $d = 5$mm is the nozzle diameter. The grid (No. 7) is used to stabilize the jet. The jet eventually passes through the grid, where the turbine sucks in the fluid which maintains the constant flow rate in the closed circuit wind tunnel. The temperature of the jet flow (T_3 = 1.8 - 2.4K) is controlled by imposing the pressure of the saturated helium bath (10 - 70mbar) using a throttle valve No. 3, while the pressure of the jet flow (2.5 - 3bar) is imposed by injecting helium gas using the valve No. 17. We recall that higher pressure of the jet flow is required to attain a supercritical state of helium (see figure IV.2) in order to avoid the formation of bubbles (i.e. boiling) close to the hot-wire (see also section I.4 for more details). In figure IV.1 h denotes the level of the helium in the saturated He bath measured by helium level indicator (see section IV.1.5). The detailed description of the temperature sensors (red filled circles) and the pressure sensors (blue filled circles) installed in this facility will be explained in the following subsections.

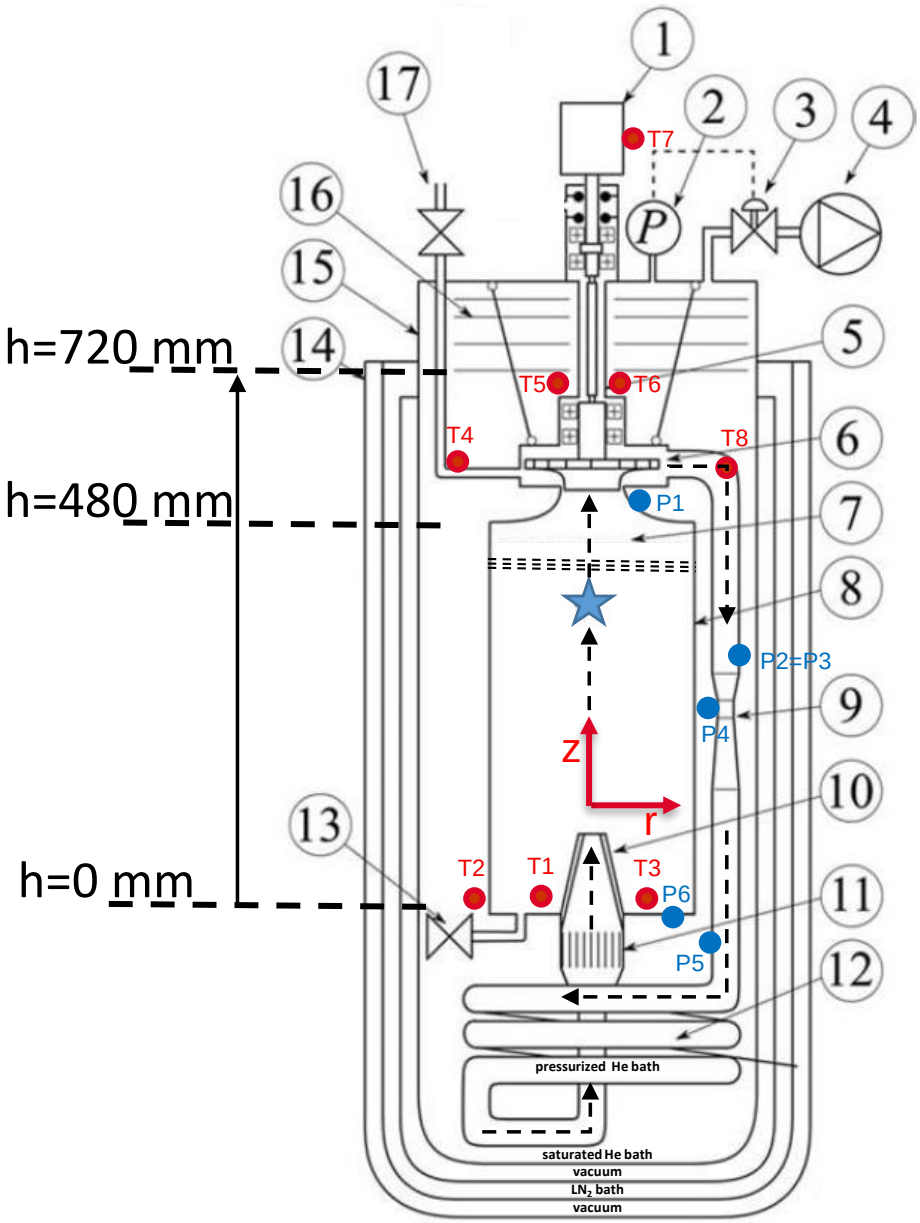

Figure IV.1: Description of the HEJET facility (not to scale, original figure from Duri [2012] modified here). 1. DC Motor 2. Saturated bath pressure sensor 3. Throttle valve (to regulate the saturated bath pressure) 4. Pumping of saturated bath 5. Motor/Pump shaft assembly 6. Turbine of centrifugal pump 7. Grid for jet stability 8. Experimental section 9. Venturimeter 10. Nozzle 11. Honeycomb 12. Helicoidal heat exchanger 13. Communication valve between pressurized and saturated He bath 14. Outer cylinder of liquid nitrogen bath 15. Inner cylinder of saturated helium bath 16. Radiation shields 17. Valve for pressurization [blue star: hot-wire location at $\frac{z}{d} = 50$ with d = nozzle diameter, z is the axial direction whereas r is the radial direction of the jet; h is the level of helium in the saturated He bath; red filled circles: Temperature sensors; blue filled circles: differential pressure measurement locations ($(\Delta P)_{pump} = P_2 - P_1$, $(\Delta P)_{venturi} = P_3 - P_4$, $(\Delta P)_{nozzle} = P_5 - P_6$)]

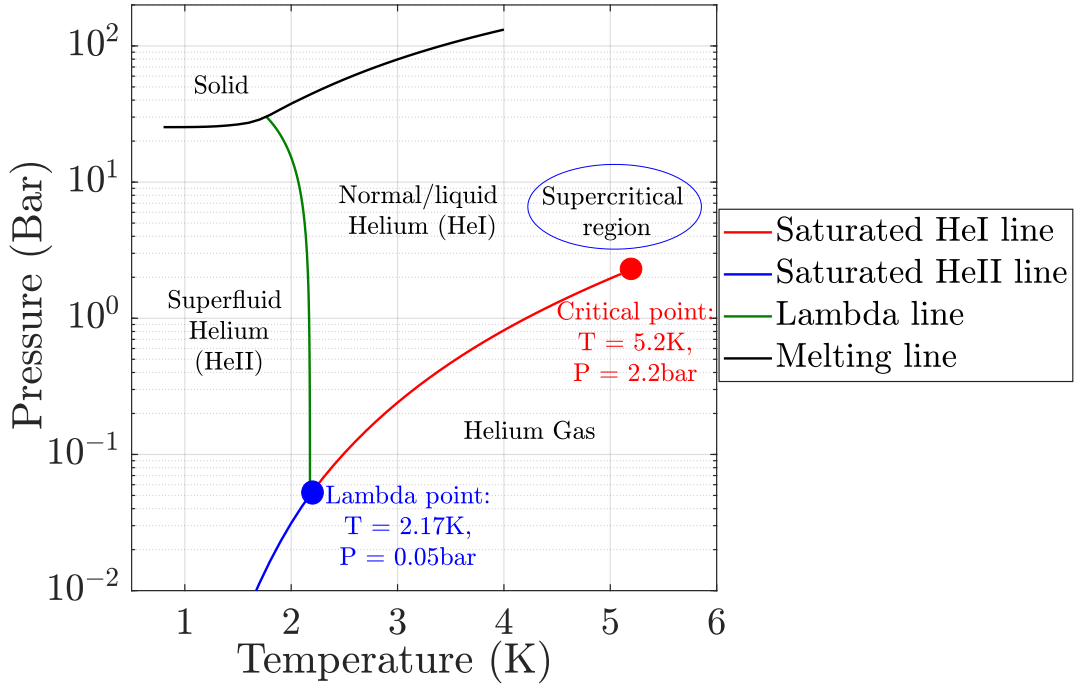

Figure IV.2: Phase diagram of ^{4}He [The phase diagram is constructed using the data obtained from HEPAK (computer program to estimate thermophysical properties of helium)]

IV.1.1 The new centrifugal pump

Traditionally, turbines are used to extract the useful energy from the flowing fluid, when coupled with the generator. On the other hand, when turbines are used to increase the pressure head of the fluid by means of an electrical energy input, they are referred as pumps. The old centrifugal pump from Duri [2012] was designed to deliver the flow rate of 85 - 400$\frac{g}{s}$ at the frequency on the order of 1450RPM. But, the flow rate delivered by the old pump was found to be very high compared to the flow rate required in the HEJET circuit. Therefore, the old centrifugal pump was not compatible with the HEJET circuit leading possibly to some kind of instability of the flow. This prompted us to design a new centrifugal pump adapted to the HEJET circuit, which can deliver the required pressure head across the pump at cryogenic temperatures. This new centrifugal pump is designed to improve its efficiency and thus the jet flow stability as compared to the old one. The new centrifugal pump is designed by the 'Optydro Concept Sàrl' and manufactured by the company 'Micro-Technic'. Figure IV.3 shows the system* requirement along with the characteristics of the newly designed centrifugal pump provided by the designer. These pump characteristics are plotted for the same size of the turbine having a diameter of 122.4mm. The $(\Delta P)_{pump}$ represents the increase in pressure head of the fluid with the use of centrifugal pump. The system characteristics (black and blue curves) are shown for the two different nozzle diameters of $d = 3$mm and $d = 5$mm respectively ($(\Delta P)_{pump} = P_2 - P_1$ in figure IV.1). In this figure, for a given flow rate, the pressure drop across the nozzle ($(\Delta P)_{nozzle} = P_5 - P_6$ in figure IV.1) is estimated based on the following procedure.

In the closed circuit of the HEJET experiment, Bernoulli's equation can be applied between any two sections. One of which is just before the heat exchanger (corresponding to point P5 in figure IV.1) and the other section within the experimental region close to the wall (corresponding

*The word 'system' is used to refer to the HEJET closed circuit wind tunnel.

to point P6 in figure IV.1). The Bernoulli's equation for these two sections can be written as:

$$P_5 + \frac{1}{2}\rho V_5^2 = P_6 + \frac{1}{2}\rho V_6^2 + Z_{5-6}, \tag{IV.1}$$

where P_5 and P_6 is the static pressure whereas V_5 and V_6 is the velocity, with the pressure drop Z_{5-6} along the flow, ρ is the density of helium. In equation IV.1 the velocity V_6 can be assumed to be zero. The pressure drop between these two section accounts for the flow through the heat exchanger (K_{HE}), the abrupt change of geometry within the nozzle (K_N) and the sudden enlargement in the cross-section after the jet exit (K_E). Therefore, the pressure drop can be expressed by:

$$Z_{5-6} = \frac{1}{2}\frac{\rho K_N \dot{Q}^2}{S_N^2} + \frac{1}{2}\frac{\rho K_E \dot{Q}^2}{S_N^2} + \frac{1}{2}\frac{\rho K_{HE} \dot{Q}^2}{S_5^2}, \tag{IV.2}$$

where S_N and S_5 is the cross-sectional area of the jet exit and at the section $P5$ respectively. $\dot{Q}$ is the volumetric flow rate in $\frac{m^3}{s}$ and $\dot{m} = \frac{\dot{Q}}{\rho}$ is the mass flow rate in $\frac{kg}{s}$ in the closed loop wind tunnel. Referring to Idelchik [1999] and Rohsenow [1998], the pressure drop coefficients in equation IV.2 are found to be $K_E = 1$, $K_N = 0.01$ and $K_{HE} = 1.06$. Considering all these constants the volumetric flow rate can be estimated from the following relations given by:

$$\dot{Q} = \sqrt{\frac{2(\Delta P)_{nozzle}}{2.62 \times 10^9 \times \rho}}, \tag{IV.3}$$

$$\dot{Q} = \sqrt{\frac{2(\Delta P)_{nozzle}}{2.01 \times 10^{10} \times \rho}}. \tag{IV.4}$$

Equation IV.3 and equation IV.4 give the estimate of the volumetric flow rate for the nozzle diameter of d = 5mm and d = 3mm respectively. The system characteristics shown in figure IV.3 are estimated using the equation IV.3 and equation IV.4. According to these system requirements, the new centrifugal pump is designed which can deliver the pressure head of 150mbar at 2400RPM for $40\frac{g}{s}$. This figure shows the pump characteristics $(\Delta P)_{pump}$ with its efficiency η (green, red and yellow curve) at different turbine frequencies provided by the pump designer. The operating point is the point where the system characteristics (HEJET) meet the pump characteristics on the plot of pressure head versus flow rate as shown by the black-filled circle in figure IV.3. For example, the operating point of the pump at the turbine frequency $\mathcal{F}_t$ = 25Hz is at the flow rate of $25\frac{g}{s}$ at which the pump efficiency is about 43%. The efficiency of the centrifugal pump will be discussed in detail in section IV.3.1.7 along with the actual experimental measurements.

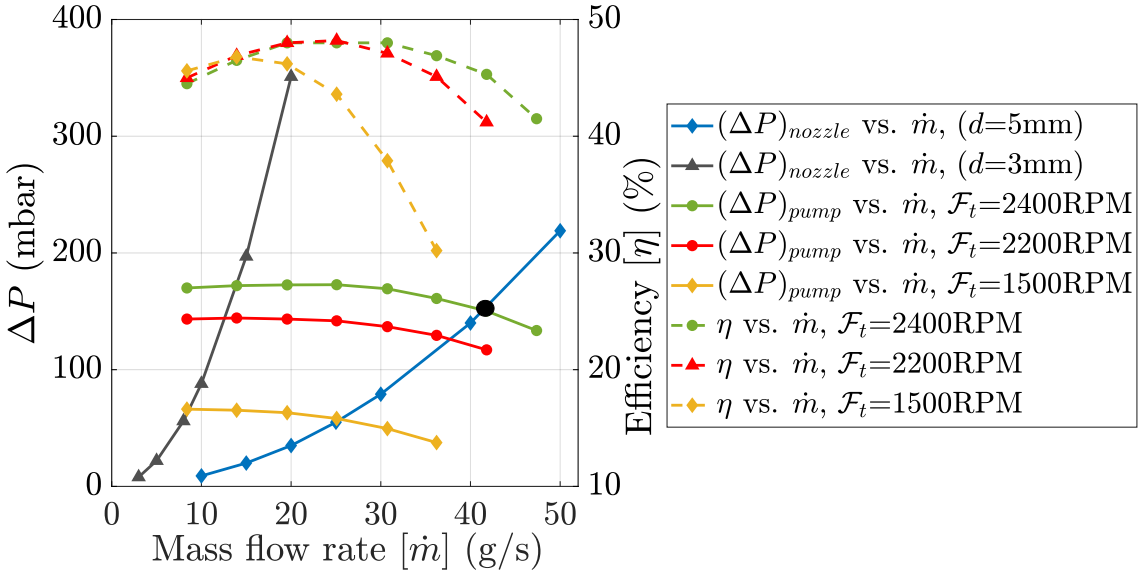

Figure IV.3: The new centrifugal pump characteristics $(\Delta P)_{pump}$ along with the system characteristics $(\Delta P)_{nozzle}$ [This plot is provided by the pump designer]

Figure IV.4 shows the newly designed turbine having a diameter of 122.4mm. This figure shows the turbine which consists of 16 identical sections each having 4 blades. Figure IV.5 shows the hub and the housing of the centrifugal pump assembly. The small distance of the order of 0.4mm between the hub and the housing allows the helium liquid to force outwards and enter the volute. The housing of the turbine embodies the rotating part of the labyrinth (+) which is then placed into the fixed part of the labyrinth (-) as shown in figure IV.5. The labyrinth helps to maintain the required pressure difference across the centrifugal pump.

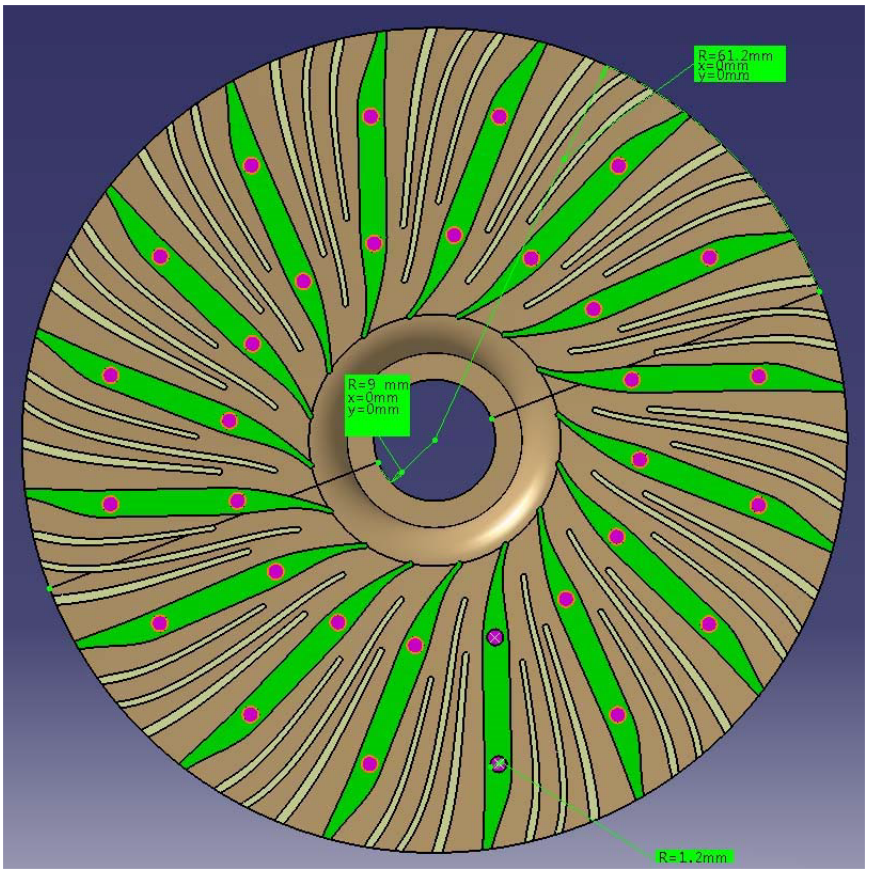

Figure IV.4: Turbine of the newly designed centrifugal pump [provided by the pump designer; sense: anti-clockwise rotation]

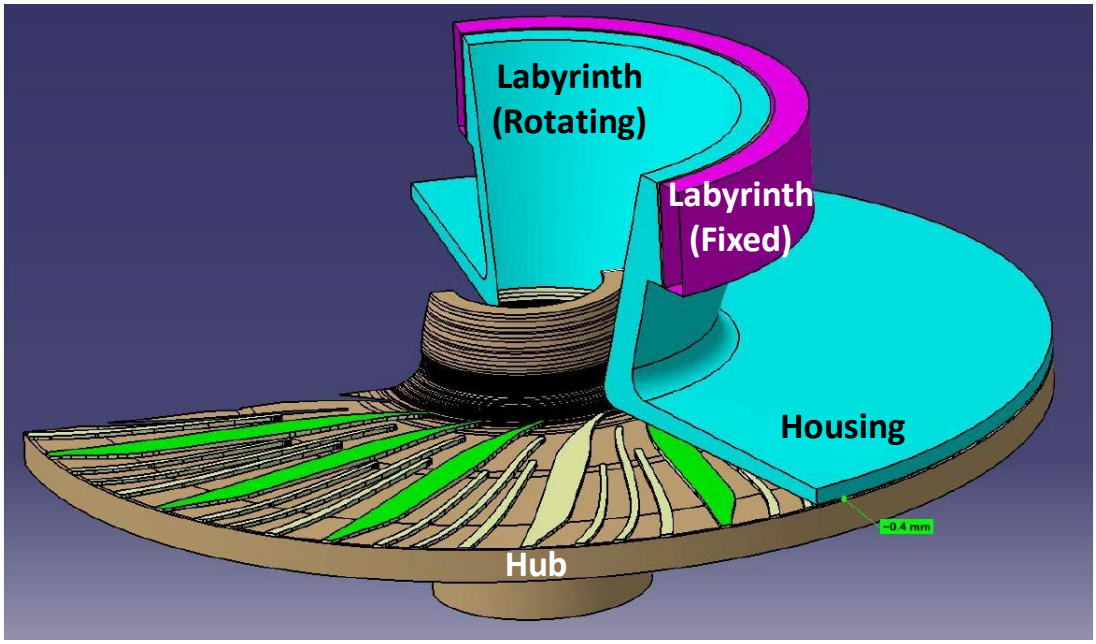

Figure IV.5: The hub and housing of the turbine [provided by the pump designer]

Figure IV.6 shows the basic elements of the centrifugal pump assembly after manufacturing, which contains turbine, volute, labyrinth (+ and -) and the diffuser (outlet). All the parts of the pump are made of stainless steel. The volute collects the helium that has been pumped by the turbine from the experimental chamber of the HEJET facility and passes it into the diffuser (shown by the red colored arrow). The high pressure side of the centrifugal pump i.e. the exit of helium through diffuser is then connected to the pipe, where a venturimeter is installed (see figure IV.1). The central part of the turbine is then finally connected to the shaft of the motor, which governs the rotation of the turbine in the centrifugal pump. While driving the centrifugal pump, the turbine rotates in the anti-clockwise direction as shown in figure IV.6 (see yellow circular arrow).

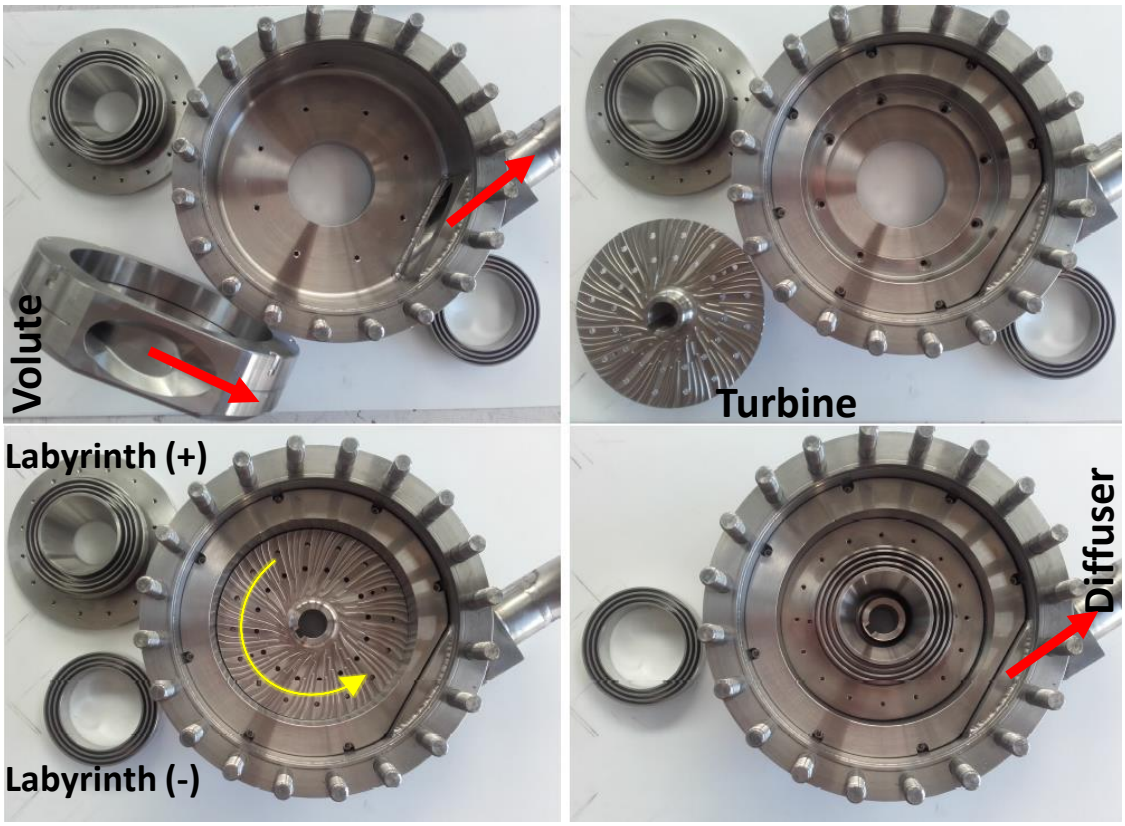

Figure IV.6: Different components of the centrifugal pump showing the turbine assembly [red arrow shows the flow of the fluid and yellow arrow shows the sense of rotation of the turbine in the centrifugal pump]

IV.1.2 Dimensions of the nozzle and the grid position

The experimental section is cylindrical in shape with a diameter of 20cm and height of 45cm. Figure IV.7 shows the nozzle of diameter $d = 5$mm mounted in the experimental section along with temperature sensors on the bottom surface. Two nozzles of diameter $d = 3$mm and 5mm are designed. The nozzle design is based on the similar adaptation of the flow profile from exit of the heat exchanger up to the nozzle exit (Duri [2012]). Just before the nozzle exit, a honeycomb of cell size 5mm and a height of 5cm is mounted for flow laminarization. A horizontal grid of 5mm height and of 3mm cell size is mounted at 40mm downstream the hot-wire support, which maintains the jet stability by breaking down the large scale structures [Chanal, 1998;

Pietropinto et al., 2003]. To avoid the effects of the wakes generated by the cables/temperature sensors installed at the bottom surface of the experimental section on the jet stability, a flat circular stainless steel plate with a hole at the center is designed and installed.

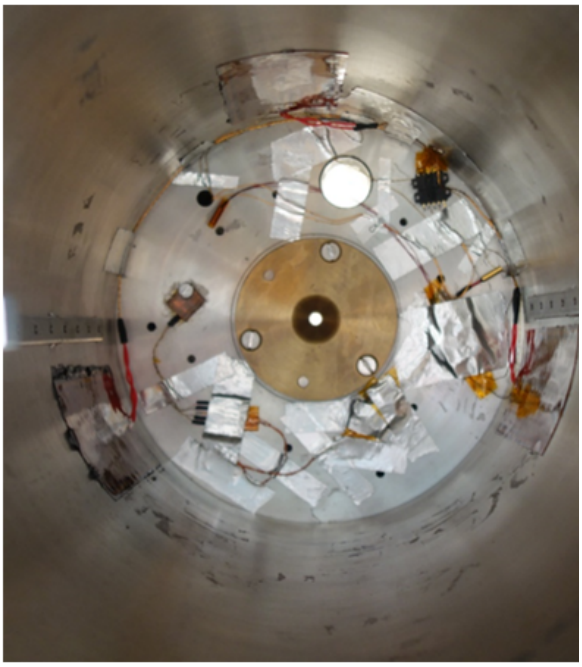

Figure IV.7: Experimental section showing temperature sensors and the nozzle of $d = 5$mm

IV.1.3 Temperature sensors

In total 8 temperature sensors are mounted within this experiment, out of which 3 temperature sensors are of platinum type (PT100), which can indicate the temperature within the range of 80K to 300K. The rest of the temperature sensors are Cernox temperature sensors, which are calibrated within the range of 1.4K to 300K. During the entire experimental campaign all the temperatures are acquired using the home-made 'CABETH' instrumentation at the frequency of 1Hz. The temperature sensors along with their corresponding location are listed below, and their approximate location are shown in figure IV.1 using red filled circles.

1. T1 - PT100: bottom surface of the experimental section (close to the nozzle exit)
2. T2 - Cernox: saturated helium bath (at the same level as of nozzle)
3. T3 - Cernox: bottom surface of the experimental section (close to the nozzle exit)
4. T4 - Cernox: point of injection of pure He gas into the pressurized bath
5. T5 - Cernox: saturated helium bath (just above the diffuser)
6. T6 - PT100: saturated helium bath (just above the diffuser)
7. T7 - PT100: mounted on motor to follow the change in motor temperature
8. T8 - Cernox: diffuser exit [fluid temperature at the exit of the centrifugal pump]

IV.1.4 Pressure sensors

Two pressure gauges are used in the HEJET/HECAL facility. One pressure gauge is installed to measure the pressure inside the saturated helium bath, whereas the second pressure gauge is installed to measure the pressure inside the pressurized helium bath. For more precise monitoring of the pressure inside the pressurized bath, a pressure sensor 'Bourdon-Sedeme EG912' is connected to the Keithley 2700 multimeter, which indicates the pressure according to the scale of 2.5Volts for one bar over a range of 0 to 5bars. Similarly, to measure the pressure of the saturated bath precisely, the 'MKS type Baratron 127A' pressure sensor is connected to the MKS 600 conditioner, which measures the pressure over a range of 1 - 100mbar. The same pressure sensor is also used to regulate the pressure inside the saturated bath using a control valve (No. 3 in figure IV.1).

Apart from these static pressure sensors mentioned above, the HEJET facility has three differential pressure sensors. The first differential pressure sensor is of the type Validyne DP10 - 26, which is installed across the venturi to estimate the flow rate in the closed circuit wind tunnel. This differential pressure sensor can measure the pressure drop ($(\Delta P)_{venturi}$) up to 60mbar. The second differential pressure sensor is of the type Validyne DP10 - 30 which measures the pressure rise ($(\Delta P)_{pump}$) across the centrifugal pump up to 100mbar. If the expected $(\Delta P)_{pump}$ >100mbar, Validyne DP10 - 38 can also be used which can measure the differential pressure up to 800mbar. The third differential pressure sensor is also of the type Validyne DP10 - 30 which measures the pressure drop across the nozzle ($(\Delta P)_{nozzle}$) i.e. between the entrance of the helicoidal heat exchanger and the bottom surface of the experimental section close to the nozzle exit. The differential pressure is measured using a Validyne 4 channel carrier demodulator CD280 with a signal output over a range of 0 to 13Volts. To summarize, the pressure differences are given by, $(\Delta P)_{pump} = P2 - P1$, $(\Delta P)_{venturi} = P3 - P4$, $(\Delta P)_{nozzle} = P5 - P6$ and their locations are as shown in figure IV.1 using blue filled circles.

The calibration of all the differential pressure sensors are performed at ambient temperature using He gas. A simple experimental set-up for Validyne differential pressure sensor calibration is made, in which the negative side (Plow) of the sensor is connected to the vacuum pump (-) and the positive side (Phigh) of the sensor is pressurized using He gas (+). The static pressure of He gas is measured using MKS baratron 600 series. To ensure the proper functioning of positive and negative sides of the sensor, the second calibration is performed, while connecting the positive side to the vacuum pump and the negative side to the pressurized He gas. Figure IV.8 shows the calibration of the differential pressure sensors for venturi, nozzle and the centrifugal pump. The two calibrations of the same differential pressure sensor show the same magnitude of pressure with opposite voltage sign, which shows the directional dependence of the flow and the equal sensitivity on either side.

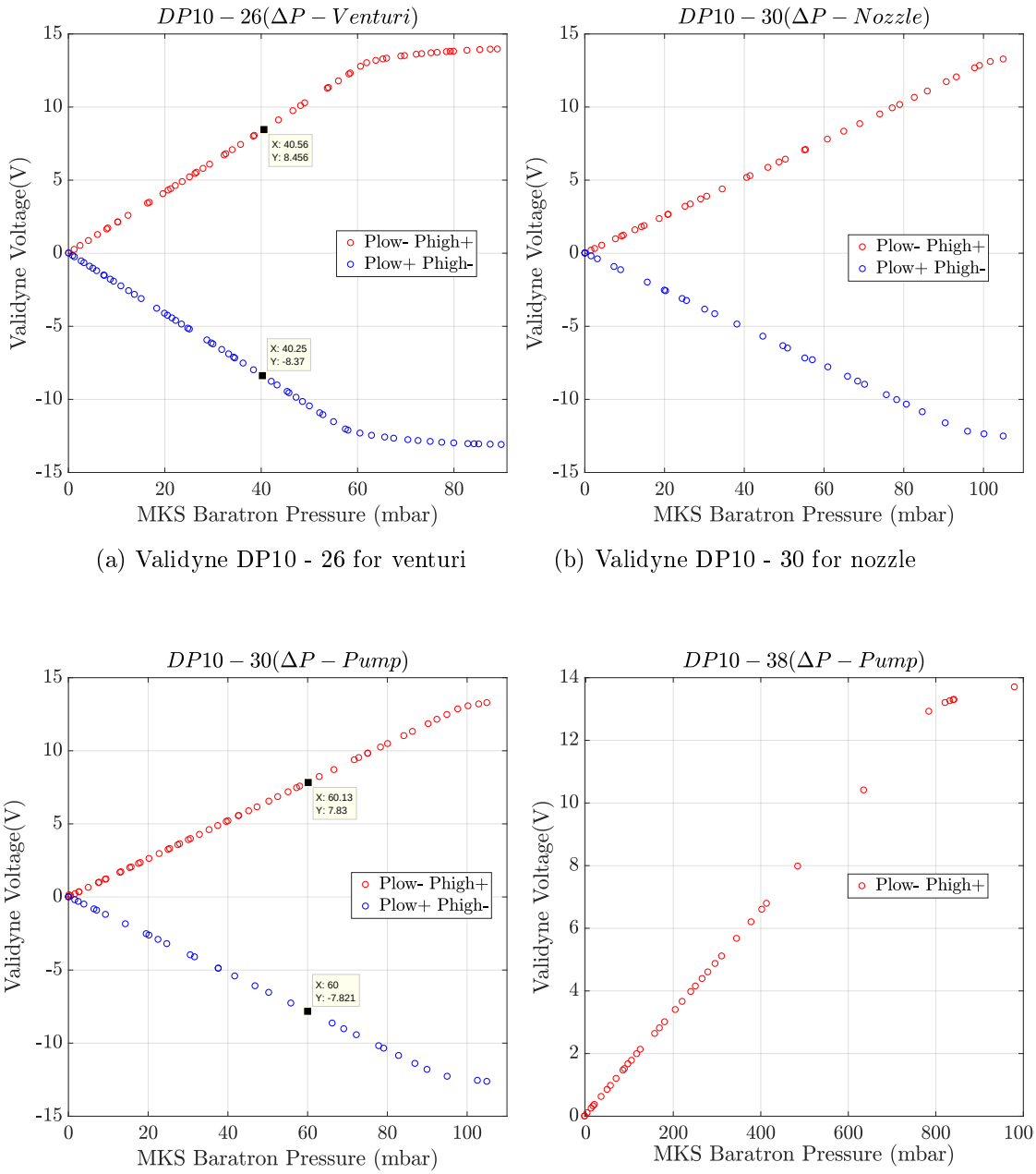

(a) Validyne DP10 - 26 for venturi

(b) Validyne DP10 - 30 for nozzle

(c) Validyne DP10 - 30 for pump

(d) Validyne DP10 - 38 for pump

Figure IV.8: Calibration of differential pressure sensors at T = 300K

IV.1.5 Helium level indicator

In order to monitor the level of helium in the saturated helium bath, the HEJET facility has two different systems. One of the systems relies on a superconducting gauge of length 750mm. This probe indicates the level of helium in the saturated bath (h) in mm once connected to the conditioner. The uncertainty associated with this helium level indicator is ±1mm. This sensor is installed in such a way that h = 0 represents the level of helium in the saturated bath up to the bottom surface of the experimental section as shown in figure IV.1 and figure IV.9. Figure IV.9 shows the actual view of the HEJET experimental facility. Typically, helium in the saturated bath is filled up to h ≈ 710mm (just below the first radiation shield). A second system

is made of a set of 6 different resistances (R1 to R6) which are mounted at six different vertical locations in the saturated bath as shown in figure IV.9. The variation of the heated resistance indicates whether the resistance is immersed in the liquid helium or not. Depending on whether the resistance is immersed in liquid helium or in He gas, the communication is made using the home-made instrumentation.

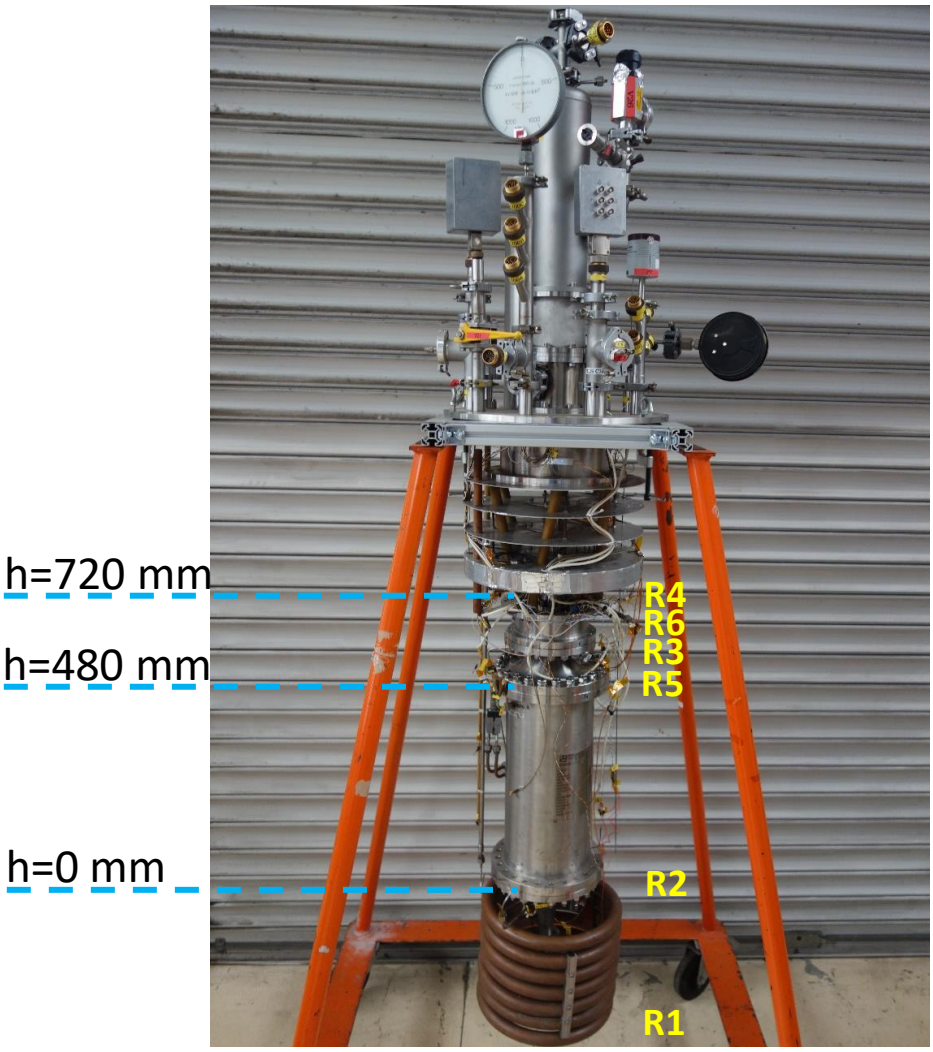

Figure IV.9: Actual view of the HEJET experimental facility [h denotes the level of helium in the saturated helium bath measured by the sensor of superconductor and R1 to R6 denotes the position (level) of 6 different resistances installed in the saturated helium bath]

IV.1.6 The hot-wire support

Figure IV.10 shows the hot-wire support used in the HEJET experiment. In the HEJET facility, the hot-wires are mounted on the horizontal metal strip, which is screwed to the inner wall of the experimental section. During each experiment, a maximum of 5 hot-wires are mounted. As shown in figure IV.10, only one hot-wire can be installed at the center (r = 0mm) whereas the distance between any two adjacent hot-wires is 10mm. The hot-wires are installed at $\frac{z}{d} = 50$ [$d = 5$mm].

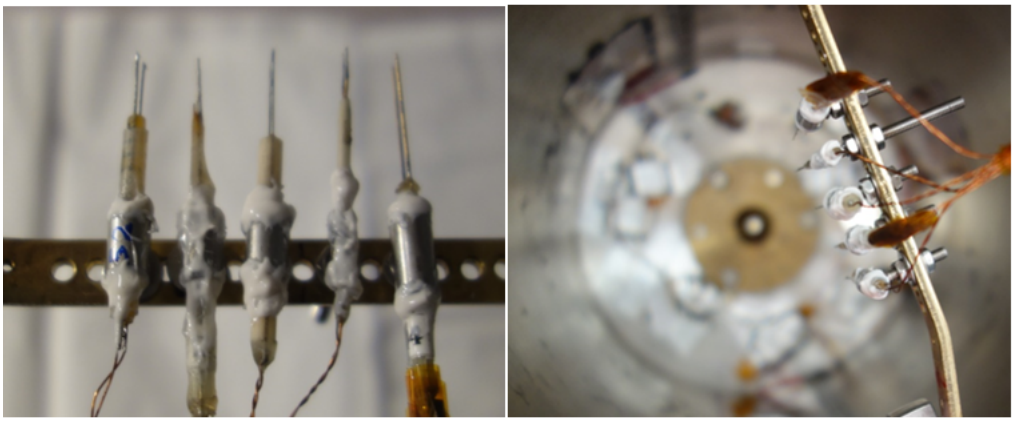

Figure IV.10: Hot wires mounted on the support which is fixed at $z = 50d$ in the experimental region [$d = 5$mm]

IV.2 Procedure to cool-down

Once the pressurized bath as shown in figure IV.1 is closed, a leak detection test is performed using a mass spectrometer. The experimental assembly is then installed in the cryostat. The rinsing operation of the saturated and pressurized baths using pure He gas is performed at least 4 - 5 times in order to ensure that no impurities/air molecules are present in the cryostat. Once the filling of liquid nitrogen bath is started, it takes about 36 - 48 hours to attain the temperature of 78K throughout the experimental assembly. Once the temperature of 78K is reached throughout the experiment, the filling of helium bath (saturated and pressurized) begins. The filling of liquid helium is performed using a cryogenic transfer line, from a 250L tank of LHe stored at atmospheric pressure and 4.2K of temperature. Depending on the flow rate used, it takes about 5 - 6 hours to fill the cryostat up to the desired level i.e. slightly below the first radiation shield (see h $\approx$ 710mm in figure IV.1). Overall, based on the optimum performance of the experiment, this facility consumes 150L of liquid helium per day.

Once the temperature within the experiment has reached 4.2K at atmospheric pressure, the pumping of the saturated bath allows to decrease the temperature (as low as 1.7K). Once the desired saturation pressure in the range of 5 to 60mbar is attained, the valve (No. 13 in figure IV.1) allowing communication between the saturated and pressurized bath is closed. Then, the injection of the pure He gas (B50) in the pressurized bath begins (see No. 17 in figure IV.1) to reach the desired absolute pressure within the range of 2.5 - 3bar while keeping the desired temperature within the range of 1.8 - 2.4K.

IV.3 Results

IV.3.1 Macroscopic characteristics of the HEJET facility: the pump, mass flow rate and the energy balance

All the results presented in this chapter belong to the experiment performed using the nozzle diameter of $d = 5$mm. The hot-wire is installed along the axis of the jet at a downstream distance from the jet nozzle of $z = 50d$. Therefore, the hot-wire is installed in the fully developed zone of the jet flow [Wygnanski and Fiedler, 1969]. Before performing the hot-wire measurements, it is of utmost importance to ensure the proper and stable operation of the centrifugal pump. In order to do so, the characterization of the newly designed centrifugal pump is performed. The characterization of a centrifugal pump is based on its performance with respect to the rotation frequency of the turbine. The frequency $\mathcal{F}_t$ of the turbine of the centrifugal pump is measured via the tachogenerator mounted on the top of a brushed Dunkermotoren DC motor GR63X55 which is the same as in the HECAL experiment. In the HEJET facility, a Keithley 2400 voltage sourcemeter is used as a command to drive the motor (see section III.2.2). The experimental measurements are performed within the range of turbine frequency $\mathcal{F}_t = 8$ - 25Hz. The performance of any centrifugal pump can be studied using the delivered flow rate, pressure head and the mechanical power with respect to the input turbine frequency. In the following subsections, the characterization of the centrifugal pump based on the turbine frequency will be discussed.

IV.3.1.1 The pressure change across the venturi, nozzle and the centrifugal pump

Based on Bernoulli's principle, it can be established that the pressure difference across each of the pump, nozzle and the venturi has a quadratic dependence on the pump frequency i.e. $\Delta P \propto \mathcal{F}_t^2$. Multiple measurements are acquired using either HeI or HeII over a period of week. All the measurements are performed at an absolute pressure of 2.5bar in the closed circuit wind tunnel. Figure IV.11 shows the measured ΔP as a function of $\mathcal{F}_t$ for different temperatures within the closed circuit flow, ranging from T = 1.8K to T = 2.4K. The temperature (T) mentioned in this and the subsequent figures corresponds to sensor T3 explained in section IV.1.3. This figure shows that ΔP in either of the venturi, nozzle or the pump has no dependence on the operating temperature investigated here, with respect to the frequency of the centrifugal pump. From this figure, we see that the experimental data points follow a quadratic fit very well, which shows the consistency of the measurements. This figure also shows that the increased ΔP across the centrifugal pump is almost equivalent to the decreased ΔP across the nozzle. The non-zero offset at $\mathcal{F}_t = 0$Hz suggests that the calibration of the Validyne differential pressure sensors has slightly evolved at low temperatures. Ideally, to resolve this problem the calibration of the Validyne differential pressure sensor should be performed at low temperatures.

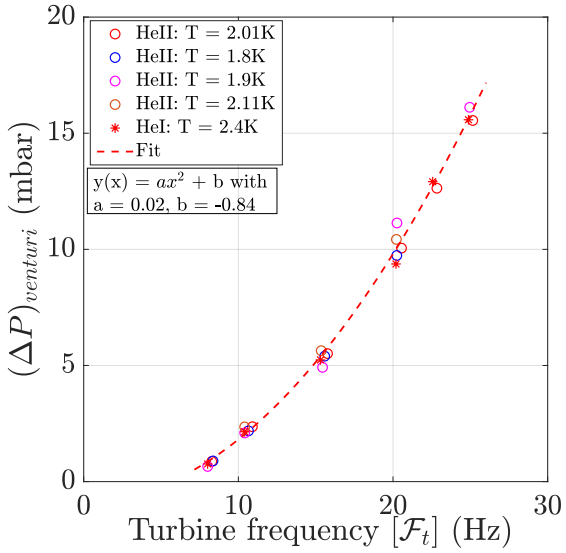

(a) ΔP across venturi as a function of turbine frequency

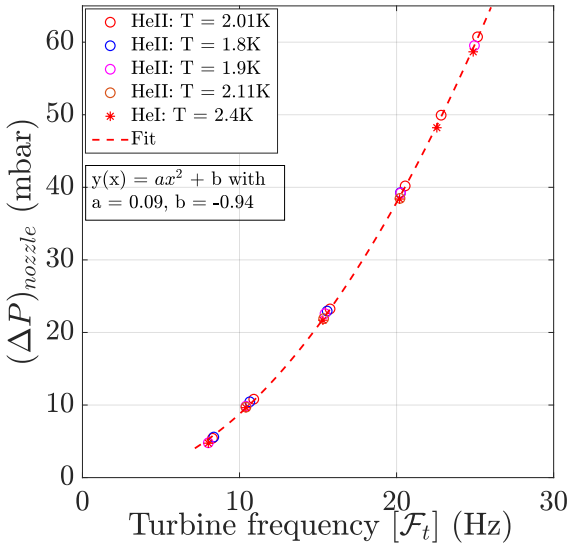

(b) ΔP across nozzle as a function of turbine frequency

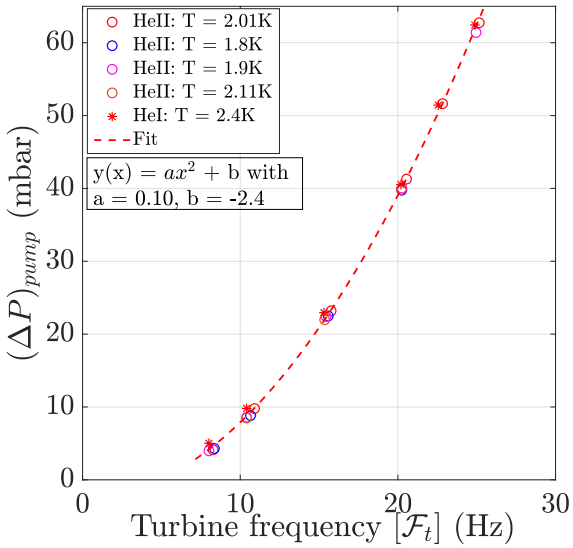

(c) ΔP across pump as a function of turbine frequency

Figure IV.11: The dependence of measured ΔP on $\mathcal{F}_t$ given by, $\Delta P \propto \mathcal{F}_t^2$ for the venturi, nozzle and the pump [the experimental fit is expressed by $y(x) = ax^2 + b$ where $y(x)$ is the pressure change in mbar and x is the turbine frequency in Hz]

IV.3.1.2 The flow rate

The flow rate in the closed circuit wind tunnel of the HEJET facility is estimated with the help of venturimeter. The inlet diameter of the venturimeter is $D_i = 20$mm and the throat diameter is $D_c = 9$mm. The flow rate using venturimeter is calculated based on the expression

given by [Van Sciver et al., 1991]:

$$\dot{Q} = \frac{\dot{m}}{\rho} = C_d \frac{\pi D_i^2}{4\rho} \sqrt{\frac{2\rho(\Delta P)_{venturi}}{\left[\left(\frac{D_i}{D_c}\right)^4 - 1\right]}}, \tag{IV.5}$$

where $\dot{Q}$ is the volumetric flow rate in $\frac{m^3}{s}$, $\dot{m}$ is the mass flow rate in $\frac{kg}{s}$, ρ is the density of helium fluid in $\frac{kg}{m^3}$, C_d is the coefficient of discharge taken as 0.95 based on the calibration of the venturimeter performed by Duri [2012] and $(\Delta P)_{venturi}$ is the pressure difference across venturimeter in Pa. Figure IV.12 shows the increase in flow rate measured using the venturimeter with respect to the turbine frequency. From figure IV.12, the linear dependence of flow rate on the operating frequency of the centrifugal pump is evident i.e. $\dot{Q} \propto \mathcal{F}_t$. From this figure we see that the flow rate in HeI and HeII is independent of the operating temperature within the closed loop. The measured volumetric flow rate ranges from 6×10^{-5} to $3 \times 10^{-4} \frac{m^3}{s}$, which corresponds to the mass flow rate of 10 to $45 \frac{g}{s}$ over the turbine frequency range $\mathcal{F}_t$ = 8 - 25Hz.

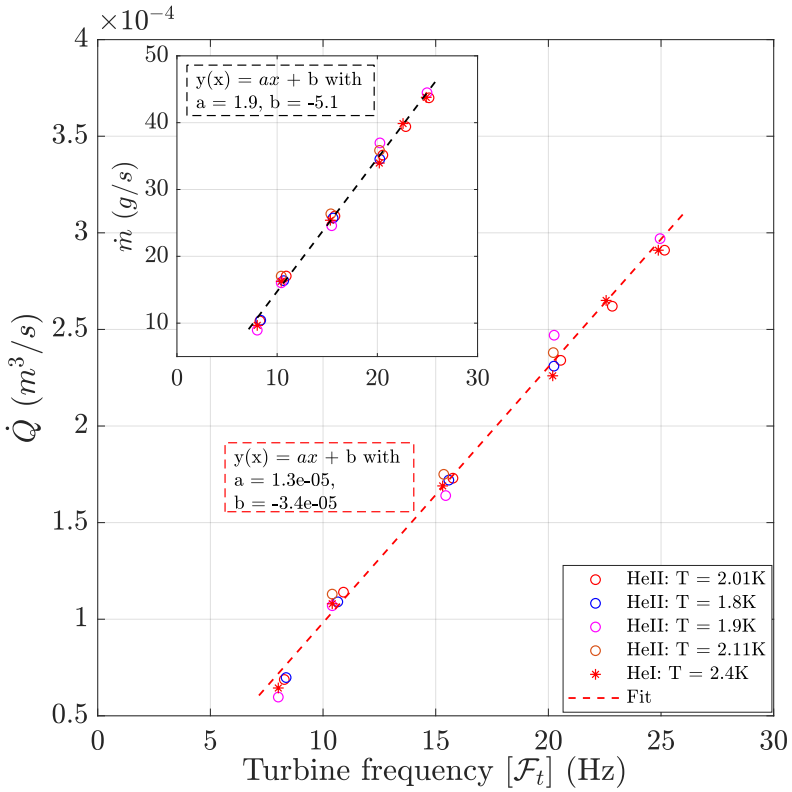

Figure IV.12: Volumetric flow rate estimated from the venturimeter as a function of turbine frequency; the inset represents the mass flow rate expressed in $\frac{g}{s}$ [the experimental fit is expressed by $y(x) = ax + b$ where $y(x)$ is the flow rate in $\frac{m^3}{s}$ or $\frac{g}{s}$ and x is the turbine frequency in Hz]

IV.3.1.3 Electrical power consumption of the motor

The electrical power consumption of the motor is estimated by measuring the voltage and the current supplied to the motor. Figure IV.13 shows the electrical power consumption of the DC motor in the HEJET facility at ambient and at low operating temperatures in the closed circuit wind tunnel. This figure shows the electrical motor power after removing the contribution of the joule heating where the terminal resistance of the motor is 0.6Ω. We see that for the

turbine frequency of 8 up to 25Hz the motor consumes about 2 to 15W of electrical power. The measurements at ambient temperature are performed using helium gas as a working fluid at T = 300K. At ambient temperature the density of He gas is very low, therefore a negligible pressure head is delivered by the centrifugal pump. This pressure head is found to be non measurable with the available differential pressure sensor ($<$ 1mbar). Because of the very low pressure head across the centrifugal pump we have a negligible mechanical power output (see next subsection) of the pump at ambient temperature. We also see that the measured electrical motor power at ambient temperature shows a linear dependence on the frequency. This linear dependence can be explained in the following way. During the operation of the centrifugal pump, frictional losses occur in the bearings of the shaft assembly as well as in the labyrinth. This frictional power is expressed by $C_{\mathcal{F}_t} \times \omega$, where $C_{\mathcal{F}_t}$ is the frictional torque in Nm, $\omega = 2\pi\mathcal{F}_t$ is the angular velocity of motor shaft in $\frac{rad}{s}$ and $\mathcal{F}_t$ is the frequency of the turbine. Assuming a constant $C_{\mathcal{F}_t}$ over the range of $\mathcal{F}_t$ investigated here, we see that the frictional power is directly proportional to the turbine frequency $\mathcal{F}_t$. Therefore, from figure IV.13 we conclude that the electrical power consumption of the motor is equal to the frictional power expressed by $C_{\mathcal{F}_t} \times \omega$ at T = 300K. Hence a corresponding linear fit is constructed at ambient temperature as shown in figure IV.13. However, at low temperatures we can expect different frictional power because of the differential contraction which may induce a different friction regime.

From figure IV.13 we see that at low temperatures the electrical power consumption of the motor is higher than at ambient temperature. We also see that the power dependence on the frequency is not linear anymore. As the density of liquid helium at low temperatures is high, the centrifugal pump provides a significant pressure head and hence the pump delivers a significant mechanical power. Therefore, at low temperatures the electrical motor power represents the contribution of both the pump mechanical power ($\propto \mathcal{F}_t^3$) and the frictional losses ($\propto \mathcal{F}_t$). Thus, at low temperatures a fit is constructed using the combination of cubic and linear dependence on $\mathcal{F}_t$. We see that the experimental data points follow this fit very well as shown in figure IV.13. From this figure, based on the value of b it is likely that the frictional losses are slightly more at low temperatures than at ambient temperature.

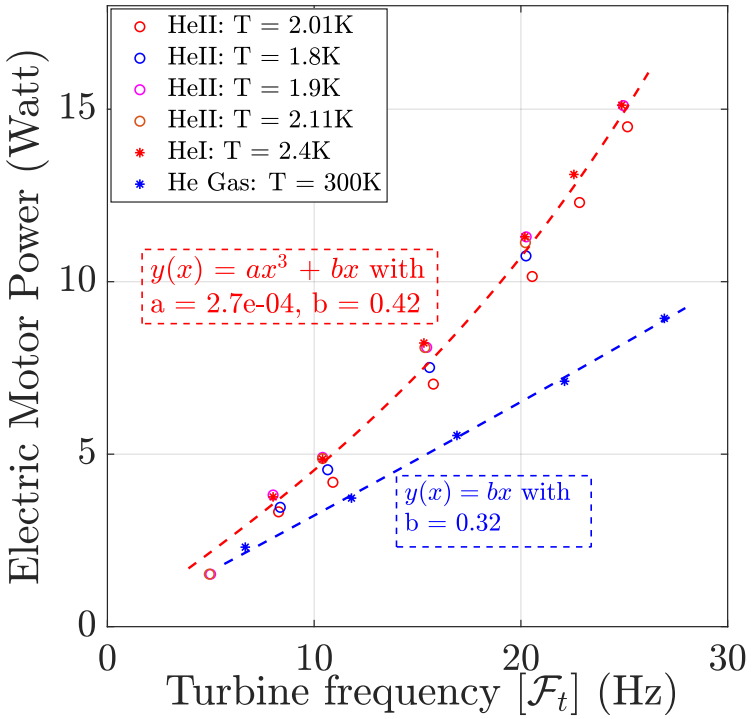

Figure IV.13: Electrical power consumption of the DC motor as a function of the turbine frequency [the experimental fit is expressed by $y(x) = ax^3 + bx$ where $y(x)$ is the electrical motor power in W and x is the turbine frequency in Hz; $a = 0$ at T = 300K]

IV.3.1.4 Mechanical power output of the centrifugal pump

The mechanical power output of the centrifugal pump is calculated from the flow rate measured using venturimeter and the pressure difference across the pump given by, $P_{mech} = \dot{Q}(\Delta P)_{pump}$, where $\dot{Q}$ is the flow rate in $\frac{m^3}{s}$ and $(\Delta P)_{pump}$ is the increase in pressure head across the pump in Pa. Figure IV.14 shows the pump mechanical power with respect to the turbine frequency at various temperatures. This power shows no particular dependence on the temperature within the range from 1.8K to 2.4K. The experimental fit clearly shows the dependence of the pump mechanical power with respect to the turbine frequency given by, $P_{mech} \propto \mathcal{F}_t^3$. Figure IV.14 shows the useful mechanical work imparted by the centrifugal pump on to the fluid which ranges from 0.1 to 1.8W for the turbine frequency of 8 to 25Hz.

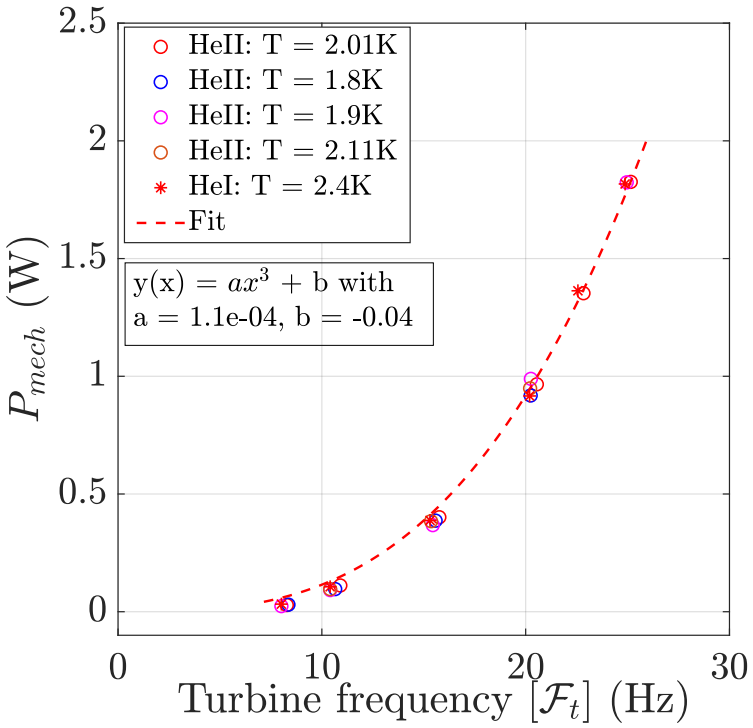

Figure IV.14: Mechanical power output of the centrifugal pump as a function of turbine frequency [the experimental fit is expressed by $y(x) = ax^3 + b$ where $y(x)$ is the pump mechanical power in W and x is the turbine frequency in Hz]

IV.3.1.5 Estimation of heat losses from evaporation

To maintain a steady temperature in the experimental region of the HEJET facility, the power injected by the turbine of the centrifugal pump and the power dissipated into heat by the turbulent process is evacuated using the heat exchanger which is dipped into the saturated helium bath (see figure IV.1). A fraction of this injected power is also evacuated by the wall of the cylindrical experimental section, in which the turbulent jet flow occurs. The evacuated power by both the heat exchanger and the wall of the experimental section causes evaporation of liquid helium in the saturated He bath. The low pressure in the saturated helium bath is maintained using the roots vacuum pump. The amount of evaporated helium from the HEJET facility can be measured using the 'Schlumberger Gallus 2000' flow meter installed after the roots vacuum pump in the helium recuperation circuit. This flow meter can measure the flow rate within the range of $\dot{Q}_{roots}$ = 0.02 - 4$\frac{m^3}{hr}$. The power corresponding to this evaporation of helium is given by, $P_{roots} = \dot{Q}_{roots} L \rho$, where $\dot{Q}_{roots}$ is the volumetric flow rate of evaporated helium in $\frac{m^3}{s}$, L is the latent heat of evaporation of liquid helium (at saturated He bath temperature) in $\frac{J}{kg}$ and ρ is the density of helium gas in the recuperation circuit at atmospheric pressure and temperature. As $P_{mech} = \dot{Q}(\Delta P)_{pump}$ is the injected mechanical power in the HEJET facility, P_{roots} is the dissipated power from the HEJET facility.

First the "natural" heat losses by means of conduction, convection and radiation of the HEJET cryostat are estimated at $\mathcal{F}_t$ = 0Hz. To do this, the flow rate of evaporated helium is measured at $\mathcal{F}_t$ = 0Hz denoted by $\dot{Q}_{N,roots}$. Then the "natural" losses at $\mathcal{F}_t$ = 0Hz are estimated as $P_{N,roots} = \dot{Q}_{N,roots} L \rho$, which accounts to about 0.9 - 1.8W depending on the height of the liquid helium in the saturated bath (see h in figure IV.1). At $\mathcal{F}_t$ >0Hz, measured P_{roots} represents the contribution of both dissipated power (as a consequence of the injected

power by pump) and the natural losses of the cryostat. Figure IV.15 shows the heat losses from evaporation as a function of turbine frequency at four different temperatures in the HEJET facility. In this figure, the contribution of $P_{N,roots}$ is already deducted from P_{roots}. Therefore, P_{roots} in this figure represents the dissipated power in the HEJET facility. As the centrifugal pump is not 100% efficient, we see that P_{roots} in figure IV.15 is higher than P_{mech} in figure IV.14. This figure also shows that the experimental data points follows the fit defined by $P_{roots} \propto \mathcal{F}_t^3$ at the temperature T = 1.8 - 2.4K.

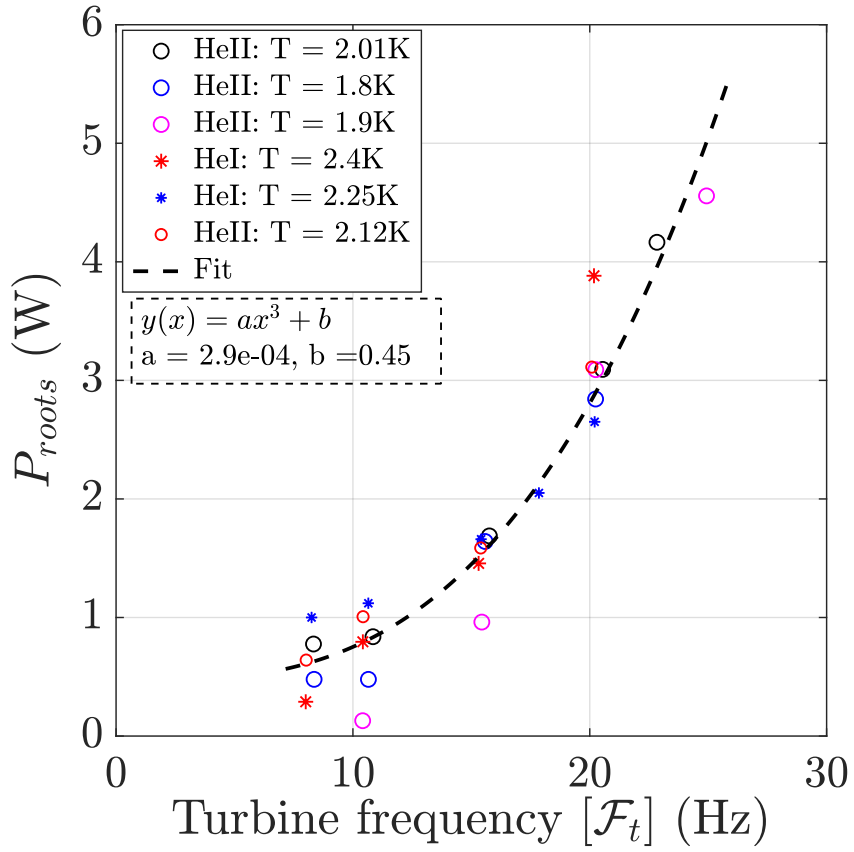

Figure IV.15: Heat losses from evaporation as a function of turbine frequency [the experimental fit is expressed by $y(x) = ax^3 + b$ where $y(x)$ is P_{roots} in W and x is the turbine frequency in Hz]

IV.3.1.6 Estimation of flow rate based on power balance in HeI

In this section, different methods to estimate the flow rate in the closed circuit wind tunnel are demonstrated. This is done in order to verify, whether the flow rate estimated from the venturimeter is reliable or not. To do this all the Cernox temperature sensors are re-calibrated in superfluid at T = 1.8K when the temperature within the entire experiment is same and steady while the turbine is at rest. The flow rate in the HEJET facility can be estimated based on the power balance. While pumping the fluid, an ideal pump does not increase the temperature of the fluid in the piping circuit. But, in practice the centrifugal pump increases the temperature of the fluid i.e. T8 > T3 (see figure IV.1). Here T8 (= 2.43K) is the temperature of the fluid at the exit of the centrifugal pump and we assume that the temperature T3 (= 2.40K) is same as the temperature at the nozzle exit. The useful work of the centrifugal pump is given by $\dot{Q}(\Delta P)_{pump}$. But, because of the non-ideal performance of the centrifugal pump the added heat corresponds

to $\dot{m}C_p(T8 - T3)$, where C_p is the specific heat of helium at constant pressure. Therefore, in steady state, the mass flow rate in the closed circuit loop can be calculated based on the power balance given by:

$$P_{roots} = \dot{Q}(\Delta P)_{pump} + \dot{m}C_p(T8 - T3) = \dot{m}\Big[\underbrace{\frac{(\Delta P)_{pump}}{\rho}}_{41.63\frac{J}{kg}} + \underbrace{C_p(T8 - T3)}_{71.14\frac{J}{kg}}\Big]. \tag{IV.6}$$

In the above equation at $\mathcal{F}_t = 25$Hz, $\frac{(\Delta P)_{pump}}{\rho}$ and $C_p(T8 - T3)$ contributes to about 41.63 and $71.14\frac{J}{kg}$. This shows an important contribution of energy linked with the non-ideal performance of the centrifugal pump. Therefore, based on the estimated P_{roots} as shown in figure IV.15 and using equation IV.6 we can find another measure of the flow rate in the HEJET facility.

The mass flow rate in the closed circuit loop can be estimated from the power balance based on the conduction through the cylindrical wall of the HEJET facility. In steady state, the injected power through the jet exit can be represented by $\dot{Q}(\Delta P)_{nozzle}$. This injected power dissipates in the turbulent jet within the experimental region of the HEJET facility. This dissipated power from the jet evacuates across the cylindrical wall of the experimental section of the HEJET facility by means of conduction, as the temperature in the saturated bath is always less than the temperature in the pressurized bath i.e. T2 < T3 (see figure IV.1). Therefore, in steady state the mass flow rate in the closed circuit wind tunnel can be calculated based on the power balance across the cylindrical wall of the experimental section given by:

$$\dot{Q}(\Delta P)_{nozzle} = \frac{\dot{m}}{\rho}(\Delta P)_{nozzle} = KA\frac{dT}{dr}, \tag{IV.7}$$

where K is the thermal conductivity of stainless steel (inox), A is the cylindrical surface area of the experimental region, dT = T3 - T2 = 2.40K - 2.28K and dr = 3mm is the thickness of the cylindrical wall. At high turbine frequency such as 25Hz the temperature in the experimental region of the HEJET facility can be considered as homogeneous because of the sufficient re-circulation and the improved mixing of the helium. Hence, we can assume that T3 represents the homogeneous temperature in the experimental region at high turbine frequency. This is an important criteria in order to use either equation IV.6 or equation IV.7 to estimate the mass flow rate. Overall, the mass flow rate in the HEJET facility can be estimated using 4 different methods which are summarized in table 4.

Table 4: Estimation of the mass flow rate in the HEJET facility based on different methods at $\mathcal{F}_t$ = 25Hz in HeI at T = 2.4K

Method	**Based on**	**Equation**	$\dot{m}$**(g/s)**
Correlation	Idelchik [1999]	Equation IV.3	26.3
Experiment	Venturimeter	Equation IV.5	44.5
Experiment	P_{roots}	Equation IV.6	44.2
Experiment	conduction through wall	Equation IV.7	43.5

Table 4 shows the consistency of the estimated mass flow rate using three different experimental approaches. But, the estimated mass flow rate from correlation differs significantly from the experimental estimates. It is observed that to use equation IV.3, $(\Delta P)_{nozzle}$ must be measured at the right position. As indicated in figure IV.1, $(\Delta P)_{nozzle} = P5 - P6$. Ideally to use equation IV.3, P6 must be measured at the immediate section of the nozzle exit which is not

feasible in the present HEJET experiment. Because of this reason the estimated mass flow rate using Equation IV.3 is lower than other experimental methods for the same $(\Delta P)_{nozzle}$. Based on these observations, it is concluded that the venturimeter gives the best estimate of the flow rate in the HEJET facility and the same is used for the further post-processing of the data.

IV.3.1.7 Efficiency of the centrifugal pump

In the HEJET experiment, we have three measures of the power: the electrical motor power consumption of the DC motor which drives the centrifugal pump, the useful mechanical work of the centrifugal pump and the dissipated power of the HEJET facility from evaporation of helium. The efficiency is defined as the ratio of useful power over the injected power. In the present context the useful power is equal to P_{mech} whereas the injected power is equal to $C_{\mathcal{F}_t} \times \omega$, where $C_{\mathcal{F}_t}$ is the measured torque on the turbine shaft and ω is the angular velocity of the shaft. In the HEJET facility we do not measure $C_{\mathcal{F}_t}$. Neverthless, in steady state the injected power in the HEJET facility accounts to the measured evacuated power via the roots pump given by P_{roots}. Thus, we use measured evacuated power instead of injected power to estimate the efficiency. Therefore, the efficiency of the centrifugal pump is given by, $\eta(\%) = \frac{P_{mech}}{(C_{\mathcal{F}_t} \times \omega)} \times 100 = \frac{P_{mech}}{P_{roots}} \times 100$. Figure IV.16 shows $(\Delta P)_{pump}$ and the centrifugal pump efficiency with respect to the mass flow rate measured using venturimeter for three different temperatures. This figure shows that the efficiency of the centrifugal pump increases with the turbine frequency i.e. with increase in flow rate. As mentioned earlier, the contribution of natural losses are deducted from P_{roots} to estimate the efficiency of pump. We see that the data points representing the efficiency are more scattered because of the uncertainty associated with the estimation of P_{roots} (see figure IV.15). During all these measurements, the level of liquid helium in the saturated bath varies within h = 430 - 710mm (see figure IV.1 and figure IV.9). Ideally, the estimation of the P_{roots} must be performed while maintaining a constant level of helium in the saturated bath. We also observed that the "natural" losses in the experiment depend on the level of liquid helium in the saturated bath and also on its saturated pressure. This accounts for the uncertainty in the estimation of "natural" losses and hence the estimation of P_{roots}, especially at low $\mathcal{F}_t$ when the "natural" losses are comparable to the dissipated power from the HEJET facility. Therefore, ideally to resolve this uncertainty the "natural" losses must be estimated after each experimental measurement. But, this has not been feasible during the experiment. Thus, there is no simple way to put error bars on the estimated efficiency of the pump. Nevertheless, the maximum efficiency of the centrifugal pump of about 32% is obtained at the turbine frequency of 20Hz, which is close to the pump characteristics provided by the turbine designer (see figure IV.3 with $\eta \approx 30\%$ at a flow rate of $37\frac{g}{s}$ at $\mathcal{F}_t$ = 25Hz, as provided by the turbine designer in figure IV.3 the efficiency of the pump is estimated as $\eta(\%) = \frac{P_{mech}}{(C_{\mathcal{F}_t} \times \omega)} \times 100$).

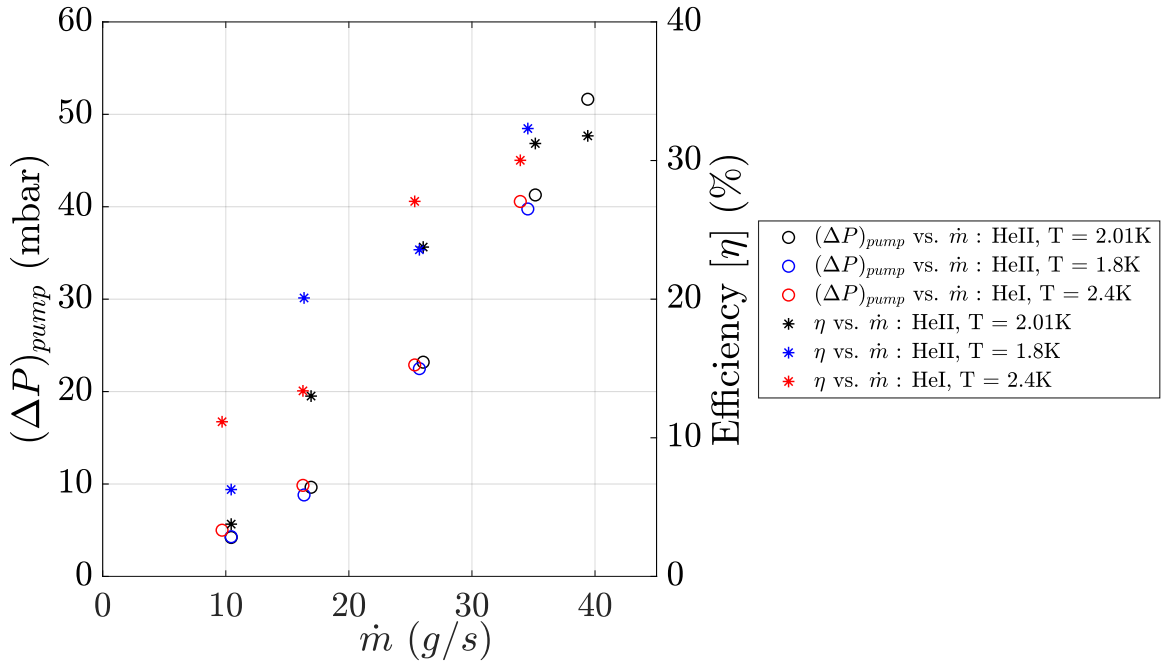

Figure IV.16: Pressure head across the pump and efficiency of the centrifugal pump with respect to mass flow rate at T = 1.8 - 2.4K

IV.3.1.8 Vibration analysis

The vibrations in the HEJET facility are induced by the rotation of the turbine within the centrifugal pump. Therefore, the entire experimental assembly and the subsequent measurements face those vibrations. The accelerometer measures the vibrations induced by the rotating components. Two of such accelerometers are installed in the HEJET facility, each one measures the vertical and radial component of vibration. The accelerometers Piezotronics PCB 351B41 are used with the sensor signal conditioner of model 482C series, having a sensitivity of $100\frac{mV}{g}$ which measures the vibrations within the frequency range of 1Hz to 2kHz. These accelerometers are mounted in the saturated helium bath at the location shown by No. 5 in figure IV.1.

Figure IV.17 shows the PSD of the raw accelerometer signal for the vertical and radial component, corresponding to the turbine frequency from 10Hz up to 25Hz in HeI at T = 2.4K. The PSD in figure IV.17a shows that the vibrations in the vertical direction induced by the centrifugal pump grow with increasing turbine frequency. From this figure we see that the frequency of vibration of the experiment in the vertical direction is about 675Hz irrespective of the turbine frequency. From figure IV.17b we see more dominant vibrations in the radial direction at $\mathcal{F}_t$ = 10Hz than at $\mathcal{F}_t$ = 15 and 20Hz, while the maximum occurs at $\mathcal{F}_t$ = 25Hz. Nevertheless, we see the same frequency of vibration in the radial direction at about 340Hz independent of the turbine frequency.

It is surprising that the frequency peaks in the PSD do not show any shift with respect to the turbine frequency. To investigate this further we have plotted the PSD of the accelerometers when the turbine is at rest as shown in figure IV.18 on the lin-log scale. The PSD in this figure shows the same frequency peaks at about 340Hz and 675Hz in the radial and vertical direction respectively at $\mathcal{F}_t$ = 0. This may suggest that these vibrations at $\mathcal{F}_t$ = 0 could be linked to the other appliances connected with the HEJET experiment such as the vacuum pump of the liquid nitrogen bath, roots vacuum pump of the saturated bath, ventilators or the solenoid valves used for filling of liquid nitrogen in the cryostat. Overall, this indicates that the vibrations in

figure IV.17 are induced by some other appliances in the HEJET facility and not only by the turbine itself. A thorough study can be performed for each appliance individually to detect the origin of these vibrations. From the PSD in figure IV.17 and figure IV.18 we see that when the turbine rotates the amplitude of vibrations in the HEJET facility increases by several orders of magnitude. The similar frequency of vibrations are also found while operating the centrifugal pump in HeII.

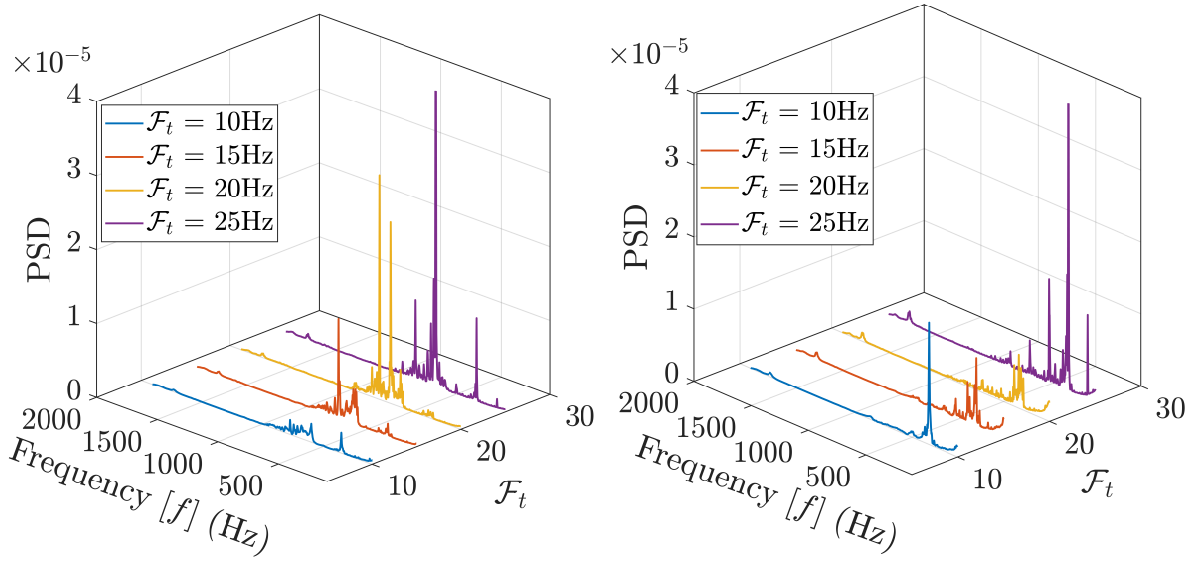

(a) For the vertical component (z) (b) For the radial component (r)

Figure IV.17: PSD of the accelerometer signal on lin-lin scale

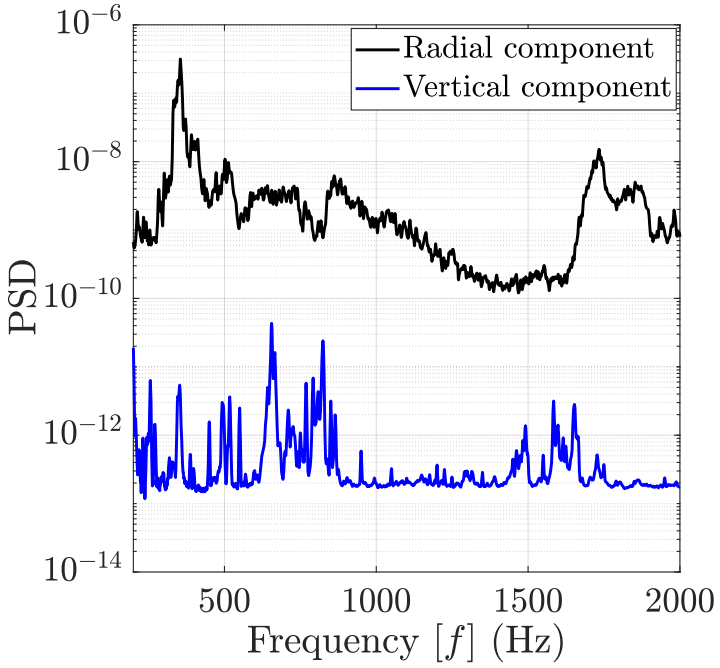

Figure IV.18: PSD of the accelerometer signal on lin-log scale at $\mathcal{F}_t = 0$

IV.3.2 Calibration of the hot-wire

To perform the calibration of the hot-wire in the HEJET experiment, a reference velocity is estimated using the measured flow rate from the venturimeter. As the flow rate in the closed circuit wind tunnel is constant, the velocity at any section can be estimated based on the cross-sectional area at that section. Hence, the nozzle exit velocity can be estimated using the volumetric flow rate from the venturimeter. Based on numerous studies performed over the development of the free jet in a stagnant environment, the velocity along the axis of the jet can be estimated using the relation given by [Pope, 2001]:

$$\frac{\langle U_{(z,r=0)} \rangle}{U_J} = B \frac{d}{(z - z_0)}, \tag{IV.8}$$

where U_J is the nozzle exit mean velocity at $z = 0$ which is estimated based on the volumetric flow rate given by $\dot{Q} = \frac{\pi d^2}{4} U_J$. $\langle U_{(z,r=0)} \rangle$ is the mean velocity at an axial distance of $z = 50d$ from the jet exit and at $r = 0$, which is also referred as the centerline velocity at a specific distance z. z_0 is the virtual origin of the jet which depends on the nozzle geometry and the experimental set-up. To measure the virtual origin z_0, it is necessary to know the jet half-angle in a particular experiment. For various turbulent jet flow studies in the past, the jet half-angle has been found to be within 7° to 20° [Horn and Thring, 1956]. For example, in the HEJET experiment with $d = 5$mm, assuming the jet half-angle of 13°, the virtual origin lies at $z_0 = 2.16d$ (which is about 4% of 50d). But, in the HEJET experiment to measure the jet half-angle, multiple hot-wires need to be installed across the jet at a particular location z and successful hot-wire measurements must be acquired for all these hot-wires. This is very difficult to achieve in the HEJET facility. Therefore, for simplicity z_0 is assumed to be equal to 0. B is the empirical constant whose value is assumed to be equal to 6, when $\frac{z}{d} \geq 50$ [Wygnanski and Fiedler, 1969; Rajaratnam, 1976; Antonia et al., 1982]. Figure IV.19 shows the calibration of the hot-wire in normal helium at T = 2.4K based on the equation IV.8. Very small mass flow rates ($< 10 \frac{g}{s}$) cannot be measured by venturimeter, hence equation IV.8 cannot be used at very low velocities (say lower than $0.4 \frac{m}{s}$). Therefore, to improve the calibration fit at small velocities, a data point corresponding to the natural convection (null velocity) is assigned to the lowest velocity (say $20 \frac{mm}{s}$). Figure IV.19 shows that the experimental data points satisfies the King's law of calibration very well.

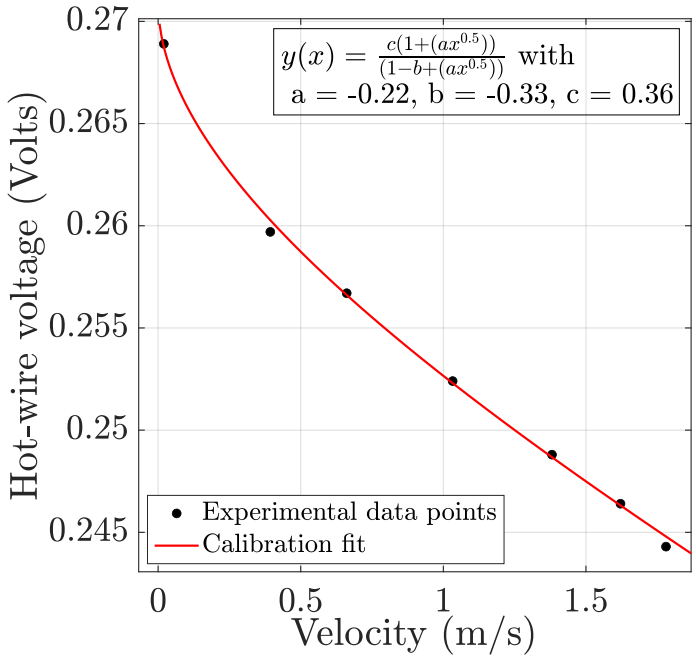

Figure IV.19: Hot-wire calibration in HeI at T = 2.4K using King's law fit in CCA mode (Hot-wire location: $\frac{z}{d} = 50$, $d = 5mm$, $d_w = 1.27\mu m$ and $l_w = 300\mu m$)

IV.3.3 PDF and compensated PSD

Figure IV.20 shows the PDFs of the raw hot-wire voltage in HeI at T = 2.4K corresponding to the turbine frequency $\mathcal{F}_t = 8$ up to 25Hz. This hot-wire is operated at an overheating of 35%. Although the PDF of hot-wire voltage need not be Gaussian, a dashed curve in this figure shows the Gaussian distribution just for comparison. All Gaussian distributions are obtained by using the mean and standard deviation of the corresponding experimental data. The hot-wire voltage to velocity conversion is performed based on the hot-wire calibration shown in figure IV.19. Figure IV.21 shows the PSD of the velocity signal in HeI at T = 2.4K at different turbine frequencies $\mathcal{F}_t = 8$ up to 25Hz. Figure IV.21a shows the PSD in the frequency domain in which no low-pass filtering of the velocity signal is performed. This figure shows peaks at the frequency $f \approx 600$ - 700Hz along with its harmonics which may be related to the vibrations in the HEJET facility (see section IV.3.1.8). From this figure we also see the $f^{-\frac{5}{3}}$ dependence in the PSD over almost one decade of frequency. We also note that the cut-off frequency of the hot-wire based on its finite time constant in the CCA mode lies within $f \approx 5-13$kHz based on the flow velocity (see section II.7). In fact, this cut-off frequency of the hot-wire in the HEJET experiment might even be less than 5kHz because the hot-wire is overheated at 35% (instead of about 18% in the SHREK experiment in which the time constant of the hot-wire is measured). This is an important aspect because the hot-wire in CCA mode incurs low-pass filtering effect due to its thermal inertia which has a major role particularly at high frequencies.

To observe the K41 prediction clearly (see equation I.10), we have plotted the compensated PSD according to K41 in the wavenumber domain as shown in figure IV.21b. The compensated PSD according to K41 is obtained after performing the empirical mode decomposition on the hot-wire signal as explained in the next section. The wavenumber $k = \frac{2\pi f}{\langle U \rangle}$ is estimated using the Taylor hypothesis as discussed in section I.6.2. The compensated PSD according to K41 is estimated by multiplying $E(k)$ with $k^{\frac{5}{3}}$ so that the inertial range appears as a horizontal line i.e. a plateau (see also figure I.5 for $E(k)$). A compensated PSD according to K41 is plotted

as a function of kL to notice the collapse of all the curves at low wavenumbers (i.e. at large scales) which shows the stationarity of large scales at different jet velocities. From this figure we see that the collapse of these curves at large scales is better at high turbine frequencies than at low turbine frequencies. We note that without the use of empirical mode decomposition these curves do not show any tendency to collapse at large scales. A vertical black-dashed line in figure IV.21b represents the spatial filter of the hot-wire at $l_w \approx 300\mu m$. Therefore, beyond $kL = 200$ the finite probe length acts as a spatial filter for the velocity fluctuations.

Following discussion is based on the simultaneous observation of figure IV.20 and figure IV.21b. As the hot-wire is operated in CCA mode, the higher hot-wire voltage represents smaller velocities and *vice versa*. Therefore, we see lowest hot-wire voltage in the PDF at $\mathcal{F}_t =$ 25Hz and highest hot-wire voltage in the PDF at $\mathcal{F}_t =$ 8Hz. From figure IV.20 we see that at $\mathcal{F}_t = 8$ and 10Hz the PDF shows two distinctive peaks (i.e. bimodal distribution) whereas at higher $\mathcal{F}_t$ the quality of PDF becomes "better" (i.e. uni-modal distribution). On the other hand, the compensated PSD in figure IV.21b shows a better $k^{-\frac{5}{3}}$ dependence (i.e. power law) over wider range of frequencies at lower $\mathcal{F}_t$ which becomes inadequate at higher $\mathcal{F}_t$. In turbulence experiments at sufficiently high Reynolds number flows such as in grid, atmospheric or open jet flows we generally observe a Gaussian distribution of velocity along with a reasonable plateau in the compensated K41 PSD. But the analysis performed in the HEJET experiment shows that these two aspects are independent from each other. Overall, we can conclude that in a turbulent flow a better "quality" of PDF (Gaussian or at least uni-modal) does not promise a good $k^{-\frac{5}{3}}$ dependence in the PSD and *vice versa*.

In fact, the effects observed in figure IV.20 and figure IV.21b are possibly due to the combination of too much overheating of the hot-wire and the jet instability. A deteriorating $k^{-\frac{5}{3}}$ dependence in figure IV.21b from $\mathcal{F}_t = 8$ to 25Hz suggests that the jet flow becomes more unstable at high $\mathcal{F}_t$ as compared to low $\mathcal{F}_t$. Although the jet is more stable at low $\mathcal{F}_t$ than at high $\mathcal{F}_t$, the natural convection of the hot-wire becomes dominant at low $\mathcal{F}_t$. At low $\mathcal{F}_t$, because of the instability of the jet it is likely that the hot-wire is off the jet for some time as a result of which the natural convection of the hot-wire becomes dominant. On the other hand, at high $\mathcal{F}_t$ even if the hot-wire is off the jet for some time there exists a finite velocity in the vicinity of the hot-wire because of which its natural convection is not dominant anymore. Therefore, in the PDF at low $\mathcal{F}_t$ the low voltage peak (high velocity) corresponds to the actual jet flow, whereas the high voltage peak (low velocity) corresponds to the natural convection of the hot-wire. As the velocity in the vicinity of the hot-wire gradually increases with $\mathcal{F}_t$, the high voltage peak in the PDF disappears.

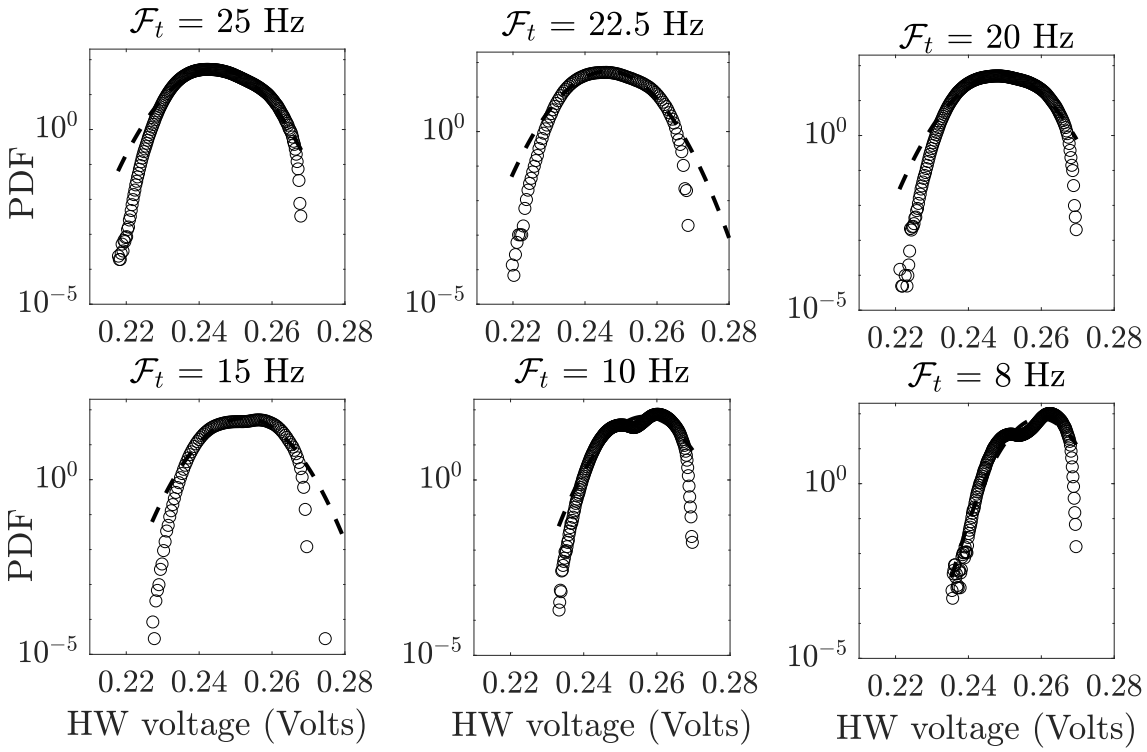

Figure IV.20: PDF of the raw hot-wire voltage in HeI at T = 2.4K (A dashed curve in each PDF shows a Gaussian distribution; HW voltage: hot-wire voltage; $\mathcal{F}_t$: turbine frequency)

In PSD at low k the instability of the jet flow induces fluctuations in the energy injected at large scales, and at smaller scales the hot-wire spatial resolution is not enough to measure fluctuations at high k. This explains the inadequacy of the compensated K41 PSD at high $\mathcal{F}_t$. The jet instability possibly originates from the re-circulation of fluid caused by the limited size of the experimental section and the Coanda effect generated due to non-uniformity in the experimental section [Voropayev et al., 2011]. Hence, to improve the jet stability future HEJET experiment will be performed using the nozzle diameter of 3mm instead of 5mm so as to minimize the effect of the confinement by the cylindrical wall surrounding the jet flow. Also, in the future HEJET experiment the hot-wire will be operated either in CTA mode or in CCA mode at much lower overheating to reduce the contribution of its natural convection.

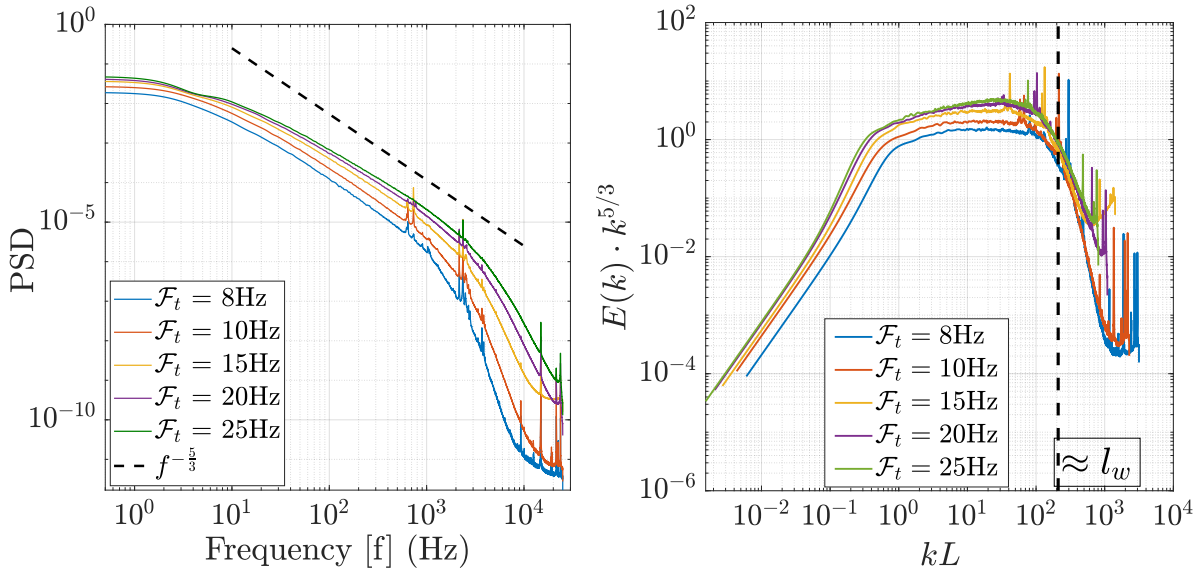

(a) PSD of the velocity signal in frequency domain with the K41 prediction $f^{-\frac{5}{3}}$

(b) Compensated PSD of the velocity signal in the wavenumber domain

Figure IV.21: PSD of the velocity signal at different turbine frequency $\mathcal{F}_t$ = 8 up to 25Hz

The above observations also lead to an important realization of the hot-wire measurements with a different perspective. The PDF of the hot-wire measurements such as in figure IV.20 at $\mathcal{F}_t$ = 8 and 10Hz gives a qualitative indication about the jet instability in terms of bi-modal distribution. Therefore, a sufficiently overheated hot-wire operated in the CCA mode can be used to detect the instability of the jet flow at small jet velocities. We note that the bi-modal distribution of the hot-wire signal is the consequence of the jet instability. And, we are able to detect this bi-modal distribution at low velocities only because the hot-wire is sufficiently overheated, thereby increasing its natural convection. In other words, in the same scenario of unstable jet, operating the hot-wire with less overheating might lead to the uni-modal distribution of the hot-wire signal. In this aspect one could install the hot-wires close to the wall in the HEJET facility which may give a qualitative indication about the jet interaction with the wall of the experimental section. This would also help to understand the jet instability at high jet velocities because at high $\mathcal{F}_t$ the natural convection of the hot-wire is less important on the axis of the jet.

IV.3.4 Empirical mode decomposition

The temporal velocity signal is converted into spatial increments with the use of Taylor hypothesis to perform further post-processing of data (see section I.6.2 for more details). After performing the hot-wire calibration, we found that the cumulative integral of the auto-correlation coefficient goes on increasing with respect to the scale. Figure IV.22a shows the cumulative integral of the auto-correlation coefficient with respect to scale r at the turbine frequency of 25Hz. From this figure we see that the cumulative integral never converges to an asymptotic value. Similar behavior is also observed at all the other turbine frequencies. We see that the value of the cumulative integral leads to nonphysical (or at least unrealistic) integral length scale. A similar plot of the cumulative time auto-correlation coefficient leads to an estimate of integral time scale of about 0.7s at about 20s as shown in figure IV.22b. From this figure we conclude that the typical time scale of the instability of the jet flow due to lateral confinement is about and maybe greater than 0.7s. From figure IV.22 we found that the estimation of the integral

scales is not straightforward in the HEJET experiment. The failure to reach an asymptotic value of the cumulative integral is linked with the jet instability at large scales (low frequencies). The aim of using empirical mode decomposition (EMD) is to separate long time instationarity from small scale spatial turbulent fluctuations [Huang et al., 1998].

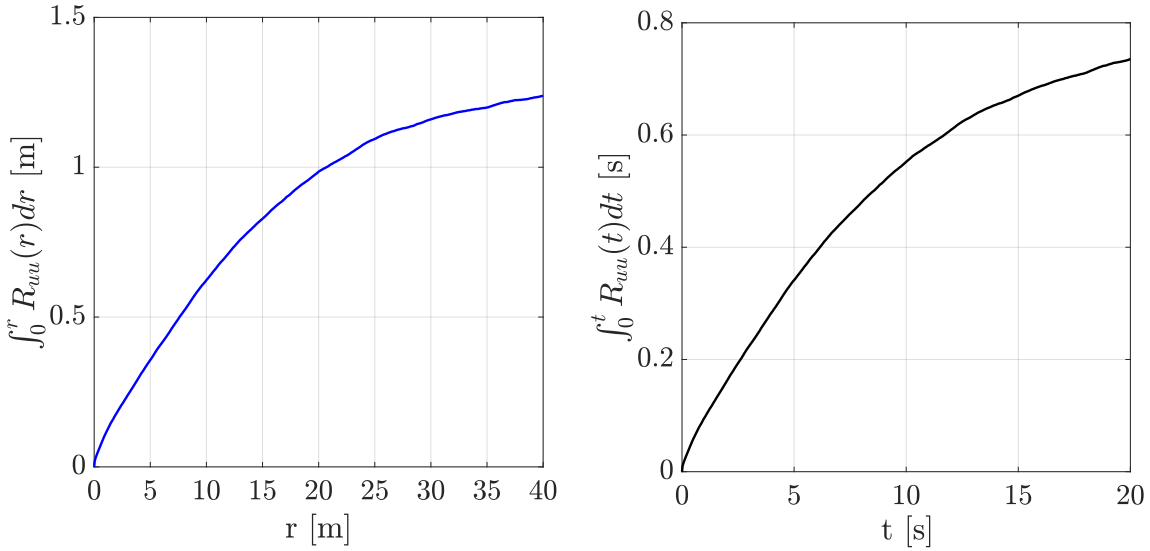

(a) Cumulative spatial auto-correlation function

(b) Cumulative temporal auto-correlation function

Figure IV.22: Cumulative integral of the auto-correlation coefficient of the velocity signal at $\mathcal{F}_t$ = 25Hz

Any turbulent hot-wire signal contains a certain range of frequencies with a definite amplitude associated with it. The idea of EMD is to break down the original signal into multiple functions each contributing to a set of frequencies and amplitudes, along with the residual of the signal. Such functions are known as intrinsic mode functions (IMFs). As the EMD is applied in the time domain, the IMFs and the residual have the same length of the original signal. The original velocity signal (U) in terms of the IMFs and the residual (R) can be written as:

$$U(t) = \sum_{i=1}^{n} IMF_i(t) + R(t). \tag{IV.9}$$

The EMD can be applied to either raw hot-wire voltage signal or to the velocity signal. The following demonstration of the EMD is shown for the velocity signal at $\mathcal{F}_t$ = 25Hz in normal helium. Figure IV.23 shows the decomposition of the velocity signal into its IMFs and residual with respect to time. The signal can be decomposed into the maximum number of IMFs, which depends on the availability of at least one maxima and minima in the last IMF. Here, the signal is decomposed into a maximum of 15 IMFs. Out of these 15, only IMF_1, IMF_5, IMF_{10} and IMF_{15} are shown in the following figure along with its residual. Just by visual inspection, we see how the frequency and the amplitude of the signal changes among the IMFs where IMF_1 shows the high frequency content and the IMF_{15} shows the low frequency content of the original velocity signal.

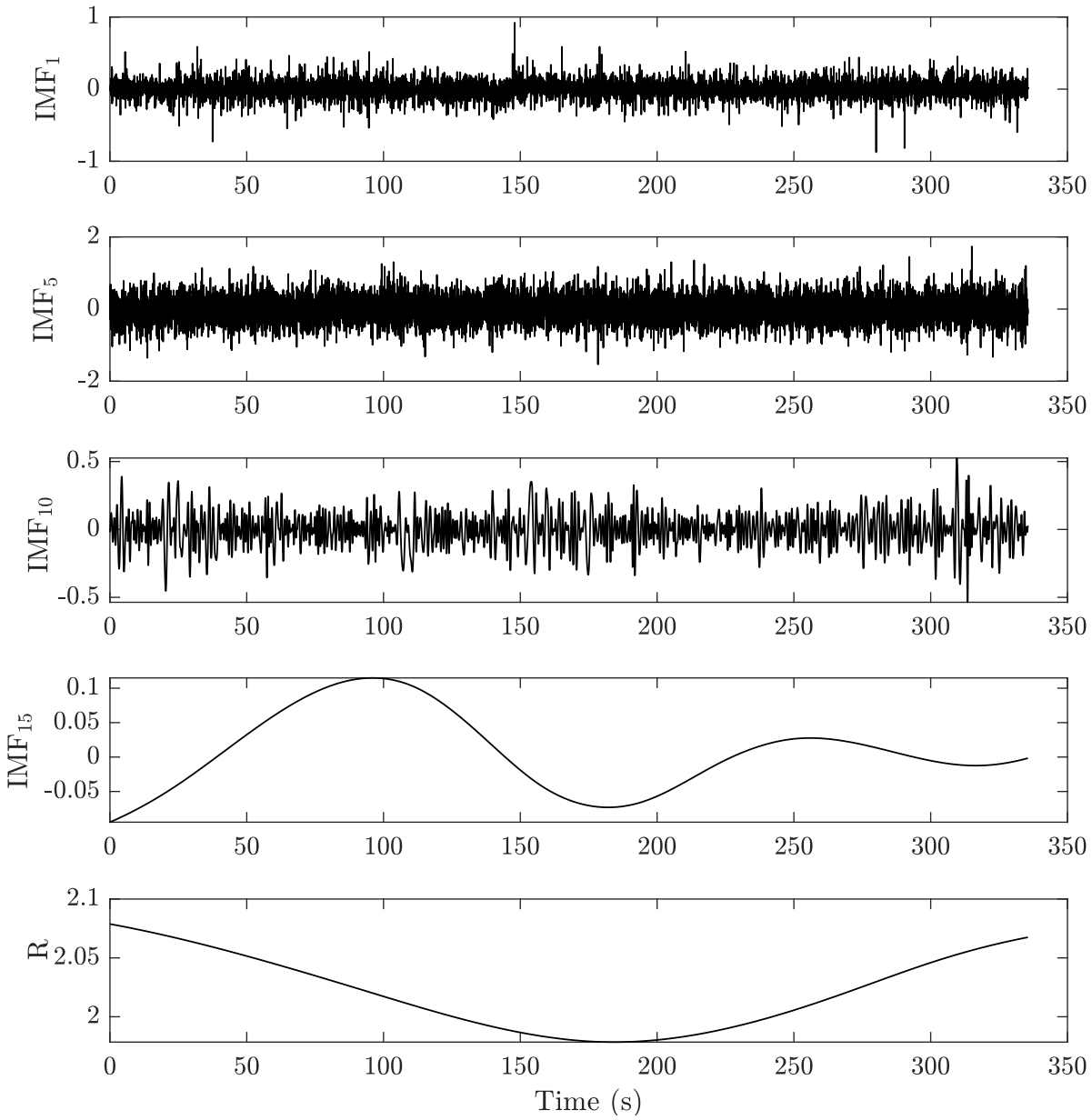

Figure IV.23: Intrinsic mode functions along with the residual of velocity signal with respect to time [out of 15 only 4 IMFs are shown here along with the residual]

To illustrate it further, the effects of the use of EMD can be easily visualized in the frequency domain using PSD. Figure IV.24 shows the PSD of the $\sum_{i=1}^{n} \text{IMF}_i$, for $n = 1$ to 15, along with the PSD of the original velocity signal. The first IMF act as a high-pass filter whereas all other IMFs acts as a band-pass filter [Rilling et al., 2005]. This figure shows that higher order IMFs contribute towards increasing the spectral content of the velocity signal. Or in other words, the higher order IMFs are related to the energy injection scale in the turbulent cascade. As expressed by equation IV.9, figure IV.24 shows that the original signal can be recovered by adding all the

IMFs where the PSD shown for the original data and $\sum_{i=1}^{n=15} \text{IMF}_i$ are always identical.

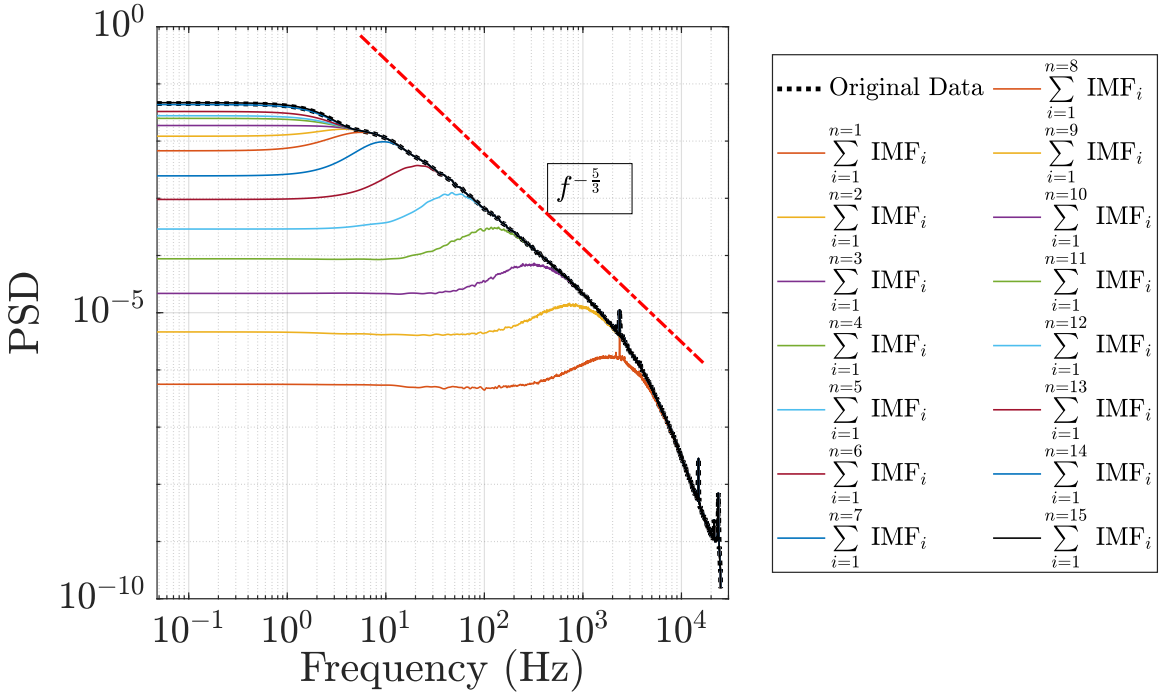

Figure IV.24: PSD showing the application of EMD on the velocity signal $\left[\sum_{i=1}^{n} \text{IMF}_i\right.$, for $n = 1$ to 15 from bottom to top; red dashed line shows the slope of $\left. f^{-\frac{5}{3}} \right]$

Similar to figure IV.22a, the cumulative integral of the auto-correlation coefficient can be plotted using different IMFs. Figure IV.25 shows the evolution of $\int_0^r R_{uu}(r)dr$ with respect to scale r using $\sum_{i=1}^{n} \text{IMF}_i$, for $n = 1$ to 15. This figure shows that the cumulative integral for the original data and the higher order IMFs diverges. Therefore, the suitable order IMFs must be chosen to express the best estimate of the integral length scale. To get the best estimate of the integral length scale at $\frac{z}{d} = 50$, the past literature discussing the free round jet flows has been referred. In a free round jet, the integral length scale increases while increasing the axial distance $\frac{z}{d}$ [Gervais et al., 2007; Burattini et al., 2005]. In the current experiment of HEJET, the hot-wire is installed at a fixed location of $\frac{z}{d} = 50$. At this location, the integral length scale has been found to be within $1.8d$ to $1.9d$ [Wygnanski and Fiedler, 1969; Burattini et al., 2005]. Hence according to figure IV.25, the best estimation of the integral length scale is given by either $\sum_{i=1}^{n=7} \text{IMF}_i$ or $\sum_{i=1}^{8} \text{IMF}_i$ or their average. A similar analysis using EMD is carried out for each of the velocity signals to perform the post-processing of the data.

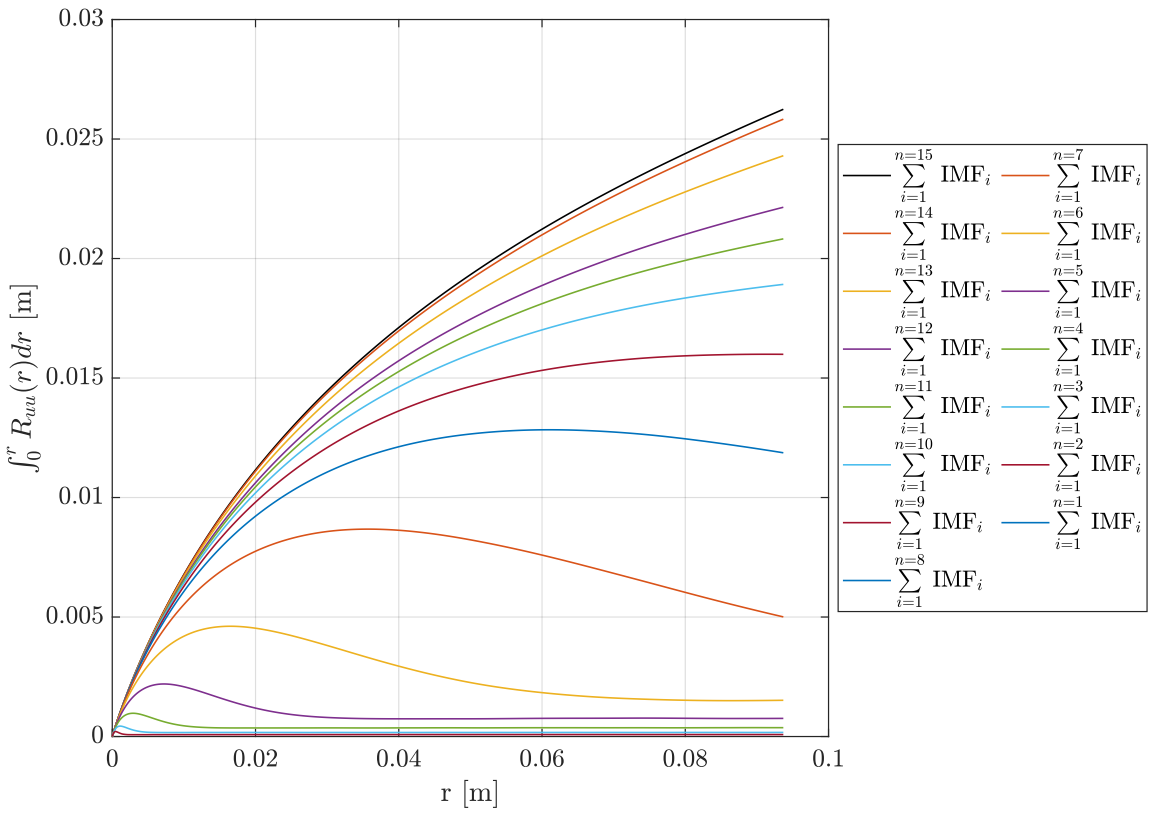

Figure IV.25: Cumulative integral of the auto-correlation coefficient with respect to scale r using EMD $\left[\sum_{i=1}^{n}\text{IMF}_i\right.$, from $n = 15$ to 1 from top to bottom$\left.\right]$

IV.3.5 Statistical analysis of the turbulent jet flow

To perform the hot-wire calibration, the turbine of the centrifugal pump is rotated in the range of 8Hz to 25Hz as shown in figure IV.19. To study the statistics of the jet flow, long acquisitions are performed at the turbine frequencies of 15, 20 and 25 Hz, each comprising of 8.38×10^7 samples using the acquisition frequency of 50kHz. The hot-wire can measure both positive and negative velocities but the problem lies in the fact that it cannot discriminate between positive and negative velocities. As the negative velocities cannot be estimated using the hot-wire calibration, the PDF shows significant low velocity cut-off [Salort et al., 2018]. The low velocity cut-off becomes more evident at $\mathcal{F}_t = 8$ and 10Hz. Because of this reason, the statistical analysis of helium jet at low $\mathcal{F}_t$ is not performed.

The PDF of the hot-wire voltage and the corresponding velocity is shown in figure IV.26. The PDFs in this figure are plotted after performing the EMD on the hot-wire signal and considering the first 7 IMFs i.e. $\sum_{i=1}^{n=7}\text{IMF}_i + R$. An electronic low-pass filter is applied on the velocity data at about 11kHz after performing the EMD. We note that the acquisition of the hot-wire data is performed using the National Instruments card PXI - 4462/4464 which includes an anti-alias filter at half the sampling frequency. The sampling frequency of 50kHz is used. A Gaussian distribution is also plotted along with the voltage/velocity PDF for easy comparison along with the value indicating the flatness (F) of the distribution. As the hot-wire is operated in the CCA mode, the hot-wire voltage drops with increase in the external velocity which can be seen in the PDF at high turbine frequency i.e. $\mathcal{F}_t = 25$Hz.

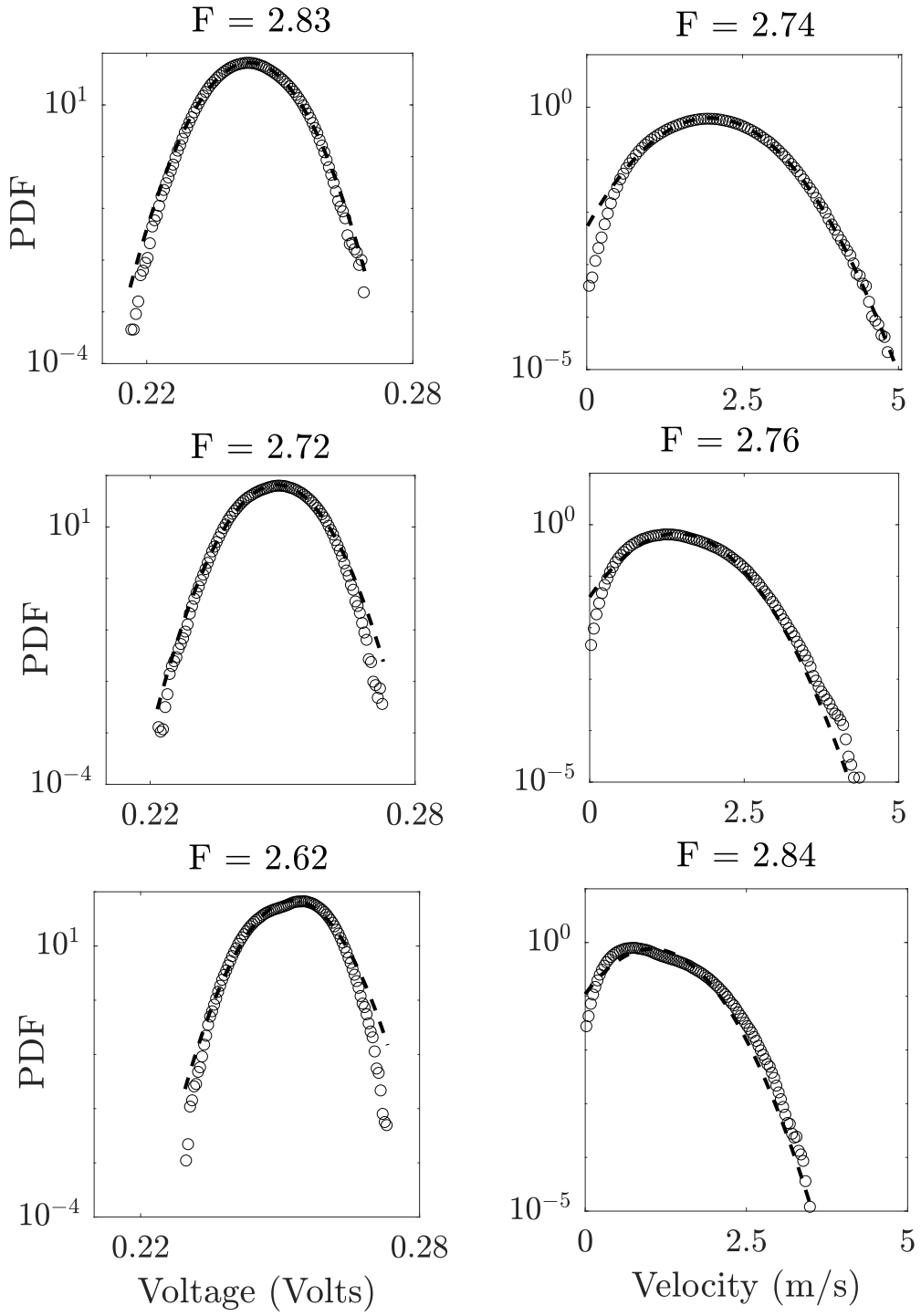

Figure IV.26: PDF of the hot-wire voltage and the calibrated velocity after performing EMD on the hot-wire signal using $\sum_{i=1}^{n=7} \mathrm{IMF}_i + R$ [From top to bottom: $\mathcal{F}_t$ = 25, 20 and 15Hz; F specify the flatness of the PDF; the dashed-line shows the Gaussian distribution in each plot]

The hot-wire voltage to velocity conversion is performed using King's law of calibration. Given that this calibration law is nonlinear, the PDFs of hot-wire voltage and velocity do not exhibit the same flatness. Typically, the turbulence intensity of a turbulent jet flow is about 30% at which the nonlinear effects of the hot-wire voltage to velocity conversion are not negligible. The turbulent jet flow in the HEJET experiment has high turbulent intensity ($\geq$ 35%) and thus the flatness of the PDF of the hot-wire voltage is not the same as the flatness of the PDF of velocity. Therefore, in CCA mode, the PDF of velocity can be seen to be flipped sideways compared to the PDF of the hot-wire voltage, but not linearly. From figure IV.26, we observed that at high turbine frequency of 25Hz, the PDF of voltage/velocity is much closer to the Gaussian distribution than at lower turbine frequency of 15Hz. And much closer Gaussian distribution of velocity may be expected at turbine frequencies more than 25Hz. Similar sub-Gaussian velocity PDFs in the circular jet flows has also been observed by Noullez et al. [1997] and Salort et al. [2018].

The main characteristics of the jet flow are given in table 5. All these statistical quantities are estimated based on the methods described in section I.6. This table shows the Reynolds number based on the nozzle diameter defined by $Re_d = \frac{U_J d}{\nu}$, which varies within 1.95 - 3.35 $\times 10^6$ for the nozzle exit velocity of 8.60 - 14.83$\frac{m}{s}$. In the round jet flow, in the far field i.e. $\frac{z}{d} \geq 30$, the turbulence intensity stays constant at a fixed inlet Reynolds number Re_d [Wygnanski and Fiedler, 1969; Burattini et al., 2005]. But, on the other hand, at a fixed axial location in the far field, the turbulence intensity shows dependence on the Re_d [Mi et al., 2013]. The same has been found out at $\frac{z}{d} = 50$, where the turbulence intensity is smaller for the high Re_d. Hence, a well documented value of 22 - 25% of turbulent intensity may be expected in the HEJET facility at turbine frequencies greater than 25Hz [Panchapakesan and Lumley, 1993; Hussein et al., 1994]. The turbulent intensity as high as 50% had also been reported in the confined jet turbulent flows by Chabaud [1992].

Table 5: Statistical quantities of the turbulent jet flow in HeI at T = 2.4K and P = 2.5bar

Turbine Frequency: ($\mathcal{F}_t$ Hz)	Nozzle exit velocity: U_J(m/s)	$Re_d = \frac{U_J d}{\nu}$	$U_{\frac{z}{d}=50}$ (m/s)	$\mathcal{I}$ (%)	L (mm)	ϵ (W/kg)	λ (μm)	η (μm)	Re_λ
15	8.60	1.95 $\times 10^6$	1.03	49	9.3	8.98	102	1.04	2450
20	11.50	2.59 $\times 10^6$	1.38	43	9.8	13.22	96	0.95	2640
25	14.83	3.35 $\times 10^6$	1.78	35	10.03	17.06	94	0.89	2860

In the turbulent jet flow, at a constant Re_d, the integral length scale grows as the jet develops downstream of the nozzle. But, the integral length scale shows no significant variation at a fixed axial location while varying the Re_d [Antonia et al., 2000]. Therefore, the estimation of the integral length scale shown in table 5 is consistent. Also, at lower Re_d Duri [2012] had found out $L = 15mm$, which was measured at $\frac{z}{d} = 60$.

The energy dissipation rate shown in table 5 is estimated based on the approach described in section I.6.7, from the third order structure function using the relation $\epsilon = -\frac{5}{4}\frac{S_3}{r}$. The compensated third order structure function in the HEJET facility is shown in figure IV.27 with respect to scale $\frac{r}{L}$ at $\mathcal{F}_t$ = 15, 20 and 25Hz. This figure also indicates the spatial low-pass filter cut-off scale due to the finite size (length of the hot-wire) of the hot-wire shown by a vertical black-dashed line corresponding to $l_w \approx 300\mu m$. As mentioned earlier, at small scales the hot-wire spatial resolution $\left(\frac{r}{L} \approx 0.03\right)$ is not enough to measure the statistics precisely, and the large scales fluctuations are affected by the jet instability. Because of this reason, figure IV.27 shows

no notable asymptotic value in the inertial range. Therefore, we rely on the maximum value in the inertial range to estimate the local dissipation rate in the HEJET experiment. From figure IV.27 we see higher dissipation rate at higher $\mathcal{F}_t$, as a consequence of higher injection of energy by the pump. At a constant Re_d i.e. at constant input forcing, the energy dissipation decreases with increase in axial distance $\frac{z}{d}$ because of the reduced inertial effects downstream the nozzle (turbulence decay) [Gervais et al., 2007]. The same effect can be seen at a fixed axial location while increasing the Re_d, which increases the energy dissipation as shown in table 5.

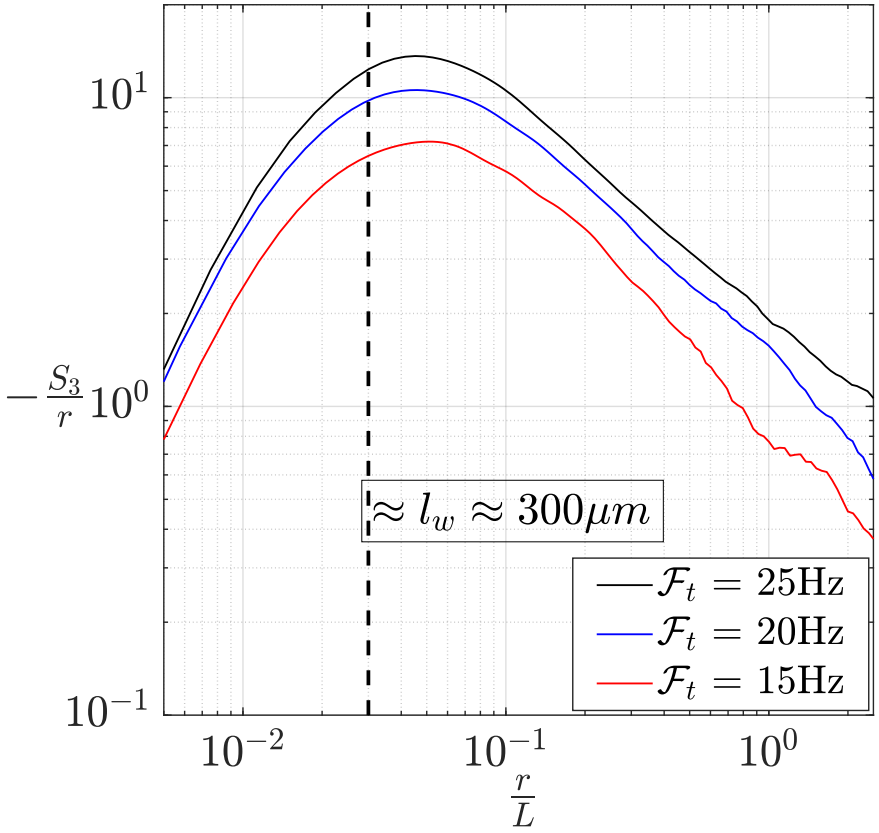

Figure IV.27: Estimation of the dissipation rate from the compensated third order structure function in the HEJET experiment

In the SHREK experiment, the estimated local dissipation rate ($\approx 2.6\frac{W}{kg}$, see section V.5 for more details) is very small as compared to the HEJET experiment ($\approx 17\frac{W}{kg}$). But, the volume within which this dissipation occur is very large in the SHREK experiment ($0.31m^3$ which contains 47kg of liquid helium) as compared to the HEJET experiment. In a free turbulent round jet flow, the dissipation mainly occurs within the turbulent jet surrounded by shear layer which separates the jet from the quiescent ambient fluid. Assuming the jet half angle of 13°, the volume of the turbulent jet accounts to about $932cm^3$ in the HEJET experiment, which contains around 0.14kg of liquid helium. Assuming homogeneous dissipation in the turbulent jet, at the turbine frequency of 25Hz the dissipated power sums up to about $P_d = 2.4$W. As mentioned earlier, the dissipation decays downstream the nozzle, hence the dissipated power given by 2.4W is very likely to be underestimated. Interestingly enough, from figure IV.15 we can see that at the turbine frequency of 25Hz the estimated P_{roots} (≈ 5W) lies within the same order of magnitude with respect to the dissipated power in the turbulent jet (P_d). Comparing the SHREK and HEJET experiment, we see that the dissipated power per unit volume is larger in the

HEJET experiment than in the SHREK experiment. But, in steady state the dissipated power in the SHREK experiment may reach as high as ≈ 300W whereas in the HEJET experiment it is ≈ 5W (see figure IV.15). This may explain the better thermal stability in the SHREK experiment (±0.1mK) than in the HEJET experiment (±10 - 15mK, see section IV.3.8).

Although, at a fixed axial distance the integral length scale has no particular dependence on the Re_d, the Taylor microscale and the Kolmogorov scale are found to be decreasing with increasing Re_d, as they are both linked to the mean energy dissipation rate [Antonia et al., 2000]. Taylor microscale is estimated from the dissipation rate using the relation given by $\lambda = \sqrt{\frac{15\nu u_{rms}^2}{\epsilon}}$ and Kolmogorov scale is estimated from the relation $\eta = \left[\frac{\nu^3}{\epsilon}\right]^{1/4}$ (see section I.6.8). Overall, comparing the Taylor and Kolmogorov scale with the SHREK experiment, we see that in the HEJET experiment λ is at least 3 times smaller and η is at least 10 times smaller than in SHREK. Also, the inertial range in the HEJET experiment is at least 10 times smaller than in SHREK. Referring to figure V.15, the ratio $\frac{L}{\lambda} \approx 90-106$ for the range of Re_λ shown in table 5 is found to be consistent. The Re_λ has a dependence on Re_d which is given by, $Re_\lambda \approx C_J \times \sqrt{Re_d}$, which indicates the increase in Re_λ with respect to increase in Re_d at a fixed location using a proportionality constant C_J [Mi et al., 2013]. Experimentally, the value of the constant C_J has found to be within 1.04 - 1.74 [Champagne, 1978; Antonia et al., 1980]. In the HEJET facility, for the current estimate of Re_λ we found the value of $C_J = 1.65$ which is in agreement with the past studies.

IV.3.6 Intermittency

The intermittency in the HEJET experiment is studied in a similar way as in the SHREK experiment. A more detailed discussion on the phenomenon of intermittency in turbulent flows is done in Chapter V and VI using the SHREK experimental data. The discussion presented in this section is limited because of the small amount of data in the HEJET experiment[§]. We recall that a numeric low-pass filter at about 11kHz is used on the velocity signal to eliminate spurious high frequency peaks in the PSD which are possibly caused by the vibrations. Figure IV.28 shows the PDFs of velocity increments at the scales from 450η up to 11240η along with the typical Gaussian distribution at large scales for the turbulent jet flow generated at the turbine frequency of 25Hz. This figure shows that like any other turbulent flow, helium jet flow also shows the phenomenon of intermittency. The intermittency in turbulent flows is characterized by the long and exponential tails of the PDFs of the velocity increments towards smaller scales. Figure IV.28 shows the intermittency as the PDFs evolve along scales. Indeed, the quantification of intermittency may be done with the help of flatness and skewness of the PDFs of velocity increments as shown in figure IV.29. A vertical black-dashed-dotted line indicates the spatial filter of the hot-wire at $l_w \approx 300\mu m$. The PDF of velocity increments and its flatness and skewness are plotted for the scales $> l_w$. This figure shows that the flatness and the skewness increases and decreases towards smaller scales respectively. At large scales Gaussian distribution of the PDFs of velocity increment is depicted by the constant value of flatness = 3 and skewness = 0 which is found to be slightly sub-Gaussian as shown in figure IV.29.

The universal slope of -0.1 which describes the dependence of flatness of the PDFs of velocity increments on scale is found to be valid for a very small range of scales below the energy injection scale. From this figure we can observe that with increase in turbine frequency the flatness of the PDFs of velocity increment shows more inclination towards the universal slope of -0.1. It is suspected that this might be linked with the jet instability.

[§]Although the reader can read this section without any discontinuity, it is recommended to read this section after Chapter V and VI where all the definitions/notions are introduced

As the spatial resolution of the hot-wire is the same we can compare the flatness of PDFs of the velocity increments at the scale $\approx l_w$ in the HEJET and SHREK experiment (see figure IV.29a and figure V.17). From these figures we can see that at scale $\approx l_w$ in the SHREK experiment the flatness is higher than in the HEJET experiment. This is not so surprising because in the SHREK experiment l_w ($\approx \lambda$) lies close to the end of inertial range whereas in the HEJET experiment l_w is at least three times higher than Taylor microscale. This suggests that the intermittency at a fixed scale (say $\approx l_w$) is different based on the type of turbulent flow (such as jet flows, von Kármán flow or grid turbulence flow) and the position of such scale within the inertial range.

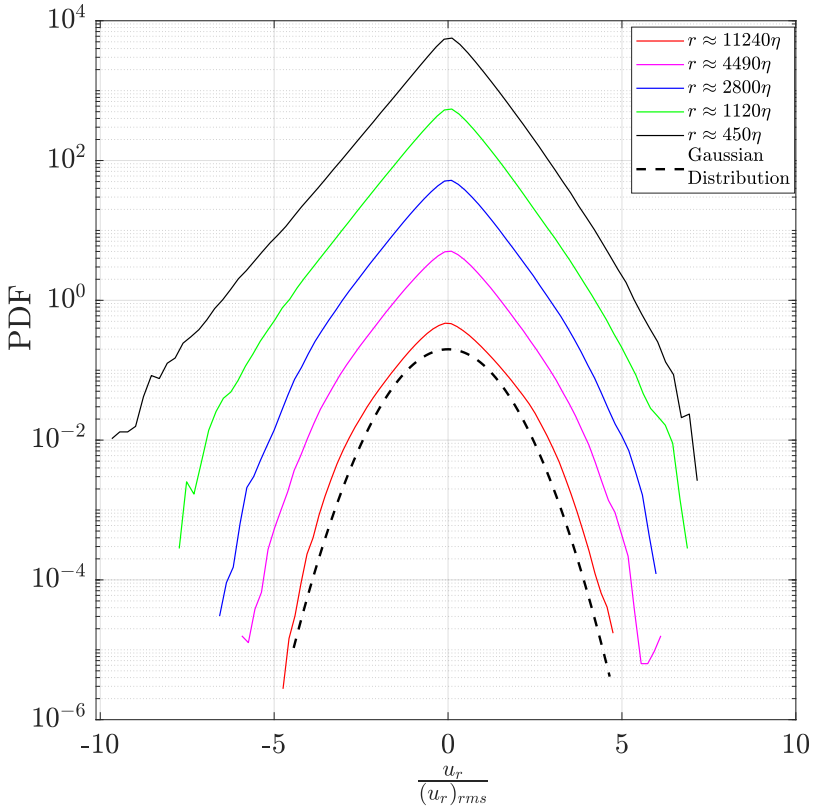

Figure IV.28: Demonstration of the phenomenon of intermittency in the HEJET experiment using the PDFs of velocity increments at different scales for $Re_\lambda = 2860$ (the curves are arbitrarily shifted for the better visualization)

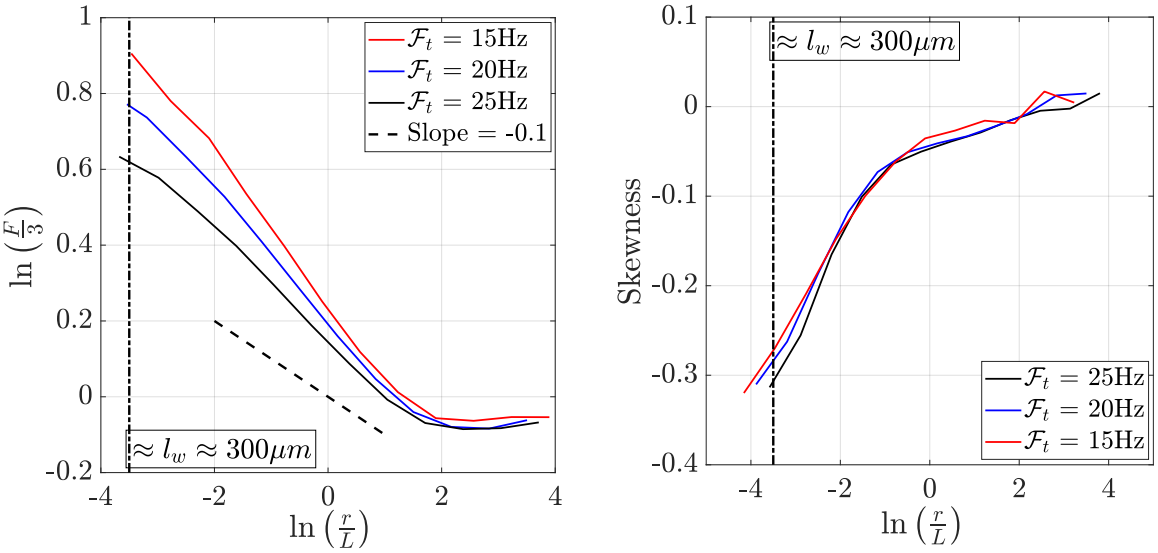

(a) Flatness with respect to scale $\frac{r}{L}$

(b) Skewness with respect to scale $\frac{r}{L}$

Figure IV.29: Quantification of intermittency using flatness and skewness of the PDFs of velocity increment at $\mathcal{F}_t$ = 15, 20 and 25Hz

Figure IV.30a shows structure functions of order $p = 2$ to 8 in the HEJET experiment at $\mathcal{F}_t$ = 25Hz. Figure IV.30a shows constant asymptotic value of the structure functions at large scales and power law in the inertial range. The scaling exponents ζ_p of the p^{th} order structure function are estimated based on the extended self similarity (ESS). Figure IV.30b shows the p^{th} order ζ_p up to the order 8 for the jet flows of $Re_\lambda = 2450$ and 2860. K41 and well known intermittency models such as Beta and Log-Poisson model are also plotted for the comparison. This figure shows that ζ_p increases with increase in Re_λ, which also supports the discussion followed in section V.9.3. Using these experimentally estimated scaling exponents, K62 intermittency parameter μ is found to be 0.21 for $Re_\lambda = 2450$ and 0.19 for $Re_\lambda = 2860$. Such a decreasing trend of intermittency parameter μ with respect to Re_λ is also observed in the SHREK experiment over a very wide range of Re_λ. Comparing K62 intermittency parameter μ in the HEJET experiment with the SHREK experiment (see figure V.28) $\mu = 0.21 - 0.19$ in the HEJET experiment is consistent with the co-rotation configuration of von Kármán flow over the range of Re_λ within 2450 to 2860. For asserting a power law and to estimate a power law exponent one needs an inertial range to exist. The inertial range in the HEJET experiment is comparatively smaller than in the SHREK experiment and in most experimental turbulent flows. In addition, it is an open question whether the jet instability has any effect on the analysis of intermittency performed in this section. To answer this question, as mentioned before, future HEJET experiments will be performed in order to improve the jet stability.

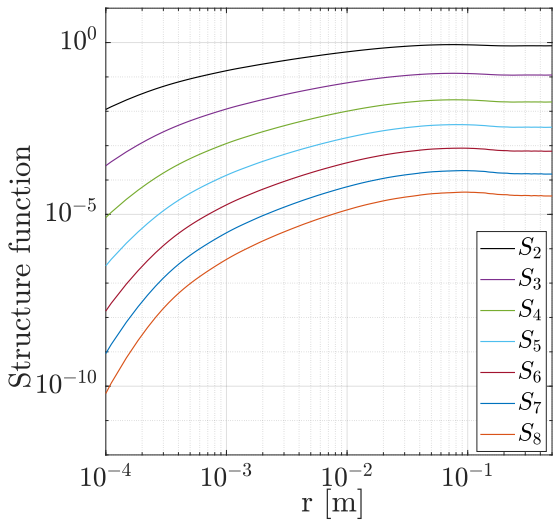

(a) Structure functions of order 2 to 8 in the HEJET facility at $\mathcal{F}_t$ = 25Hz (For clarity the curves are arbitrarily shifted in the vertical direction and odd order structure functions are estimated using absolute values of the velocity increments.)

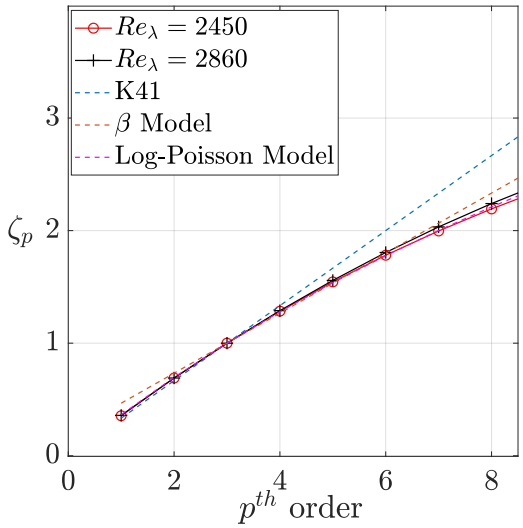

(b) Different intermittency models showing the scaling exponent ζ_p along with the experimentally estimated values using ESS for the turbulent jet flow at Re_λ = 2450 and 2860

Figure IV.30: Structure functions and its scaling exponents up to order p = 8 in the HEJET experiment

The accuracy of estimated scaling exponents can be assessed by plotting the compensated structure functions with respect to scale r. Figure IV.31 shows the structure functions of order p = 2 to 7 compensated by $r^{-\zeta_p}$ with respect to scale r at Re_λ = 2860. In this figure, we expect that the structure functions show a plateau in the inertial range (see equation I.11). In fact, in figure IV.31 we observe a plateau over a small range of scales in the inertial range. But, the quality and width of this plateau becomes poorer towards higher order structure functions. We believe that the presence of small inertial range is mainly caused by the large scale instationarity of the turbulent jet flow in the HEJET experiment and also because of the limited spatial and temporal resolution of the hot-wire. On the other hand, the deteriorating "quality" of the plateau towards higher order structure functions is also related with the limited statistical convergence.

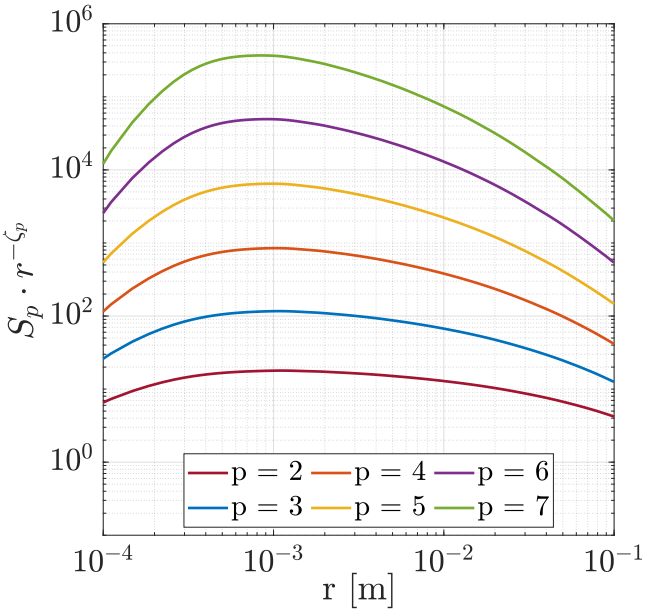

Figure IV.31: Compensated structure functions with respect to scale r [For clarity the compensated structure functions are arbitrarily shifted in the vertical direction]

An approach of Fokker-Planck equation[¶] is explored to describe the turbulent cascade in the HEJET experiment. Markovian property within the turbulent cascade is essential in order to use Fokker-Planck equation. While doing the analysis, it is found that the Markovian property does not hold for the turbulent velocity data. It is suspected that this may have occurred because of the jet instability at large scales. Therefore, the Fokker-Planck analysis of the turbulent jet flow could not be performed. Nevertheless, we expect a good quality of data from the future HEJET experiments and accordingly the Fokker-Planck analysis will be performed.

IV.3.7 Observations in HeII

In the HEJET experiment, we could not perform a successful hot-wire calibration in HeII because of the lack of thermal stability (see section IV.3.8). Because of this reason Taylor hypothesis could not be applied, therefore the PSD in this section are discussed with respect to frequency instead of wavenumber. Also, the PSD in this section are shown at finite turbine frequencies and at $\mathcal{F}_t = 0$ at which wavenumber cannot be defined. Figure IV.32 shows the PSD of the raw hot-wire signal in the turbulent jet flow generated by varying the turbine frequency in the HEJET facility at various superfluid temperatures. The hot-wire details and its location are the same as in HeI. The hot-wire is operated in CCA mode at I = 15.44mA at the pressurized helium bath temperatures of T = 1.77K up to 2.11K and at I = 10.83 mA for the normal helium at T = 2.33K. In fact, in both HeI and HeII the hot-wire is operated at the constant overheating of 35%.

Figure IV.32a to IV.32c show the PSD of the raw hot-wire voltage for varying turbine frequency at T = 1.9, 2.0 and 2.1K respectively. At $\mathcal{F}_t = 0$Hz, these figures show the PSD of the counterflow turbulence of hot-wire itself. At $\mathcal{F}_t > 0$Hz the hot-wire response is the superposition of external flow on the counterflow turbulence of the hot-wire itself. These figures show how the PSD of the hot-wire evolves with respect to the external turbulent flow from $\mathcal{F}_t = 5$ to 25Hz. One of the main observations of this figure suggests that there is absolutely no influence of the

[¶]This approach is extensively discussed and applied to the SHREK experimental data as described in Chapter VI.

external flow on the frequency content of the spectrum higher than ≈ 3kHz. This means that the velocity fluctuations of the external flow are not being measured over such high frequencies by the hot-wire. Or in other words, the counterflow turbulence generated by the hot-wire contains the largest part of frequencies $f \geq 3$kHz. We also note that the cut-off frequency of the hot-wire in CCA mode lies within $f \approx 5$ - 13kHz which causes an attenuation of the hot-wire signal at high frequencies. It is observed that at frequencies $f \geq 3$kHz the spectrum shows the slope of ≈ -3.5 on log-log plot. This slope also depends on the overheating of the hot-wire as shown in figure III.22. Nevertheless, at frequencies $f \leq 3$kHz the PSD shows a clear dependence on the increase in turbine frequency. This gives an important indication that the power spectrum is evolving and getting closer towards the classical $f^{-\frac{5}{3}}$ slope. The same effect is also observed at T = 2.0K as shown in figure IV.32b. Based on the PSD in figure IV.32a and figure IV.32b, we can expect to observe the classical $f^{-\frac{5}{3}}$ slope at even higher turbine frequencies (say ≈ 35Hz) at this particular overheating of the hot-wire. But, in the present work no $f^{-\frac{5}{3}}$ dependence in the PSD is seen at T = 1.9K or T = 2.0K in the HEJET facility.

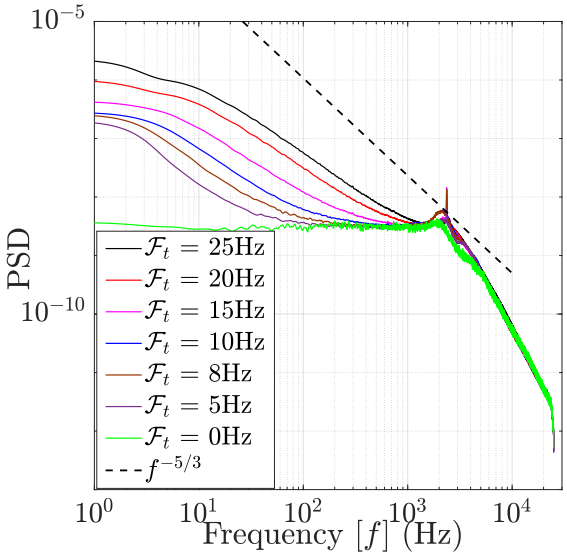

(a) At T = 1.9K

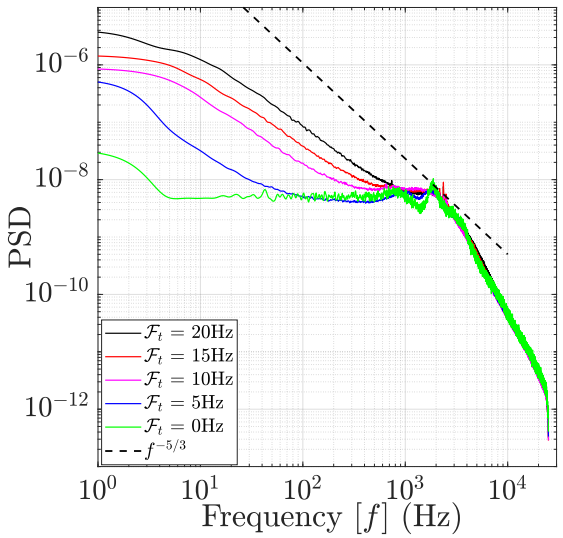

(b) At T = 2.0K

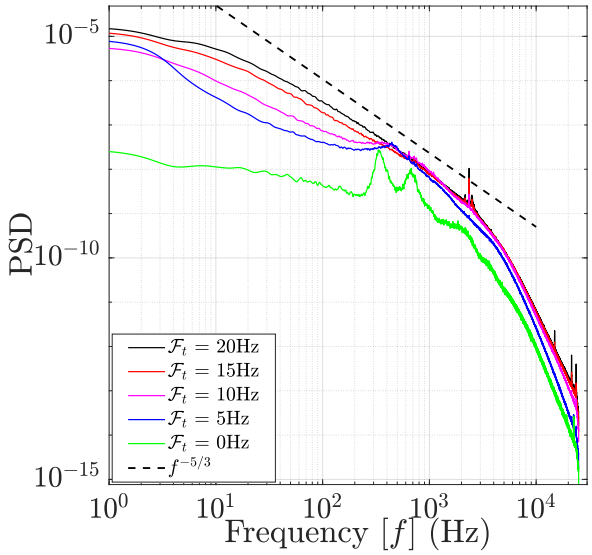

(c) At T = 2.1K

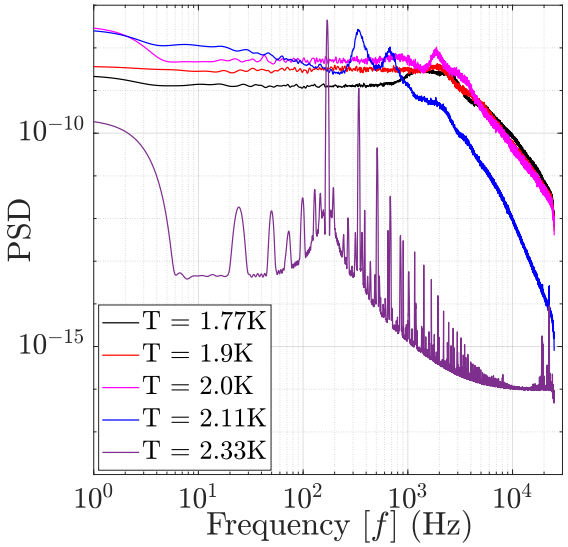

(d) PSD at null velocity at different bath temperatures in HeI and HeII

Figure IV.32: PSD of the raw hot-wire signal at different turbine frequency in the HEJET facility at various pressurized bath temperature using CCA mode [$d_w = 1.27\mu m$ and $l_w = 300\mu m$]

Figure IV.32c shows that at the bath temperature of T = 2.1K and at the turbine frequency of 20Hz we have attained the slope of PSD which is same as that to the classical $f^{-\frac{5}{3}}$ slope. Also at the bath temperature of T = 2.1K, the counterflow turbulence of the hot-wire itself is comparatively less dominant than at T = 1.9K possibly because of the less $\frac{\rho_s}{\rho}$ (see figure I.2). Therefore, the external flow is measured accurately by the hot-wire at higher turbine frequencies. Figure IV.32d shows the evolution of the counterflow turbulence of the hot-wire in perspective of the PSD at various bath temperatures from 1.77K to 2.11K at the same overheating of 35%. This figure shows that PSD of the counterflow turbulence at T = 1.77, 1.9 and 2.0K are comparatively similar for frequencies $f \geq 3$kHz. The PSD at T = 2.33K in figure IV.32d show the similar peak as discussed in figure III.22c which is associated with the natural convection in HeI. Similar observations are also reported by Diribarne et al. [2021b].

Therefore, to measure the external flow precisely, the extent of counterflow turbulence generated by the hot-wire should be kept as minimum as possible. In other words this suggests that to measure the external flow accurately in HeII the counterflow turbulence of the hot-wire must be compensated. This can be done using either of the following three strategies. This includes operating the hot-wire at the least possible overheating (yet a sufficient signal to noise ratio), increasing the velocity fluctuations (u_{rms}) of the external flow or by simply increasing the pressurized helium bath temperature towards T_λ (hence decreasing the percentage of superfluid in the external flow). Overall, figure IV.32 indicates that with increase in u_{rms} the PSD of hot-wire signal shows stronger inclination towards the classical $f^{-\frac{5}{3}}$ slope which has been observed in the HEJET facility.

IV.3.8 Importance of thermal stability

The thermal stability of the SHREK experiment is about ±0.1mK. This means that while performing the SHREK experiment at 2.0K the temperature within the experimental region fluctuates around 2.0K ± 0.1mK. Therefore, the thermal stability in the SHREK experiment

is very well controlled. Similarly, from the experimental measurements it is found that the thermal stability of the HEJET experiment is about $\pm 10 - 15$mK. Although this does not pose any serious problem for the hot-wire measurements in HeI, it has significant effects in the HeII (because of the better thermal conductivity of the superfluid). The hot-wire in superfluid is very sensitive to the change in bath temperature as this evolves the counterflow turbulence around the hot-wire. To understand this further, the sensitivity of the hot-wire with respect to the change in bath temperature (HeII) is measured at null velocity. The hot-wire measurements are performed while increasing the pressurized helium bath temperature from 1.9K to 2.05K in the HEJET facility as shown in figure IV.33 for the hot-wire of $d_w = 1.27\mu m$ and $l_w = 300\mu m$. From this figure, the sensitivity of the hot-wire is found to be about $14\frac{\Omega}{K}$. This corresponds to the change in hot-wire voltage of ± 3.2mV for a bath temperature change of ± 15mK. This is significant considering the whole dynamic range of the hot-wire voltage ($\approx$ 20 - 30mV) during calibration. This change is totally attributed to the pure counterflow turbulence of the hot-wire itself. Similarly, the sensitivity of the hot-wire of $d_w = 0.5\mu m$ and $l_w = 300\mu m$ is found to be about $95\frac{\Omega}{K}$. Because of this reason no successful calibration of the hot-wire in superfluid could be performed in the HEJET facility[‖].

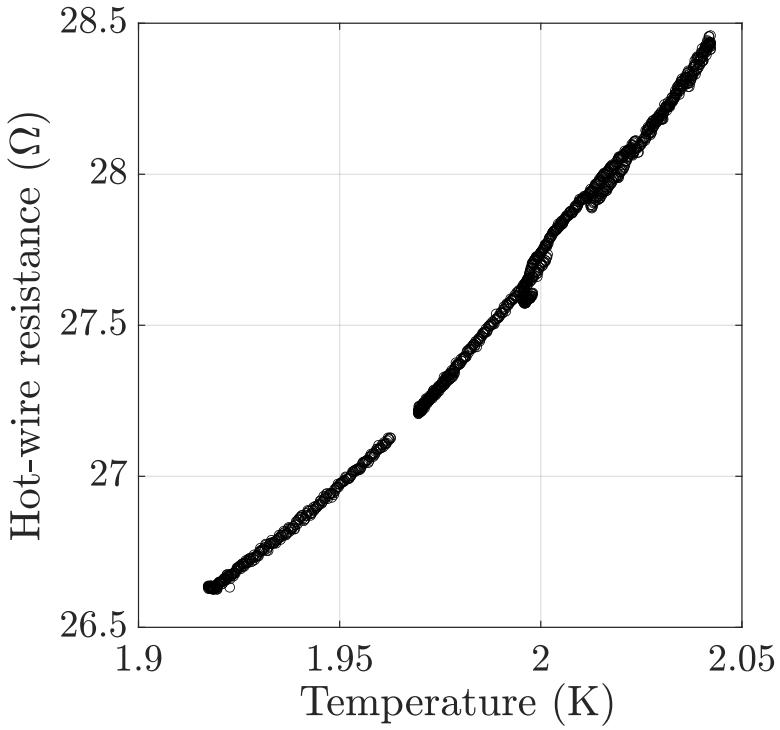

Figure IV.33: Change in the hot-wire resistance with respect to the increasing pressurized helium bath temperature in the HEJET facility at null velocity [$d_w = 1.27\mu m$ and $l_w = 300\mu m$; the hot-wire is operated at 35% overheating]

[‖]In CCA mode the hot-wire voltage decreases with increase in the external flow velocity. But to perform the hot-wire calibration in superfluid the experimental data points are found to be scattered because of the lack of sufficient thermal stability in the HEJET facility. Also, in the present work while operating the HEJET facility at T = 1.9K and T = 2.0K the $f^{-\frac{5}{3}}$ decay in the inertial range is never observed.

IV.4 Conclusion

In this chapter a detailed procedure to operate the HEJET facility at cryogenic temperatures is explained. The experimental set-up of the HEJET facility is shown along with the turbine assembly of the newly designed centrifugal pump. Based on the system characteristics and the new pump characteristics, operating points for the HEJET facility are obtained. The characterization of the newly designed centrifugal pump is performed in HeI and HeII in view of the dependence of its pressure head, flow rate and mechanical power output with respect to the operating turbine frequency. From the measurements of the differential pressure, it is found that the flow rate, pressure head and the mechanical power output of the centrifugal pump have a linear, quadratic and cubic dependence on the operating turbine frequency respectively, which shows the proper functioning of the pump. Using this facility it is possible to generate the mass flow rate of 10 - 45$\frac{g}{s}$ in the closed circuit wind tunnel using the nozzle diameter of $d = 5mm$ at the operating temperature range of 1.8 - 2.4K. The maximum cooling capacity of the cryostat used in the HEJET facility is found to be about 5W while operating this facility at T = 1.8 - 2.4K. The efficiency of the centrifugal pump is found to be increasing with increase in flow rate. Experimentally, a maximum pump efficiency of 32% at the turbine frequency of 20Hz is obtained, which agrees well with the pump characteristics provided by the pump designer. Four different methods to estimate the flow rate in the HEJET closed circuit are shown and we confirm that the venturimeter provides an accurate estimation of the flow rate. The vibration analysis of the HEJET assembly is performed in HeI and HeII using accelerometers which show the vibrations of the HEJET facility at the frequency of 675Hz and 340Hz in the vertical and radial direction respectively. We find that the vibrations at these frequencies are mainly originating from some other appliances connected to HEJET facility, in addition to the vibrations caused by the turbine itself. Essentially, the new centrifugal pump has been designed in order to achieve high efficiency and better jet flow stability. Although, with the new pump we have managed to attain high efficiency, the present measurements of the hot-wire indicate that the jet instability still exists which is most probably linked to the confinement and dissymmetry of the cylindrical experimental chamber.

The calibration of the hot-wire is performed using King's law of calibration in HeI at T = 2.4K. The empirical mode decomposition is used to eliminate the large scale instationarity in the velocity signal which is believed to be the consequence of the jet instability. The statistical analysis of cryogenic turbulent jet is performed at the turbine frequencies of 15, 20 and 25Hz. Because of the combined effects of jet instability and natural convection of the hot-wire a bimodal PDF of hot-wire voltage is observed at low turbine frequencies whereas at high turbine frequencies typical unimodal PDF is observed. On the other hand, the compensated PSD of velocity signal shows a "deteriorating" Kolmogorov spectrum at higher turbine frequencies possibly because of the jet instability. We conclude that in the turbulent flow a Gaussian distribution of velocity does not promise a rigorous Kolmogorov spectrum and *vice versa*. The PDFs of the velocity are found to be sub-Gaussian with much closer Gaussian distribution at higher flow rates. The present study of the turbulent jet flow represents Re_λ of 2449 - 2861 which is found out to be $\approx 1.65\sqrt{Re_d}$. The integral length scale, Taylor microscale and Kolmogorov scale is found to be $\approx 1.9d$, $\approx 100\mu m$ and $\approx 1\mu m$ respectively. The local energy dissipation is found to be increasing with increase in input forcing. The dissipated power within the turbulent jet estimated from the hot-wire is found to be reasonably coherent with the total power consumption of the cryostat. The phenomenon of intermittency in the turbulent jet flow is studied. We confirm the presence of intermittency in unstable turbulent jet flows. The PDFs of velocity increments show an increase of deviations from Gaussianity towards smaller scales. The flatness and the skweness of these PDFs of velocity increments is found to be increasing and decreasing towards

smaller scales respectively. In fact, we noticed that the flatness grows rapidly towards small scales in the unstable turbulent jet flows.

The hot-wire response is investigated based on the observations in HeII at T = 1.9, 2.0 and 2.1K. The sensitivity of the hot-wire of $d_w = 1.27\mu m$ and $d_w = 0.5\mu m$ is found to be about $14\frac{\Omega}{K}$ and $95\frac{\Omega}{K}$ respectively in CCA mode at an overheating of 35%. From PSD, we observed that the counterflow turbulence of the hot-wire depends on the surrounding temperature which shows that the peak in the PSD shifts towards higher frequency at lower temperatures. The hot-wire response to the external flow in HeII shows that the PSD evolves with increase in turbine frequency, which indicates the inclination towards the classical $f^{-\frac{5}{3}}$ slope. Therefore, at high turbine frequencies in HeII we may expect a Kolmogorov spectrum in the inertial range.

Essentially, all cryogenic jet flows are confined jet flows where the size of the experimental section/cylinder is limited by the dimensions of the cryostat. During the past several HEJET experiments we have learned that the jet instability is of major concern especially at high turbine frequencies. Because of the confinement and non-uniformity of the experimental section there is a possibility that the cryogenic jet interacts with the wall. Considering the limited size of the cryostat, to improve the jet stability we propose to perform future HEJET experiments in the coming months using the nozzle of diameter 3mm instead of 5mm. Therefore, while reducing the size of jet we may expect lesser interaction of the jet with the wall. In addition, in the future HEJET experiments, to reduce the effects of the natural convection of hot-wire at low turbine frequencies the hot-wire will be operated either in CCA mode with low overheating or in CTA mode. Thus, applying these strategies in the future HEJET experiment we expect to have a good quality of data and accordingly the study of intermittency will be performed.

V SHREK EXPERIMENT

SHREK stands for the large size von Kármán apparatus called **S**uperfluid **H**igh **RE**ynolds von **K**ármán experiment at CEA-Grenoble. This is a unique world class facility to generate very high Reynolds number flows even comparable to the atmospheric turbulence on the laboratory scale. This apparatus has been designed to study turbulent flows at very high Reynolds numbers at cryogenic temperatures as low as 1.6K. The von Kármán flow is basically the flow driven by one or two disks/turbines in a confined space. The von Kármán flows are studied because of their ability to produce very high turbulent intensity flows. This apparatus has been designed to study the turbulence scaling from a very large energy injection scale to very small dissipative scales which can lead to an inertial range over a span of three decades. This facility can be used from room temperatures up to the lowest temperatures of 1.6K.

This chapter describes the experimental set-up in brief along with the von Kármán cell specifications and the different types of turbines used. The measurements are primarily acquired with the help of the hot-wire anemometry. The results from the hot-wires at T = 2.2K in HeI will be discussed in detail in view of effects of forcing on dissipation, Reynolds number, scaling laws and intermittency. The results of the von Kármán flows in HeI are complemented with the inspection of these flows in HeII at T = 2.0K.

V.1 Experimental set-up

Figure V.1 shows the detailed sketch of the SHREK apparatus. Detailed dimensions and specifications of the experiment are described in Rousset et al. [2014]. This facility has a saturated bath and a subcooled/pressurized bath. The entire apparatus is of a diameter 1100mm with a height of 2515mm. It is then mounted in the multi purpose cryostat which is cooled by a high cooling power refrigerator of the standard capacity of 400W at 1.8K. According to the Carnot's theorem (and also the second law of thermodynamics), the maximum efficiency of a thermal engine is $\frac{T_{cold}}{T_{hot}-T_{cold}}$ leading to the fact that to extract 400W at T_{cold} = 1.8K, with a refrigerator working at the ambient temperature of T_{hot} = 300K, the input power to the refrigerator is about 400kW. In the saturated bath, on the top of the von Kármán cell, 83 copper tubes are mounted, which act as heat exchangers.

V.1.1 von Kármán cell and hot-wire position

Figure V.1 shows the exact dimensions of the von Kármán cell. The diameter of this cell is 780mm (R = 390mm) with the height of 1160mm. The diameter of the turbine is 720mm and the distance between upper and lower turbine is $\mathcal{H}$ = 702mm, which thereby defines the ratio $\mathcal{H}$/R = 1.8. Figure V.2 shows the inner view of the von Kármán cell. During each campaign of SHREK, different sensors are installed such as pitot tubes, cantilevers, second sound probes and hot-wires. Most commonly the sensors are installed slightly above the equatorial plane, but they can also be installed close to the turbine. Figure V.2b shows the actual position of the hot-wire inside the SHREK experiment. The hot-wires are mounted at a distance of 35 - 40mm from the wall of von Kármán cell, and at 40mm above the equatorial plane. The hot-wire is installed at this position so that there is always a non-zero mean velocity around the hot-wire, which allows to use Taylor hypothesis. The hot-wires are mounted in such a way that they are sensitive to either azimuthal and axial or azimuthal and radial components of the velocity. The sense of rotation of turbines in the von Kármán flow is properly tuned so that the mean flow comes towards the hot-wire from the front side but not from the back side.

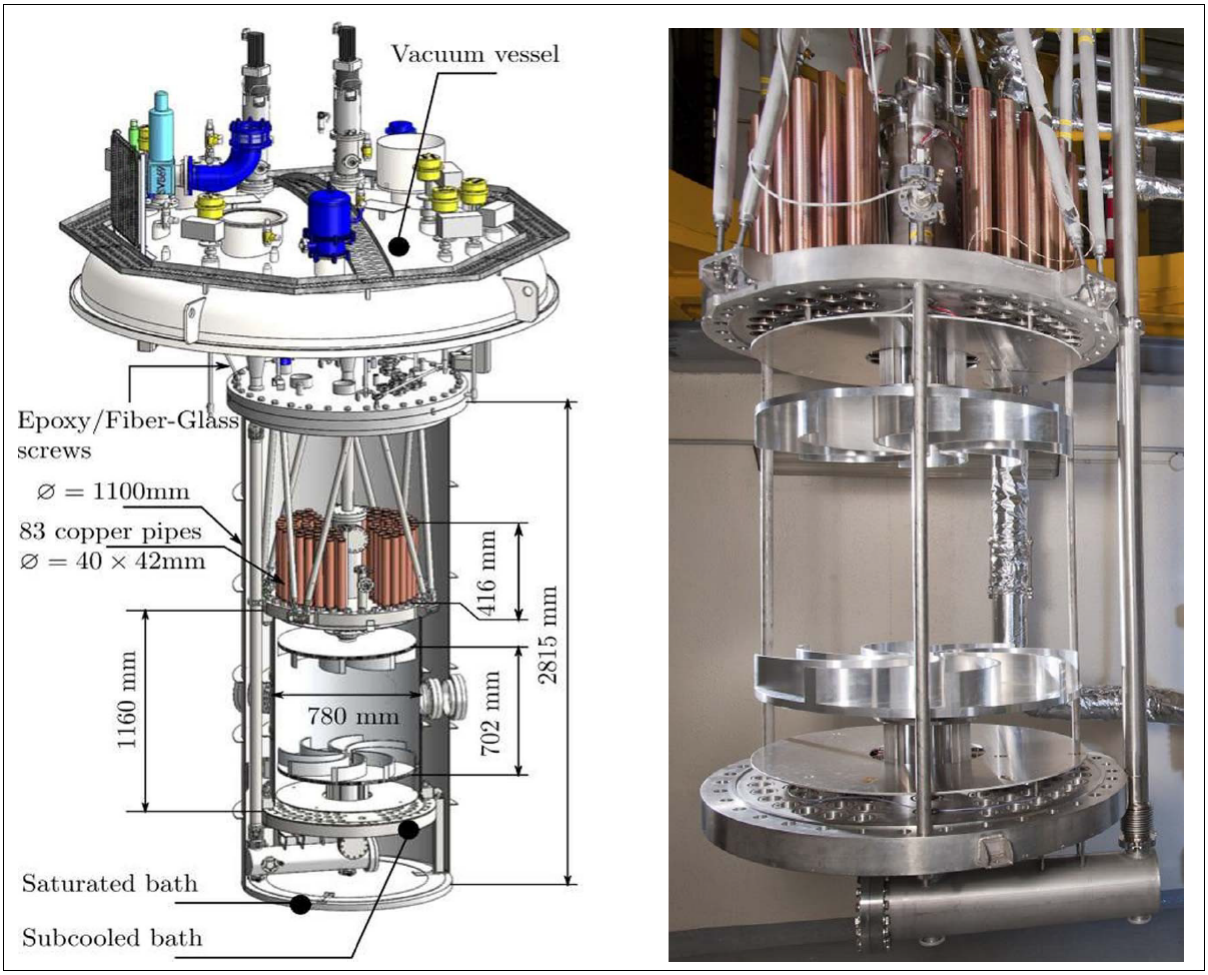

Figure V.1: Detailed sketch of SHREK facility; Left: Dimensions of various parts in the SHREK experiment; Right: von Kármán cell with the turbines with curved blades

.

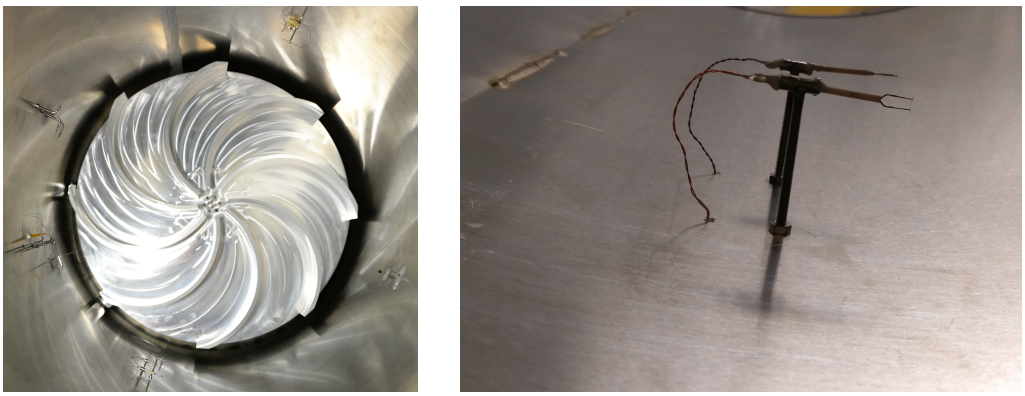

(a) Various sensors mounted on the periphery of the von Kármán cell

(b) Hot-wire mounted at 40mm away from the wall of von Kármán cell

Figure V.2: Bottom view of the von Kármán cell along with the hot-wire

V.1.2 Different types of turbines

Different types of turbines can be used in the SHREK experiment. Figure V.3 shows them: curved, rectangular/straight/radial, fractal and turbine without blades i.e. smooth disks. The results presented in this chapter are mainly concerned with experiments in which either curved (8 blades) or rectangular (4 blades) blades of the turbine are used. A study of the von Kármán flow using turbines of different radius, number of blades and exit angle of blades has been performed by Ravelet [2005] and Saint-Michel [2013] at CEA-Saclay.

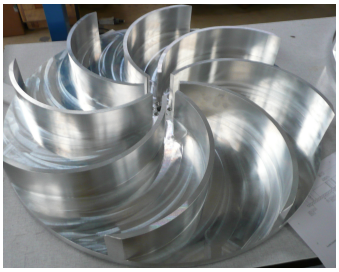

(a) Turbine with curved blades

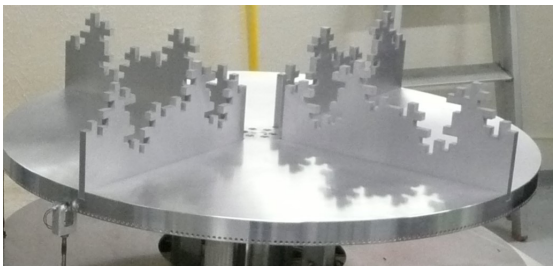

(b) Turbine with fractal blades

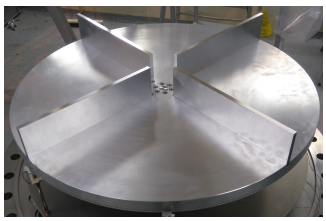

(c) Turbine with rectangular/straight/radial blades

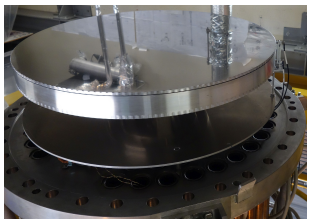

(d) Turbine without blades i.e. disks

Figure V.3: Different types of turbine blades used in the SHREK experiment

V.1.3 Conventions of rotation of turbine

It is important to establish the sign conventions used in the SHREK experiment for the rotation of turbines. The same conventions will be used entirely in this thesis to distinguish the results from each other. From figure V.1 and figure V.3a of the von Kármán cell, we see that the blades of the upper and lower turbines are curved and have an opposite orientation to each other. From the shape of the blades of the turbines, we have established the conventions which are based on the convex and concave side of the turbines blades. Depending upon which side of the blade pushes the fluid decides the direction of rotation of turbine which can be either positive (+) or negative (-). A pictorial representation of conventions of rotation of turbine is shown in figure V.4.

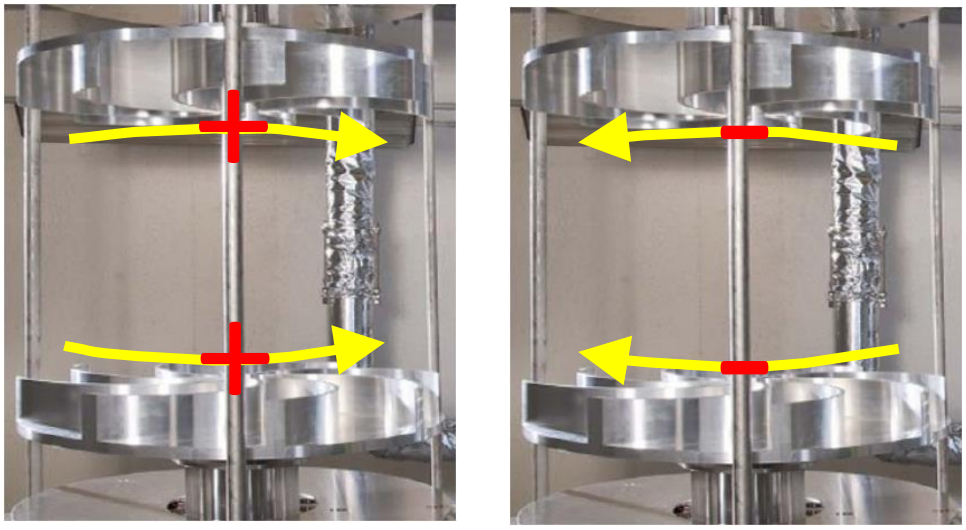

(a) Co-rotation configuration

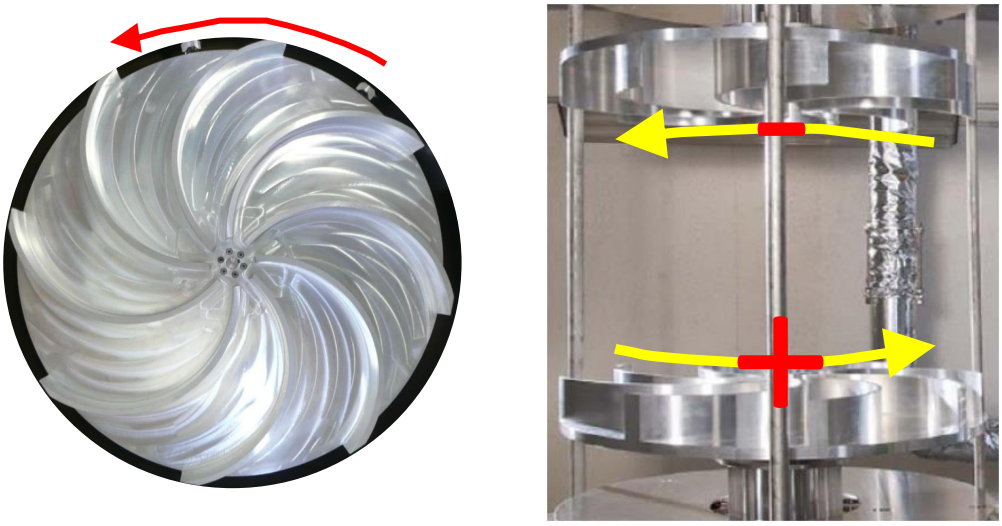

(b) Contra configuration

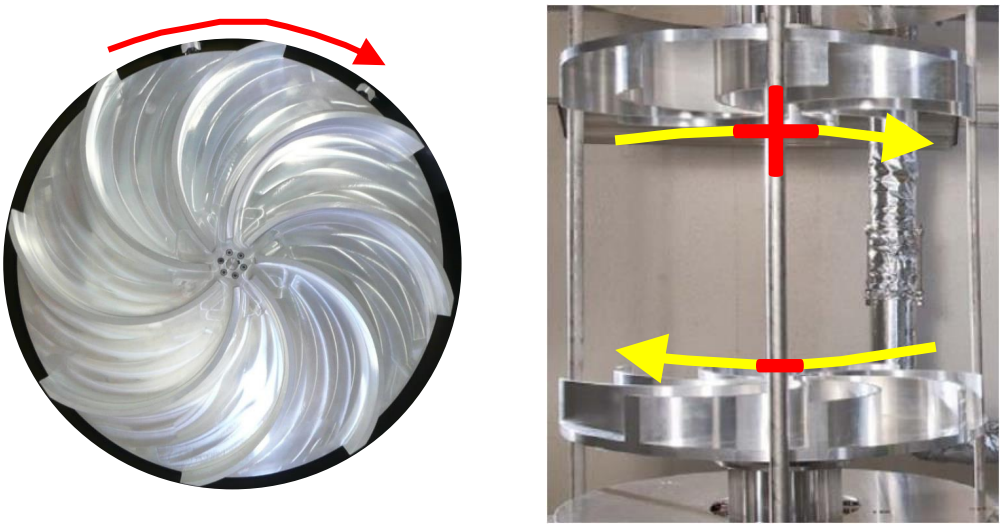

(c) Anti-contra configuration

Figure V.4: Sign conventions used in the SHREK experiment: co-rotation, contra and anti-contra configuration

The conventions of the von Kármán flow used in this thesis deal with either positive or negative direction for each of the co-rotation, contra and anti-contra configurations. Looking at each of the turbines from the top (see figure V.1), the anticlockwise rotation of each of the turbines is associated with positive (+) sign whereas the clockwise rotation of the turbine is associated with negative (-) sign. If both turbines rotate in the same direction either in positive or in negative direction, then it is referred as co-rotation configuration as shown in figure V.4a. This configuration results in an almost solid body rotation of the fluid and hence this configuration is used for the calibration of the hot-wire. When the convex side of the blades of each of the turbine pushes the fluid then it is referred as the contra configuration as shown in figure V.4b. When the concave side of the blades of each of the turbine pushes the fluid then it is referred as anti-contra configuration as shown in figure V.4c. The anti-contra is the configuration which generates the von Kármán flow having the highest turbulent intensity, whereas the co-rotation configuration generates the flows with a lower turbulence intensity. The upper/top turbine is referred as *Haut* (hereafter H) and the lower/bottom turbine is referred as *Bas* (hereafter B). The convention of rotation of turbines is also explained with the help of following examples:

1. - 0.12(H) + 0.18(B)

This is a contra configuration in which convex part of the blades of each turbine pushes the fluid which corresponds to figure V.4b. -0.12(H) tells us that the upper turbine is rotating in the negative direction (i.e. clockwise direction when viewed from top and hence the negative sign). 0.12 is the frequency of rotation of the upper turbine in Hertz (Hz). +0.18(B) tells us that the lower turbine is rotating in the positive direction (i.e. anticlockwise direction when viewed from top and hence the positive sign) with the frequency of rotation of 0.18Hz.

2. + 0.9(H) - 0(B)

This is an anti-contra configuration in which the concave part of the blades of the upper

turbine pushes the fluid which corresponds to figure V.4c. +0.9(H) means that the upper turbine is rotating in the anticlockwise direction i.e. positive direction at a frequency of 0.9Hz. -0(B) indicates that the lower turbine is at rest.

In the case of straight or fractal blades, the convention of direction of rotation is the same (either + or -), but there is no difference in the contra and anti-contra flow configuration. It is worth to mention that the convention of von Kármán flow used in this thesis are not the same as in the experiments of von Kármán flow at CEA-Saclay (for more details see Ravelet et al. [2008]; Kuzzay et al. [2015]).

V.1.4 Classification of experimental data

In what follows, we present experimental results from different configurations of the von Kármán flow. The experimental data sets are classified based on the type of flow configuration and the operating frequency of the top and bottom turbine. For easy comparison, the data sets are named as A to G as mentioned in table 6. $\mathcal{F}_1$ is the frequency of top turbine whereas $\mathcal{F}_2$ is the frequency of bottom turbine which can vary within 0.05 - 1.6Hz. The rotation number is defined by $\theta = \frac{(\mathcal{F}_1 - \mathcal{F}_2)}{(\mathcal{F}_1 + \mathcal{F}_2)}$, whose value for each of the flow configuration is mentioned in table 6.

Table 6: Details of the configurations of the von Kármán flow, $\mathcal{F}_1$ & $\mathcal{F}_2$ are the frequencies of top and bottom propellers respectively

Data set	**Flow Configuration**	$\mathcal{F}_1$ & $\mathcal{F}_2$	$\theta = \frac{(\mathcal{F}_1 - \mathcal{F}_2)}{(\mathcal{F}_1 + \mathcal{F}_2)}$
A	Co-Rotation	+ $\mathcal{F}_1$ + $\mathcal{F}_2$ ($\mathcal{F}_1 = \mathcal{F}_2$)	0
B	Contra	- 0 + $\mathcal{F}_2$	-1
C	Contra	- $\mathcal{F}_1$ + $3\mathcal{F}_1$	-0.5
D	Contra	- $\mathcal{F}_1$ + $1.2\mathcal{F}_1$	-0.1
E	Contra	- $\mathcal{F}_1$ + $1.5\mathcal{F}_1$	-0.2
F	Anti-Contra	+ $\mathcal{F}_1$ - 0	0
G	Anti-Contra	+ $\mathcal{F}_1$ - $\mathcal{F}_1$ ($\mathcal{F}_1 = \mathcal{F}_2$)	1

The hot-wire is operated in either CTA or CCA mode in the SHREK experiment. The hot-wire is operated in the CTA mode, for the SHREK experiment performed with turbines with curved blades. For the SHREK experiment performed with turbines with radial blades, the hot-wire is operated in CCA mode. In both of these experiments, similar but not identical hot-wires are used having $d_w = 1.27\mu m$ and $l_w = 300\mu m$. Also, in all of these experiments the hot-wire is installed slightly above the equatorial plane.

V.2 PSD of velocity signal

The calibration of the hot-wire is performed as previously discussed in section II.1 and section II.2. Figure V.5 shows a PSD of the velocity signal in the SHREK experiment for the anti-contra configuration at $\mathcal{F}_1 = \mathcal{F}_2 = 0.6$Hz. Figure V.5a shows a PSD of the velocity signal while the hot-wire is operated in CTA mode. This PSD is obtained in the SHREK experiment performed with turbine with curved blades. Figure V.5b shows a PSD of the velocity signal while the hot-wires are operated in CCA mode. This PSD is obtained in the SHREK experiment performed with turbine with radial blades. In this experiment, one hot-wire is installed at the equatorial plane whereas the other hot-wire is installed at 15cm away from the equatorial plane (close to the top turbine). The PSD in both figure V.5a and figure V.5b shows a very wide inertial range ($f^{-\frac{5}{3}}$ dependence) almost over three decades of frequencies. At high frequencies we see the spikes in the PSD which may be due to the vibrations of the SHREK experiment originating from other

appliances such as the pump, compressor, motor or the refrigerator. This may also result from the vibrations of the prongs of the hot-wire itself. In figure V.5a we see a peak in PSD at about $f \approx 0.48$Hz which represents the periodic forcing at large scales (8 blades $\times$ 0.6Hz). The similar peak is also visible in figure V.5b at about $f \approx 2.4$Hz (4 blades $\times$ 0.6Hz) in the PSD of the hot-wire which is installed close to the top turbine. In fact, we have discussed similar kind of peaks (i.e. periodic oscillations) which are related to the number of blades of the turbine in the autocorrelation coefficient (see section I.6.5).

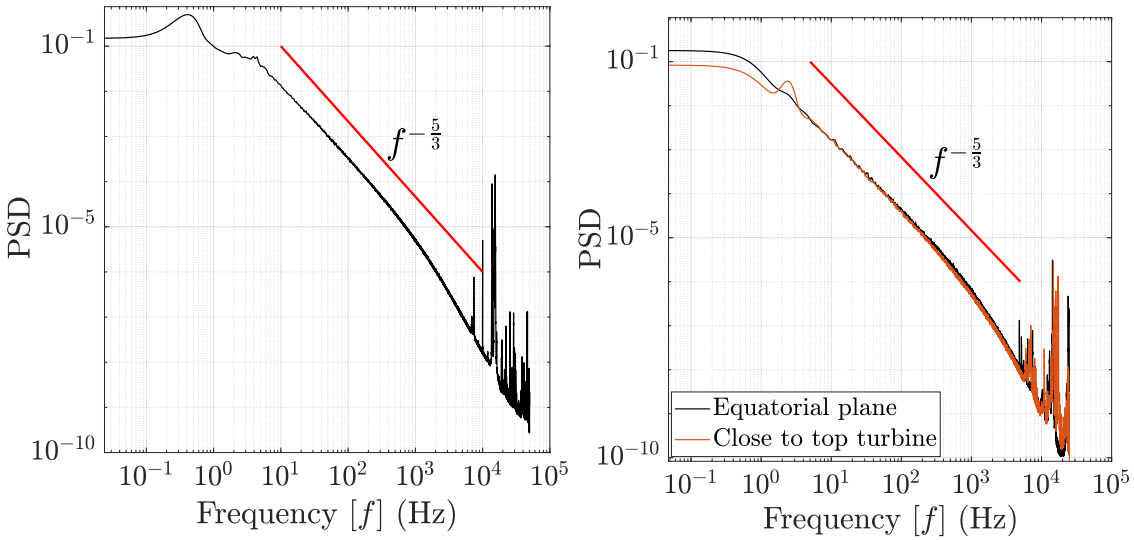

(a) Hot-wire in CTA mode close to equatorial plane(SHREK experiment with turbine with curved blades)

(b) Hot-wire in CCA mode (SHREK experiment with turbine with radial blades)

Figure V.5: PSD of the velocity signal in the SHREK experiment for anti-contra configuration at $\mathcal{F}_1 = \mathcal{F}_2 = 0.6$Hz

We note that whether the hot-wire is operated in the CTA or CCA mode, the spatial filter of the hot-wire ($l_w \approx 300\mu m$) is equally applicable in both scenarios (see also figure I.5). On the other hand, as the hot-wire is maintained at constant temperature in CTA mode the hot-wire has very negligible thermal inertia whereas in CCA mode the hot-wire has finite thermal inertia. In section II.7 we have shown that the cut-off frequency of the hot-wire based on its time constant lies within 5 - 13kHz. From the PSD in figure V.5, we see the spurious peaks (i.e. vibrations) beyond the frequency say $\approx$ 5kHz in the SHREK experiment. Overall, this necessitates the use of the numeric low-pass filter beyond the frequency of 5kHz, irrespective of the mode of operation of the hot-wire.

V.3 PDF of velocity signal

Figure V.6 shows the PDFs of the velocity signal in the SHREK experiment performed with curved blades. In this experiment, the hot-wire is operated in the CTA mode and is located close to the equatorial plane. These PDFs are shown for the co-rotation configuration from $\mathcal{F}_1 = \mathcal{F}_2 = 0.6$Hz to $\mathcal{F}_1 = \mathcal{F}_2 = 1.2$Hz. Figure V.7 shows the PDFs of the velocity signal in the SHREK experiment performed with radial blades. In this experiment, the hot-wire is operated in the CCA mode and is also located close to the equatorial plane. These PDFs are shown for the co-rotation configuration at $\mathcal{F}_1 = \mathcal{F}_2 = 1.0$Hz and $\mathcal{F}_1 = \mathcal{F}_2 = 1.2$Hz. In both figure V.6 and figure V.7 a comparison of the PDF of experimental data is done with a corresponding Gaussian

distribution shown by the dashed-line. Each Gaussian distribution is obtained by using the mean and standard deviation of the corresponding experimental data. From both figure V.6 and figure V.7 we see that the PDFs of the velocity signal in the SHREK experiment are in fact close to the Gaussian distribution (see also section I.6.10).

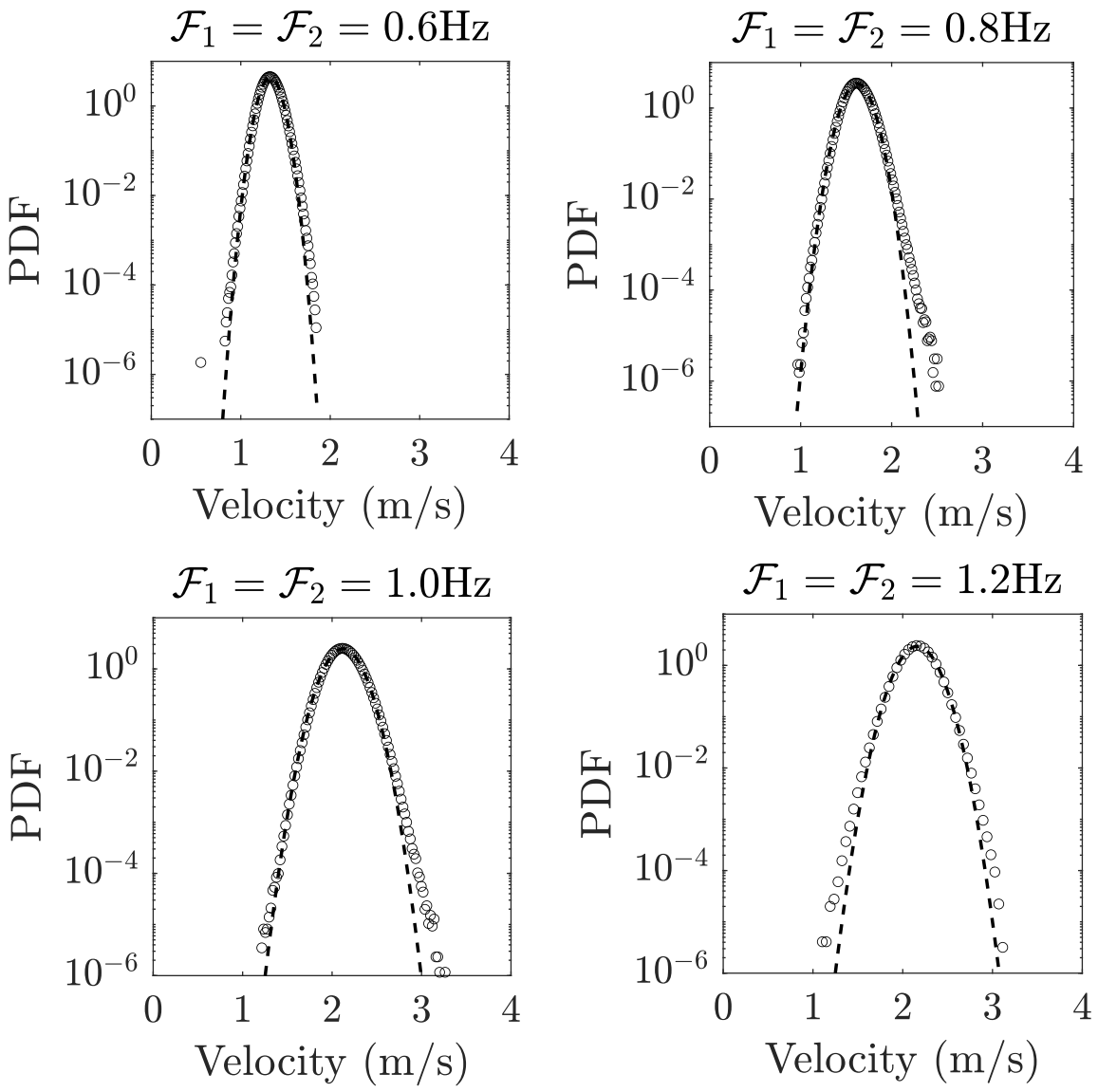

Figure V.6: Probability density function (PDF) of the velocity signal in the SHREK experiment with curved blades for the co-rotation configuration [black circles show the PDF of experimental data and the dashed-line shows the Gaussian distribution in each plot; the hot-wire is operated in the CTA mode with 0.7% overheating]

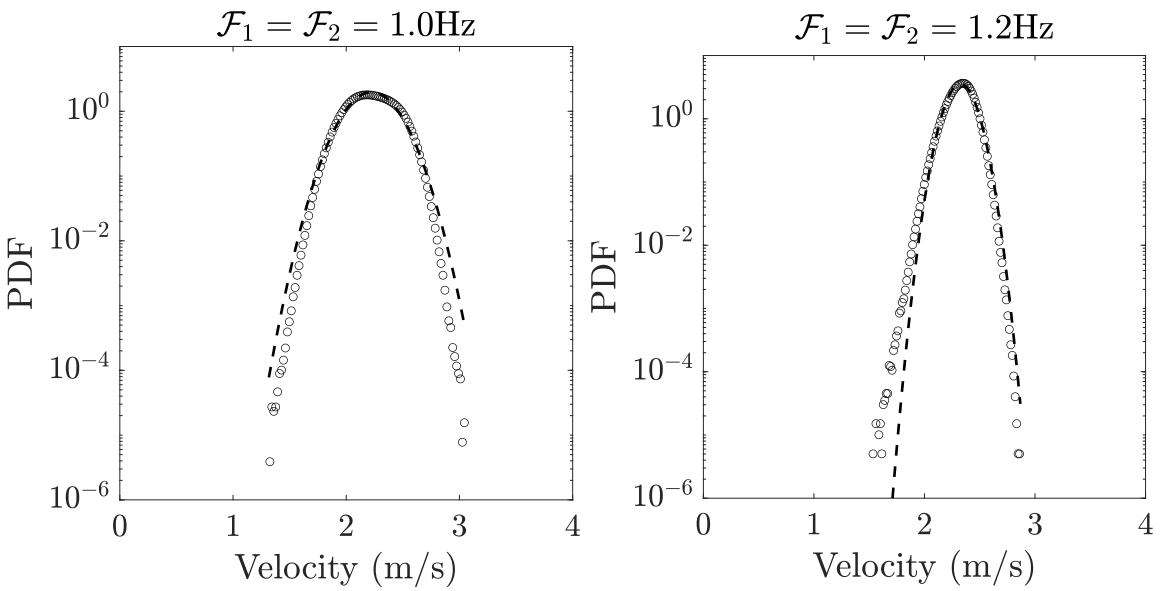

Figure V.7: Probability density function (PDF) of the velocity signal in the SHREK experiment with radial blades for the co-rotation configuration [black circles show the PDF of experimental data and the dashed-line shows the Gaussian distribution in each plot; the hot-wire is operated in the CCA mode with 18% overheating]

V.4 Effects of forcing on dissipation and Kolmogorov scale

The local dissipation rate $\left(\frac{m^2}{s^3}\right.$ or $\left.\frac{W}{kg}\right)$ is an important quantity in turbulent flows (especially in the cryogenic experiments), as it gives an information about the power which must be evacuated from the experimental region in order to maintain the thermal stability. The injection of energy (i.e. forcing) in the von Kármán cell is controlled by the tuning of the frequency of top and bottom turbines. The local dissipation rate in the SHREK experiment is estimated using the approach described in section I.6.7. With this approach the dissipation rate is estimated from the third order structure function using the relation $\epsilon = -\frac{5}{4}\frac{S_3}{r}$. As already said earlier, using $-\frac{S_3}{r}$ we get an estimation of the energy transfer rate, which is expected to be constant in the inertial range (if it exists) and equal to the dissipation rate assuming steady state conditions. Figure V.8 shows the dissipation rate as a function of scale r for co-rotation, contra and anti-contra flow configuration. In this figure a vertical black-dashed line indicates the spatial filter of the hot-wire at $r \approx l_w \approx 300\mu m$. In this figure we see a plateau over a certain range of scales in the inertial range which represents the energy transfer rate towards smaller scales. The dissipation rate is then estimated from the average of this asymptotic value in the inertial range. From this figure we see that in co-rotation the dissipation rate is relatively smaller whereas it is much higher in contra and anti-contra flow configuration. A higher dissipation rate in anti-contra configuration is in agreement with the fact that the turbulent torques exerted by the fluid on the turbines is higher in the anti-contra/contra rotation than in co-rotation flow configuration (indicating that a higher power rate is injected in the flow).

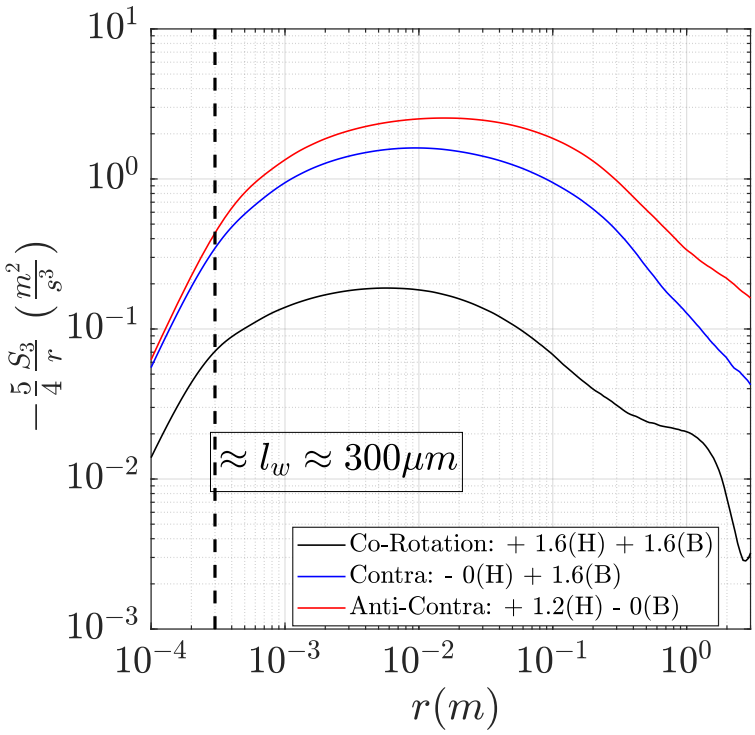

Figure V.8: Estimation of local dissipation rate in the SHREK experiment from third order structure function [Co-Rotation: $Re_\lambda = 4410$; Contra: $Re_\lambda = 6180$; Anti-Contra: $Re_\lambda = 8100$]

Figure V.9 shows the dissipation rate and the corresponding Kolmogorov scale with respect to turbine frequency. From figure V.9a, we see that dissipation increases as the frequency increases. In fact, for the same amount of forcing (i.e. at same $\mathcal{F}_1$ or $\mathcal{F}_2$) a higher dissipation is observed for the anti-contra configuration than for the contra, and it is least for the co-rotation configuration of the flow. This shows that at the same turbine frequency, a different dissipation rate occurs in the von Kármán cell depending on the flow configuration. The co-rotation configuration creates a solid body rotation which involves the least possible energy injection within the fluid and hence the least dissipation compared to other configurations.

The Kolmogorov scale is estimated from the dissipation rate and kinematic viscosity of fluid given by, $\eta = \left[\frac{\nu^3}{\epsilon}\right]^{1/4}$. From figure V.9b, we see that with increase in the turbine frequency the Kolmogorov scale becomes smaller [Zocchi et al., 1994]. The Kolmogorov scale for all the configurations ranges within 1 - 25μm with smallest for the anti-contra and largest for the co-rotation configuration of the flow, for the same turbine frequency. The current home-made hot-wires have a spatial resolution of 200 - 300μm, therefore in order to study the turbulence at dissipative scales, it would require to reduce the hot-wire length at least by 10 times.

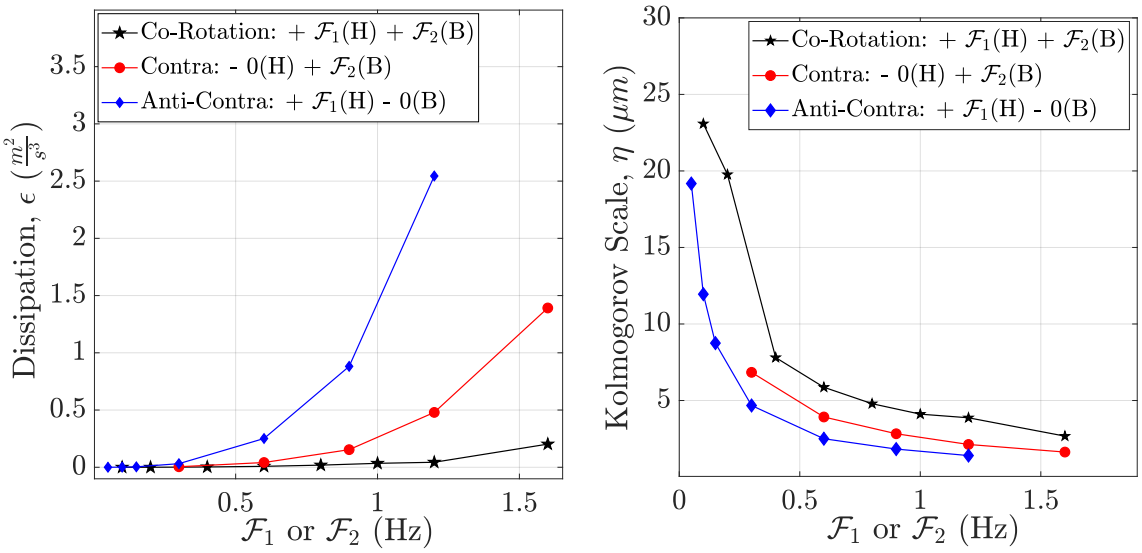

(a) Dissipation with applied forcing

(b) Kolmogorov scale with applied forcing

Figure V.9: Variation of dissipation and Kolmogorov scale with applied forcing for different configurations of the von Kármán flow

V.5 Dimensionless dissipated power per unit mass

It has been argued that the dimensionless dissipated power per unit mass reaches a constant value at sufficiently high Reynolds number flows [Saint-Michel et al., 2014; Kuzzay et al., 2015]. Similar analysis is performed for the SHREK experiment to address the validity of that statement. The energy injected in the flow transfers from large to small scales in the inertial range. Eventually, this transferred energy dissipates into heat at the smallest scales within the dissipation range. It follows that in the steady state the injected, transferred and the dissipated power are equal. In the von Kármán flow, the energy is dissipated in the control volume between the top and bottom turbine. The volume of the von Kármán cell in the SHREK experiment contributes to about $V_{He} = 0.31m^3$ which contains around $M_{He} = 47kg$ of liquid helium at T = 2.2K and at an absolute P = 3bar. Assuming an homogeneous dissipation rate in the von Kármán cell, $\epsilon = 2.6\frac{W}{kg}$ for the data set G with $\mathcal{F}_1 = \mathcal{F}_1 = 0.6$Hz corresponds to the dissipated power $P_d = 122$W.

In an ideal case, the injected power (P_i) must be equal to the dissipated power in order to maintain the steady temperature inside the von Kármán cell (T = 2.2K ±0.1mK). In the von Kármán cell, $P_i = 2\pi\mathcal{F}_1 C_{\mathcal{F}_1} + 2\pi\mathcal{F}_2 C_{\mathcal{F}_1}$, where $C_{\mathcal{F}_1}$ and $C_{\mathcal{F}_1}$ are the measured torques (N-m) on the top and bottom propellers respectively [Rousset et al., 2014]. For the above example of data set G with $\mathcal{F}_1 = \mathcal{F}_2 = 0.6$Hz the measured injected power adds up to $P_i = 108$W. This value is close to the estimated dissipated power which shows the consistency of P_i and P_d within the same order of magnitude (for data set G with $\mathcal{F}_1 = \mathcal{F}_2 = 0.45$Hz, $P_d = 44$W and $P_i = 51W$). P_d and P_i are also found to be compatible with the cooling capacity of the refrigerator used in the SHREK facility.

In order to discuss the dimensionless dissipated power per unit mass, following nomenclature is used. R is the radius of the von Kármán cell and $\mathcal{H}$ is the height of the turbulent flow region between two turbines. The angular velocity $\Omega = \frac{2\pi(\mathcal{F}_1+\mathcal{F}_2)}{2}$. The Reynolds number $Re = \frac{\pi(\mathcal{F}_1+\mathcal{F}_2)R^2}{\nu}$. The rotation number $\theta = \frac{(\mathcal{F}_1-\mathcal{F}_2)}{(\mathcal{F}_1+\mathcal{F}_2)}$. And finally, the dimensionless dissipated power is given by, $\mathcal{P} = \frac{\epsilon M_{He}}{\rho R^4 \Omega^3 \pi \mathcal{H}}$, where ρ is the density of HeI. Figure V.10 shows $\mathcal{P}$ with respect to Re for different von Kármán flow configurations for which θ varies from -1 to 1. From

this figure, we see that $\mathcal{P}$ reaches a fixed asymptotic value depending on the flow configuration, which shows that we have attained a regime where $\mathcal{P}$ is independent of Re. Based on the relatively high shear and rotation rates induced by the turbine frequency from $\theta = 0$ to $\theta = \pm 1$, $\mathcal{P}$ increases from the co-rotation to contra and is maximum for the anti-contra von Kármán flow configuration as shown in figure V.10. The estimated $\mathcal{P}$ for anti-contra configuration agrees well with the study performed in the von Kármán flow by Cadot et al. [1997].

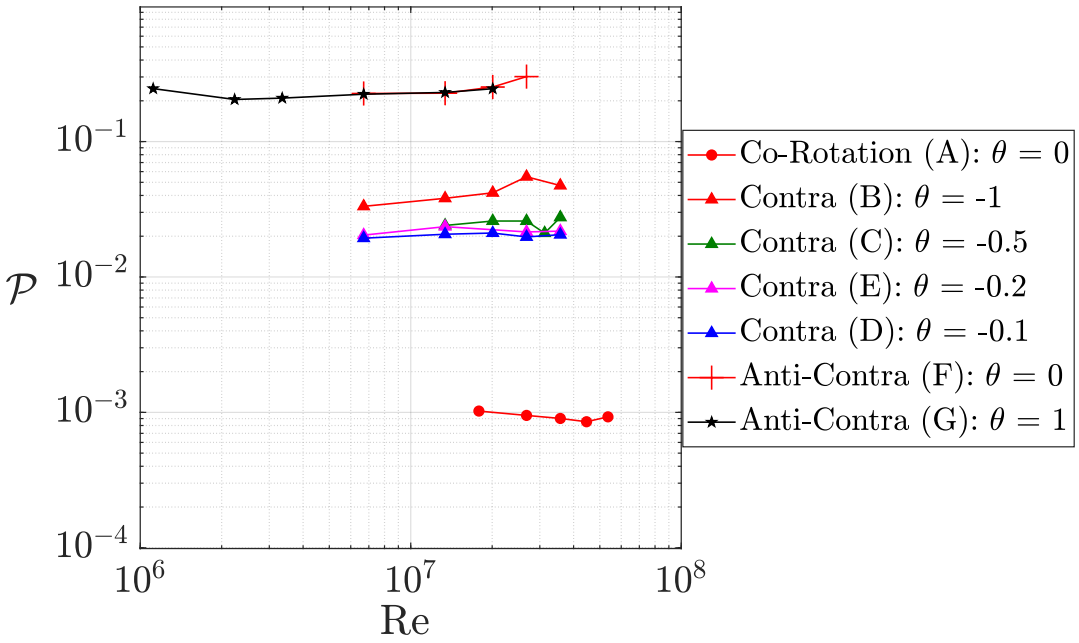

Figure V.10: Dimensionless dissipated power per unit mass as a function of $Re = \frac{\pi(\mathcal{F}_1+\mathcal{F}_2)R^2}{\nu}$

V.6 Effects of forcing on Re_λ

The variation of Re_λ is governed by the simultaneous variation of the rms value of the fluctuating velocity and its associated Taylor microscale (see section I.6.9). For a specific flow configuration, with increase in turbine frequency the velocity fluctuation increases (see figure I.6a). On the other hand, we know that with increase in Reynolds number of the flow the inertial range widens and the Taylor microscale become smaller (see figure V.15). Figure V.11 shows the variation of $Re_\lambda = \frac{u_{rms}\lambda}{\nu}$ with respect to turbine frequency. From this figure, we see that Re_λ increases with increase in turbine frequency because the relative increase (% increase) of u_{rms} is higher than the relative decrease of Taylor microscale. From figure V.11, we see that different flows of Re_λ in the range of 720 to 13600 can be generated in the SHREK facility which allows to study the evolution of turbulence (the scaling laws and intermittency) over a wide range of Reynolds numbers. From figure V.11, we see that Re_λ increases from co-rotation to contra and anti-contra configuration of flows for the same turbine frequency.

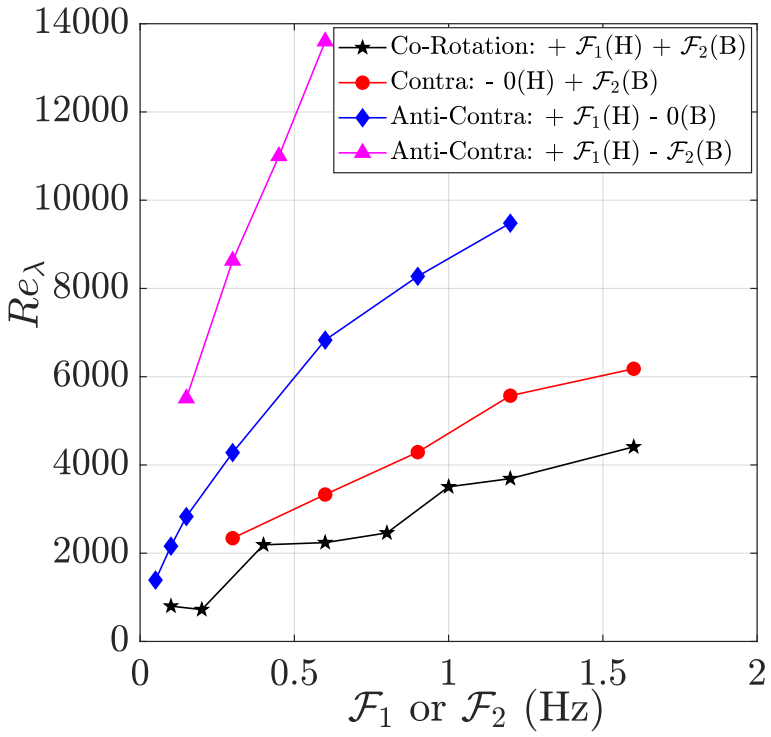

Figure V.11: Variation of Re_λ with applied forcing

V.7 Scaling laws

Based on the estimation of quantities discussed in the previous sections, some scaling laws which have been previously reported in the literature for classical turbulence are explored for cryogenic turbulence using normal helium at 2.2K. The scaling laws are explored here in order to address their validity for very high Reynolds number flows in the SHREK experiment. The theoretical procedure to establish the scaling laws of turbulence is explained in detail in Pope [2001]. Experimentally, it is important to validate the scaling laws in order to ascertain the classical turbulence measurements in the experiments. The turbulence in a fluid flow is governed by different scales of motion such as integral (L), Taylor (λ) and Kolmogorov (η) scales, which vary in response to the applied forcing, and can be quantified by the global Reynolds number defined by $Re = \frac{u_{rms}L}{\nu}$.

V.7.1 $\frac{\lambda}{\eta} \propto Re^{\frac{1}{4}}$

The ratio between Taylor microscale and Kolmogorov scale can be expressed by the scaling law given by, $\frac{\lambda}{\eta} \propto Re^{1/4}$. Figure V.12 shows the variation of $\frac{\lambda}{\eta}$ with respect to Re for three different flow configurations. In this figure, the Taylor microscale is estimated from the relation given by, $\lambda = \sqrt{\frac{15\nu u_{rms}^2}{\epsilon}}$. The Kolmogorov scale is estimated as explained in figure V.9b from the relation given by, $\eta = \left[\frac{\nu^3}{\epsilon}\right]^{1/4}$. For easy comparison, a dashed line corresponding to $\frac{\lambda}{\eta} \propto Re^{0.25}$ is drawn on log-log plot so that the scaling law can be visualized as a straight line. From figure V.12 we see that $\frac{\lambda}{\eta}$ increases as the Re increases for all flow configurations. In this figure, we see that all the experimental data points falls on a line parallel to each other apart from different prefactors of proportionality. Experimentally, the power exponent of Re is found to be 0.19 for co-rotation, 0.24 for contra and 0.25 for the anti-contra configuration of flow. From figure V.9b

and figure V.12, we can observe that the Taylor microscale decreases with increase in turbine frequency [N. Mordant et al., 1997]. This is in accordance with the fact that higher amount of forcing extends the inertial range further towards the smaller scales. In figure V.12 we observe maximum $\frac{\lambda}{\eta} \approx 200$ at highest $Re \approx \mathcal{O}(10^7)$ in the SHREK experiment.

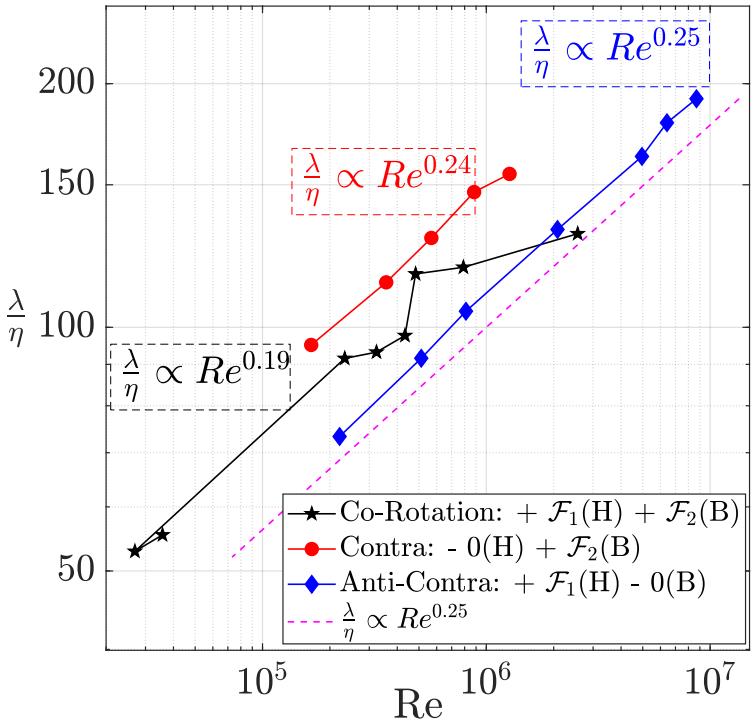

Figure V.12: Scaling of $\frac{\lambda}{\eta}$ with Re

V.7.2 $\frac{\eta}{L} \propto Re^{-\frac{3}{4}}$

The scaling law for entire energy cascade from integral scale to the Kolmogorov scale is expressed by, $\frac{\eta}{L} \propto Re^{-3/4}$. Figure V.13 shows the experimental data points for three configurations with estimated exponent of Reynolds number on a log-log plot. Specifically, it shows that the range of scales i.e. the ratio $\frac{L}{\eta}$ increases with increase in forcing. This figure shows that the estimated $\frac{\eta}{L}$ follows the trend of $Re^{-0.75}$ very well. After fitting the experimental data, the power exponent of Re is found to be -0.78 for co-rotation, -0.75 for contra and -0.73 for anti-contra configuration of flow. This figure shows the highest cascade length ratio $\frac{L}{\eta} \approx \mathcal{O}(10^5)$ at $Re \approx \mathcal{O}(10^7)$ for the anti-contra flow configuration. Such a huge cascade length ratio can only be attained in the atmospheric turbulence or in turbulent flows at cryogenic temperatures [Pietropinto et al., 2002]. The experimental data points corresponding to the highest Re in figure V.13 are in good agreement with the atmospheric turbulence studied by Cleve et al. [2004]. The ratio $\frac{L}{\eta}$ also signifies the number of steps in the energy cascade from large integral scale to smallest Kolmogorov scale. The ratio $\left(\frac{L}{\eta}\right)^3 \propto Re^{\frac{9}{4}}$ can also be taken as the measure of the number of degrees of freedom N of a turbulent flow [Frisch, 1995]. From the perspective of 3D numerical simulation of very high Reynolds number flows ($Re \approx \mathcal{O}(10^7)$) we see that N i.e. the number of grid points ($N \approx \mathcal{O}(10^{15})$) grows very rapidly. Therefore, we can imagine that the 3D numerical simulation of turbulent flow at $Re \approx \mathcal{O}(10^7)$ is not feasible for a very long time. This also explains the interest of designing the SHREK experiment.

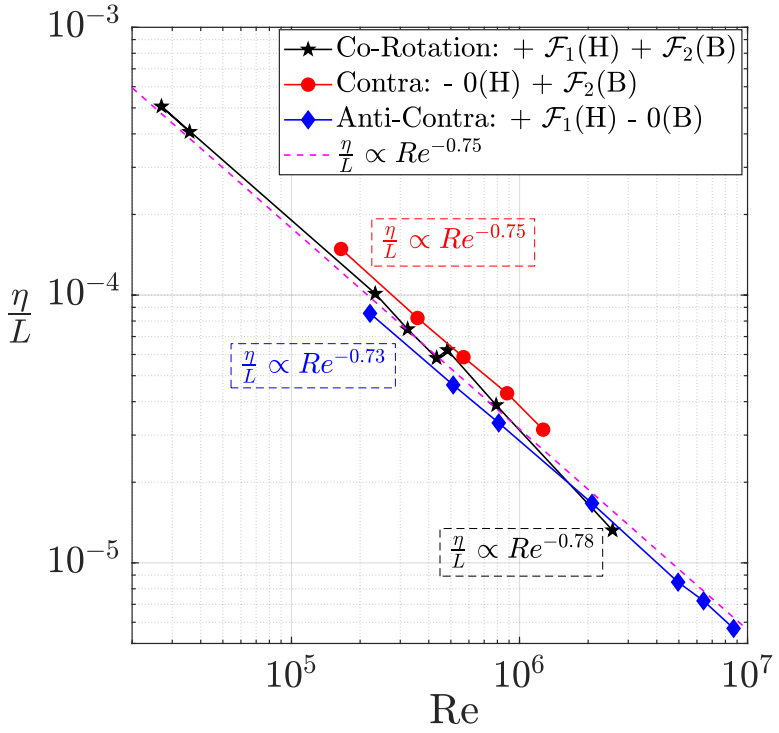

Figure V.13: Scaling of $\frac{\eta}{L}$ with Re

V.7.3 $\frac{u_\eta}{u_{rms}} \propto Re^{-\frac{1}{4}}$

The velocity constructed from the dissipation rate ϵ and the kinematic viscosity of fluid ν is the Kolmogorov velocity which is given by, $u_\eta = (\epsilon\nu)^{1/4}$ [Pope, 2001]. Reynolds number based on the velocity u_η and Kolmogorov length η is given by, $Re_\eta = \frac{u_\eta \eta}{\nu}$. The dissipation in the turbulent flow is completely dominant at $Re_\eta = 1$. The velocity scaling based on the u_η and the characteristic velocity scale of the flow u_{rms} is given by, $\frac{u_\eta}{u_{rms}} \propto Re^{-1/4}$. Figure V.14 shows the scaling of $\frac{u_\eta}{u_{rms}}$ with Re for three different configurations of the flow on log-log scale. In this figure, we see that the velocity ratio $\frac{u_\eta}{u_{rms}}$ decreases as Re increases. We see that the velocity ratio follows the theoretical prediction of $Re^{-0.25}$ very well. The experimental fit gives the power exponent of Re to be -0.21 for co-rotation, -0.24 for contra and -0.25 for anti-contra flow configuration.

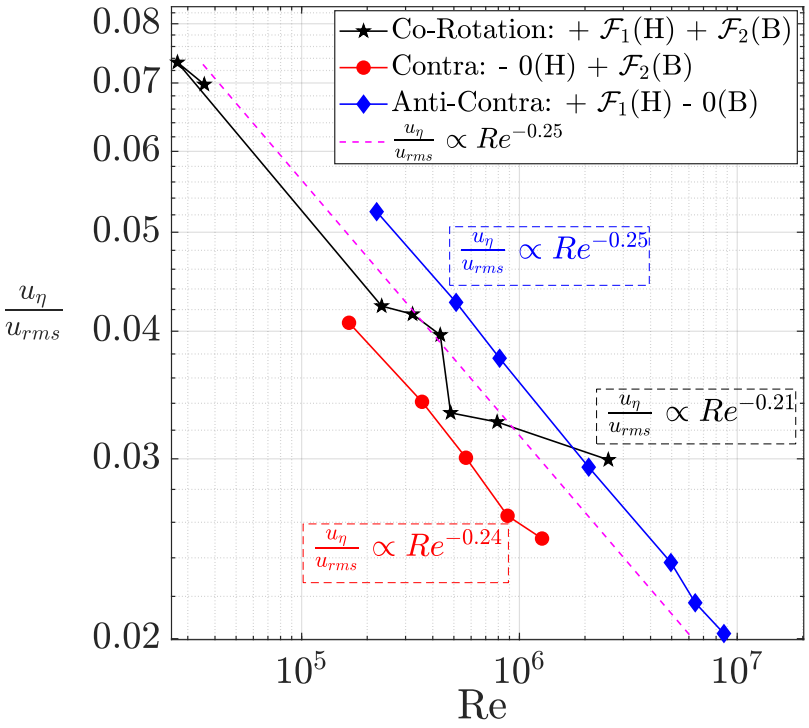

Figure V.14: Scaling of $\frac{u_\eta}{u_{rms}}$ with Re

V.8 Re_λ effect on $\frac{L}{\lambda}$

We know that with increase in the global Reynolds number the ratio $\frac{L}{\lambda}$ increases [Vassilicos, 2015]. This has been extensively investigated in case of fractal grid generated turbulence up to the $Re_\lambda = 400$ [Mazellier and Vassilicos, 2010] and in case of active grid turbulence up to the $Re_\lambda = 1000$ [Mora et al., 2019]. This dependence of $\frac{L}{\lambda}$ with respect to Re_λ is explored in case of von Kármán flows. Figure V.15 shows the ratio of integral scale to Taylor microscale over a broad range of Re_λ for different flow configurations. In a specific von Kármán flow configuration (data set A to G) the integral length scale is relatively constant. But, the Taylor microscale decreases as the turbine frequency increases (see figure V.9b and figure V.12). Therefore, in figure V.15 we see that irrespective of the flow configuration $\frac{L}{\lambda}$ always increases with increasing Re_λ. The largest $\frac{L}{\lambda} \approx 1000$ shows that a very large inertial range can be attained in the von Kármán flows at cryogenic temperatures, which is typically $\frac{L}{\lambda} \approx \mathcal{O}(10^1)$ at ambient temperatures in different kinds of turbulent flows [Mazellier and Vassilicos, 2008].

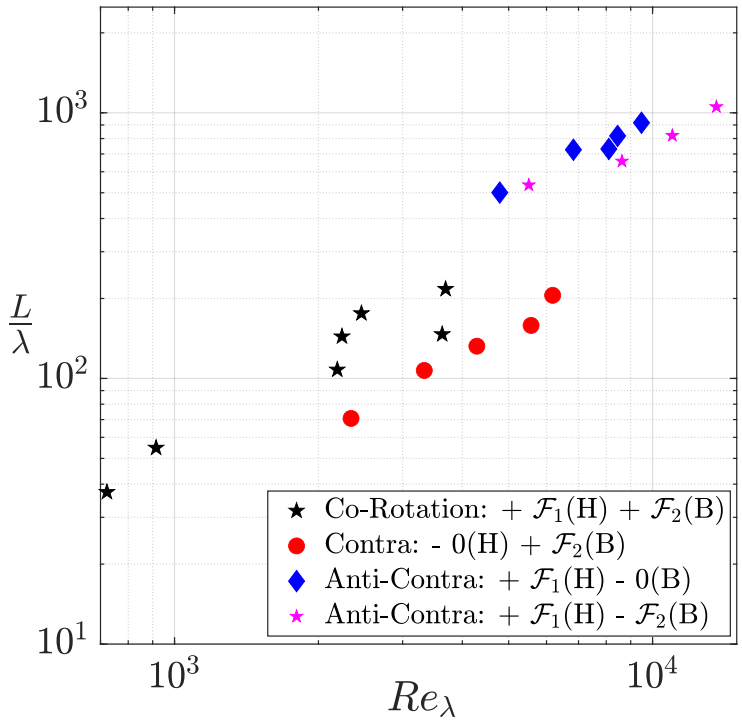

Figure V.15: The evolution of ratio of integral scale to Taylor microscale with respect to Re_λ

V.9 Intermittency

For the theoretical description/definition of intermittency in turbulent flows you are referred to section I.3.1. The term intermittency refers to the random fluctuations of the dissipation across scales in the turbulent flow. The direct evidence of this uneven dissipation across scales is the occurrence of strong gusts of wind over small time scales. From the visual perspective it can refer to the strong bursts of velocity in the signal. The self-similarity of the random velocity field is the main assumption of K41 theory. In fact, we know that a self-similar signal is not intermittent at any scale. This means that according to K41 the flatness (or any other order quantity) of the PDFs of velocity increments at all scales should remain constant i.e. does not grow towards smaller scales. In most experiments and numerical simulations of fully developed turbulence the velocity field and PDF of velocity increments at integral length scale is found to be Gaussian (i.e. normal distribution which may be understood as a consequence of the central limit theorem and of the fact that turbulent flows have a very large number of degrees of freedom $\approx Re^{\frac{9}{4}}$). This is why a Gaussian distribution is taken as a reference to compare intermittency at small scales as its flatness is always equal to 3. But, from the numerous experimental evidences we now know that the turbulent velocity field is not self-similar across different scales. Such non self-similar velocity field shows strong intermittent events across smaller scales. There are many ways to define, interpret and quantify intermittency in turbulent flows. The simplest way is the visual inspection of the PDFs of velocity increment at small scales. In this section, the interpretation of the phenomenon of intermittency is performed using the flatness and skewness of PDFs of velocity increments at small scales. The K41 theory predicts the scaling of p^{th} order structure function in the inertial range given by $S_p \propto r^{\zeta_p}$ with $\zeta_p = \frac{p}{3}$ (see equation I.11 and equation I.12). Experimental evidence suggests corrections to this K41 scaling law which are called intermittency corrections. The intermittency correction proposed by the K62 model is also addressed in this section (see equation I.17). Typically, in the SHREK experiment, Taylor

microscale is of the order of the spatial resolution of the hot-wire ($\lambda \approx l_w \approx 300\mu m$). For this reason, in the SHREK experiment the phenomenon of intermittency is studied only until Taylor microscale in the inertial range.

V.9.1 Flatness and skewness of PDFs of velocity increments

The growing departure from the Gaussian distribution towards smaller scales is an evidence of intermittency. This approach to study the intermittency relies on the estimation of flatness and skewness of the velocity increments $u_r = u(x+r) - u(x)$ on scale r in the inertial range. A simple visual inspection of the phenomenon of the intermittency can be performed based on the PDF of velocity increments at the scales ranging from L down to the scale η [Anselmet et al., 1984; Kahalerras et al., 1998]. Figure V.16 shows the PDFs of velocity increments at various scales for the contra configuration of -0.12(H)+0.18(B) for which highest number of samples $\approx 1.39 \times 10^9$ are available. The integral length scale for this configuration is 14.8cm whereas the Kolmogorov scale η is $8\mu m$. The main characteristics of figure V.16 are the long tails of the PDFs of velocity increments for smaller scales, which depicts the phenomenon of intermittency. In view of easy comparison, a Gaussian distribution is also plotted. From this figure, we can see that the scales close to the integral length scale show almost Gaussian behavior whereas the intermittency starts to build up towards smaller scales.

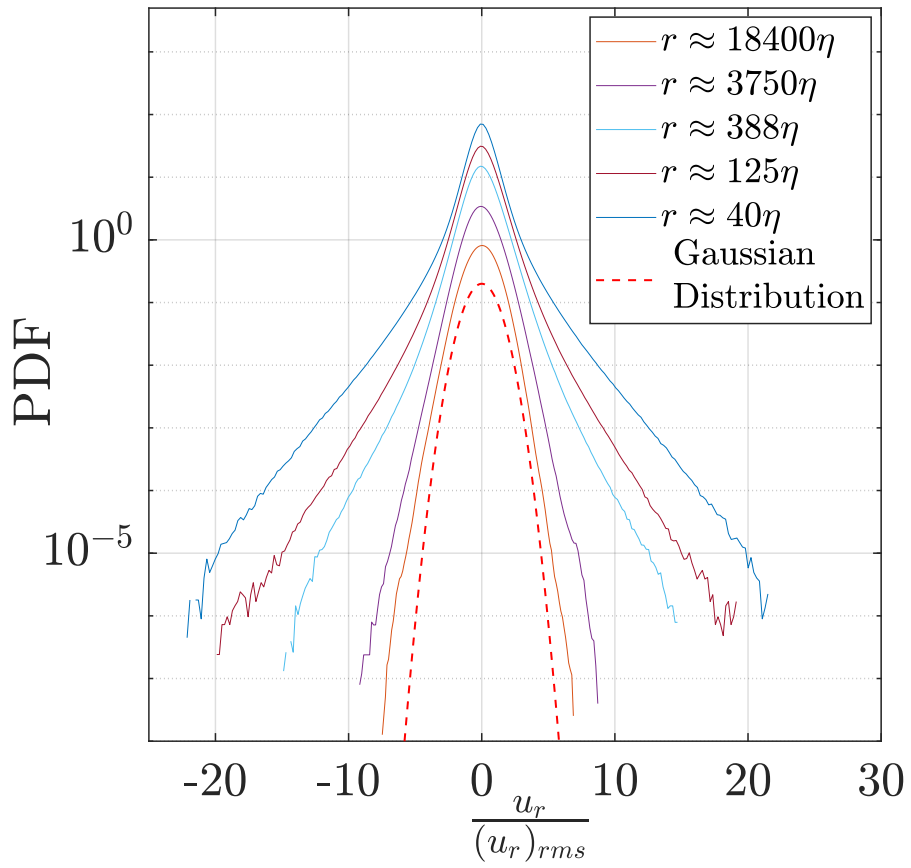

Figure V.16: PDFs of velocity increment at different scale on lin-log plot [for better clarity the curves are arbitrarily shifted in vertical direction]

The effects of intermittency shown in figure V.16 can be quantified by two of the most common statistical quantities such as flatness and skewness of the PDFs of velocity increment at

a given scale. The skewness S and flatness F are defined as normalized third and fourth order statistical moments of the velocity increments respectively which are given by:

$$S(r) = \frac{\left\langle \left(u_r\right)^3 \right\rangle}{\left\langle \left(u_r\right)^2 \right\rangle^{3/2}}, \tag{V.1}$$

$$F(r) = \frac{\left\langle \left(u_r\right)^4 \right\rangle}{\left\langle \left(u_r\right)^2 \right\rangle^2}. \tag{V.2}$$

The skewness gives the information about the tilt of any random variable about its mean. It is a measure of the asymmetry of the probability density function. The flatness (also called kurtosis) is a measure of the width of the tails of any random valued distribution. For a Gaussian distribution $F = 3$ ($S = 0$); its value increases as the tails of probability distribution widen. Therefore, a quantity of $\frac{F(r)}{3}$ is preferred to compare the non-Gaussian nature of small scale statistics. In other words, the quantity $\frac{F(r)}{3}$ gives us a quantitative measure of intermittency. In section I.3.1 we have seen that the K41 model predicts a constant flatness and skewness at all scales. In other words, from equation I.11 the K41 predictions can be expressed as:

$$F(r) = \frac{S_4}{S_2^2} = \frac{C_4 \langle\epsilon\rangle^{\frac{4}{3}} r^{\frac{4}{3}}}{\left(C_2 \langle\epsilon\rangle^{\frac{2}{3}} r^{\frac{2}{3}}\right)^2} = \text{Constant [K41]}, \tag{V.3}$$

$$S(r) = \frac{S_3}{S_2^{\frac{3}{2}}} = \frac{C_3 \langle\epsilon\rangle\, r}{\left(C_2 \langle\epsilon\rangle^{\frac{2}{3}} r^{\frac{2}{3}}\right)^{\frac{3}{2}}} = \text{Constant [K41]}. \tag{V.4}$$

Figure V.17 shows the flatness of the PDFs of velocity increments with respect to scale along with the effects of the use of low-pass filtering on the velocity signal. In this figure, $\ln\left(\frac{F}{3}\right)$ is plotted with respect to $\ln\left(\frac{r}{L}\right)$, where ln is the natural logarithm of the desired quantity. A vertical black-dashed line indicates the spatial filter of the hot-wire at $l_w \approx 300\mu m$. The plot of the flatness is reproduced for the present experimental data using the detailed approach described in Chevillard et al. [2005]. From figure V.17, we see that the flatness of the PDFs of velocity increments for the scales larger than L is almost equal to 3, which is nothing but the flatness of a Gaussian distribution. For the scales smaller than L, the flatness gradually increases while attaining a slope of -0.1 in the inertial range which properly evidences the intermittency in the SHREK experiment as already measured in other experiments [Chevillard et al., 2012]. If the data are filtered using a low-pass filter (say at 5 - 6kHz), a saturated value of flatness is observed at smaller scales, which is a consequence of damping of fluctuations after filtering of the data (see blue and red curve in figure V.17). The damping of the fluctuations results in a decrease of the rms value of the increments which thereby increases the flatness (see equation V.2). The scale at which the flatness starts to saturate depends on the frequency at which the low-pass filter is used. Applying the low-pass filter at lower frequencies (say 3 - 4kHz instead of 5 - 6kHz) results into the saturation of flatness starting from comparatively large scale. Thus, the flatness of the low-pass filtered data saturates at higher flatness value than the unfiltered data as shown in figure V.17. All experiments and numerical simulations of turbulent flows performed so far suggests that the flatness of the PDFs of velocity increment increases as the scale decreases because of the occurrence of large velocity gradients towards smaller scales as compared to a purely Gaussian statistical distribution. On the other hand, looking at the unfiltered curve (see blue and red stars in figure V.17), we see the common trend of increasing flatness up to a certain length scale and then the flatness drops possibly because of the limited spatial resolution of the hot-wire [Chevillard et al., 2012].

A similar plot showing the skewness of the PDFs of velocity increment with respect to $\ln\left(\frac{r}{L}\right)$ is shown in figure V.18 in which a vertical black-dashed line indicates the spatial filter of the hot-wire at $l_w \approx 300\mu m$. In this plot, the skewness is shown only when the low-pass filter is used to filter the data. Again, from this figure, the skewness for the scales larger than L is close to zero which is nothing but the skewness for the Gaussian distribution. After a closer look at the plot of PDFs of velocity increment, we see that all the curves are slightly negatively skewed. We note that the skewness is a signed quantity, always negative as a consequence of irreversibility associated to viscous dissipation. It is observed that the PDF of velocity increment is more negatively skewed for smaller and smaller scales. This is also a peculiar property of classical turbulence as discussed in the past literature [Mordant, 2008]. The same reasoning as for flatness is applicable for the saturated value of the skewness at smaller scales.

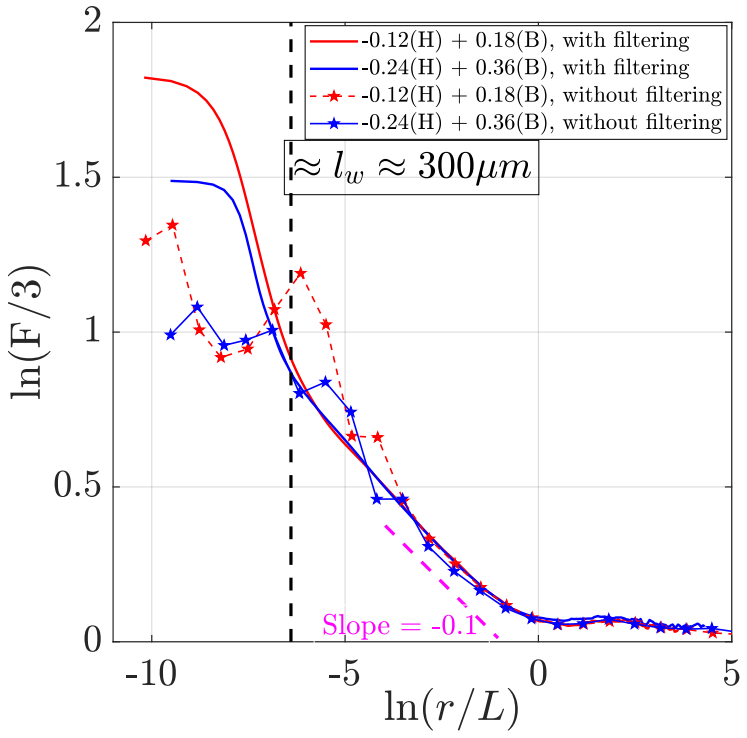

Figure V.17: Flatness of PDFs of velocity increment as a function of scale $\ln\left(\frac{r}{L}\right)$ [ln stands for natural logarithm]

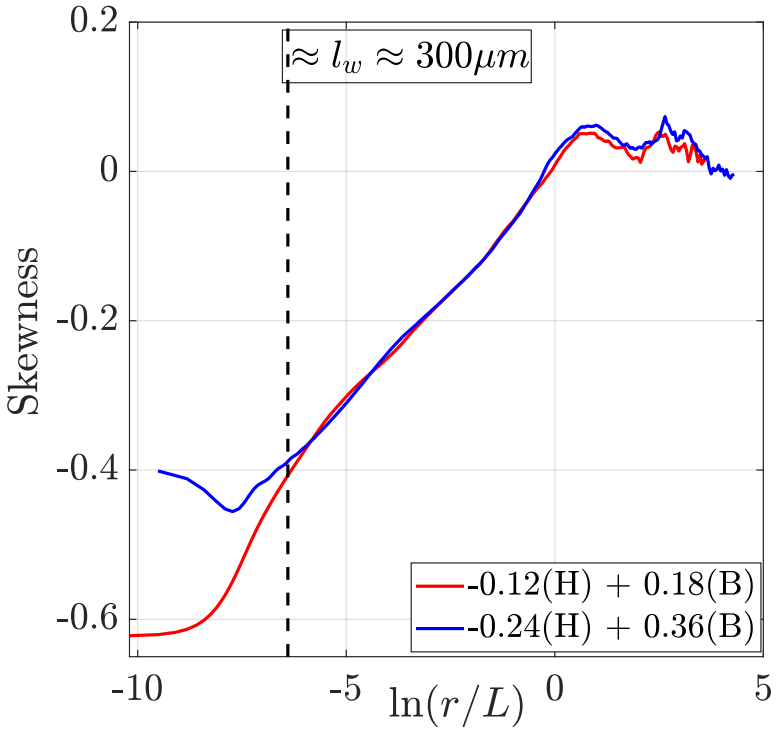

Figure V.18: Skewness of PDFs of velocity increment as a function of scale $\ln\left(\frac{r}{L}\right)$

V.9.2 Dependence of flatness and skewness of PDFs of velocity increments on Re_λ

In the above section, we have seen how the flatness and the skewness of PDFs of velocity increments evolve with respect to scale. We observed that the flatness of the PDFs of velocity increment increases from scale L down to the smallest resolved scale in the measurements. The dependence of flatness with respect to scale has been established very well by many authors [Knebel, 2011], but its dependence on the Re_λ has not been explored for very high Reynolds numbers (> 1000) so far. The dependence of flatness or skewness of PDFs of velocity increment with respect to Re_λ at the smallest scales in dissipation range has been studied by Sreenivasan and Antonia [1997]; Van Atta and Antonia [1980]; Tabeling and Willaime [2002] and Tang et al. [2017]. All these authors have found that the flatness of the PDFs of velocity increments increases with respect to Re_λ, which is only true for the smallest measurable scale in the dissipation range. The analysis presented here belongs to the scales in the inertial range.

Figure V.19 shows the flatness of PDFs of velocity increments with respect to Re_λ on log-log scale. The flatness is plotted for different data sets from A to G as mentioned in table 6, which corresponds to different configurations of the von Kármán flow (while increasing the turbine frequency). To illustrate this, in figure V.19 different representations of flatness with Re_λ are shown either at fixed $\frac{r}{\lambda}$ or at fixed r. At the scale $\frac{r}{\lambda} = 4$ or $\frac{r}{\lambda} = 8$, we see that the flatness of PDFs of velocity increments increases with increase in Re_λ for all the data sets. But, here, it should be noted that either $\frac{r}{\lambda} = 4$ or $\frac{r}{\lambda} = 8$ does not represent the same physical length scale in flows from A to G. In section V.7.1, it is shown that the Taylor microsale decreases as Reynolds number increases, and this means that the physical scale r represented by either $\frac{r}{\lambda} = 4$ or $\frac{r}{\lambda} = 8$ decreases with increase in Re_λ. Therefore, based on the discussion followed from figure V.17, it is apparent that the flatness of PDFs of velocity increment increases for smaller scales. To make this point more observable, the flatness has been plotted at a fixed physical scale of $r = 2mm$ and $r = 10mm$. At $r = 2mm$ or $r = 10mm$, we see that the flatness of PDFs of

velocity increments is relatively constant for each different data set from A to G with respect to increasing Re_λ. This suggests that the flatness is independent of Re_λ at a fixed scale r, provided that the scale r is in the inertial subrange [Chevillard et al., 2012]. This delivers an interesting interpretation of intermittency at a scale r. As long as the scale r is in the inertial range for which the viscous effects are negligible, there is a certain intermittency at this scale, which is independent of the Reynolds number of the flow. This does not simply imply that the flatness of PDFs of velocity increment at the scale r (say $r = 2mm$) is universal, because this value of flatness is dependent on different types of turbulent flows.

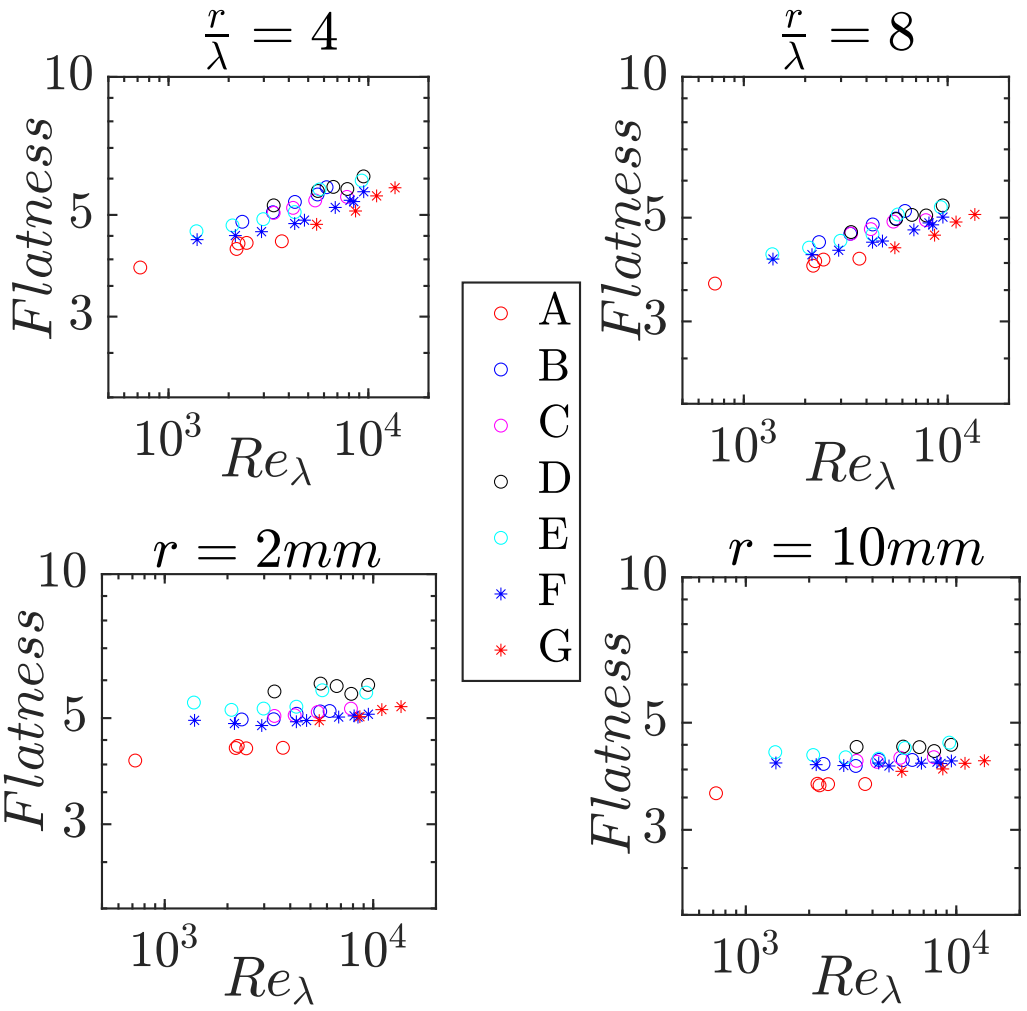

Figure V.19: The dependence of flatness of PDFs of velocity increment on Re_λ for different flow configurations mentioned in table 6

The above interpretation and the description of intermittency can also be fortified using the skewness of PDFs of velocity increments. Figure V.20 shows the skewness for different data sets A to G at $\frac{r}{\lambda} = 4, 8$ and $r = 2, 10mm$ for increasing Reynolds numbers. From this figure, we see that the skewness decreases with increasing Re_λ for all data sets at $\frac{r}{\lambda} = 4$ and $\frac{r}{\lambda} = 8$ (see figure V.18 for more details). On the other hand, as expected, at $r = 2mm$ or $r = 10mm$ the skewness of PDFs of velocity increment is nearly constant for each of the different data sets with

respect to Re_λ [Chevillard et al., 2006]. This shows that in the inertial range the flatness and skewness of PDFs of velocity increments at a certain scale r are linked with a fixed magnitude of intermittency which is independent of the Re_λ and dependent on the type of turbulent flows.

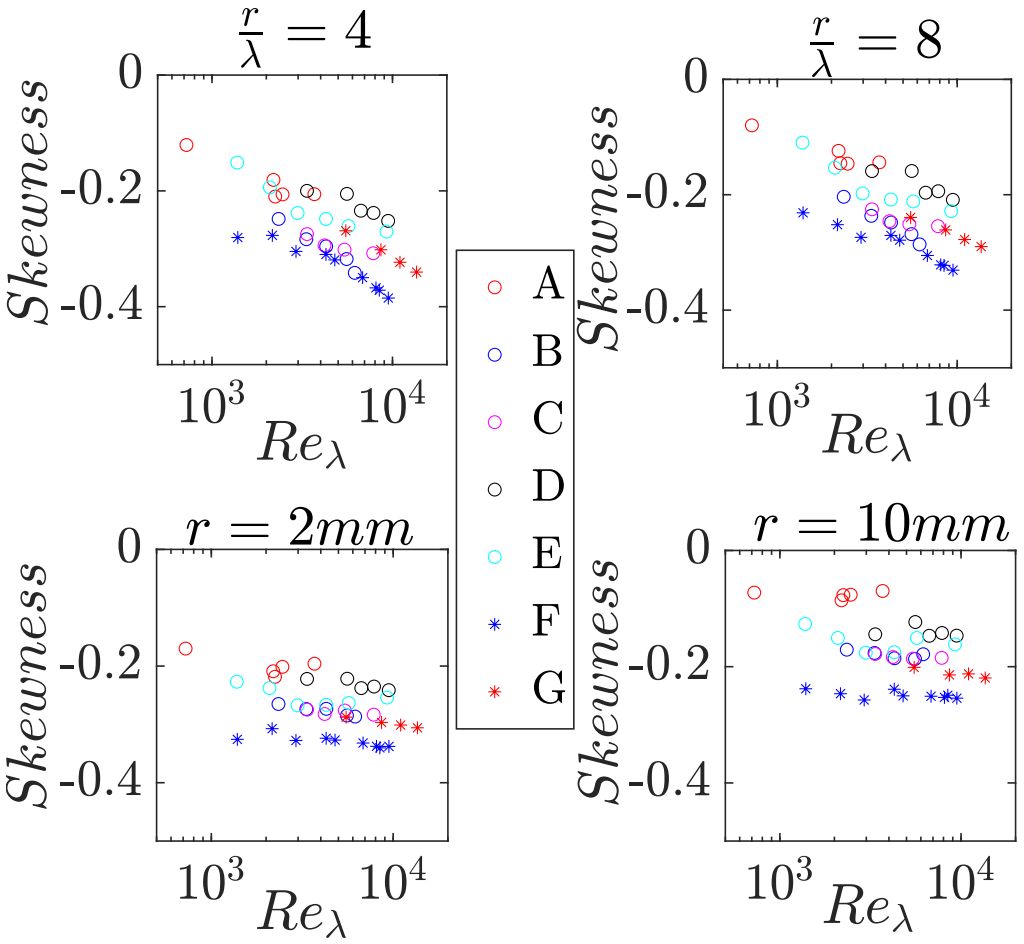

Figure V.20: The dependence of skewness of PDFs of velocity increment on Re_λ for different flow configurations mentioned in table 6

V.9.3 Dependence of scaling exponent ζ_p on Re_λ

Using extended self similarity (ESS), we can estimate the scaling exponent ζ_p for p^{th} order structure functions, knowing that $\zeta_p = 1$ for third order structure function according to the Karman-Howarth equation given by $S_3(r) = -\frac{4}{5}\epsilon r$ (see equation I.13). ESS is a method by which we can extend the domain of the power law behavior and thus to improve the estimation of the scaling exponents [Benzi et al., 1993]. The extended self similarity is expressed by $T_p \propto T_3^{\zeta_p}$ $\propto \langle |u_r|^3 \rangle$, where $T_p(r) = \langle |u_r|^p \rangle$, $\eta << r << L$. $\langle | \cdot | \rangle$ represents an ensemble average of the absolute values. The use of absolute values of the velocity increments is initiated because these structure functions (i.e. T_p) are statistically more stable than the usual structure functions defined without the use of absolute values (i.e. S_p). This is mainly important for the use of odd ordered structure function, as T_p and S_p are exactly identical for even order. Figure V.21 shows the structure functions of order $p = 2$ to 8 as a function of scale r for the contra configuration of SHREK experiment performed with straight blades at $\mathcal{F}_1 = \mathcal{F}_2 = 1.0$Hz. For this configuration, the estimated $L = 0.4$m and $\lambda = 350\mu m$. From figure V.21, we see a very wide inertial range which spans over almost three decades of scale r on the log-log plot.

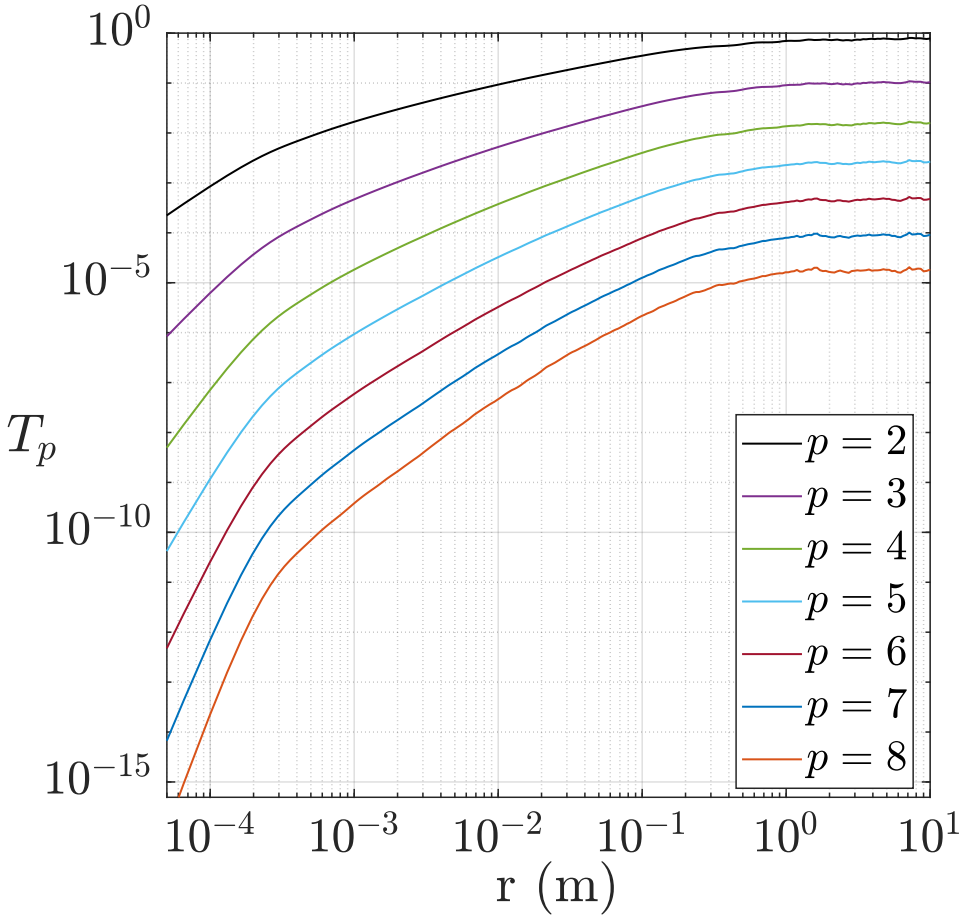

Figure V.21: Structure functions of order $p = 2$ to 8 as a function of scale r for the contra configuration: + 1.0(H) - 1.0(B) in the SHREK experiment performed with straight blades [For clarity the structure functions are shifted arbitrarily in the vertical direction]

To have a better estimate of ζ_p, it is necessary to have huge amount of statistics which needs to be examined for convergence. The statistical convergence test for velocity increments is performed to ensure the best estimate of ζ_p. To ascertain the authenticity of ζ_p up to certain p^{th} order, it is required to look into the convergence of the statistical moment of the velocity increments [Tabeling et al., 1996; Sreenivasan and Schumacher, 2010]. Such a plot for statistical convergence can be made for each p^{th} order velocity increment at each different scale. Figure V.22a shows the evolution of the integrand $(u_r)^p \times PDF(u_r)$ for $p = 10$ at a scale of 31 cm ($\approx \mathcal{O}(L)$), while figure V.22b shows the integrand for $p = 7$ at a scale of $313\mu m$ ($\approx \mathcal{O}(l_w)$). These plots suggest that the convergence is reached even for the 10^{th} order velocity increment for the scales of $\approx \mathcal{O}(L)$. On the other hand, the fluctuating tails can be easily seen in the convergence of integrand for the 7^{th} order velocity increment for the scales of $\approx \mathcal{O}(l_w)$. This suggests that the statistics are not very well converged for the velocity increments of order more than 7 at scales $< 313\mu m$.

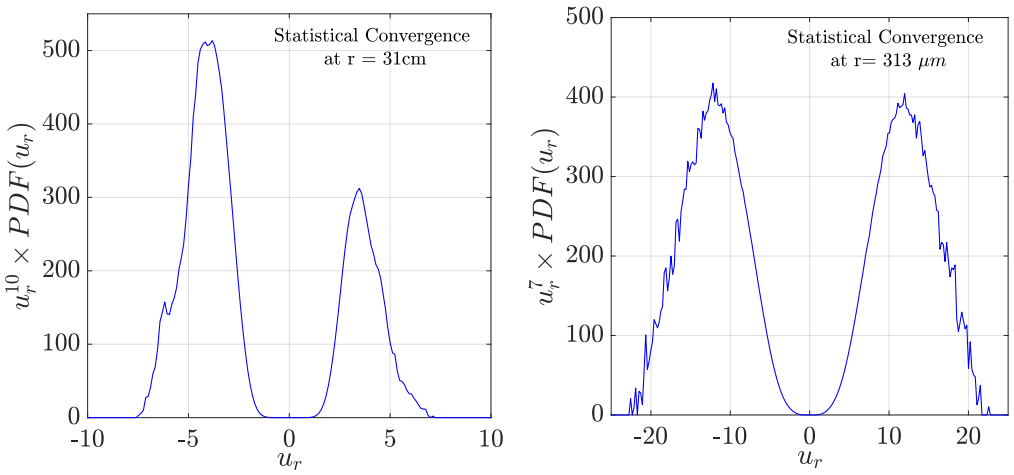

(a) At the scale of the order of length L for 10^{th} order velocity increment

(b) At the scale of the order of η for 7^{th} order velocity increment

Figure V.22: Statistical convergence test

The scaling exponent ζ_p estimated using extended self similarity represents the global intermittency in a sense that ζ_p is estimated from the entire inertial range, whereas the flatness and skewness of PDFs of velocity increments characterize the local intermittency at a particular scale r. Hence, these two approaches are rather different in terms of intermittency interpretation. Different models such as K41, K62, β model and Log-Poisson model have been proposed to describe the dependence of scaling exponents ζ_p as a function of p [Frisch, 1995]. All these models are summarized in table 7.

Table 7: Various intermittency models for the scaling exponent ζ_p

Model	**Scaling exponent** (ζ_p)
K41	$\frac{p}{3}$
K62 or Log-Normal	$\frac{p}{3}$ - $\frac{\mu p(p-3)}{18}$
β	$\frac{p}{3} + (3-D)(1-\frac{p}{3})$
Log-Poisson or She-Leveque	$\frac{p}{9} + 2 - 2(\frac{2}{3})^{p/3}$

The scaling exponents ζ_p for all the data sets are estimated based on the approach of extended self similarity. Figure V.23 shows the demonstration to estimate the scaling exponents for one of the data set in the SHREK experiment, in which p^{th} order structure function $\ln(T_p)$ is plotted against $\ln(T_3)$ for the scales ranging from L down to λ. From this figure, we see a clear power law dependence of $\ln(T_p)$ with respect to $\ln(T_3)$. Based on the ESS method, ζ_p is estimated as the slope of the linear fit of $\ln(T_p)$ as a function of $\ln(T_3)$ in the inertial range of scales. In this figure, the black-dashed lines shows the linear fit for each of the corresponding structure functions. From the visual inspection of figure V.23 we also see that the scaling exponents increase towards higher order. The estimated scaling exponents from figure V.23 are plotted in figure V.26b which corresponds to $Re_\lambda = 13450$.

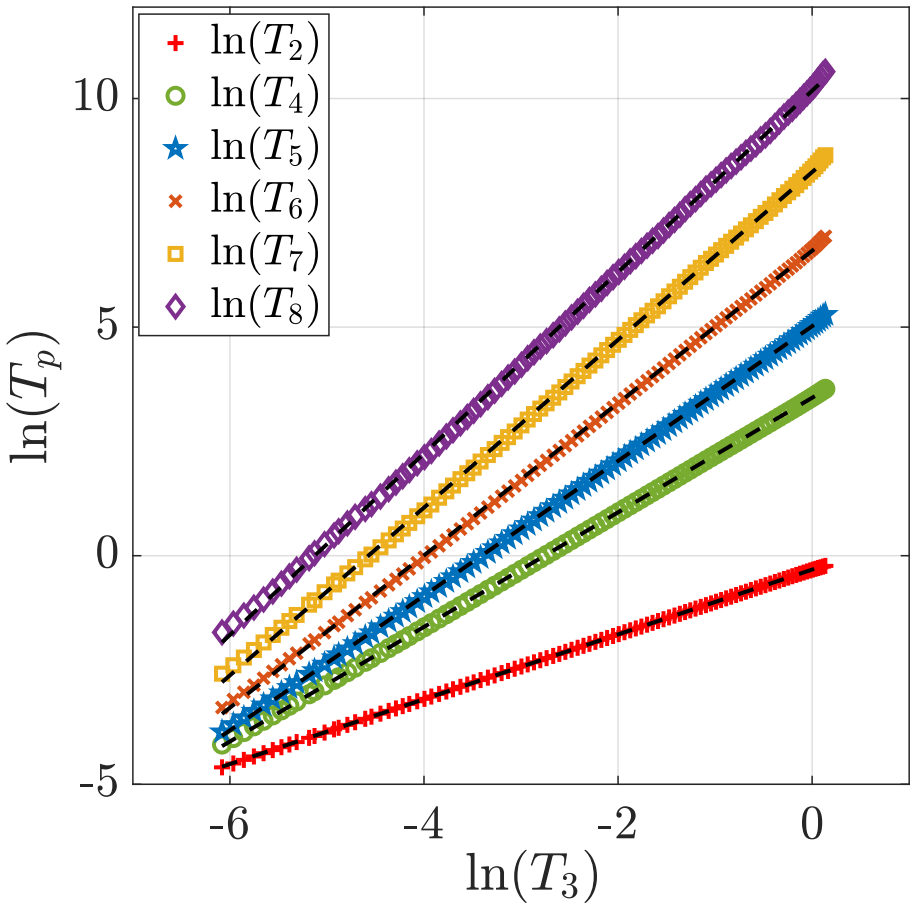

Figure V.23: p^{th} order structure function $\ln(T_p)$ with respect to $\ln(T_3)$ for the scales ranging from L down to λ for the contra configuration: + 1.0 (H) - 1.0 (B) in the SHREK experiment with radial blades [black-dashed line is the linear fit for the corresponding structure function]

The validity of these experimentally estimated scaling exponents can be investigated by observing the constancy of compensated structure functions in the inertial range of scales (see equation I.11). Figure V.24 shows such compensated structure functions from order p = 2 to 7. From this figure we see that all the structure functions compensated with the estimated/correct scaling exponents (not the ones predicted by K41 i.e. $\zeta_p = \frac{p}{3}$) show a constant value i.e. a plateau in the inertial range. We also see that for higher orders say p = 6 and 7 the quality of the plateau starts to deteriorate because of the slightly inaccurate estimation of scaling exponents at high orders which is associated with the limited statistical convergence.

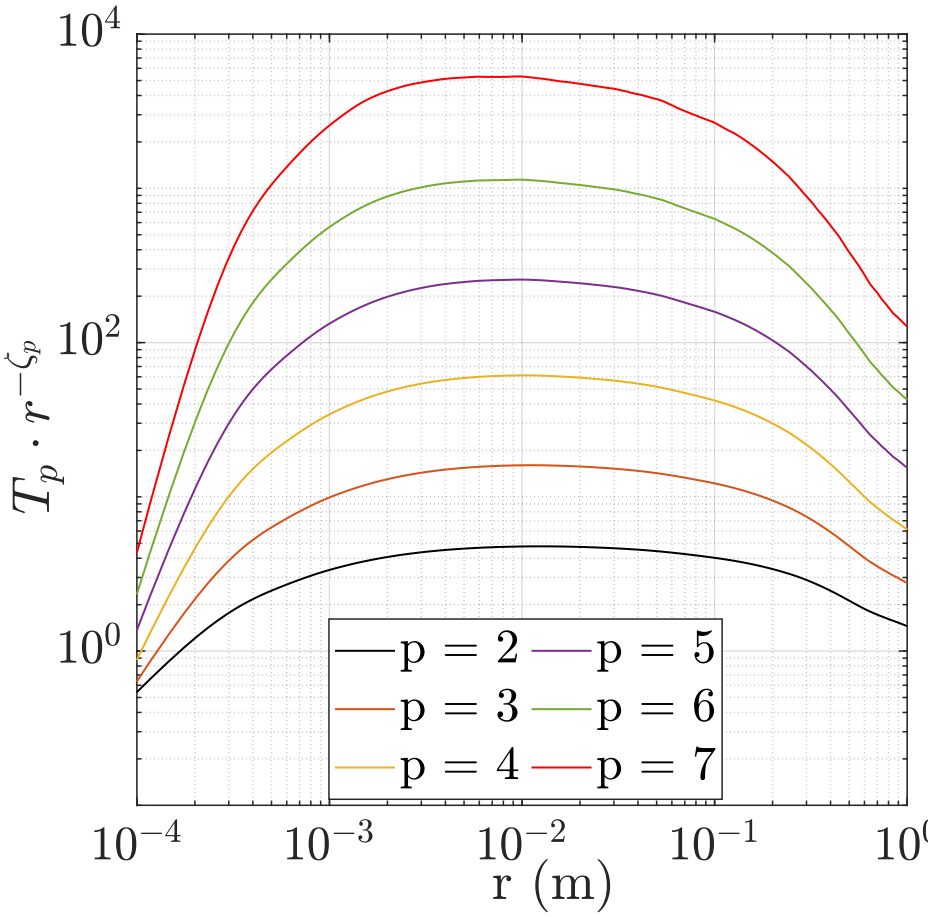

Figure V.24: Compensated structure functions $\left(\text{i.e. } \frac{T_p}{r^{\zeta_p}}\right)$ with respect to scale r [For clarity the structure functions are arbitrarily shifted in the vertical direction].

The scaling exponents estimated from the experimental data are plotted in figure V.25 for different data sets as mentioned in table 6. This figure shows ζ_p up to order $p = 8$. Such analysis is carried out for each type of flow considering the lowest and highest Re_λ ensuring the maximum number of statistics available. For convenience of comparison, the experimentally estimated scaling exponents ζ_p are plotted along with K41, β and log-Poisson model. The experimentally estimated scaling exponents show a significant deviation from the K41 prediction, which describes the phenomenon of intermittency in turbulent flows. From all figures in figure V.25, the dependence of the scaling exponents ζ_p on Re_λ is partly visible. In figure V.25 we also notice that ζ_p increases with increase in Reynolds number which has already been reported by Lundgren [2003]; Antonia et al. [2017]. We see that the scaling exponents at high Reynolds number flows are closer to the K41 model. Such type of behavior is observed for all the flow configurations in the SHREK experiment. The same dependence of ζ_p on Re_λ is also found for the data from another SHREK experiment performed using radial blades as shown in figure V.26.

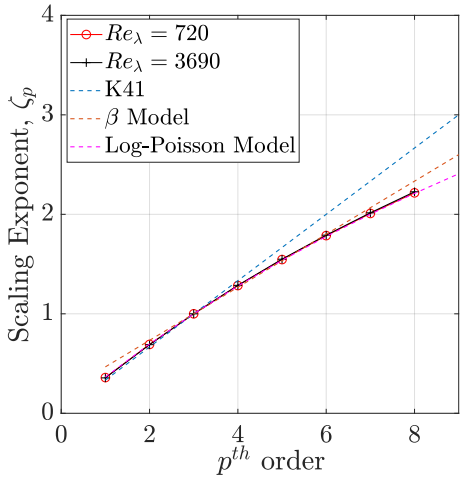

(a) Data set A

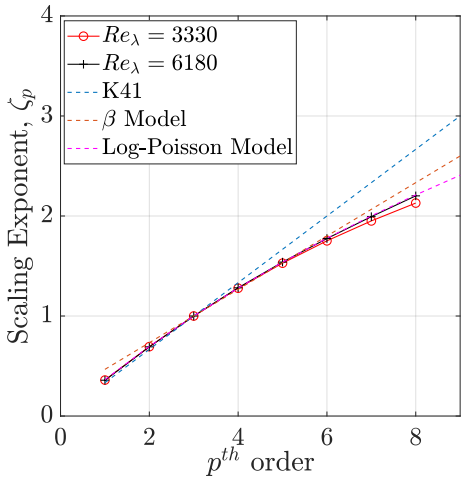

(b) Data set B

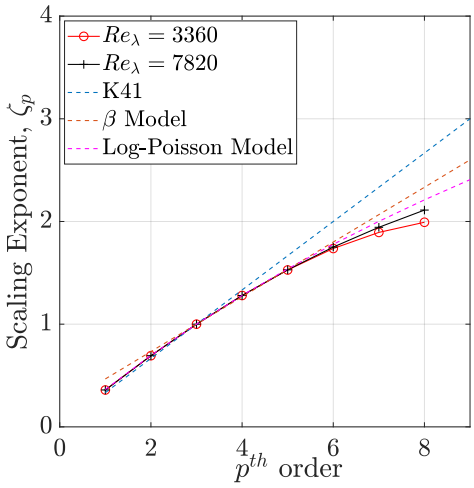

(c) Data set C

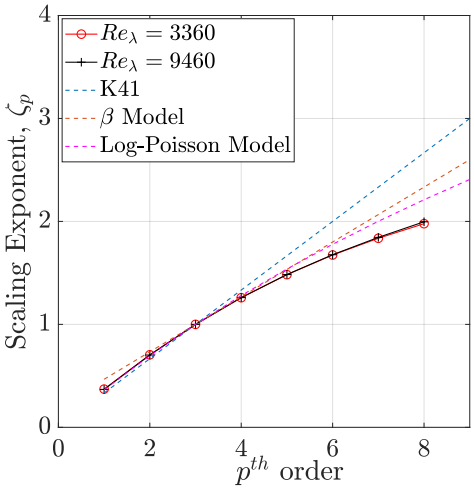

(d) Data set D

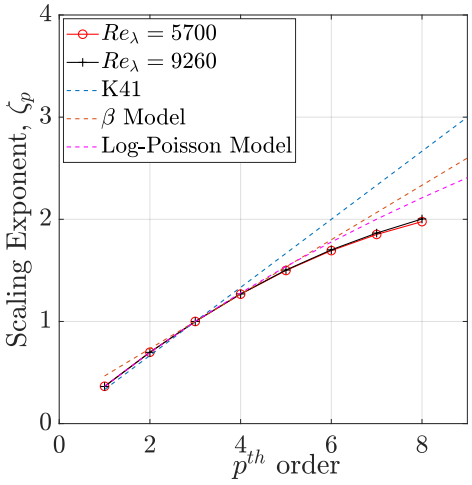

(e) Data set E

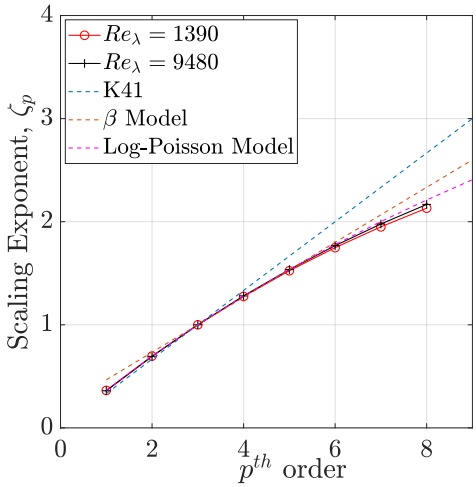

(f) Data set F

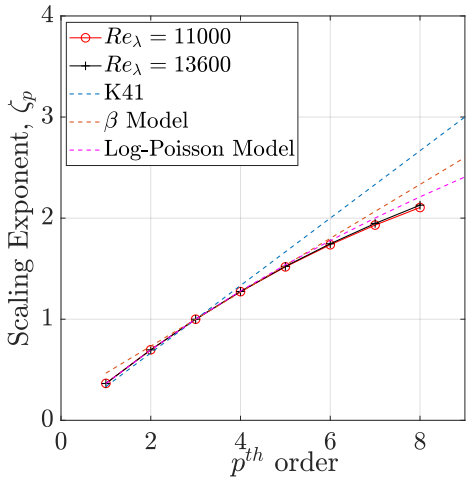

(g) Data set G

Figure V.25: Different intermittency models showing the scaling exponents ζ_p for each of the lower and higher Re_λ flows of data set A to G mentioned in table 6 (SHREK experiment with turbine with curved blades)

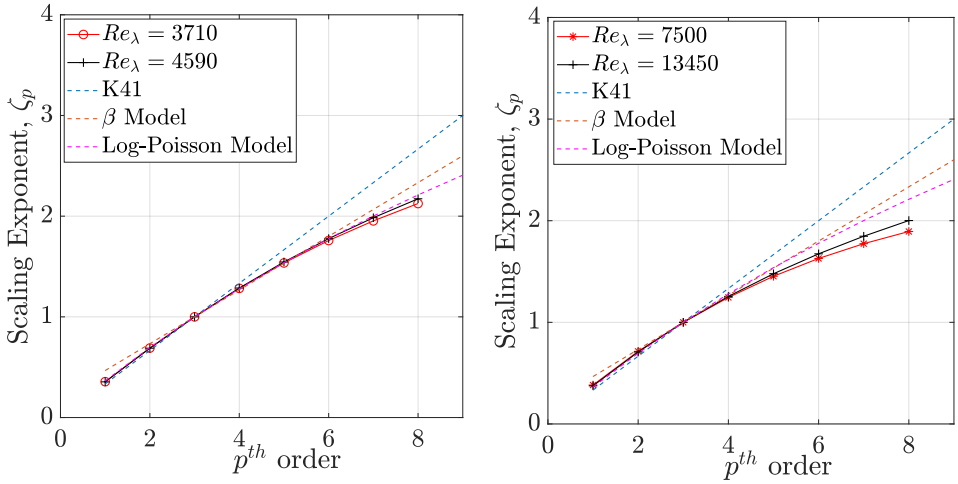

(a) Data set E' (b) Data set G'

Figure V.26: Different intermittency models showing the scaling exponents ζ_p for each of the lower and higher Re_λ flows of data set E' and G' mentioned in table 6 (data set E' and G' belongs to the SHREK experiment with turbine with radial blades)

To make it clear how close the scaling exponents ζ_p are to the K41 model, an experimental fit is implemented for each data set in order to find the K62 intermittency parameter μ, which is defined in table 7 (see also section I.3.1). Figure V.27 shows the demonstration to estimate μ for one of the data sets according to the fit given by: $\zeta_p = \frac{p}{3} - \frac{\mu p(p-3)}{18}$, i.e. the K62 model. The K62 fit shown in this figure gives the parameter $\mu = 0.2460 \pm 0.009$. The intermittency parameter μ is estimated for all the other data sets shown in figure V.25 and figure V.26 in a similar way. Praskovsky and Oncley [1997] studied the dependence of K62 intermittency parameter μ over a very large range of Reynolds number achieved in the atmospheric surface layer measurements. Cleve et al. [2004] also carried out extensive investigation of dependence

of this intermittency parameter on Reynolds number for different types of turbulence flows such as atmospheric boundary layer flows, wind tunnel flows and gaseous helium jet flows. Figure V.28 shows the dependence of the K62 intermittency parameter μ with respect to Re_λ for all configurations of the von Kármán flows studied in SHREK experiment with the turbines with either curved or radial blades. From figure V.28 we see that the intermittency parameter μ decreases with increase in Reynolds number for each of the flow configuration. This indicates that the hypothesis of K41 (i.e. $\mu = 0$) may hold for infinite Re_λ flows [Antonia et al., 2019]. A convergence of intermittency parameter μ towards a value of 0.2 for higher Re_λ flows is also in agreement with the study performed over atmospheric boundary layer data by Praskovsky and Oncley [1997] and Cleve et al. [2004]. Overall, the intermittency parameter μ varies within a range of 0.2 to 0.35 for all von Kármán flows studied here and it also suggests that the value of the intermittency parameter μ depends on the type of flow [Tang et al., 2017].

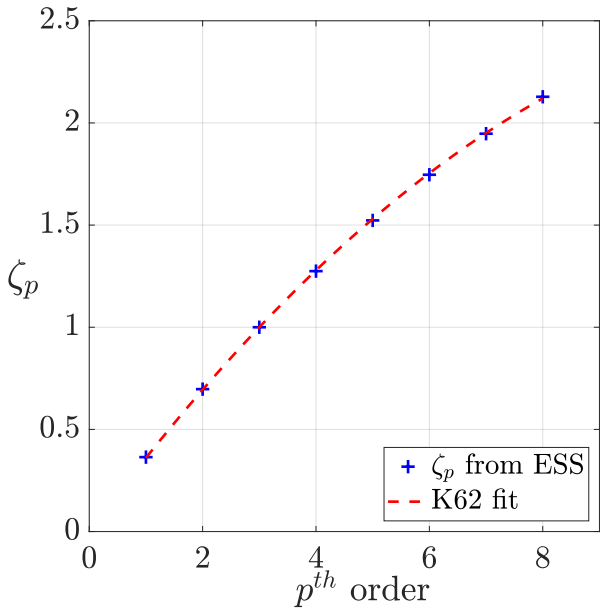

Figure V.27: Estimation of K62 intermittency parameter μ from the scaling exponents ζ_p estimated using ESS for the anti-contra configuration: + 0.6 (H) - 0.6 (B) in the SHREK experiment with curved blades

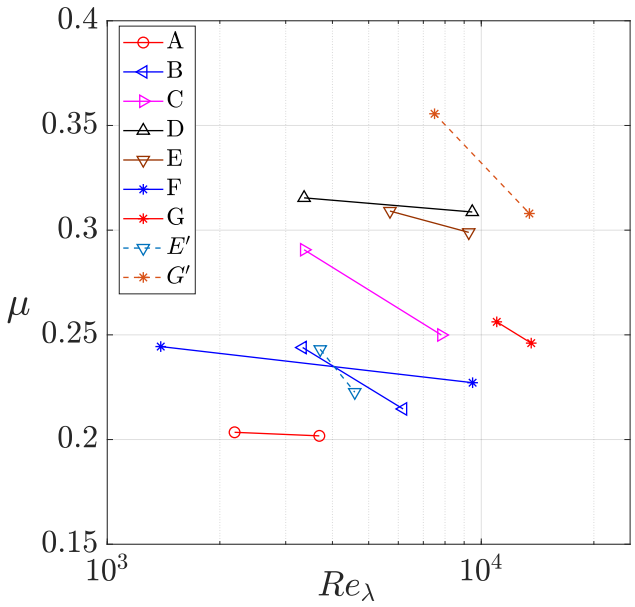

Figure V.28: K62 intermittency parameter μ with respect to Re_λ for the data sets A to G, E' and G' are the data sets using straight blades

V.10 Observations in HeII

Based on the observations in HeII in the HEJET experiment (see figure IV.32) it is then decided to investigate the similar dependence of u_{rms} on the PSD of the hot-wire signal in the SHREK experiment. Huge amount of hot-wire data is available from various SHREK experiments. Out of all these data only the data corresponding to the anti-contra configuration in the SHREK experiment (data set G or G' in table 6) which induces highest u_{rms} is chosen to explore the understanding of the hot-wire signal in superfluid. As mentioned earlier, the terminologies of contra and anti-contra flow configuration are applicable only to the SHREK experiment performed with curved blades (see section V.1.3), whereas in the SHREK experiment performed with straight or fractal blades the contra and anti-contra configuration are exactly the same.

V.10.1 PSD of hot-wire signal

Figure V.29 shows the PSD of the raw hot-wire signal for the anti-contra flow configuration in the SHREK facility ($+\mathcal{F}_1$(H)$-\mathcal{F}_2$(B)). Figure V.29a shows the PSD of raw hot-wire signal in the SHREK experiment performed with radial blades. In this experiment the hot-wire is operated in CCA mode with 21% of overheating. Figure V.29b shows the PSD of raw hot-wire signal in the SHREK experiment performed with fractal blades. Also in this experiment the hot-wire is operated in CCA mode but with only 5% of overheating. Figure V.29c shows the PSD of raw hot-wire signal in the SHREK experiment performed with curved blades. In this experiment the hot-wire is operated in CTA mode with much less overheating of 0.6%. In each of these experiments different but similar sized hot-wires are used. In each of these experiments the hot-wire is installed 4cm above the equatorial plane.

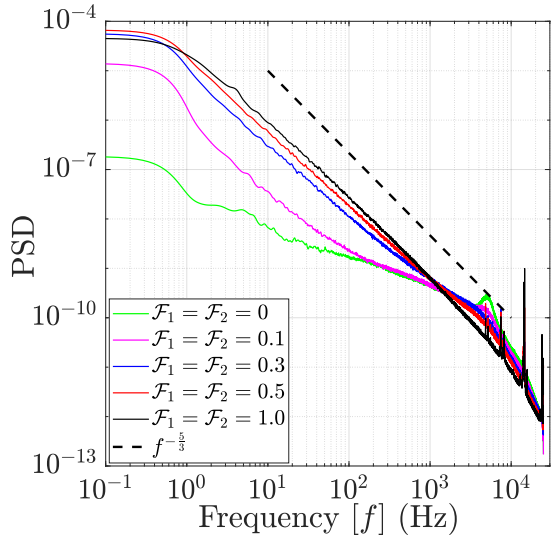

(a) SHREK experiment with radial blades [hot-wire in CCA mode (overheating 21%)]

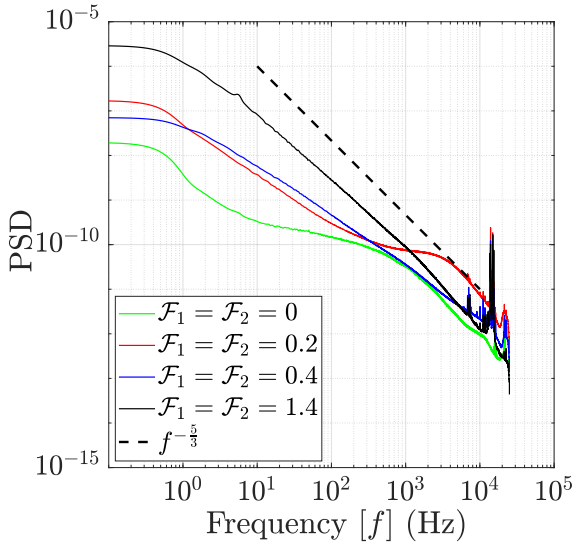

(b) SHREK experiment with fractal blades [hot-wire in CCA mode (overheating 5%)]

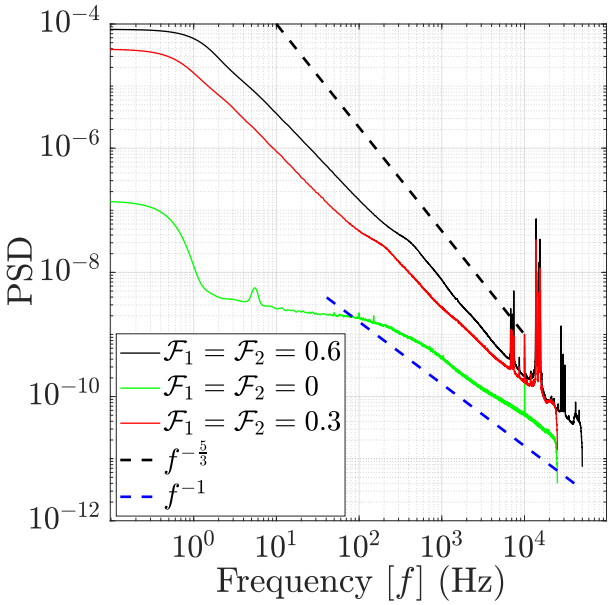

(c) SHREK experiment with curved blades [hot-wire in CTA mode (overheating 0.6%)]

Figure V.29: PSD of the raw hot-wire signal in the anti-contra configurations of the SHREK experiment in HeII at T = 2.0K [$d_w = 1.27\mu m$ and $l_w = 300\mu m$; $\mathcal{F}_1$ and $\mathcal{F}_2$ denotes the frequency of top and bottom turbine respectively (see data set G in table 6 where $\mathcal{F}_1 = \mathcal{F}_1$)]

In figure V.29, the turbine frequency of $\mathcal{F}_1 = \mathcal{F}_2 = 0$ represents the PSD at null velocity. Durì et al. [2015] had observed the PSD of the hot-wire signal with the f^{-1} dependence over the frequency range of 0.1 - 5kHz in the HEJET facility at null velocity while operating the hot-wire in CTA mode. The null velocity PSD in the SHREK facility (see figure V.29c) also shows the f^{-1} dependence over the frequency range of 0.8 - 20kHz. These observations from figure V.29,

specially figure V.29c are in good agreement with the PSD of the hot-wire signal reported by Durì et al. [2015] in the HEJET facility.

All these figures show that the PSD evolves towards $f^{-\frac{5}{3}}$ slope with increase in turbine frequencies. We have also seen the similar observations in the HEJET experiment while increasing the turbine frequency (see figure IV.32). In fact, figure V.29a and figure V.29b show that the PSD follows the classical $f^{-\frac{5}{3}}$ slope at the highest turbine frequency of $\mathcal{F}_1 = \mathcal{F}_2 = 1.0$Hz and $\mathcal{F}_1 = \mathcal{F}_2 = 1.4$Hz respectively. In figure V.29c the $f^{-\frac{5}{3}}$ slope is not attained for the experiment performed using the maximum frequency of $\mathcal{F}_1 = \mathcal{F}_2 = 0.6$Hz, which can be expected at $\mathcal{F}_1 = \mathcal{F}_2 > 0.6$Hz. It is important to mention that in superfluid at 2.0K, the classical $f^{-\frac{5}{3}}$ slope is observed only in the anti-contra flow configuration but neither in contra nor in co-rotation flow configuration. In other words, at the same mean velocity the co-rotation and contra configurations of von Kármán flow do not show the classical $f^{-\frac{5}{3}}$ slope. This confirms that both the mean velocity and the rapid fluctuations (u_{rms}) around the hot-wire are important to detect $f^{-\frac{5}{3}}$ slope in superfluid with the hot-wire. We note that whether the incoming turbulent flow across the hot-wire is of HeI or HeII, in the very close vicinity of the hot-wire (within the boundary layer of the hot-wire) normal fluid always exists. This is because of the temperature gradient between the hot-wire temperature and the incoming fluid temperature.

In classical fluid (HeI) a different overheating (in CCA or CTA mode) does not alter the frequency dependence in PSD. This means that in HeI whether the hot-wire is operated at the overheating of 0.5% or 35%, the classical $f^{-\frac{5}{3}}$ slope will always be retained, which we have found to be not true for HeII. The first observation of K41 spectrum in the inertial range of the superfluid turbulent flow was found by Maurer and Tabeling [1998] with pitot tube. Later, Salort et al. [2010] also found K41 spectrum in the superfluid turbulent flows with cantilever. And recently, it has also been found by Barenghi et al. [2014]. This suggests us that the experimental measurement performed in the SHREK facility at $\mathcal{F}_1 = \mathcal{F}_2 = 1$ in figure V.29a is the accurate description of the superfluid turbulent flow. More importantly, all figures in figure V.29 (including figure III.22 and figure IV.32) lead to the main conclusion which states that in superfluid turbulent flow the classical $f^{-\frac{5}{3}}$ energy decay can be detected in the inertial range using the hot-wire provided that the hot-wire is operated at the least possible overheating and the flow has high turbulence intensity**. Based on our findings at $\mathcal{F}_1 = \mathcal{F}_2 = 1$ in figure V.29a we performed further studies about the statistics and the intermittency related to this superfluid turbulent flow in the SHREK facility, which will be discussed in the following subsections.

V.10.2 Calibration of the hot-wire

To carry out the statistical investigation of the superfluid von Kármán turbulent flow shown in figure V.29a, the calibration of the hot-wire in superfluid at 2.0K is performed based on the procedure mentioned in section II.1. Figure V.30a shows the calibration of the hot-wire in superfluid at 2.0K in the SHREK experiment performed with straight blades. The experimental data points show a clear dependence on the velocity. But, we can see that the King's law is not well satisfied in the superfluid which has also been discussed in section III.3.3. This hot-wire calibration is used to study the anti-contra flow configuration shown in figure V.29a (at $\mathcal{F}_1 = \mathcal{F}_2 = 1$ at which we have observed the classical $f^{-\frac{5}{3}}$ decay in the PSD). Figure V.30b shows the PSD of the velocity signal in normal and superfluid helium which depicts the large inertial range over almost three decades of frequencies. This figure shows that in superfluid the inertial range seems to extend further down to the smaller scales as compared to the normal helium. It also shows spurious frequency peaks beyond 5kHz which could be related to the vibrations

**Anti-contra flow configuration is the flow configuration in the SHREK facility with the highest turbulent intensity (see figure I.6b)

of the experiment or the hot-wire itself. The wider inertial range in HeII can also be expected because the time constant of the hot-wire in superfluid is less than in normal helium (see figure II.13). This hot-wire is operated at the same resistance in both HeI and HeII while overheating the hot-wire at about 18% in HeI and about 21% in HeII. We note that at the same overheating, in HeII the hot-wire response may gets perturbed by a greater extent because of the counterflow turbulence it generates. In other words, when exposed to an external turbulent flow, in HeII the contribution of counterflow turbulence over the hot-wire itself may be significant on contrary to the negligible effect of natural convection of the hot-wire in HeI. This is important because the wider inertial range in HeII as shown in figure V.30b may also be linked to the counterflow turbulence over the hot-wire at higher frequencies ($>$ 1kHz).

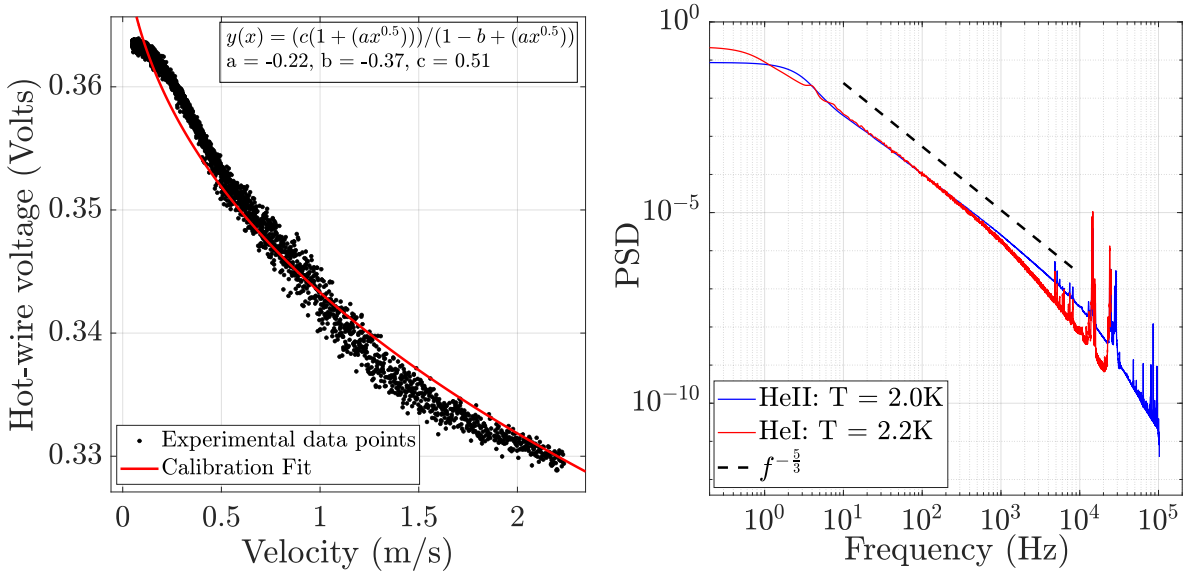

(a) Calibration fit using King's law in HeII in CCA mode

(b) PSD of velocity signal in HeI and HeII

Figure V.30: Calibration of the hot-wire and PSD in HeII at T = 2.0K in the SHREK experiment with straight blades for von Kármán flow configuration: +1.0(H) -1.0(B) [$d_w = 1.27\mu m$ and $l_w = 300\mu m$]

V.10.3 Statistical analysis of velocity signal

The observed classical $f^{-\frac{5}{3}}$ decay in the PSD in superfluid has prompted us to explore this measurement in view of the statistical analysis. The post-processing of the velocity signal in superfluid is performed with the same procedure as applied to the normal helium. The kinematic viscosity of HeII (ν) is estimated from the ratio of dynamic viscosity of HeI (μ) and total density of helium (ρ) at T = 2.0K i.e. $\nu = \frac{\mu}{\rho}$. Figure V.31 shows the compensated third order structure function (S_3) with respect to the scale $\frac{r}{L}$ for the anti-contra configuration of SHREK performed with straight blades in HeI and HeII. This figure shows the compensated S_3 for the highest Reynolds number ($Re_\lambda \approx \mathcal{O}(10^4)$) attained in the SHREK experiment. We believe that the inadequacy to notice a clear plateau in figure V.31 is possibly related to the lack of homogeneity in the von Kármán flows as previously mentioned in section I.6.7. Nevertheless, for the estimation of energy dissipation rate we rely on the maximum value of $-\frac{S_3}{r}$ in figure V.31. From this figure, we see that the energy transfer rate in the inertial range is almost equal in HeI and HeII. Some of the statistical quantities for this anti-contra configuration in HeI and HeII are summarized in

table 8.

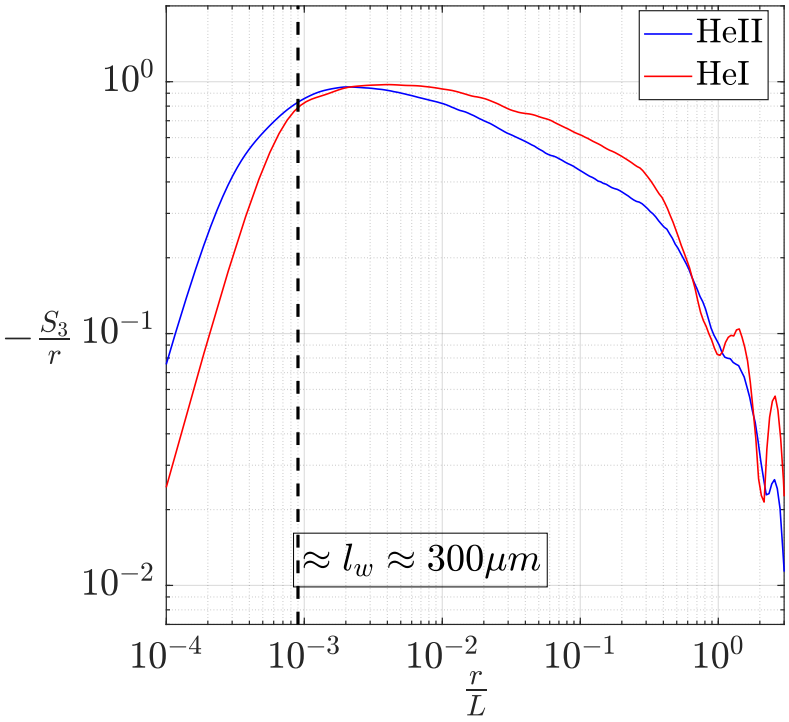

Figure V.31: Third order structure function S_3 compensated by the scale r with respect to the scale $\frac{r}{L}$ for HeI and HeII in the SHREK experiment performed with straight blades for the anti-contra flow configuration: + 1.0(H) - 1.0(B) [A vertical black-dashed line indicates the spatial filter of the hot-wire at $l_w \approx 300\mu m$].

Table 8: Summary of the statistical quantities in HeI and HeII for the anti-contra configuration: +1.0(H) - 1.0(B) in the SHREK experiment performed with straight blades

	T (K)	$\langle U \rangle$ (m/s)	$\mathcal{I}$ (%)	ϵ (W/kg)	L (m)	λ (μm)	Re_λ $\times 10^4$	μ (K62)	d_{22} at $\frac{r}{\lambda}$=4	$\langle \Delta S_{tot} \rangle$
HeI	2.2K	1.87	40	1.22	0.40	383	1.34	0.30	0.02	0.75
HeII	2.0K	1.28	44	1.19	0.27	206	1.19	0.10	0.01	0.63

Considering the lack of proper hot-wire calibration in superfluid slight discrepancy in the statistical quantities may be expected while comparing with HeI. The mean velocity of the signal is much less in HeII than in HeI, which also explains the increased turbulence intensity in HeII. The energy transfer rate estimated from the third order structure function is found to be almost the same in HeI and HeII which is in good agreement with the study performed by Salort et al. [2012]. On the other hand, the inertial scale, Taylor microscale and Re_λ in HeII are found to be less than in HeI. The large eddy turnover time can be estimated from the raw hot-wire voltage signal. In both HeI and HeII it is found to be equal to 0.22 $\pm$0.01s which shows that the input forcing in both HeI and HeII is same [Salort et al., 2010]. Because of the lower effective kinematic viscosity of HeII we expect Re_λ to be higher in HeII than HeI, but the uncertainty associated with the estimated u_{rms} and λ resulted into lower Re_λ for HeII. Table 8 also shows the intermittency parameter μ for the superfluid turbulent flow which will be discussed in the following subsections. The parameters d_{22} and $\langle \Delta S_{tot} \rangle$ will be discussed in next chapter.

V.10.4 Study of intermittency

In order to study the phenomenon of intermittency in superfluid a similar approach is used as in normal helium. Figure V.32a shows the PDFs of velocity increments at different scales for the anti-contra configuration of von Kármán flow in superfluid at T = 2.0K. This figure shows the classical behavior of the PDFs of velocity increments which is characterized by the long expanding tails towards the small scales. This figure also shows that at large scales the PDF of velocity increments shows nearly Gaussian distribution. Figure V.32b shows the flatness of the PDF of velocity increment in superfluid with its comparison with normal helium. This figure shows that up to a certain scale in the inertial range the flatness shows the same dependence with respect to scale which also follows the well known slope of -0.1 in the near inertial range. But on the other hand, towards smaller scales, we see that the flatness increases less rapidly in superfluid than in normal helium. This has also been observed by Biferale et al. [2018], where they performed the numerical analysis and found that the flatness of the PDF of velocity increments at a fixed scale is less for the superfluid component than for the normal component at T = 2.0K. Altogether, figure V.32 gives the clear indication that the intermittency also exists in the turbulent superfluid flow, at least in the inertial range investigated here.

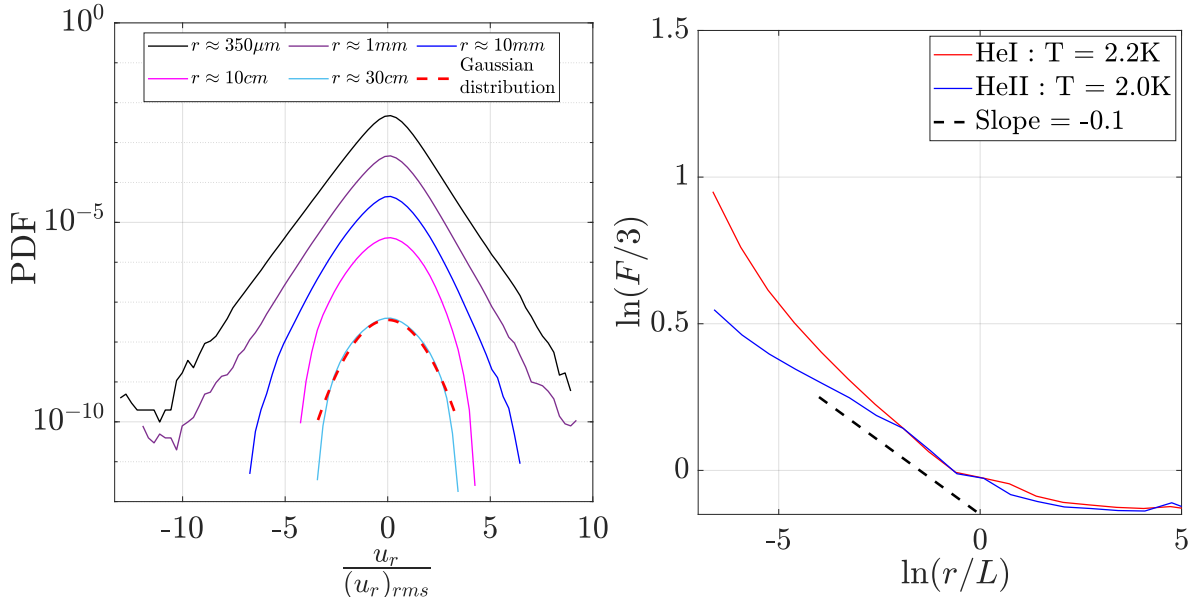

(a) PDFs of velocity increment at various scales in HeII [For clarity the PDFs are arbitrarily shifted in the vertical direction]

(b) Flatness of PDFs of velocity increment with respect to the scale [ln stands for the natural logarithm]

Figure V.32: Phenomenon of intermittency in superfluid at T = 2.0K

V.10.5 Structure functions and scaling exponents

Figure V.33 shows the structure functions of order 2 to 7 with respect to the scale r for the superfluid turbulent flow. For clarity the structure functions are arbitrarily shifted in vertical direction. From these structure functions we can observe the inertial range over the span of the scales varying from $\approx 0.3m$ down to $\approx 200\mu$m. Qualitatively, these structure functions in superfluid demonstrate the classical behavior as always observed in HeI. To detect the possible deviation of the structure functions in HeII with respect to HeI, scaling exponents are estimated.

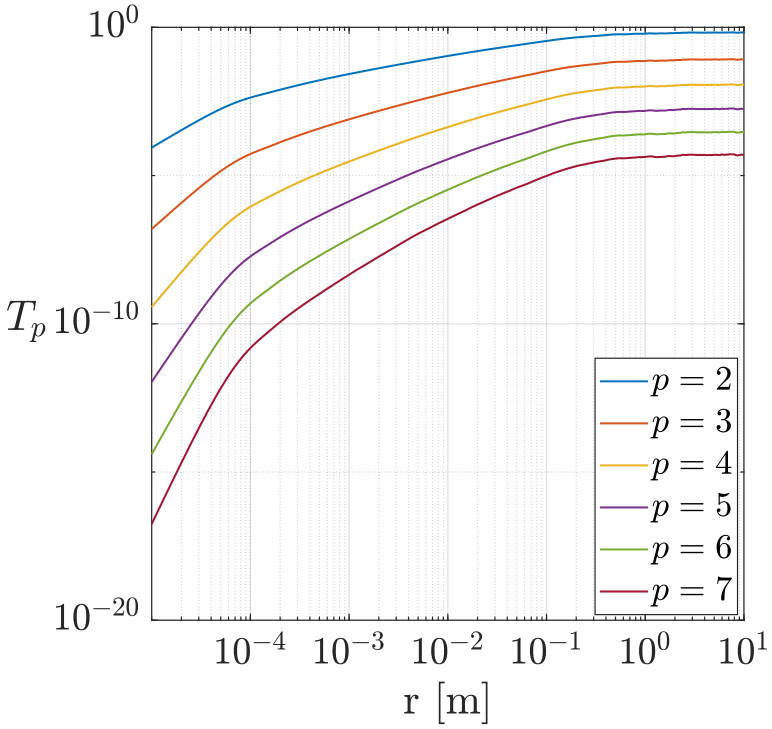

Figure V.33: p^{th} order structure function T_p for order p = 2 to 7 in HeII at T = 2.0K [For clarity the structure functions are shifted arbitrarily in the vertical direction]

The estimated scaling exponents ζ_p based on ESS are shown in figure V.34 for HeI and HeII. Based on the estimated ζ_p, K62 intermittency parameter μ is found to be 0.10 for HeII and 0.30 for HeI which shows the inclination of ζ_p towards K41 for superfluid turbulent flows. Such a less intermittent behavior of superfluid turbulent flow at T = 2.0K had also been reported by Shukla and Pandit [2016]. From figure V.25, figure V.26 and figure V.34, we observe that in HeI the estimated ζ_p are always less than the ones proposed by the β and Log-Poisson model. On the other hand, in HeII we observe that the estimated ζ_p are higher than the ones proposed by the β and Log-Poisson model.

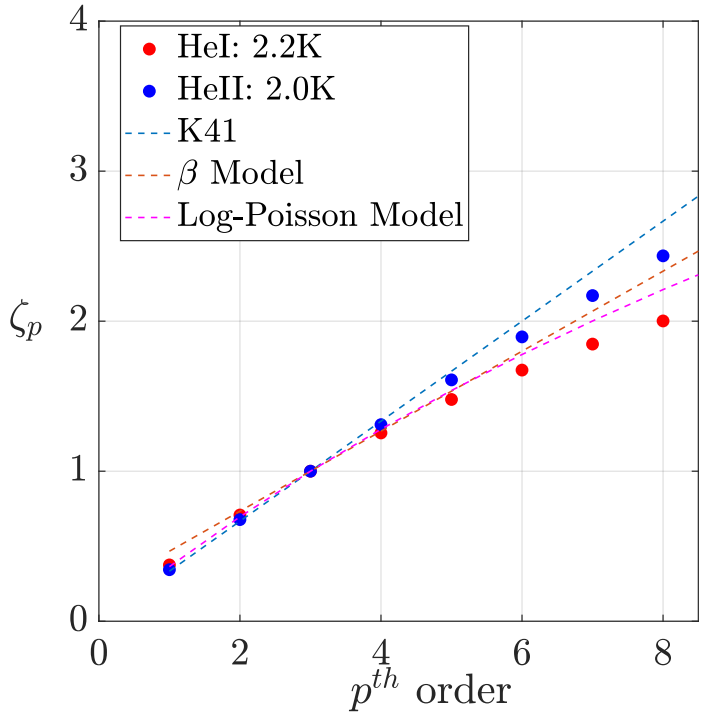

Figure V.34: Estimation of scaling exponents ζ_p based on ESS in HeI and HeII and its comparison with other intermittency models

V.11 Conclusion

Multiple SHREK experiments are performed with turbines with curved, fractal and straight blades to investigate the von Kármán flows in HeI at T = 2.2K and in HeII at T = 2.0K. Local hot-wire measurements are carried out to measure instantaneous velocity in the von Kármán cell. A detailed investigation of the statistics of von Kármán flow is performed for co-rotation, contra and anti-contra flow configuration. The effects of forcing in terms of input turbine frequency on the energy dissipation and Kolmogorov scale are discussed. The maximum amount of energy dissipation is found to be for anti-contra configuration. The estimated Kolmogorov scale in the SHREK experiment lies within $1 - 25\mu m$. It is shown that the measured injected power in the von Kármán cell is of the same order of magnitude with the estimated dissipated power from the hot-wire measurements. It is found that the dimensionless dissipated power per unit mass shows an asymptotic value with respect to Reynolds number. The various laws of scaling applicable to classical turbulence are validated in case of HeI turbulence at 2.2K, which validates the reliability of the SHREK experiment along with the hot-wire measurements. The very high Re_λ achieved in the SHREK experiment ensured the maximum of $\frac{\lambda}{\eta} \approx 200$, $\frac{L}{\eta} \approx \mathcal{O}(10^5)$ and $\frac{L}{\lambda} \approx 1000$.

A first analysis of the phenomenon of intermittency in the inertial range is performed for the cryogenic turbulence in HeI at T = 2.2K. This is demonstrated using the PDFs of velocity increments at different scales within the inertial range. These PDFs indicate the growing departure from Gaussian distribution towards smaller scales, which is quantified using its flatness and skewness. It is found that the flatness of the PDFs of velocity increments increases towards small scales, while the skewness grows negatively towards smaller scales. The universal slope (≈ -0.1) of flatness of PDFs of velocity increment near the inertial range is observed. We found that the skewness and the flatness of the PDFs of velocity increments at a fixed scale r in the

inertial range is independent of the Re_λ, but depends on the type of flow configuration. The scaling exponents ζ_p of the structure functions are explored based on the method of extended self similarity. The scaling exponents show a significant inclination towards K41 with increase in Re_λ. A comparison of those scaling exponents with the other proposed models is also shown. Based on the estimated scaling exponent using ESS, the K62 intermittency parameter μ is estimated for all types of the von Kármán flows. We found that the intermittency parameter μ shows a tendency to decrease with increase in Re_λ which strongly depends on the type of flow.

The hot-wire response in superfluid von Kármán flows at T = 2.0K shows that the PSD evolves with increase in the turbine frequency, which indicates the inclination towards the classical $f^{-\frac{5}{3}}$ slope. Similar observations are noticed in three different SHREK experiments for the most turbulent anti-contra flow configuration. While operating the hot-wire in both CCA and CTA mode in the SHREK experiment, the classical $f^{-\frac{5}{3}}$ decay is observed at higher turbine frequencies. From these observations, we conclude that the classical $f^{-\frac{5}{3}}$ decay in the inertial range of superfuid turbulent flow can be measured by the hot-wire, given that the flow has very high velocity fluctuations (u_{rms}).

Noticing the classical $f^{-\frac{5}{3}}$ decay in superfluid at T = 2.0K for the anti-contra flow configuration (+1.0(H)-1.0(B)) in the SHREK experiment, further studies are performed in the perspective of statistics and the phenomenon of intermittency. For this purpose the hot-wire calibration is performed which shows that the King's law is not well satisfied in superfluid. The energy transfer rate estimated from the third order structure function shows similar values in HeI and HeII. The phenomenon of intermittency is observed in superfluid and its comparison with HeI is performed. It is found that towards smaller scales the flatness of PDFs of velocity increments increases slowly in HeII than in HeI. The structure functions in HeII are showed and the scaling exponents of the structure functions are estimated based on the method of extended self similarity. The scaling exponents in HeI and HeII are found to be lower and higher than the ones proposed by β and Log-Poisson model respectively. It is found that K62 intermittency parameter μ is higher in HeI than in HeII. This indicates an inclination towards K41 in HeII. Overall, the statistical investigation of superfluid von Kármán flow suggests that the interplay of energy cascade and intermittency in the inertial range is similar to the classical fluids.

VI DESCRIPTION OF TURBULENT CASCADE USING FOKKER-PLANCK EQUATION IN THE SHREK EXPERIMENT

We have seen that in turbulent flows the injected energy at large scale transfers towards smaller scales according to the Kolmogorov spectrum with a power law $k^{-\frac{5}{3}}$. However, the third order structure function does not exhibit the clear plateau which we would expect from the high value of the Reynolds number: indeed, this is in a great extent due to the finite resolution of the hot wire anemometer: its length usually allows to resolve scales up to the Taylor microscale. From this follows that only a limited part of the inertial range is available to study intermittency. This is the reason, why our interest was raised by a Fokker-Planck description of the cascade, as it was observed in earlier studies that this process can be viewed as a Markov process in scale, for scales above a certain scale (the Einstein-Markov length), of the order of Taylor microscale. Also, the usual approach of the structure functions to study intermittency assumes power law scaling in the inertial range whereas the use of Fokker-Planck model does not imply any power law assumption. In this chapter, our objective is therefore to use this alternative method to evidence intermittency in the turbulent cascade. In order to apply the Fokker-Planck approach, it is necessary to first verify that the cascade fulfills a Markov property in scale. Once this is verified, the drift and diffusion coefficients – which are sufficient to describe the cascade process – are derived, and their dependence on the scale and velocity increment are calculated.

The fulfillment of Markov property is an essential criterion to use the Fokker-Planck approach on any random process such as the turbulent cascade. We have attempted to perform the Fokker-Planck analysis for the experimental data in the HEJET facility. But, in contrast to other jet flows studied in the literature we found that in the HEJET experiment, Markov property ceases to hold. In other words, the turbulent cascade process in the jet flow of the HEJET experiment is not a memoryless process. We believe that this may be related to the lack of Gaussian distribution at large scales, which is originating from the instability of the jet flow in the HEJET facility. Because of this reason, we could not perform the Fokker-Planck analysis in the HEJET experiment. Nevertheless, we found that Markov property do hold for the turbulent cascade process in the SHREK experiment, where we always have Gaussian distributions at large scales. Therefore, we analyzed the experimental hot-wire data from the SHREK experiment in order to derive the drift and diffusion coefficients for the numerous experiments performed in the SHREK facility, essentially in normal helium. Based on this study, the description of the turbulent cascade is presented. We compare different flows with various Reynolds numbers. Such analysis using Fokker-Planck equation is performed over a very large range of Re_λ = 720 -13600 which has never been explored so far.

VI.1 The turbulent cascade as a Markov process

VI.1.1 Markov process

Let us consider a random variable X with its realizations $x_n, x_{n-1}, x_{n-2}, ..., x_0$ at time $t_n > t_{n-1} > t_{n-2} > ... > t_0$ respectively. Given the joint probability density function $p(x_n, t_n; x_{n-1}, t_{n-1})$ the conditional probability density function $p(x_n, t_n|x_{n-1}, t_{n-1})$ is defined as:

$$p(x_n, t_n|x_{n-1}, t_{n-1}) = \frac{p(x_n, t_n; x_{n-1}, t_{n-1})}{p(x_{n-1}, t_{n-1})}, \tag{VI.1}$$

where $p(x_n, t_n|x_{n-1}, t_{n-1})$ denotes the conditional probability density function for realization x_n at time t_n given the realization x_{n-1} at time t_{n-1}. Similarly, higher order conditional probabil-

ities can be defined based on the following expression:

$$p(x_n, t_n|x_{n-1}, t_{n-1}; ...; x_0, t_0) = \frac{p(x_n, t_n; x_{n-1}, t_{n-1}; ...; x_0, t_0)}{p(x_{n-1}, t_{n-1}; ...; x_0, t_0)}. \tag{VI.2}$$

A stochastic process of a random variable X in time t is a Markov process, if the conditional probability density functions fulfill the following criteria [Van Kampen, 2007]:

$$p(x_n, t_n|x_{n-1}, t_{n-1}) = p(x_n, t_n|x_{n-1}, t_{n-1}; x_{n-2}, t_{n-2}; ...; x_0, t_0). \tag{VI.3}$$

We see that on the right hand side of equation VI.3 we need information at all times whereas on the left hand side only two recent realizations of the variable X are sufficient to express the conditional probability. This explains the physical interpretation of the Markov property described by equation VI.3 as a memoryless process in time. But, for any realistic Markov process the criteria mentioned by equation VI.3 is only valid for two realizations of the variable X over a time $\Delta t > t_{EM}$, where t_{EM} can be referred as the Einstein-Markov time scale [Nickelsen, 2014].

VI.1.2 Historical approach: Chapman-Kolmogorov equation

A direct consequence of the Markov property described by equation VI.3 is the Chapman-Kolmogorov equation given by [Van Kampen, 2007]:

$$\begin{aligned} p(x_n, t_n|x_{n-2}, t_{n-2}) &= \int p(x_n, t_n|x_{n-1}, t_{n-1}) p(x_{n-1}, t_{n-1}|x_{n-2}, t_{n-2}) dx_{n-1}, \\ &\vdots \\ p(x_2, t_2|x_0, t_0) &= \int p(x_2, t_2|x_1, t_1) p(x_1, t_1|x_0, t_0) dx_1. \end{aligned} \tag{VI.4}$$

The Chapman-Kolmogov equation states that the conditional (i.e. transition) probability from time t_{n-2} to t_n can be subdivided into conditional probabilities from time t_{n-2} to t_{n-1} and then from time t_{n-1} to t_n. Equation VI.4 can be written for any two realizations of variable X within initial time t_0 up to final time t_n, which eventually forms a Markov chain.

For the first time, Friedrich and Peinke [1997a] checked the fulfillment of the Chapman-Kolmogorov equation on the experimental turbulence data. They considered the velocity increments u_r at scale r in the turbulent cascade being the random variable in the Chapman-Kolmogorov equation. And, they found that the turbulent cascade indeed obeys the Chapman-Kolmogorov equation in scale. As non-Markovian processes which fulfill the Chapman-Kolmogorov equation are rare, they concluded that the turbulent cascade was a Markov process. We note that this Markov process in the turbulent cascade is not in time but in scale. The initial condition (i.e. u_r) is taken at integral length scale which evolves towards smaller scales. The Chapman-Kolmogorov equation expressing the stochastic process of velocity increment u_r in scale r is expressed by [Friedrich and Peinke, 1997a,b; Naert et al., 1997]:

$$\begin{aligned} p(u_{r_1}, r_1|u_{r_3}, r_3) &= \int p(u_{r_1}, r_1|u_{r_2}, r_2) p(u_{r_2}, r_2|u_{r_3}, r_3) du_{r_2}, \\ p(u_{r_1}|u_{r_3}) &= \int p(u_{r_1}|u_{r_2}) p(u_{r_2}|u_{r_3}) du_{r_2}. \end{aligned} \tag{VI.5}$$

with $r_1 < r_2 < r_3$. In what follows, we use the short notation $p(u_{r_1}|u_{r_3})$ (instead of $p(u_{r_1}, r_1|u_{r_3}, r_3)$) for the conditional probability density function (CPDF) of the velocity increment u_{r_1} at scale r_1 given that the velocity increment u_{r_3} at scale r_3. Above equation describes the transition

probability of velocity increment u_{r_3} at scale r_3 to u_{r_1} at scale r_1. The interpretation of above Chapman-Kolmogorov equation is that we can estimate a CPDF $p(u_{r_1}|u_{r_3})$ which can be subdivided into a transition from r_3 to r_2, and then from r_2 to r_1. In other words, it depicts the memoryless process in the turbulent cascade from larger scale r_3 to a smaller scale r_1 for the scale separation $\delta = r_2 - r_1 = r_3 - r_2$. Figure VI.1 shows the CPDFs estimated from both sides of the equation VI.5 for the SHREK experimental data. This figure shows that for the most part of u_{r_1} and u_{r_3} equation VI.5 holds. Some deviations at extremities are visible possibly because of the lack of statistical convergence. Such validity of Chapman-Kolmogorov equation is checked for multiple triplets of r_1, r_2 and r_3 within the turbulent cascade from inertial scale down to Taylor microscale. Therefore, from figure VI.1 we confirm that in the SHREK experiment the turbulent cascade fulfill the Chapman-Kolmogorov equation, and is very likely to be a Markov process. However, Friedrich and Peinke [1997a] verified that Markov property is fulfilled for the scale separation greater than Einstein-Markov length (see next section).

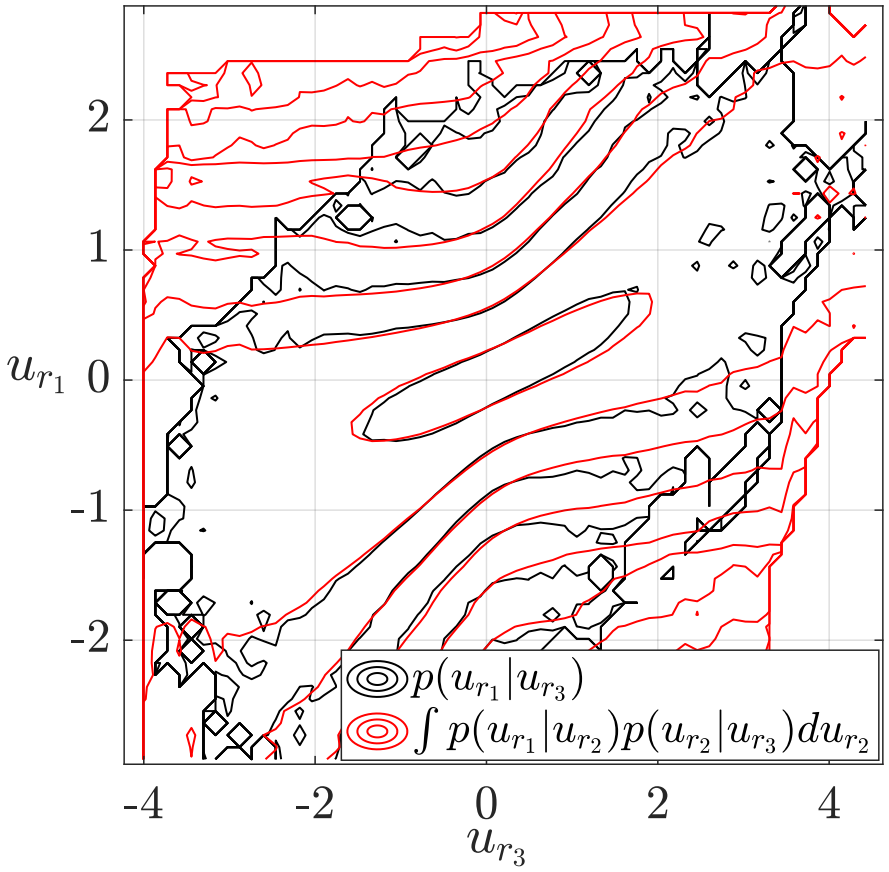

Figure VI.1: Fulfillment of Chapman-Kolmogorv equation (i.e. Markov property) for the SHREK experimental data [$\lambda \approx 400\mu m$, $r_1 = \lambda$ and $\delta = \lambda$]

VI.1.3 Further tests of the Markovian property

In addition to the use of Chapman-Kolmogorov equation we can also apply two other methods used in the literature to validate a Markov process within the turbulent cascade. These two methods are described in the following sections.

VI.1.3.1 Wilcoxson test

Quantitatively, the Markov property can be checked using a statistical test called Wilcoxson test [Renner et al., 2001; Lueck et al., 2006]. The Wilcoxson test compares two empirically determined conditional PDFs. Moreover, it allows to determine the smallest scale for the validity of the Markov property. To perform this test, two data sets of the velocity increments named as x and y are created such that:

$$\begin{aligned} x(u_{r_2}, r_1, r_2) &= u_{r_1}|_{u_{r_2}}, \\ y(u_{r_2}, u_{r_3}, r_1, r_2, r_3) &= u_{r_1}|_{u_{r_2}, u_{r_3}}, \end{aligned} \tag{VI.6}$$

where $r_1 < r_2 < r_3$ and the scale separation $\delta = r_2 - r_1 = r_3 - r_2$ with $\delta > 0$. The data sets x and y contain N and M number of elements respectively. The x and y data are sorted in an ascending order and the number of inversions are counted for each y value. If the Markov property holds the total number of inversions Q has the expectation value $\langle Q_e \rangle = \frac{MN}{2}$ and the standard deviation $\sigma_e = \sqrt{\frac{MN(M+N+1)}{12}}$. The quantity defined by $\Delta Q = \frac{|Q - \langle Q_e \rangle|}{\sigma_e}$ has a mean value equal to $\sqrt{2/\pi}$. If the Markovian properties are fulfilled the expectation value of $\Delta Q^* = \frac{\Delta Q}{\sqrt{2/\pi}}$ should be equal to one. Therefore, the quantity $\langle \Delta Q^* \rangle$ is estimated for various scale increment δ to calculate Einstein-Markov length (l_{EM}). The estimation of l_{EM} based on the Wilcoxson test is shown in figure VI.2 for the co-rotation configuration in the SHREK experiment. From figure VI.2, we see that $\langle \Delta Q^* \rangle$ converges to the value of one at $\approx 442\mu m$ which is taken as the measure of the Einstein-Markov length. We found that l_{EM} estimated from figure VI.2 is very close to the Taylor microscale $\approx 468\mu m$ for this data set [Renner et al., 2001; Lueck et al., 2006]. In fact, we found that to obtain the convergence of $\langle \Delta Q^* \rangle$ we need that the spatial length of the hot-wire be much less than the expected Einstein-Markov length. As Taylor microscale in the SHREK experiment is very close to the spatial length of the hot-wire, the estimation of l_{EM} for all the flow configurations using Wilcoxson test has not been possible. Therefore, this method is not used to estimate l_{EM} in the SHREK experiment.

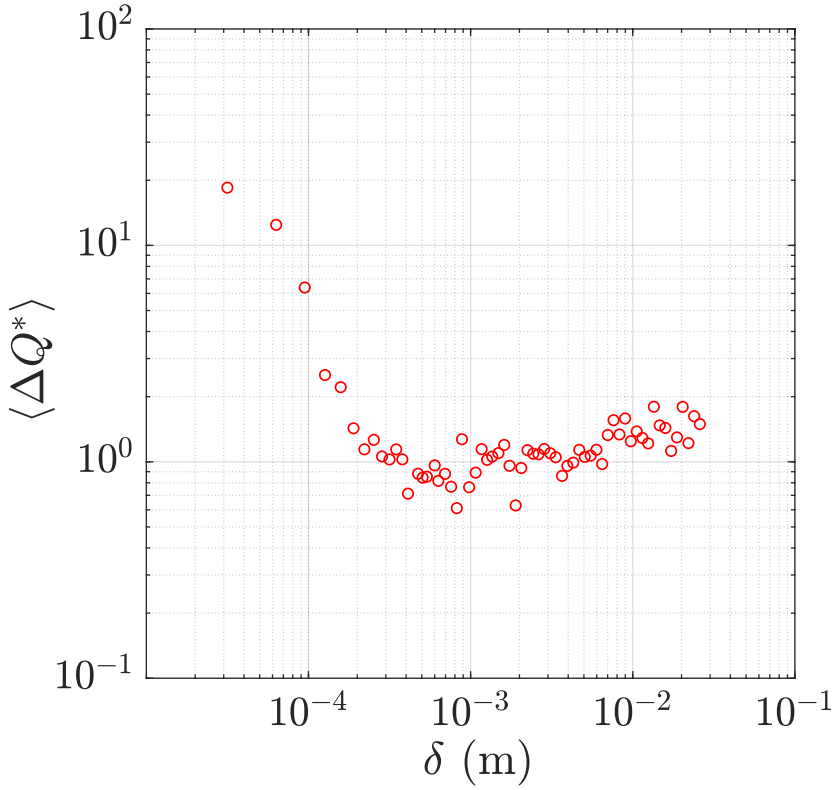

Figure VI.2: Estimation of Einstein–Markov length based on the Wilcoxson test for the +0.8Hz co-rotation configuration of the SHREK experiment with curved blades [$l_{EM} \approx 442\mu m$ and $\lambda \approx 468\mu m$]

VI.1.3.2 Single conditioned and double conditioned PDF

To estimate l_{EM} another qualitative approach can be used. The Markov property can be verified by comparing the single conditioned PDF with the double conditioned PDF of the velocity increment u_r using the following criteria given by:

$$p(u_{r_1}|u_{r_2};u_{r_3}) = p(u_{r_1}|u_{r_2}), \tag{VI.7}$$

where $r_1 < r_2 < r_3$ and scale separation $\delta = r_2 - r_1 = r_3 - r_2$. In the above equation, the CPDF on the left hand side is double conditioned, whereas the CPDF on the right hand side is single conditioned on the velocity increment. In order to have a better estimation of double conditioned PDF $p(u_{r_1}|u_{r_2};u_{r_3})$, the condition of $u_{r_3} = 0 \pm 0.1$ is chosen which gives the maximum number of statistics. The physical interpretation of equation VI.7 is that $p(u_{r_1}|u_{r_2})$ does not depend on the statistics at large scale r_3 which indicates the memoryless/Markov process in the turbulent cascade from large towards small scales. Equation VI.7 can be used to verify Markovian property by choosing multiple values of δ. The smallest scale separation at which the above criteria cease to hold is called the Einstein-Markov length l_{EM} [Renner et al., 2001].

Figure VI.3 shows the comparison of conditional PDF $p(u_{r_1}|u_{r_2})$ and $p(u_{r_1}|u_{r_2};u_{r_3})$ at scale $r_1 = \lambda$ with $\delta \approx 400\mu m$. In this figure, the velocity increments are normalized by the quantity $\sigma_\infty = \sqrt{2}\sigma$, where σ is the standard deviation of the velocity. We see that for most part of the distribution figure VI.3 shows good agreement in $p(u_{r_1}|u_{r_2})$ and $p(u_{r_1}|u_{r_2};u_{r_3})$ which indicates the fulfillment of Markovian criteria expressed by equation VI.7. We see that at extremities of the distribution function there is a relatively poor agreement in these two PDFs which may be

related to the lack of convergence of statistics. To observe this conditional PDF more precisely, a vertical cut (shown by black dashed line) in figure VI.3 is made to compare the conditional PDFs at $\frac{u_{r2}}{\sigma_\infty}$ = -0.09 as shown in figure VI.3b. Figure VI.3b shows a reasonable alignment of the single and double conditioned PDF of $\frac{u_{r1}}{\sigma_\infty}$, which is a sign of Markovian process.

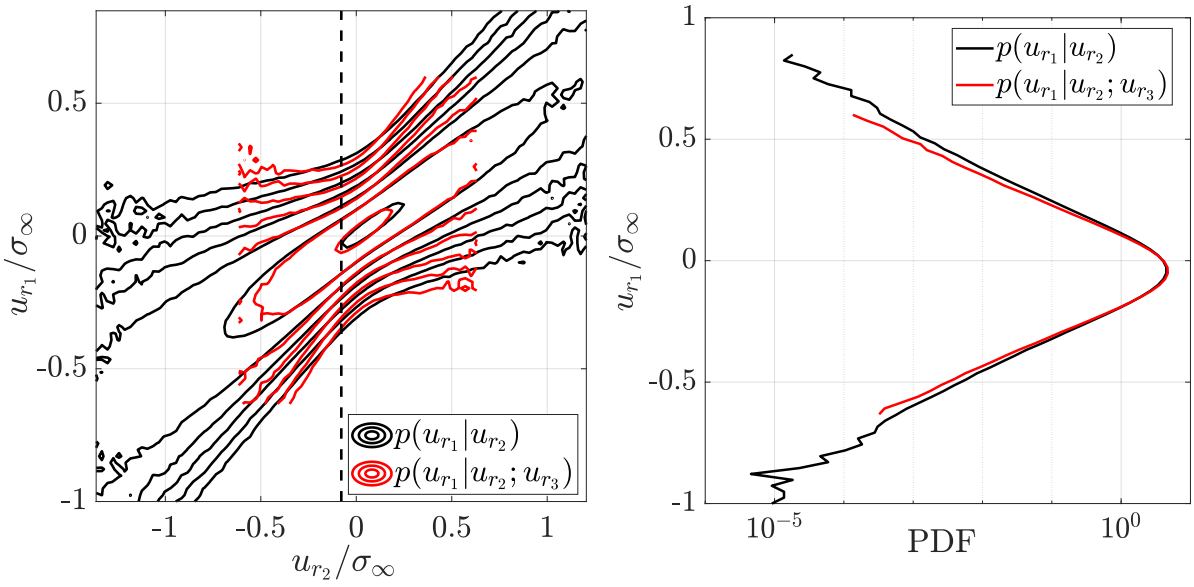

(a) Single and double conditioned PDF for $\delta \approx 400\mu m$; dashed line shows a vertical cut at $\frac{u_{r_2}}{\sigma_\infty}$ = -0.09

(b) PDF of $\frac{u_{r_1}}{\sigma_\infty}$ at $\frac{u_{r_2}}{\sigma_\infty}$ = -0.09

Figure VI.3: Markovian process at $\delta \approx 400\mu m$ $[r_1 = \lambda]$

Figure VI.4 shows the non-Markovian process based on equation VI.7, at the scale separation $\delta \approx 100\mu m$ which is much less than the hot-wire spatial resolution ($l_w = 300\mu m$) and the Einstein-Markov length. To have a better visual representation of non-Markovian process, a vertical cut at $\frac{u_{r2}}{\sigma_\infty}$ = -0.09 is made on figure VI.4a. Figure VI.4b shows the misalignment of PDF of $\frac{u_{r1}}{\sigma_\infty}$, which is a sign of non-Markovian process.

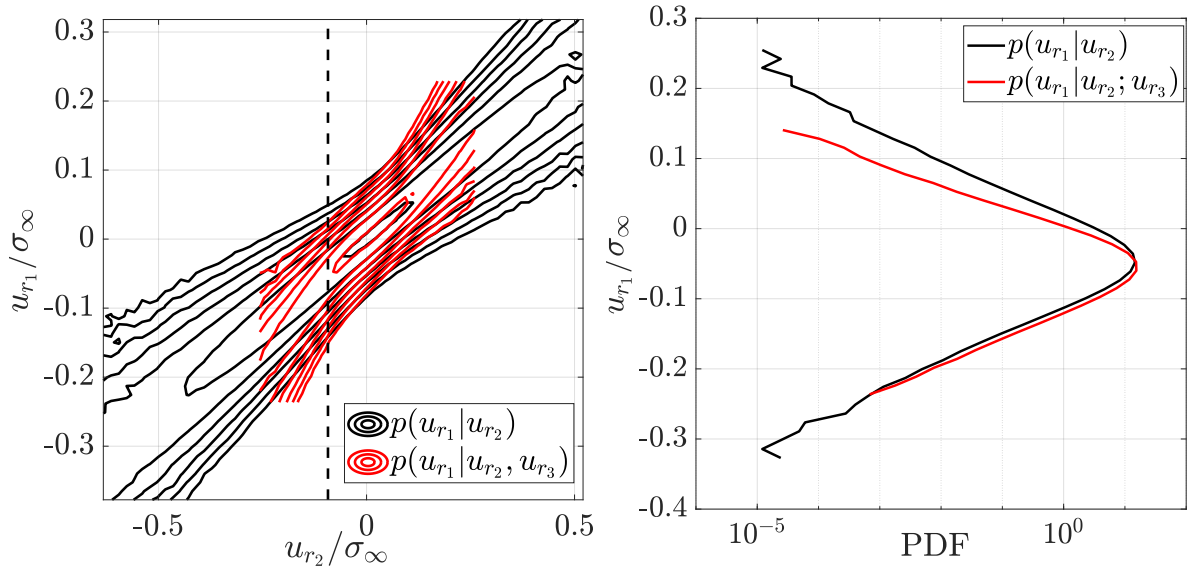

(a) Single and double conditioned PDF for $\delta \approx 100\mu m$; dashed line shows a vertical cut at $\frac{u_{r_2}}{\sigma_\infty}$ = -0.09

(b) PDF of $\frac{u_{r_1}}{\sigma_\infty}$ at $\frac{u_{r_2}}{\sigma_\infty}$ = -0.09

Figure VI.4: Non-Markovian process at $\delta \approx 100\mu m$

We have seen that Einstein-Markov length can be calculated by using one of the three methods shown above which are also discussed extensively in Renner et al. [2001]; Lueck et al. [2006]; Stresing et al. [2011]. l_{EM} had been found to be of the order of Taylor microscale λ for various kinds of flows by Renner et al. [2001] and Lueck et al. [2006]. In general, in the SHREK experiment we also find that $l_{EM} \approx \lambda$. But, for certain data sets the spatial resolution of the hot-wire ($l_w = 300\mu m$) is not good enough to measure l_{EM} precisely. Thus, to avoid any discrepancy we assume $l_{EM} \approx \lambda$ for all the data sets in the SHREK experiment.

VI.2 Description of the turbulent cascade through a Fokker-Planck equation

So far, we have seen that the turbulent cascade in the SHREK experiment is likely to be a Markov process in scale based on our investigation of Chapman-Kolmogorov equation, Wilcoxson test and an agreement within signal and double conditioned PDFs. In what follows, we will establish the stochastic differential equation for the evolution of conditional PDF of velocity increments across scales.

VI.2.1 Kramers-Moyal expansion of the evolution of the conditional PDF in scale

The Chapman-Kolmogorov equation expressed in equation VI.5 can be formulated in a differential form which leads to an evolution equation for the conditional PDF of velocity increments $p(u_{r_1}|u_{r_2})$ given by [Risken, 1989; Friedrich and Peinke, 1997a,b; Naert et al., 1997]:

$$-\frac{\partial}{\partial r}p(u_r|u_{r'}) = \sum_{n=1}^{\infty}\left(\frac{-\partial}{\partial u_r}\right)^k D^{(k)}(u_r)p(u_r|u_{r'}), \tag{VI.8}$$

where $p(u_r|u_{r'})$ is the conditional PDF of u_r conditioned on $u_{r'}$ where $r < r'$. Equation VI.8 is the Kramers-Moyal expansion of the evolution of the conditional PDF in scale. The negative sign on the left hand side of equation VI.8 indicates the direction of turbulent cascade from large

scales towards smaller scales. $D^{(k)}$ are called Kramers-Moyal coefficients (KMCs) of k^{th} order (see section VI.2.1.2 for the definition of $D^{(k)}$).

VI.2.1.1 Fokker-Planck equation

In equation VI.8, if the fourth order Kramers-Moyal coefficient $D^{(4)}$ vanishes, then according to Pawula's theorem the Kramers-Moyal expansion leads to the Fokker-Planck equation [Risken, 1989]. Briefly, the theorem of Pawula states that the Kramers-Moyal expansion may stop either after the first term or after the second term, if it does not stop after the second term it must contain an infinite number of terms ([Risken, 1989], Page. 70). In addition to Pawula's theorem, experimental analysis performed by Friedrich and Peinke [1997b] also showed that the higher order KMCs ($D^{(k\geq 3)}$) can be neglected based on their weak dependence on the scale and velocity increment. The experimental analysis of turbulence data performed by Renner et al. [2001] and recently by Peinke et al. [2019] also showed that $D^{(4)}$ is significantly smaller than $D^{(2)}$ and hence can be considered as negligible. In our data, we also verified that $D^{(4)} << D^{(2)}$. The Fokker-Plank equation (FPE) expressing the evolution of the conditional PDFs of velocity increments is given by [Risken, 1989; Friedrich and Peinke, 1997a,b; Naert et al., 1997]:

$$-\frac{\partial}{\partial r}p(u_r|u_{r'}) = -\frac{\partial}{\partial u_r}[D^{(1)}(u_r)p(u_r|u_{r'})] + \frac{\partial^2}{\partial u_r^2}[D^{(2)}(u_r)p(u_r|u_{r'})]. \tag{VI.9}$$

FPE given by equation VI.9 is a second order partial differential equation in scale r and in velocity increment u_r. It describes the evolution of CPDF $p(u_r|u_{r'})$ within scales using drift coefficient $D^{(1)}$ and diffusion coefficient $D^{(2)}$. The drift and diffusion coefficients are the Kramers-Moyal coefficients (KMCs) of first and second order respectively. On the account of comparability between different data sets, the velocity increments are normalized by the quantity $\sigma_\infty = \sqrt{2}\sigma$, where σ is the standard deviation of the velocity. In fact, σ_∞ is chosen because the variance of the velocity increments at large scale L is equal to twice the variance of the velocity (i.e. $\sigma_\infty^2 = \sigma_{u_{r=L}}^2 = 2\sigma^2$). The scale r is normalized by the Taylor microscale λ. This gives dimensionless KMCs dependent on the velocity increment $\frac{u_r}{\sigma_\infty}$ at scale $\frac{r}{\lambda}$. The coefficients $D^{(1)}$ and $D^{(2)}$ can be directly calculated from the experimental data of velocity time series.

VI.2.1.2 Estimation of the Kramers-Moyal coefficients

The FPE is characterized by the drift coefficient $D^{(1)}$ and the diffusion coefficient $D^{(2)}$ estimated for each of the scale r and the velocity increment at that scale u_r. To estimate these coefficients, the following conditions are used during the data post-processing: The total number of bins used are 200. A bin is considered to be significant only if the maximum number of events in that bin are more than 400. The provision of the minimum number of events/counts is for avoiding the appearance of noise and hence for better fitting of parameters. The drift and diffusion coefficients are estimated at 20 logarithmically spaced scales within the integral scale L down to 2λ. To perform the Fokker-Planck analysis of 1D turbulence data, we have developed an open source MATLAB package jointly with the University of Oldenburg [Fuchs et al., 2021b]. In this thesis, we have used this package to estimate the drift and diffusion coefficients.

VI.2.1.2.1 Conditional moment of first and second order

To estimate the drift and diffusion coefficients in the FPE we first need to estimate conditional moments of first and second order. These conditional moments can be directly calculated from the experimentally evaluated conditional PDFs according to the following relation given by [Reinke et al., 2018]:

$$M^k(u_{r_2}, \delta = r_2 - r_1) = \int_{-\infty}^{\infty} (u_{r_1} - u_{r_2})^k p(u_{r_1}|u_{r_2}) du_{r_1}, \tag{VI.10}$$

where k = 1 for the first order conditional moment and k = 2 for the second order conditional moment with $r_1 < r_2$. δ is the scale separation ($> l_{EM}$) accessible between conditional PDFs i.e. $r_2 = r_1 + \delta$. The conditional moments are estimated at the smallest resolved scale separation δ as shown in figure VI.5. The range of scale separation δ ($450\mu m$ to $900\mu m$ in figure VI.5) is chosen from l_{EM} to $2l_{EM}$ (i.e. from λ to 2λ). The conditional moment of first and second order for velocity increment $u_{r_2} = 0 \pm 0.1$ at a scale of $r_2 = \frac{L}{2}$ is shown in figure VI.5 as a function of scale separation δ. We note that the estimation of conditional moments at $\delta < 300\mu m$ may not be precise because of the lack of spatial resolution of the hot-wire ($l_w \approx 300\mu m$).

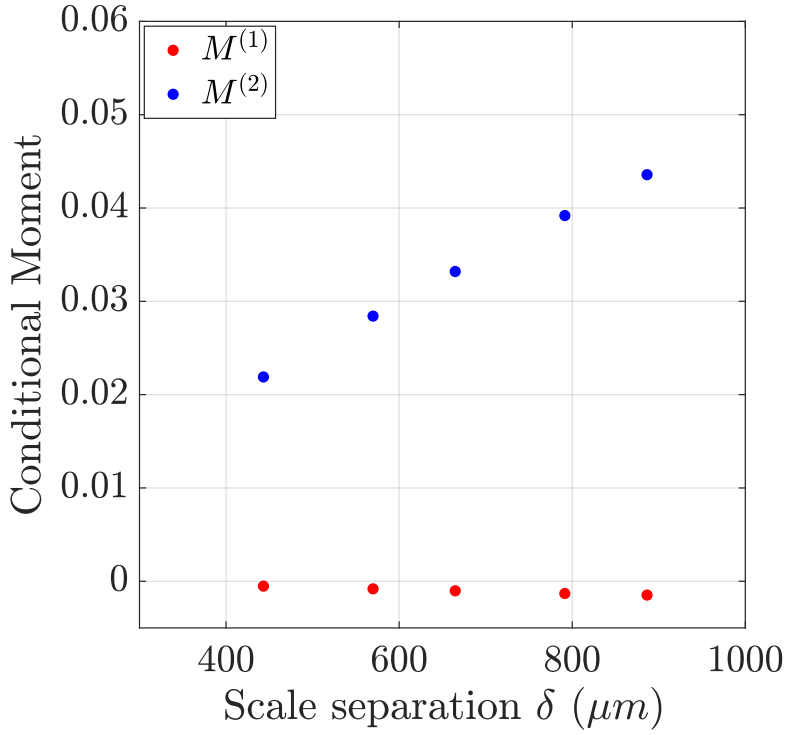

Figure VI.5: Conditional moments of first and second order with respect to scale separation δ at scale $r_2 = \frac{L}{2}$ and for velocity increment $u_{r_2} = 0 \pm 0.1$

VI.2.1.2.2 Dependence of $D^{(1)}$ and $D^{(2)}$ on scale and velocity increments

After the calculation of conditional moments, the drift and diffusion coefficients are estimated based on the extrapolation of conditional moments as $\delta \to 0$ given by [Reinke et al., 2018]:

$$D^{(k)}(u_{r_2}) = \lim_{\delta \to 0} \frac{1}{k!\delta} M^{(k)}(u_{r_2}, \delta), \tag{VI.11}$$

where $r_2 > 2\lambda$. From equation VI.11, we calculate the KMCs for each scale r and corresponding to each different velocity increment u_r. The drift and diffusion coefficients for the co-rotation

configuration in the SHREK experiment with turbine with radial blades is shown in figure VI.6. The experimental hot-wire data for this flow configuration is acquired over a duration of 6 hours using the sampling frequency of 50kHz. This corresponds to huge number of large eddy turnover times of $\mathcal{O}(10^5)$. Such large number of statistics assures to get an accurate and precise estimation of drift and diffusion coefficients. The optimization of the experimentally estimated drift and diffusion coefficients is performed at each scale using the approach of short time propagator (see equation VI.15) explained in Risken [1989]; Nawroth et al. [2007]; Reinke et al. [2018]; Peinke et al. [2019]. The optimization is performed in order to minimize the distance between the experimental and the reconstructed CPDFs of velocity increments (see section VI.2.2.1 for more details). This optimization is based on the minimization of Kullback-Liebler distance between these two CPDFs as explained in Reinke et al. [2018].

Figure VI.6a and figure VI.6b show the evolution of drift and diffusion coefficients with respect to scale $\frac{r}{\lambda}$ and normalized velocity increment $\frac{u_r}{\sigma_\infty}$ respectively. We also confirmed that the higher order KMCs such as $D^{(3)}$ and $D^{(4)}$ are found to be negligible in the SHREK experiment. In these figures, the optimized drift and diffusion coefficients are shown by black filled circles. These optimized coefficients are used to design a surface fit with independent parameters of $\frac{r}{\lambda}$ and $\frac{u_r}{\sigma_\infty}$. The corresponding surface fit is shown in figure VI.6 along with the corresponding colorbar. From figure VI.6a we see that for a positive velocity increment the drift coefficient is negative and vice versa. We see that the drift coefficient is linear with respect to velocity increment u_r. From figure VI.6b we see that the diffusion coefficient is parabolic with respect to velocity increment u_r. We also note that the diffusion coefficient is always positive. For the first time, the linear and parabolic dependence of drift and diffusion coefficient on u_r had been found by Friedrich and Peinke [1997a]. Similar dependence is also observed in the SHREK experiment as shown in figure VI.6.

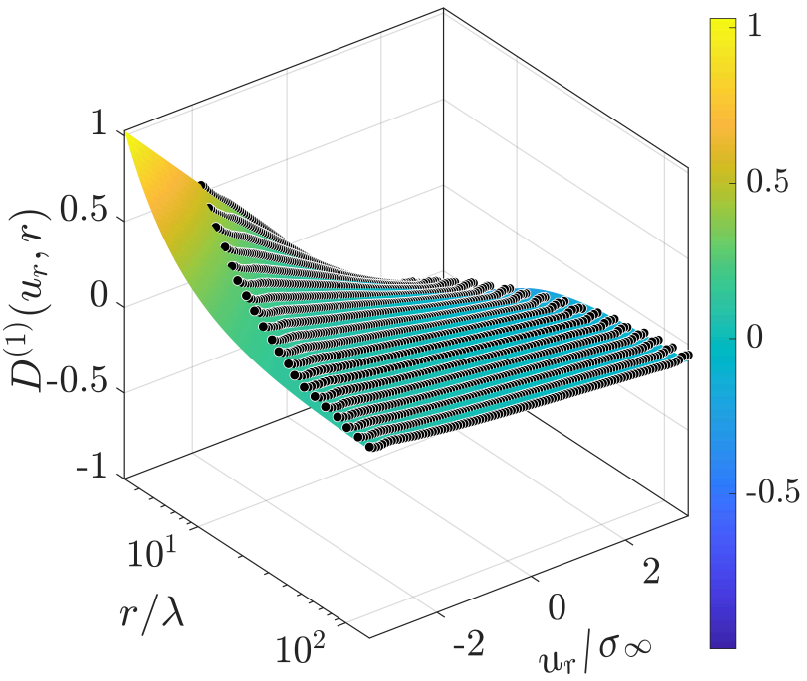

(a) Drift Coefficient

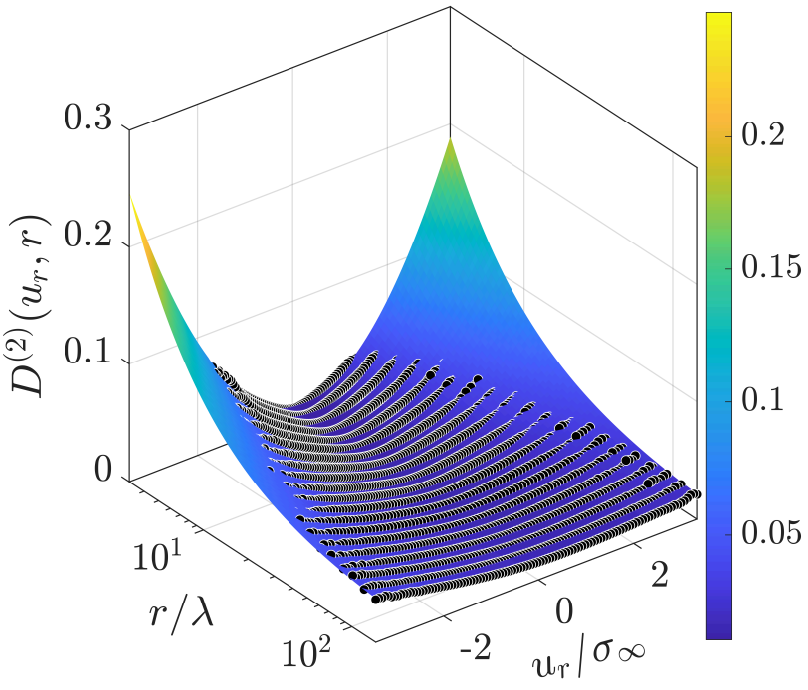

(b) Diffusion Coefficient

Figure VI.6: Drift and diffusion coefficient for +1.2Hz co-rotation configuration in the SHREK experiment with turbine with radial blades

Such analysis is performed for 38 different data sets for the flow configurations mentioned in table 6 and hence multiple drift and diffusion coefficients can be plotted for each type of flow configuration. But, to compare these coefficients on the basis of three dimensional figures like in figure VI.6 is very cumbersome and difficult. From figure VI.6a, we see that the slope of $D^{(1)}$ varies from low $\frac{r}{\lambda}$ to high $\frac{r}{\lambda}$. Similarly, from figure VI.6b, we see that the extent of parabolic behavior of $D^{(2)}$ changes from low $\frac{r}{\lambda}$ to high $\frac{r}{\lambda}$. Therefore, the quantification of linear dependence of drift coefficient and the parabolic dependence of diffusion coefficient on u_r is performed by expressing the KMCs in terms of parameters d_{ij} expressed in the following way [Marcq and Naert, 2001; Renner et al., 2001; Reinke et al., 2018; Peinke et al., 2019; Fuchs et al., 2019]:

$$D^{(1)}(u_r) = d_{11}(r)u_r, \tag{VI.12}$$

$$D^{(2)}(u_r) = d_{22}(r)u_r^2 + d_{21}(r)u_r + d_{20}(r). \tag{VI.13}$$

$d_{11}(r)$ is the slope of the drift coefficient (linear in u_r) at scale r. In other words, $d_{11}(r)$ is the prefactor of linear term of the drift coefficient. $d_{20}(r)$ is the positive intercept of the diffusion coefficient at scale r and at velocity increment $\frac{u_r}{\sigma_\infty} = 0$. $d_{21}(r)$ shows the inclination (positive or negative) of the diffusion coefficient at scale r with respect to $\frac{u_r}{\sigma_\infty}$. $d_{22}(r)$ shows the extent of quadratic dependence of the diffusion coefficient at scale r with respect to $\frac{u_r}{\sigma_\infty}$. In other words, d_{22} and d_{21} are the prefactors of the quadratic and linear term of the diffusion coefficient and d_{20} is the additive constant.

VI.2.1.3 Langevin formulation

The turbulent cascade can also be described using the Langevin equation which describes the evolution of the velocity increment u_r with respect to scale r given by [Peinke et al., 2019]:

$$-\frac{\partial u_r}{\partial r} = D^{(1)}(u_r) + \sqrt{D^{(2)}(u_r)}\xi_r, \tag{VI.14}$$

where ξ_r is the random (i.e. fluctuating) force which must respect $\langle \xi_r \rangle = 0$ at all scales [Van Kampen, 2007]. The negative sign on the left-hand side of equation VI.14 accounts for the physical direction of turbulent cascade from large scale towards small scales. We note that in Langevin equation $D^{(1)}$ and $D^{(2)}$ depicts the evolution of u_r whereas in FPE the same $D^{(1)}$ and $D^{(2)}$ depicts the evolution of conditional PDF $p(u_r|u_{r'})$ with respect to scale r [Peinke et al., 2019]. If the diffusion coefficient is uniquely expressed in terms of $d_{20}(r)$ such that $D^{(2)}(u_r) = d_{20}(r)$, in this case $D^{(2)}$ is called additive noise. On the other hand, if the diffusion coefficient is uniquely expressed in terms of $d_{22}(r)$ such that $D^{(2)}(u_r) = d_{22}(r)u_r^2$, in this case $D^{(2)}$ is called multiplicative noise.

VI.2.2 Assessment of the Fokker-Planck description of the turbulent cascade

One of the important question to address is, whether the FPE describes the turbulent cascade process correctly or not? To answer this question, we have performed the assessment of the estimated drift and diffusion coefficients using two different methods which are described as follows.

VI.2.2.1 Reconstruction of PDFs of velocity increment using drift and diffusion coefficient

The FPE models the evolution of conditional PDFs of velocity increments across scales (see equation VI.9). The conditional PDFs of velocity increments can be accurately reconstructed by solving the FPE if the estimation of drift and diffusion coefficients is correct. The short time propagator allows to reconstruct the CPDF from the estimated drift and diffusion coefficients which is given by [Risken, 1989]:

$$p_{stp}(u_{r_1}|u_{r_2}) \approx \frac{1}{\sqrt{4\pi D^{(2)}(u_{r_2}, r_2) l_{EM}}} exp\left[-\frac{(u_{r_1} - u_{r_2} - D^{(1)}(u_{r_2}, r_2) l_{EM}^2)^2}{4D^{(2)}(u_{r_2}, r_2) l_{EM}} \right], \tag{VI.15}$$

with $r_2 > r_1$ and $r_2 = r_1 + l_{EM}$. $p_{stp}(u_{r_1}|u_{r_2})$ is the reconstructed conditional PDF from the short time propagator expressing the drift and diffusion coefficients. Like the finite difference scheme is an approximation of the true derivative and this approximation is much precise if the step size is small, similarly, the quality of the short time propagator is good for the small step size of l_{EM}. If we use a large step size the approximation in equation VI.15 may not be valid. The following demonstration of the reconstruction analysis is performed on the data set which belongs to the co-rotation configuration in the SHREK experiment with curved blades at $\mathcal{F}_1 = \mathcal{F}_1 = 0.8$Hz. In figure VI.7, the comparison of experimental conditional PDF $p_{exp}(u_{r_1}|u_{r_2})$ with the conditional PDF reconstructed using short time propagator is shown. Figure VI.7a shows $p_{exp}(u_{r_1}|u_{r_2})$ and $p_{stp}(u_{r_1}|u_{r_2})$ at scale $r_1 = l_{EM} \approx \lambda$ whereas figure VI.7b shows it at scale $r_1 = L$. From figure VI.7 we see that $p_{stp}(u_{r_1}|u_{r_2})$ is in good agreement and well aligned with respect to $p_{exp}(u_{r_1}|u_{r_2})$.

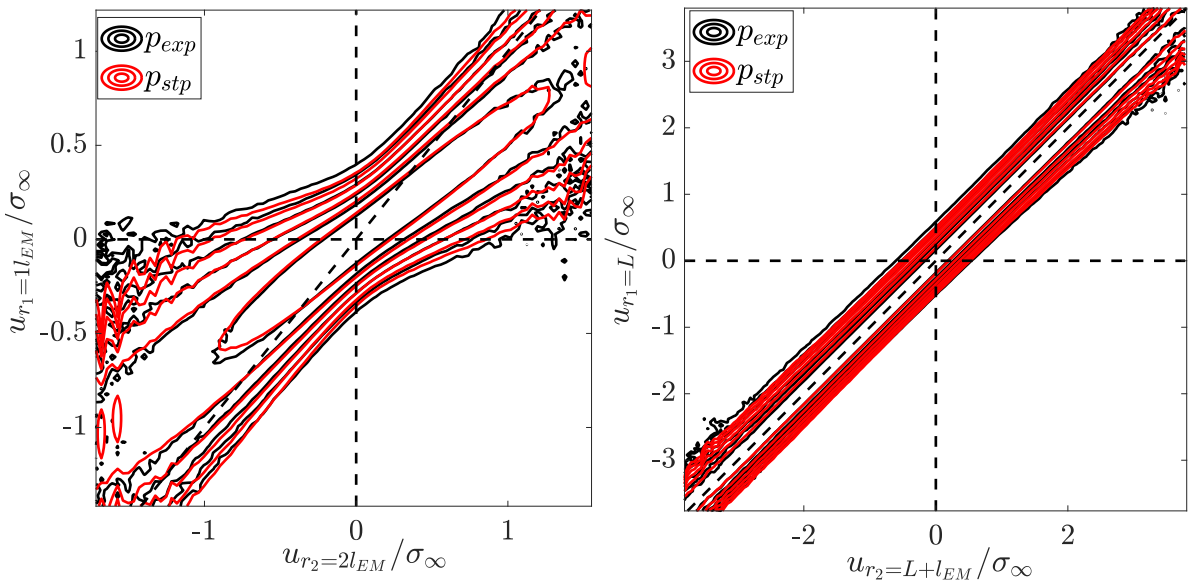

(a) At scale $r_1 = l_{EM} \approx \lambda$ (b) At scale $r_1 = L$

Figure VI.7: Contour plots showing experimental and reconstructed conditional PDFs using short time propagator

To have a more precise qualitative comparison of $p_{exp}(u_{r_1}|u_{r_2})$ and $p_{calc}(u_{r_1}|u_{r_2})$ at multiple scales, unconditional PDF of velocity increments can be compared. The unconditional PDF of velocity increment at scale r_1 is estimated by integrating the reconstructed conditional PDF $p_{stp}(u_{r_1}|u_{r_2})$ which can be mathematically expressed as:

$$p_{calc}(u_{r_1}) = \int_{-\infty}^{\infty} p_{stp}(u_{r_1}|u_{r_2}) p(u_{r_2}) du_{r_2}, \tag{VI.16}$$

where $p_{calc}(u_{r_1})$ is the reconstructed/calculated unconditional PDF of velocity increment u_{r_1} from $p_{stp}(u_{r_1}|u_{r_2})$. Thus, the short time propagator allows to calculate PDF of velocity increment at scale r_1 knowing the PDF of velocity increment at scale r_2 with $r_2 - r_1 = l_{EM}$. From the above equation, we see that to reconstruct $p_{calc}(u_{r_1})$ we need the initial unconditional PDF $p(u_{r_2})$ (i.e. $p_{exp}(u_{r_2})$) from the experimental data. In the following, the comparison of $p_{calc}(u_{r_1})$ is performed with the PDF of velocity increment estimated from the experimental data i.e. $p_{exp}(u_{r_1})$. According to the equation VI.16, following two scenarios exist to reconstruct unconditional PDF $p_{calc}(u_{r_1})$.

In the first scenario, equation VI.16 is solved using $p(u_{r_2})$ estimated from the experimental data at each scale independently. In other words, at each scale r_1, $p_{calc}(u_{r_1})$ is estimated using the experimental PDF of velocity increment at scale $r_2 = r_1 + l_{EM}$. Following this procedure, we obtain $p_{calc}(u_{r_1})$ at scale $r_1 = \lambda$, 5λ, 10λ, 50λ, 100λ and $175\lambda \approx L$. Figure VI.8 shows the comparison of $p_{calc}(u_{r_1})$ with $p_{exp}(u_{r_1})$. This figure shows the common picture of intermittency phenomenon as previously discussed in section V.9. From figure VI.8, we see that $p_{exp}(u_{r_1})$ and $p_{calc}(u_{r_1})$ are in very good agreement. In fact, the agreement in these two PDFs is good because the optimization of the drift and diffusion coefficients is performed at each scale independently. This figure shows that the FPE with optimized drift and diffusion coefficients describes the turbulent cascade accurately depicting the intermittency phenomenon.

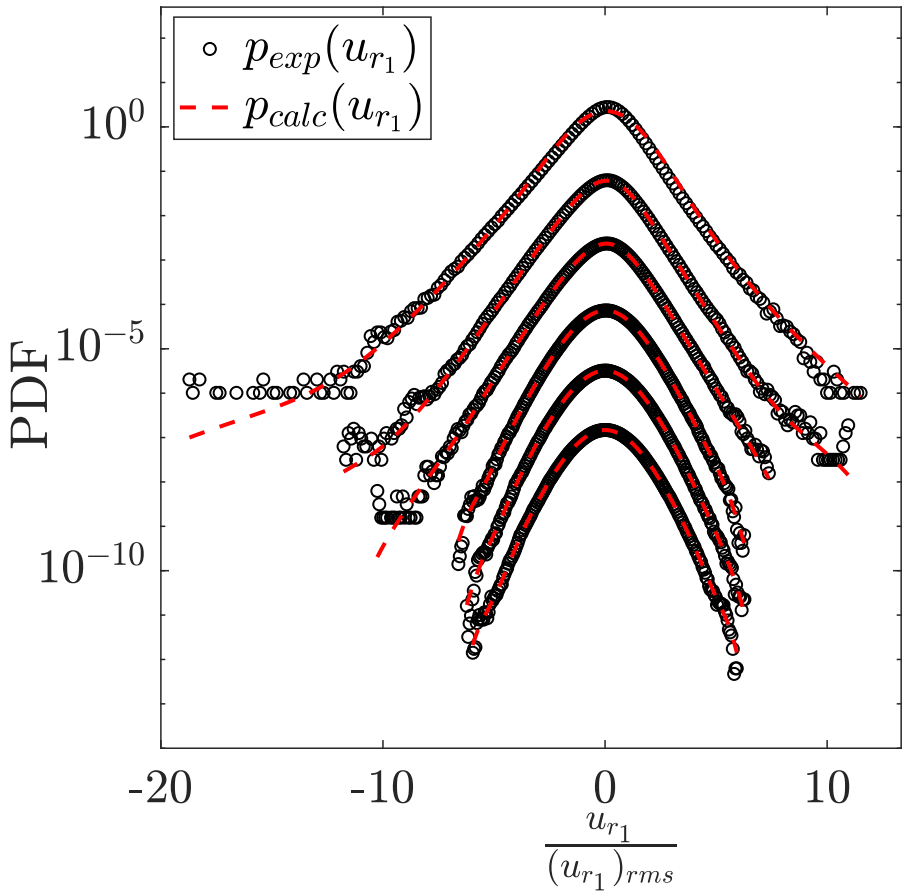

Figure VI.8: Comparison of experimental ($p_{exp}(u_{r_1})$) and reconstructed ($p_{calc}(u_{r_1})$) PDF of velocity increment at various scales r_1 using the first scenario; From top to bottom $r_1 = \lambda$, 5λ, 10λ, 50λ, 100λ and $175\lambda \approx L$ where $\lambda = 450\mu m$ and $L = 0.08m$ [For better visualization, the PDFs at various scales are shifted in the vertical direction]

In the second scenario, equation VI.16 is solved using $p(u_{r_2})$ from the experimental data only at scale L in the first step and an iterative process is used towards smaller scales. In other words, the entire turbulent cascade is reconstructed using only the initial solution at large scale L from the experimental data. In the first step, we estimate $p_{calc}(u_{r_1})$ at scale $r_1 = L$ using $p(u_{r_2})$ estimated from the experimental data at scale $r_2 = L + l_{EM}$. In the second step, to estimate $p_{calc}(u_{r_1})$ at scale $r_1 = L - l_{EM}$ we use $p(u_{r_2}) = p_{calc}(u_{r_1})$ at scale $r_1 = L$ and so on. Following this procedure, we obtain figure VI.9 which shows $p_{exp}(u_{r_1})$ and $p_{calc}(u_{r_1})$ at scale $r_1 = \lambda$, 5λ, 10λ, 50λ, 100λ and $175\lambda \approx L$. This figure shows that at large scales $p_{exp}(u_{r_1})$ and $p_{calc}(u_{r_1})$ are in good agreement whereas comparatively at smaller scales the agreement becomes poorer. We see that the error between $p_{exp}(u_{r_1})$ and $p_{calc}(u_{r_1})$ grows towards smaller scales during the iterative process. As mentioned earlier, this is because the drift and diffusion coefficients are estimated locally at each scale by optimization. Therefore, some uncertainties/error are likely to be introduced while predicting the statistics at next small scale. This error between $p_{exp}(u_{r_1})$ and $p_{calc}(u_{r_1})$ may be reduced by performing a scale dependent optimization from large scale L to small scale λ. Nevertheless, figure VI.9 shows that the most part of the PDFs of velocity increments can be reconstructed using the short time propagator using an iterative approach.

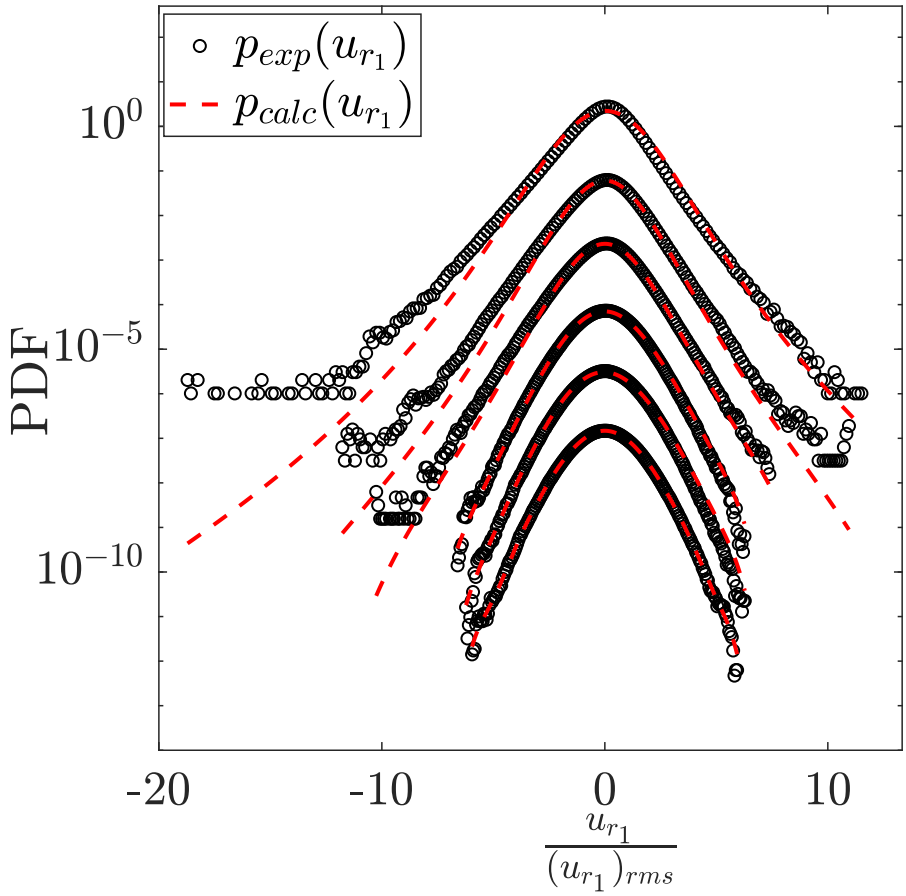

Figure VI.9: Comparison of experimental ($p_{exp}(u_{r_1})$) and reconstructed ($p_{calc}(u_{r_1})$) PDF of velocity increment at various scales r_1 using the second scenario; From top to bottom $r_1 = \lambda$, 5λ, 10λ, 50λ, 100λ and $175\lambda \approx L$ where $\lambda = 450\mu m$ and $L = 0.08m$ [For better visualization, the PDFs at various scales are shifted in the vertical direction]

In what follows, we perform the assessment of the diffusion coefficient in particular to address the parameter d_{21}. In equation VI.13 we have expressed the diffusion coefficient in terms of the parameters d_{20}, d_{21} and d_{22}. Fuchs et al. [2019, 2020] used the same formulation of the diffusion coefficient expressed by equation VI.13 whereas Reinke et al. [2018] and Fuchs et al. [2021a] used the diffusion coefficient without the contribution of d_{21}. Fuchs et al. [2019] also showed that all the parameters d_{11} ,d_{20}, d_{21} and d_{22} contributes towards the reconstruction of PDFs of velocity increments. Reinke et al. [2018] also discussed the influence of the accuracy of the drift and diffusion coefficients on the validity of integral fluctuation theorem. These studies conducted so far do not address specifically the relevance of the parameter d_{21}. Therefore, we address the contribution of the parameter d_{21} in view of the reconstruction of PDFs of velocity increments.

Figure VI.10 shows the parameters d_{20}, d_{21} and d_{22} for the co-rotation configuration in the SHREK experiment with curved blades at $\mathcal{F}_1 = \mathcal{F}_1 = 0.8$Hz. The dependence of these parameters with respect to scale will be discussed in detail later in this chapter. In figure VI.10, we tested two cases: (i) we impose $d_{21} \neq 0$ by fitting $D^{(2)}(u_r) = d_{22}(r)u_r^2 + d_{21}(r)u_r + d_{20}(r)$ and we found that $d_{21}(r)$ is in fact very small. (ii) we impose $d_{21} = 0$ by fitting $D^{(2)}(u_r) = d_{22}(r)u_r^2 + d_{20}(r)$ and we found that it does not change the quality of the results. From this figure, we see that the contribution of d_{21} in the diffusion coefficient has very little influence on

the value of d_{20} and d_{22}.

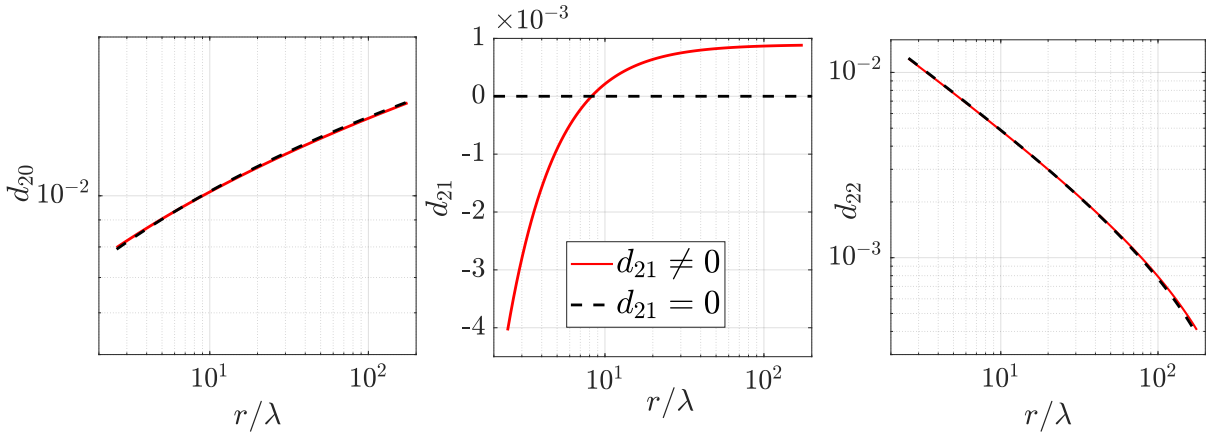

Figure VI.10: The parameter d_{20} and d_{22} with and without the contribution of d_{21}

Figure VI.11 shows the reconstruction of the PDFs of the velocity increments based on the first scenario explained in section VI.2.2.1. The reconstruction in this figure is performed using the parameters d_{11}, d_{20} and d_{22} while using $d_{21} = 0$. From this figure we see that at all scales the reconstructed PDFs agrees well with the PDFs extracted from the experimental data. Thus, we conclude that the parameter d_{21} plays a very limited role in the reconstruction of PDFs.

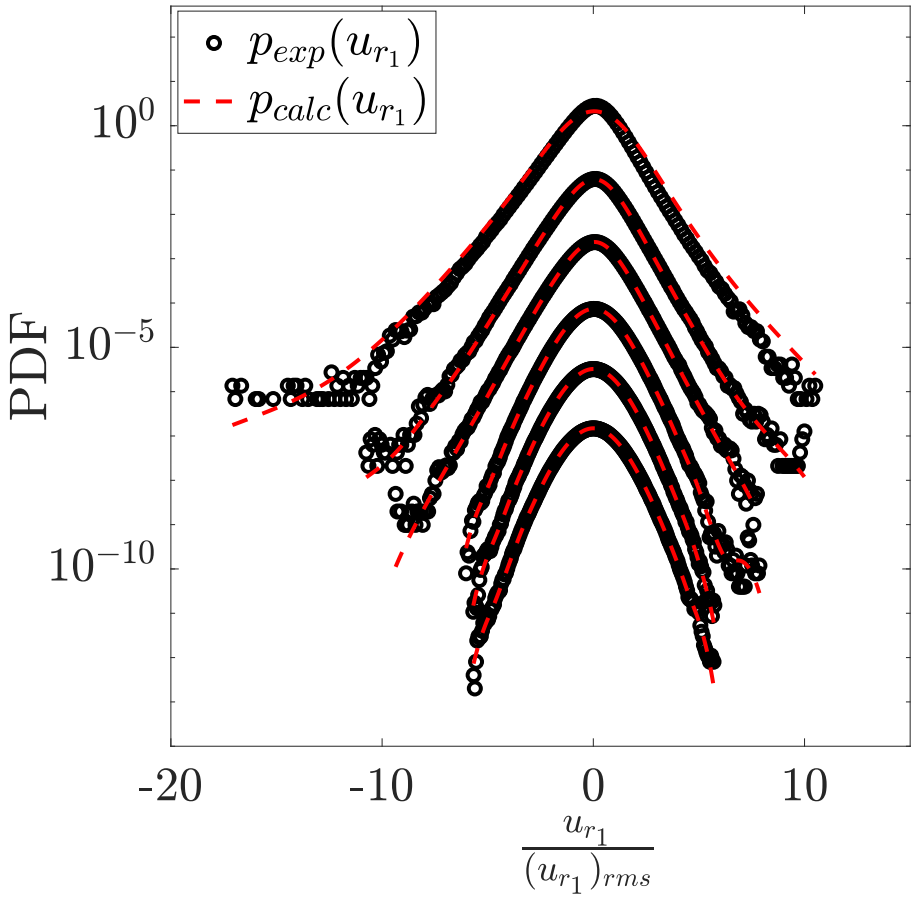

Figure VI.11: Comparison of experimental ($p_{exp}(u_{r_1})$) and reconstructed ($p_{calc}(u_{r_1})$) PDFs of velocity increment at various scales r_1 using the first scenario explained in section VI.2.2.1 while using $d_{21} = 0$; From top to bottom $r_1 = \lambda$, 5λ, 10λ, 50λ, 100λ and $175\lambda \approx L$ where $\lambda = 450\mu m$ and $L = 0.08m$ [For better visualization, the PDFs at various scales are shifted in the vertical direction]

VI.2.2.2 Integral fluctuation theorem verification

The field of stochastic thermodynamics has strongly evolved in the recent years [Seifert, 2008]. A comprehensive review on this topic was also proposed by the same author [Seifert, 2012]. It allows to define an entropy to each trajectory of particles which experience deterministic and random forces from a medium. An example of this type of situation is given by the Brownian motion of colloidal particles in a fluid of temperature T. The equation of motion of these particles is given by a Langevin equation. It is possible to show that this Langevin equation for the individual particles is equivalent to a Fokker-Planck equation which governs the PDF of the particles. The medium is characterized usually with a temperature, but more generally by the properties which generate drift and diffusion coefficients of the Fokker-Planck equation. In the case of turbulence, we have seen that the cascade process (in scale!) fulfills within a good approximation the Fokker-Planck equation (see equation VI.9), with drift and diffusion coefficients which depend on scale and velocity increment, and which we can calculate. The usual definition of Gibbs entropy suggests to define a trajectory-dependent entropy as:

$$s(r) = -\ln p(u_r, r), \tag{VI.17}$$

for a particle or system which consists in a trajectory u_r along scales, where $p(u_r, r)$ is the probability of velocity increment u_r at scale r. This system interacts with the medium (which represents the type of flow, defined by its drift and diffusion coefficients, and which we calculate, for example: co-rotation or contra-rotation flow), and it can exchange heat with the medium, so that the sum of the two averaged entropies (system + medium) should fulfill the second law of thermodynamics. A derivation of the entropies for a particular system and medium is given in Seifert [2005] for the case of overdamped Brownian motion, and given with more details for the turbulent cascade specifically in Nickelsen and Engel [2013]; Nickelsen [2014].

In the following, two special types of trajectories of the velocity increments are shown and discussed to give qualitative interpretation of stochastic entropy in view of turbulent cascade. A very "probable" trajectory of the velocity increment $|u_r|$ with respect to scale $\frac{r}{\lambda}$ is shown in figure VI.12. The word "probable" is used because in turbulence big structures are typically generated at large scales which eventually break down to smaller structures towards smaller scales. Indeed, we see that the large velocity increment at large scale L eventually decays to smaller velocity increments till scale λ. On the other hand, figure VI.13 shows a very "rare" trajectory of the velocity increment $|u_r|$ with respect to scale $\frac{r}{\lambda}$. The word "rare" is used because from figure VI.13, we see that the velocity increment at small scale λ is very high whereas the velocity increment at large scale L is low. In fact, such trajectories of the velocity increments are very rare in the numerous independent realizations of the turbulent cascade. Such large velocity increments at small scales are likely to depict the phenomenon of intermittency in the turbulent cascade [Fuchs et al., 2020]. Nickelsen and Engel [2013] and Fuchs et al. [2020] also showed that the velocity increment trajectories similar to one shown in figure VI.12 give rise to positive total production of entropy whereas the trajectories similar to one shown in figure VI.13 give rise to negative total production of entropy. This explains the qualitative interpretation of these two "probable" and "rare" velocity increment trajectories occurring in the turbulent cascade.

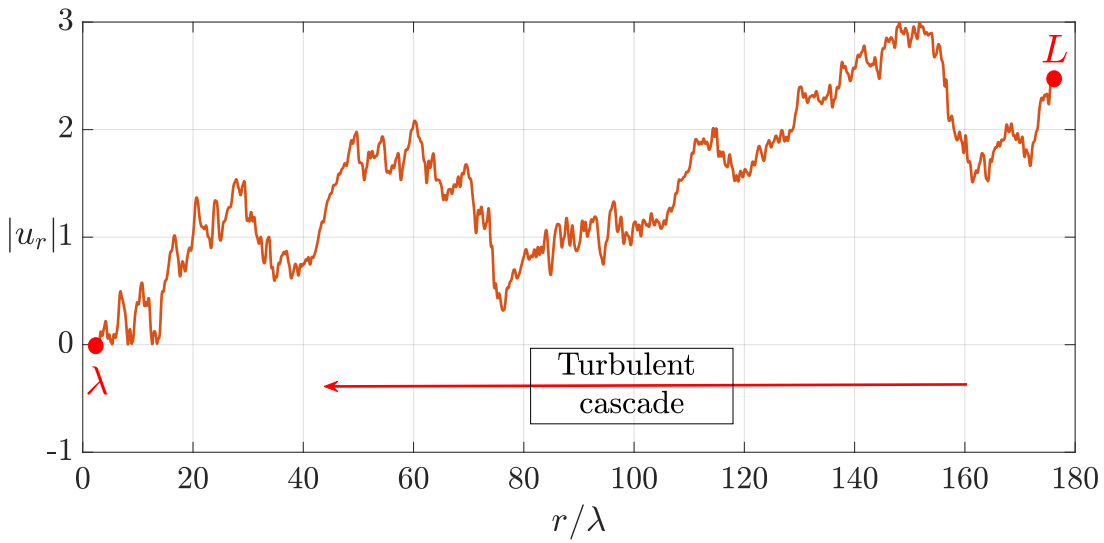

Figure VI.12: A "probable" trajectory of the evolution of velocity increment $|u_r|$ with respect to scale $\frac{r}{\lambda}$

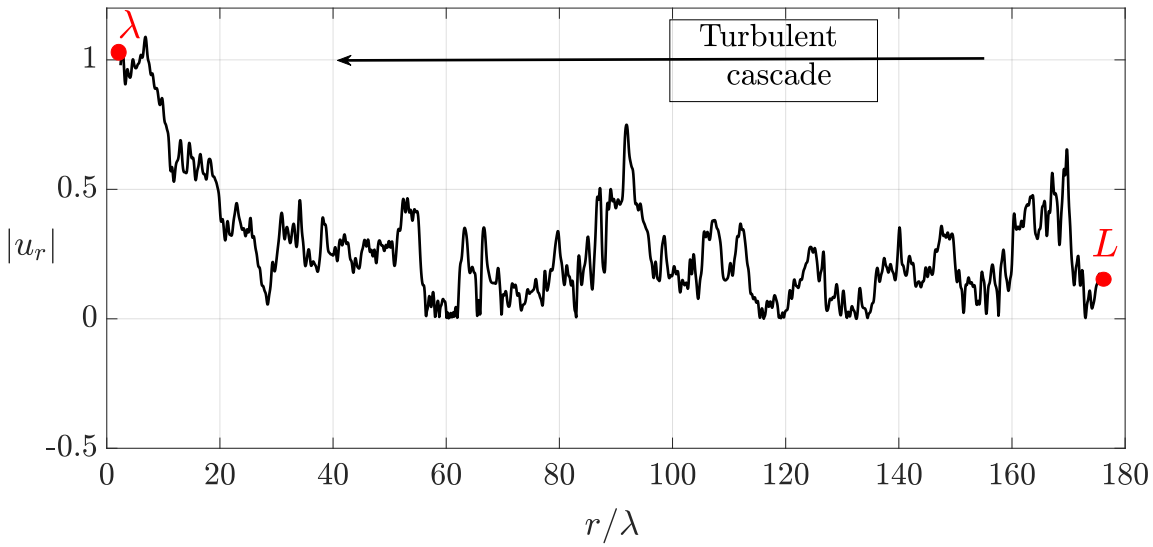

Figure VI.13: A "rare" trajectory of the evolution of velocity increment $|u_r|$ with respect to scale $\frac{r}{\lambda}$

The turbulent cascade can be seen as the evolution from a state characterized by $p(u_L, L)$ to a state $p(u_\lambda, \lambda)$. Figure VI.12 and figure VI.13 show that different velocity increments occur at various scales in the turbulent cascade. An individual velocity increment trajectory can be characterized by the corresponding production of entropy. Based on the initial and final states of the trajectory of the velocity increment a change in system entropy ΔS_{sys} is defined by Seifert [2005] and is given by [Seifert, 2012; Nickelsen and Engel, 2013]:

$$\begin{aligned} \Delta S_{sys} &= (S_{sys})_{final} - (S_{sys})_{initial}, \\ \Delta S_{sys} &= -\ln p(u_\lambda, \lambda) + \ln p(u_L, L), \\ \Delta S_{sys} &= -\ln \frac{p(u_\lambda, \lambda)}{p(u_L, L)}, \end{aligned} \tag{VI.18}$$

where $p(u_L, L)$ is the probability of velocity increment u_L on scale L and $p(u_\lambda, \lambda)$ is the probability of velocity increment u_λ on scale λ. System entropy accounts for the initial and final velocity increment in the turbulent cascade whereas medium entropy accounts for the path experienced by the velocity increment (i.e. turbulence structures) from large to small scale. The medium entropy represents the interaction of the trajectory of the velocity increment with the surrounding medium. As each velocity increment is associated with a particular value of the drift and diffusion coefficients (see figure VI.6a and figure VI.6b), from the stochastic thermodynamics the change in the medium entropy ΔS_{med} can be estimated using the relation given by [Seifert, 2012; Nickelsen and Engel, 2013; Nickelsen, 2014]:

$$\begin{aligned} \Delta S_{med} &= (S_{med})_{final} - (S_{med})_{initial}, \\ \Delta S_{med} &= \int_L^\lambda \partial_r u_r \frac{D^{(1)}(u_r, r) - \partial_u D^{(2)}(u_r, r)}{D^{(2)}(u_r, r)} dr. \end{aligned} \tag{VI.19}$$

The total entropy change ΔS_{tot} of each individual turbulent cascade trajectory from L down to λ is estimated from the sum of the medium entropy change and the system entropy change given by: $\Delta S_{tot} = \Delta S_{med} + \Delta S_{sys}$.

So far, we have seen that drift and diffusion coefficients in the FPE enables to define the stochastic measure of total entropy in the turbulent cascade. The integral fluctuation theorem

originates from the second law of thermodynamics which states that in a non-equilibrium process the total entropy of production has to increase i.e. $\langle \Delta S_{tot} \rangle \geq 0$ [Nickelsen and Engel, 2013]. The integral fluctuation theorem is given by [Nickelsen and Engel, 2013; Reinke et al., 2018; Peinke et al., 2019]:

$$\langle e^{-\Delta S_{tot}} \rangle = 1. \tag{VI.20}$$

Based on the nature of cascade trajectories as shown in figure VI.12 and figure VI.13, the trajectory can be either entropy producing $\Delta S_{tot} > 0$ or entropy consuming $\Delta S_{tot} < 0$. The balance of entropy producing and entropy consuming trajectories defines the equality of $\langle e^{-\Delta S_{tot}} \rangle_N$ to unity for N independent trajectories. From the IFT, we see that the exponential weightage is given to $-\Delta S_{tot}$, which means that the rare occurrence of negative entropy cascade processes needs to be compensated by the huge number of positive entropy cascade processes. The entropy consuming trajectories are very rare which are characterized by the presence of extreme or rare events at small scales [Fuchs et al., 2020] (see figure VI.13). Therefore, in order to satisfy integral fluctuation theorem huge amount of statistics (large eddy turnover times $> \mathcal{O}(10^4)$) are required to compensate large number of entropy producing trajectories with a relatively few number of entropy consuming trajectories.

Figure VI.14 shows the evolution of $\langle e^{-\Delta S_{tot}} \rangle_N$ as a function of number of trajectories N in log-lin plot for the co-rotation configuration of the von Kármán flow. The system entropy and medium entropy are estimated from the drift and diffusion coefficients using equation VI.18,and equation VI.19 respectively. From this figure, we see that after taking in to account the minimum of 10^4 number of independent cascade trajectories, the IFT is satisfied with a good order of accuracy. Considering the total number of trajectories ($\approx \mathcal{O}(10^6)$), the fulfillment of integral fluctuation theorem can be verified within the accuracy of 0.2%, accounting to the $\langle e^{-\Delta S_{tot}} \rangle_{max(N)} = 0.9974$. The error bars in this figure are estimated based on the law of large numbers. We see that the larger is the number of trajectories considered the better is the convergence of IFT to unity. This analysis is performed on the hot-wire data which is acquired over a duration of 6 hours at an acquisition frequency of 50kHz. Acquiring a signal for such a long duration while maintaining the thermal stability is only possible in a well controlled laboratory scale turbulent flows such as in the SHREK facility. A better thermal stability and reproducibility in the SHREK experiment promises stable hot-wire measurements over longer duration. To our knowledge, so far, figure VI.14 shows the fulfillment of IFT for the highest number of independent cascade trajectories acquired over the longest duration of 6 hours. Figure VI.15 shows the validity of IFT for various contra configurations of the von Kármán flow. Thus, apart from the successful reconstruction of the conditional PDFs, once again the validity of IFT also ensured the accurate estimation of drift and diffusion coefficients in the SHREK experiment.

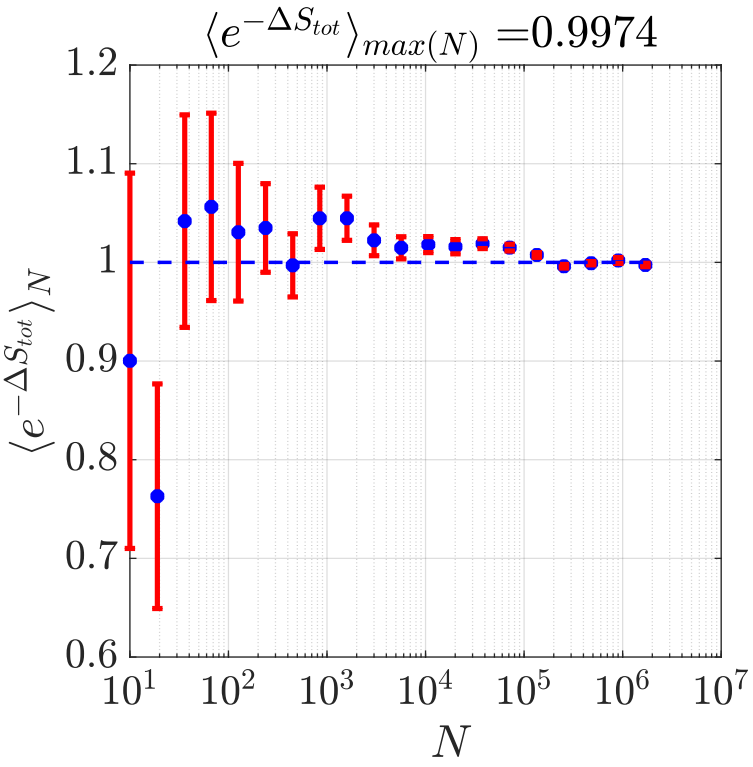

Figure VI.14: Evolution of $\langle e^{-\Delta S_{tot}} \rangle_N$ as a function of number of independent trajectories N on log-lin scale for the co-rotation configuration in the SHREK experiment [The horizontal blue-dashed line indicates the fulfillment of IFT i.e. $\langle e^{-\Delta S_{tot}} \rangle_N = 1$]

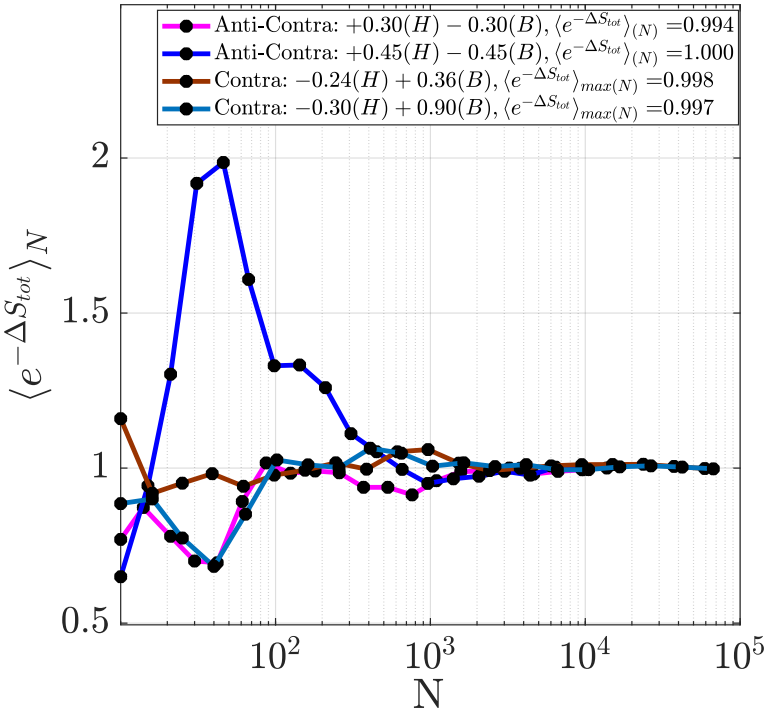

Figure VI.15: Evolution of $\langle e^{-\Delta S_{tot}} \rangle_N$ for various contra configurations

In what follows, we show the influence of the parameter d_{21} on the fulfillment of the integral fluctuation theorem. This analysis is performed for the same data set for which the reconstruction of PDFs of velocity increments is shown in figure VI.11 (see also figure VI.10). Figure VI.16 shows the effect of parameter d_{21} on the fulfillment of integral fluctuation theorem. From this figure we see that IFT is valid for both the case of $d_{21} \neq 0$ and $d_{21} = 0$ with $\langle e^{-\Delta S_{tot}} \rangle_N \approx 1.00 \pm 1\%$. From both the reconstruction of the PDFs and IFT we conclude that the contribution of parameter d_{21} is negligible. Therefore, the diffusion coefficient can be modelled using the only parameters of d_{20} and d_{22} without any significant loss of information.

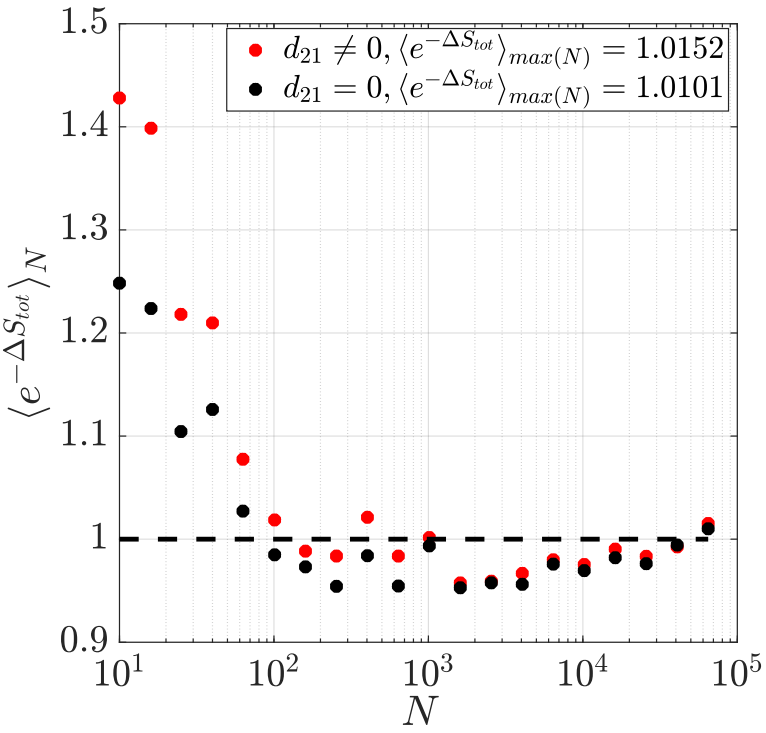

Figure VI.16: Validity of integral fluctuation theorem with and without the parameter d_{21} [The horizontal black-dashed line indicates the fulfillment of IFT i.e. $\langle e^{-\Delta S_{tot}} \rangle_N = 1$]

VI.3 Discussion on the drift and diffusion coefficients

The approach of using Fokker-Planck equation to describe turbulent cascade is far-reaching and global. Global in a sense that other well-known turbulence models such as K41 and K62 can be recovered from the FPE by applying certain assumptions. In what follows, we will show the link between particular cases of drift and diffusion coefficients of the FPE with the existing turbulence models.

VI.3.1 Interpretation of some coefficients linked with K41 and K62

According to K62 intermittency model, the scaling exponent of the p^{th} order structure function is given by $\zeta_p = \frac{p}{3} - \frac{\mu p(p-3)}{18}$, where μ is the K62 intermittency parameter (see also section I.3.1 and table 7). This model is based on the assumption of a log-normal distribution of the dissipation events. The intermittency parameter μ expresses the evolution of the variance of $\ln(\epsilon_r)$ across scales within the turbulent cascade (see equation I.16). In fact, the K62 model is the very first attempt of the modelization of the turbulent cascade as a multiplicative process. For the first time, the K62 intermittency model had been recovered from the FPE by Friedrich and Peinke [1997a]. The procedure to recover this model is also explained by Renner et al. [2001]; Nickelsen [2014] and more recently by Peinke et al. [2019]. We consider a special case of drift and diffusion coefficients in the FPE which leads to recover K62 model such that [Nickelsen and Engel, 2013; Nickelsen, 2017]:

$$D^{(1)}(u_r, r) = d_{11}(r)u_r, \quad D^{(2)}(u_r, r) = d_{22}(r)u_r^2 \quad (K62), \tag{VI.21}$$

with $d_{11}(r) = -\frac{3+\mu}{9r}$, $d_{22}(r) = \frac{\mu}{18r}$ and we assume that $d_{20} = d_{21} = 0$. Equation VI.21 is a particular case of FPE in which the drift and diffusion coefficients are purely expressed by

the linear and quadratic dependence on u_r respectively. From the above equation we see that according to K62 intermittency model, $d_{11}(r)$ and $d_{22}(r)$ are inversely proportional to scale r. We see that the multiplicative noise d_{22} in the diffusion coefficient of FPE is linked with the K62 intermittency parameter μ whereas the contribution of μ in d_{11} is rather weak. Therefore, $d_{22}(r)$ represents the intermittency within the turbulent cascade at scale r. Furthermore, if we consider a special case of FPE with $D^{(2)} = 0$ i.e. $\mu = 0$, we recover the K41 model given by [Nickelsen, 2014]:

$$D^{(1)}(u_r, r) = d_{11}(r)u_r, \quad D^{(2)}(u_r, r) = 0 \quad (K41), \tag{VI.22}$$

where $d_{11} = -\frac{1}{3r}$. From the above equation we see that the K41 model includes no contribution of the multiplicative diffusion coefficient (i.e. no intermittency) whereas it only includes the contribution of drift coefficient.

VI.3.2 Dependence of parameters d_{11}, d_{20} and d_{22} on scale

We have seen that the parameter d_{21} has a negligible influence on the diffusion coefficient based on our analysis of the reconstruction of PDFs of velocity increments and fulfillment of IFT. Therefore, in what follows, we only discuss the evolution of parameters d_{11}, d_{20} and d_{22} with respect to scale and Reynolds number. Based on equation VI.12 and VI.13, drift and diffusion coefficients are expressed in terms of parameters d_{11}, d_{20} and d_{22}. Figure VI.17 shows the parameters d_{11}, d_{20} and d_{22} as a function of scale $\frac{r}{\lambda}$ for the drift and diffusion coefficients plotted in figure VI.6. Because of the large range of $\frac{r}{\lambda}$, these parameters are plotted on a log-log scale. Figure VI.17 shows that $|d_{11}|$ (absolute value of d_{11}) decreases linearly with increase in $\frac{r}{\lambda}$ and then saturates at large scales. We found that the parameter d_{20} linearly increases with respect to scale $\frac{r}{\lambda}$. We see that the dependence of d_{20} on the scale $\frac{r}{\lambda}$ is rather weak. The parameter d_{22} linearly increases towards smaller scales within the inertial range. We observe that the additive noise d_{20} is acting predominantly on large scales and the multiplicative noise d_{22} on the small scales in the turbulent cascade.

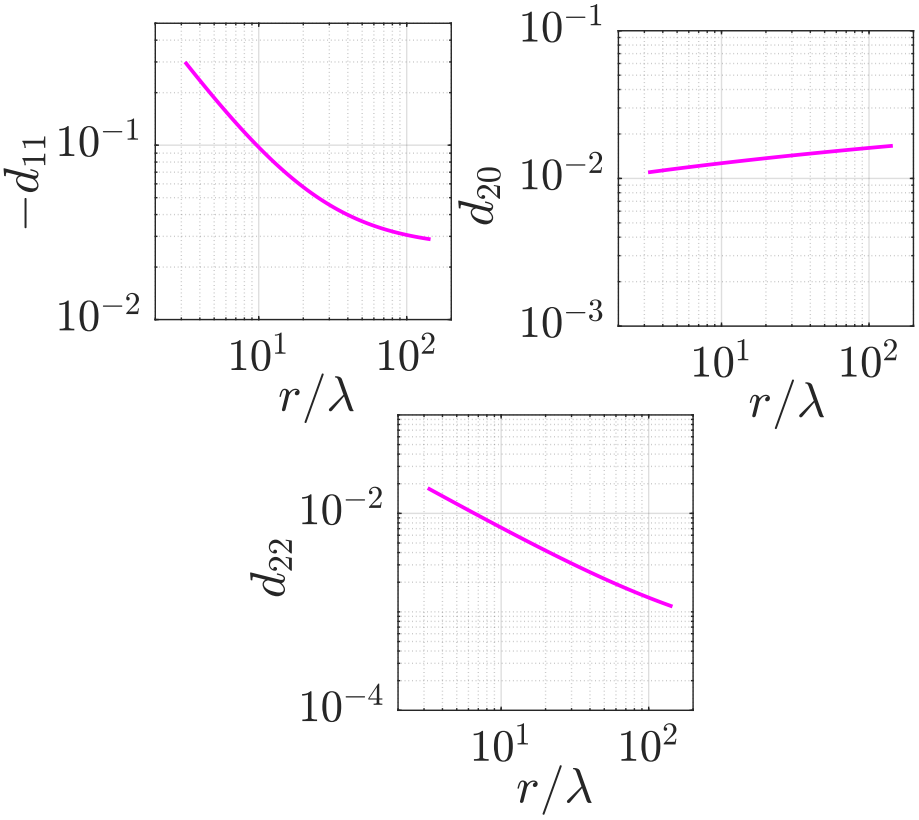

Figure VI.17: The parameters d_{11}, d_{20} and d_{22} as a function of $\frac{r}{\lambda}$ for the drift and diffusion coefficients plotted in figure VI.6

VI.3.3 Dependence of parameters d_{11}, d_{20} and d_{22} on Re_λ

We have seen the dependence of d_{11}, d_{20} and d_{22} with respect to scale $\frac{r}{\lambda}$. Such type of parametric analysis is performed for all the data sets in the SHREK experiment as mentioned in table 6 to study their dependence on the Reynolds number Re_λ. Figure VI.18 shows the variation of these parameters for data sets A to G with respect to $\frac{r}{\lambda}$, based on smaller to higher Reynolds number flows.

Figure VI.18 shows that for each configuration of the von Kármán flow, d_{11}, d_{20} and d_{22} exhibit similar behavior with respect to scale $\frac{r}{\lambda}$, yet distinctive with respect to Re_λ. From figure VI.18a to figure VI.18g, we see that $|d_{11}|$ increases with decrease in $\frac{r}{\lambda}$ for all flow configurations. Extrapolating $|d_{11}|$ for all the data sets down to $\frac{r}{\lambda} = 2$ leads to the value of ≈ 0.5 which is consistent with the study performed by Reinke et al. [2018] for various types of turbulent flows. In each flow configuration, at large scales $|d_{11}|$ saturates at higher value for low Re_λ flow. This is also consistent with the studies performed by Renner et al. [2002] over $Re_\lambda = 85$ - 1181. It is found that the linear behavior of $|d_{11}|$ with respect to $\frac{r}{\lambda}$ lasts longer for the high Re_λ flows having wider inertial range.

As mentioned earlier, d_{20} in the diffusion coefficient characterizes the additive noise in the turbulent cascade. From all the data sets A to G we found that the d_{20} decreases as $\frac{r}{\lambda}$ decreases as shown in figure VI.18. Overall, a weak dependence of d_{20} with respect to $\frac{r}{\lambda}$ on log-log plot is observed for all Re_λ flows. The dependence of d_{20} on Re_λ is clearly visible for all the data sets. This is mainly because of the availability of large range of Re_λ flows for each flow configuration. Throughout the post processing of the experimental data, the velocity increment u_r is normalized by the quantity $\sigma_\infty = \sqrt{2}\sigma$. And this plays an important role in the value of the

parameter d_{20} [Reinke et al., 2018; Fuchs et al., 2021b]. For each flow configuration the standard deviation σ increases with increase in $\mathcal{F}_1$ and $\mathcal{F}_2$ i.e. Re_λ. As a consequence, the difference of velocity increments in equation VI.10 $\left(\text{i.e. } \frac{(u_{r_1}-u_{r_2})}{\sigma_\infty}\right)$ is smaller for high Re_λ flows. Therefore, the parameter d_{20} is lower for high Re_λ flows in all flow configurations. In figure VI.18a, we see that d_{20} is higher at $Re_\lambda = 720$ as compared to $Re_\lambda = 3690$. This is because at $Re_\lambda = 720$ the standard deviation $\sigma = 0.01\frac{m}{s}$ whereas at $Re_\lambda = 3690$ the standard deviation $\sigma = 0.17\frac{m}{s}$.

From figure VI.18, we see that for all flow configurations d_{22} is lower for high Re_λ and *vice versa*. We see that d_{22} varies linearly with respect to scale $\frac{r}{\lambda}$ on the log-log plot. In figure VI.18b at $Re_\lambda = 6180$ and figure VI.18f at $Re_\lambda = 9480$, we see that the dependence of parameters d_{20} and d_{22} with respect to scale $\frac{r}{\lambda}$ differ significantly from other Re_λ flows. This may have occurred because in these two flows the estimated Taylor microscale $\approx 250\mu m$ (and hence the Einstein-Markov length) is smaller than the hot-wire spatial resolution. This causes an error in the estimation of the conditional moments which leads to the inaccurate estimation of diffusion coefficient by means of an extrapolation (see figure VI.5 and equation VI.11). Here, we also confirmed that the convergence of statistics is not an issue as enough statistics are available for these data sets. We also note that for these flows at $Re_\lambda = 6180$ and $Re_\lambda = 9480$ the integral fluctuation theorem is not satisfied. This is possibly because of the inaccurate drift and diffusion coefficients.

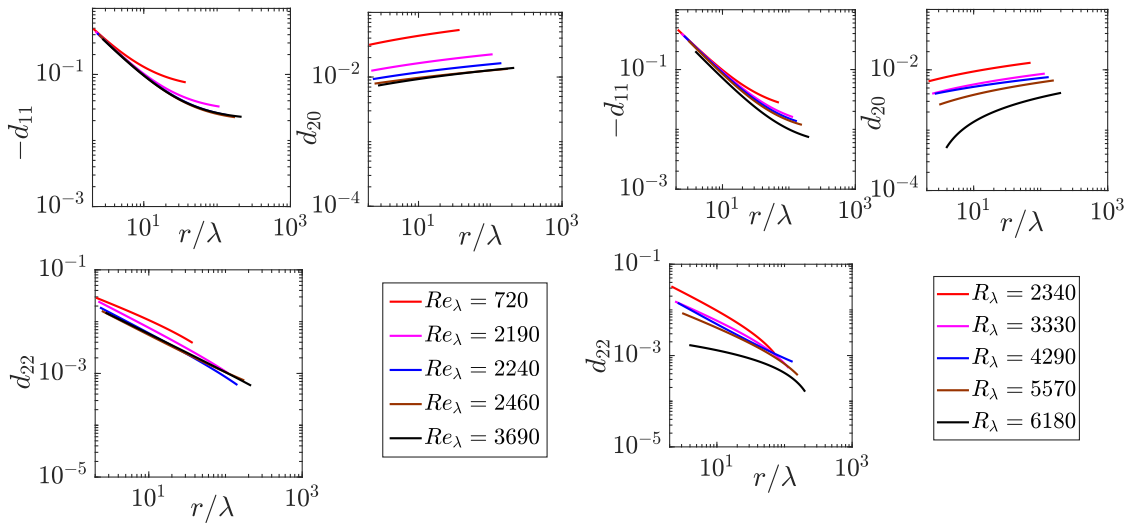

(a) Data set A

(b) Data set B

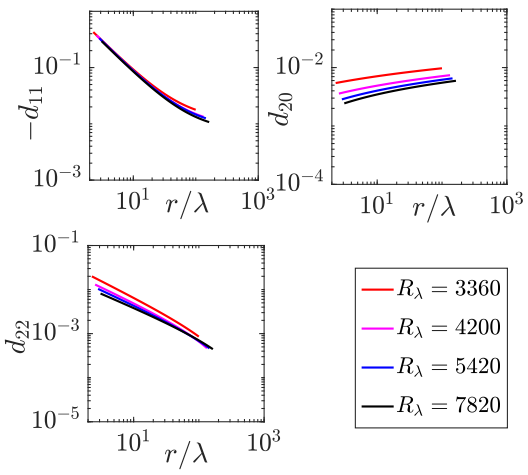

(c) Data set C

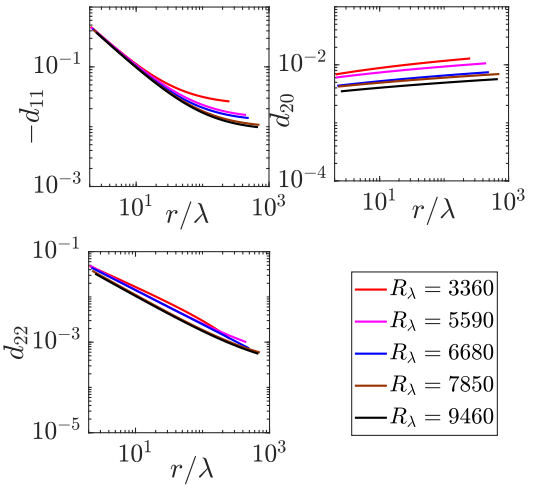

(d) Data set D

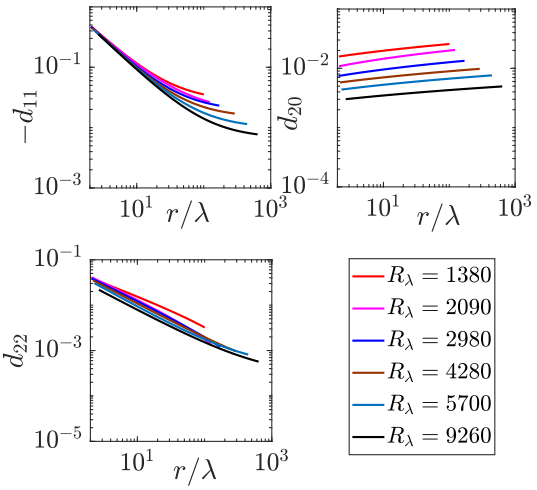

(e) Data set E

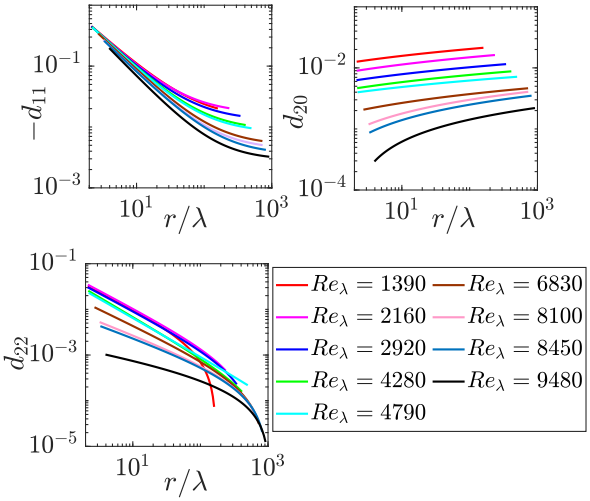

(f) Data set F

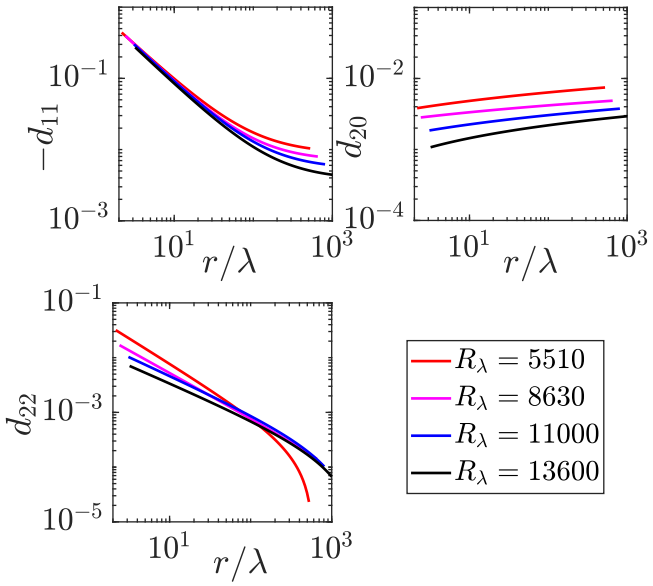

(g) Data set G

Figure VI.18: The parameters d_{11}, d_{20} and d_{22} as a function of scale $\frac{r}{\lambda}$ for various Re_λ corresponding to different configurations of flow as mentioned in table 6

We found a power law dependence of parameters d_{11} and d_{22} with respect to scale $\frac{r}{\lambda}$ corresponding to different flow configurations shown in figure VI.18 based on "low" to high Re_λ flows in the SHREK experiment. We found this power law for the small scales below $\frac{r}{\lambda} = 20$. The power law dependence of d_{11} and d_{22} is expressed as:

$$\begin{aligned} |d_{11}| &= \mathcal{P}_1 \left(\frac{r}{\lambda}\right)^{-\gamma}, \\ d_{22} &= \mathcal{P}_2 \left(\frac{r}{\lambda}\right)^{-\beta}, \end{aligned} \tag{VI.23}$$

where γ and β are the power law exponents of the parameters d_{11} and d_{22} respectively. And, $\mathcal{P}_1$ and $\mathcal{P}_2$ are the prefactors in the power law dependence of d_{11} and d_{22} respectively. Figure VI.19 shows the power law exponents of parameter d_{11} and d_{22} with respect to Re_λ for the flow configurations shown in figure VI.18. In figure VI.19a we see that $\gamma \approx 1.0$ for all Re_λ flows. We find that $|d_{11}| \propto \left(\frac{r}{\lambda}\right)^{-\gamma}$ holds universally for all types of von Kármán flows with $\gamma \approx 1.0$. In fact, we found that $\gamma \approx 1.0$ is in agreement with equation VI.21 and equation VI.22 i.e. $d_{11} \propto \frac{1}{r}$. From figure VI.19b we found that the power law exponent $\beta \approx 0.5 - 0.8$ for all flow configurations which also shows a slight decreasing tendency of β with respect to Re_λ. Thus, we do not observe any universal features of intermittency in terms of β in all flow configurations. We note that $\beta = 1.0$ (i.e. $d_{22} \propto \frac{1}{r}$) is a situation encountered in the K62 model (see equation VI.21). Thus, although we do not follow the K62 model, we are not far from the predictions of K62 model.

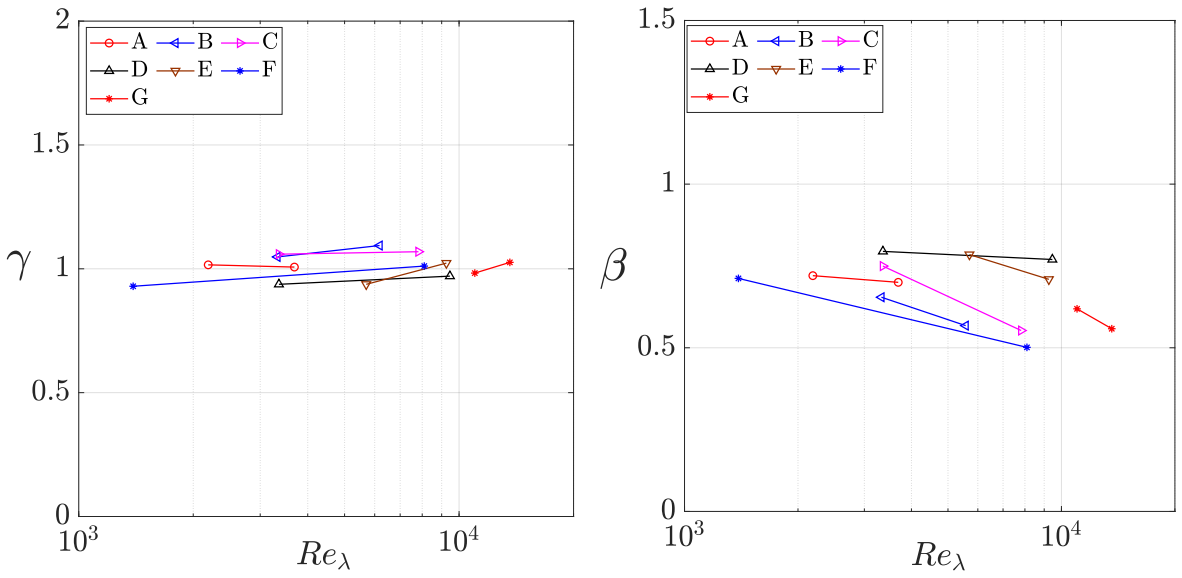

(a) Variation of γ with respect to Re_λ (b) Variation of β with respect to Re_λ

Figure VI.19: Power law exponents of parameter d_{11} and d_{22} with respect to Re_λ for all the flow configurations shown in figure VI.18

To study the dependence of parameters d_{11}, d_{20} and d_{22} on Re_λ, the following strategy is used where the above observations in figure VI.18 are showed in a more concise manner. In figure VI.18, a vertical cut is made at scale $\frac{r}{\lambda} = 4$ and $\frac{r}{\lambda} = 8$ and the corresponding parameters are plotted as a function of Reynolds number within the range of $Re_\lambda = 720 - 13600$. Figure VI.20 shows the dependence of d_{11} with respect to Re_λ at a scale $\frac{r}{\lambda} = 4$ and 8. From figure VI.20, we see that the change in d_{11} is very small (-0.26 to -0.22 at $\frac{r}{\lambda} = 4$ and -0.15 to -0.1 at $\frac{r}{\lambda} = 8$) with respect to Re_λ. The range of parameter d_{11} i.e. -0.15 to -0.1 at $\frac{r}{\lambda} = 8$ is in good agreement with the previous studies performed by Reinke et al. [2018]. It would have been interesting to plot the parameter d_{11} at $\frac{r}{\lambda} = 2$, which would converge around a unique value of -0.5. But, because of the lack of spatial resolution of the hot-wire, it has not been possible to estimate the drift and diffusion coefficients at $\frac{r}{\lambda} = 2$ for all types of flows considered in this study. In addition, to study the dependence of d_{11} on Reynolds number we have also plotted the prefactor $\mathcal{P}_1$ in equation VI.23 with respect to Re_λ as shown in figure VI.21. From this figure we see that $\mathcal{P}_1 \approx 1.0$ for all types of flows independent of the Re_λ of the flow. This confirms that d_{11} has negligible dependence on Re_λ for all types of the von Kármán flows.

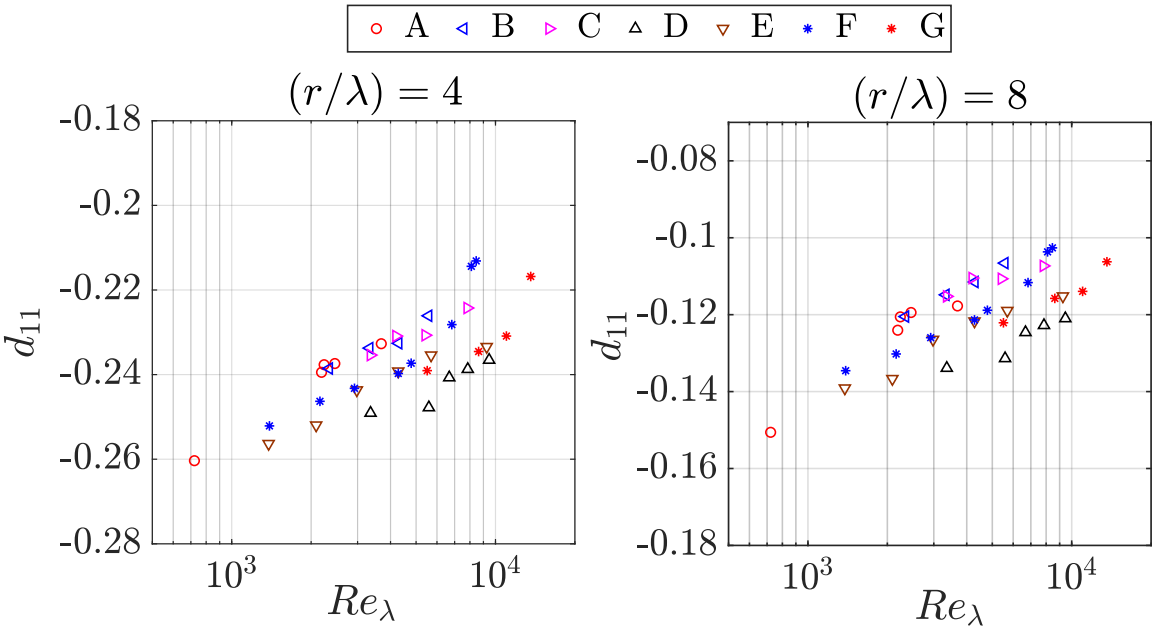

Figure VI.20: Parameter d_{11} as a function of Re_λ for data sets A to G

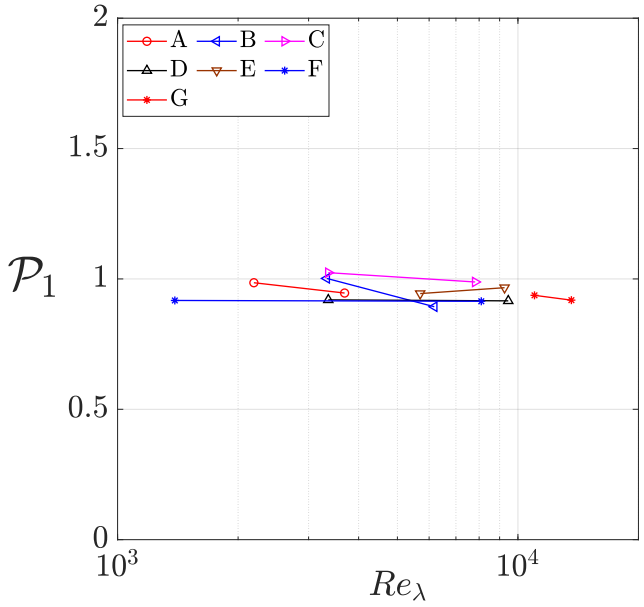

Figure VI.21: Prefactor $\mathcal{P}_1$ in equation VI.23 with respect to Re_λ for data sets A to G

Figure VI.22 shows the dependence of d_{20} with respect to Re_λ at a scale $\frac{r}{\lambda} = 4$ and 8. From figure VI.22, we see that d_{20} has a stronger dependence on Re_λ. For each type of flow, smallest value of parameter d_{20} is observed for highest Re_λ flow. Hence, for sufficiently high Re_λ flows, even higher than the Re_λ presented in this study, the parameter d_{20} can be neglected [Renner et al., 2002]. Such type of Fokker-Planck model with zero additive noise ($d_{20} = 0$) has already been proposed by Castaing [1997]. The decreasing trend of d_{20} with respect to Re_λ is also found

to be coherent with the studies performed by Renner et al. [2001]; Reinke et al. [2018]. Thus, at very large Reynolds number we expect $d_{20} \approx 0$.

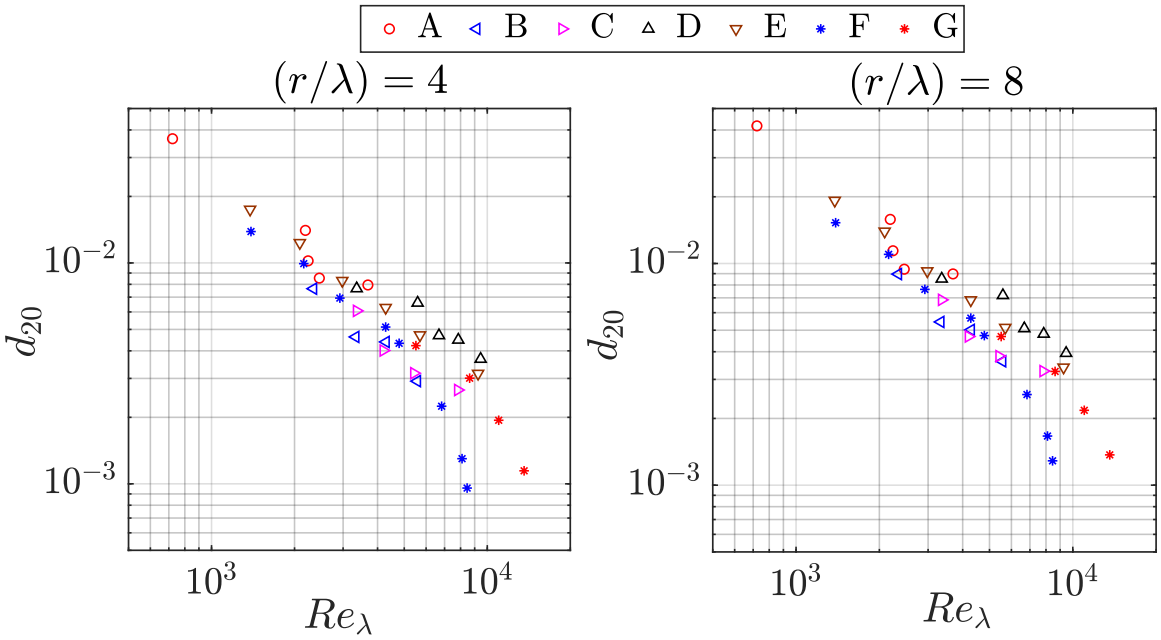

Figure VI.22: Parameter d_{20} as a function of Re_λ for data sets A to G

Figure VI.23 shows the variation of d_{22} at scale $\frac{r}{\lambda} = 4$ and $\frac{r}{\lambda} = 8$ with respect to Re_λ. From figure VI.23, we see that d_{22} decreases with increase in Re_λ for all flow configurations of von Kármán flow. This is in agreement with some of the results presented by Reinke et al. [2018]. We note that none of the previous studies were conducted for a closed type of flow such as the von Kármán flow. Also, none of the previous studies were conducted for the high Re_λ investigated in this thesis. From figure VI.23, it is evident that in the von Kármán flow at a fixed $\frac{r}{\lambda}$ we do not find the same multiplicative noise (d_{22}) while increasing the Re_λ of the flow. Furthermore, to study the dependence of d_{22} on Reynolds number we have also plotted the prefactor $\mathcal{P}_2$ in equation VI.23 with respect to Re_λ as shown in figure VI.24. From this figure we see that $\mathcal{P}_2$ lies within 0.02 - 0.07 and slightly decreases with respect to Re_λ for all types of flows configurations. This may suggest that the multiplicative noise gets damped out as a consequence of increase in Re_λ of the flow. Therefore, based on figure VI.23 and figure VI.24 for infinite Re_λ limit we may expect a vanishing multiplicative noise i.e. $d_{22} = 0$ which would lead to the prediction of the K41 model.

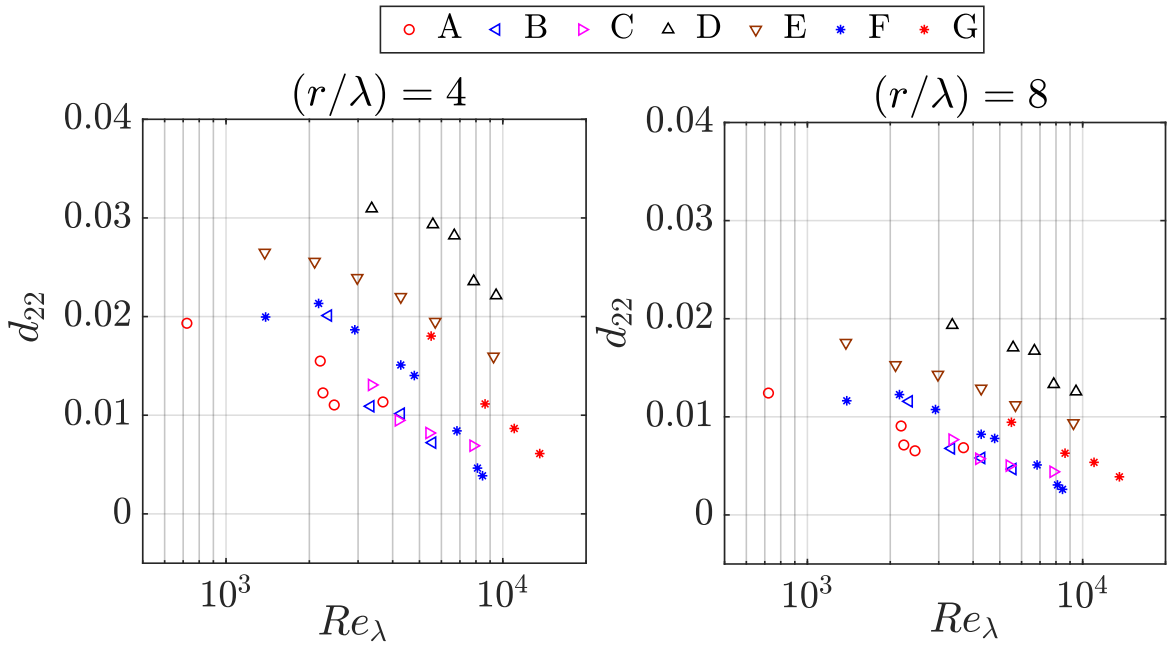

Figure VI.23: Parameter d_{22} as a function of Re_λ for data sets A to G

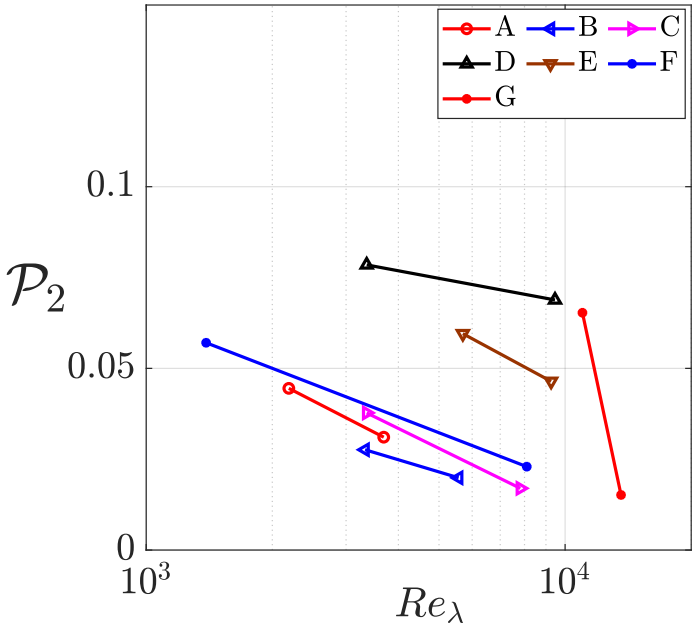

Figure VI.24: Prefactor $\mathcal{P}_2$ in equation VI.23 with respect to Re_λ for data sets A to G

In section V.9.3 we have seen that the K62 intermittency parameter μ represents the intermittency over the entire inertial range in the turbulent cascade. On the other hand, we know that $d_{22}(r)$ characterizes the intermittency at a particular scale just like the flatness of the PDFs

of velocity increments at a particular scale. In order to perform qualitative comparison of the intermittency parameters d_{22} and μ according to K62 model (i.e. $d_{22} = \frac{\mu}{18r}$) we can compare figure VI.23 and figure V.28. Both of these figures show a similar decreasing trend of the intermittency parameters d_{22} and μ with respect to Re_λ. We also see that the order of magnitude of μ in figure V.28 is in agreement with $\approx 18rd_{22}$. Here, we emphasize that μ and d_{22} are estimated based on completely different methods of ESS and FPE respectively. Figure VI.23 and figure V.28 also show the consistency of these two different methods/approaches to study the intermittency in the turbulent cascade. Both of these figures suggest that in the limiting case of infinite Reynolds number, we may expect that d_{22} and hence μ may tend to zero. In that case, K41 model can be seen as the limiting model for infinite Reynolds number flows.

VI.4 Application of FPE and IFT in HeII

In Chapter V (see section V.10.4) we have observed that the phenomenon of intermittency is also present in the superfluid turbulent flow. That analysis is presented for the anti-contra configuration of von Kármán flow in HeII at T = 2.0K, for which we have observed the Kolmogorov spectrum. Here, we have made an attempt to describe the turbulent cascade in HeII in terms of FPE. To investigate further the intermittency in such superfluid turbulent flows the approach of FPE is used to estimate the drift and diffusion coefficients. We confirmed that the Markov property is fulfilled in superfluid turbulent flow and hence further Fokker-Planck analysis is performed in a similar way as applicable to HeI.

Figure VI.25 shows the parameters of drift and diffusion coefficients for superfluid and normal helium for the data set G with $\mathcal{F}_1 = \mathcal{F}_1 = 1$ (see table 6). From this figure, we see that the parameter d_{11} shows no difference in HeI and HeII with respect to the scale $\frac{r}{\lambda}$ at least in the domain of scales accessible to our hot-wire probes. This means that the non-intermittent contribution governed by the FPE in the turbulent flow of HeI and HeII is same. The parameter d_{20} shows similar dependence on the scale $\frac{r}{\lambda}$ with higher magnitude in HeII than in HeI. As mentioned earlier, this parameter depends on the quantity σ_∞ used for the normalization of the velocity increment. The σ_∞ is larger for the data in HeI than in HeII, which explains the lower magnitude of d_{20} in normal helium than in superfluid. The parameter d_{22} shows the similar dependence in HeI and HeII in the inertial range. This suggests that the phenomenon of intermittency in the inertial range of the energy cascade of HeI and HeII is fundamentally analogous. From figure VI.25, we see that at $\frac{r}{\lambda} = 4$ the value of the intermittency parameter d_{22} is 0.02 and 0.01 for HeI and HeII respectively. This is also coherent with the decrease in the K62 intermittency parameter μ in HeII as compared to HeI ($d_{22} = \frac{\mu}{18r}$, see also section V.10.5).

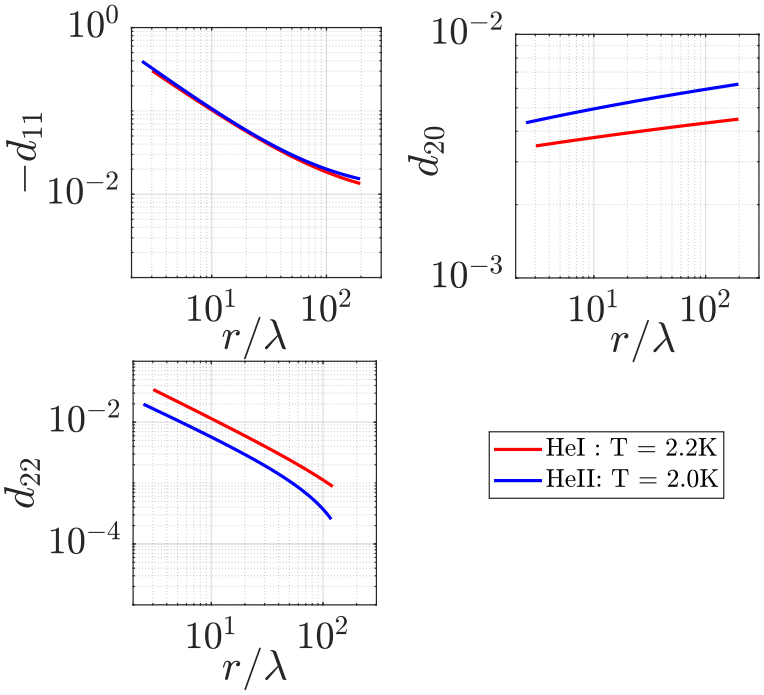

Figure VI.25: Drift and diffusion coefficients in superfluid at T = 2.0K and its comparison with normal helium for +1.0(H) - 1.0(B) anti-contra configuration in the SHREK experiment with turbine with radial blades

To investigate the reliability of the estimated drift and diffusion coefficients in superfluid, the validity of the integral fluctuation theorem is addressed. Figure VI.26 shows the validity of the integral fluctuation theorem in superfluid at T = 2.0K. This figure shows that the IFT is satisfied for HeI and HeII but with an error of 4% and 9% respectively. This enlightens that the drift and diffusion coefficients estimated for HeII are not entirely reliable which may have occurred because of the inadequacy of the Taylor hypothesis of frozen turbulence in the superfluid turbulent flows. This might well be associated with the lack of proper hot-wire calibration in superfluid (see figure V.30a). Also, we might expect some effects of the counterflow turbulence of the hot-wire itself at scales comparable to Taylor microscale. We find that the total mean entropy of production $\langle \Delta S_{tot} \rangle$ in HeI and HeII is 0.75 and 0.63 respectively (see table 8). To make these observations of FPE and IFT in superfluid in a more concrete sense further investigations are still necessary.

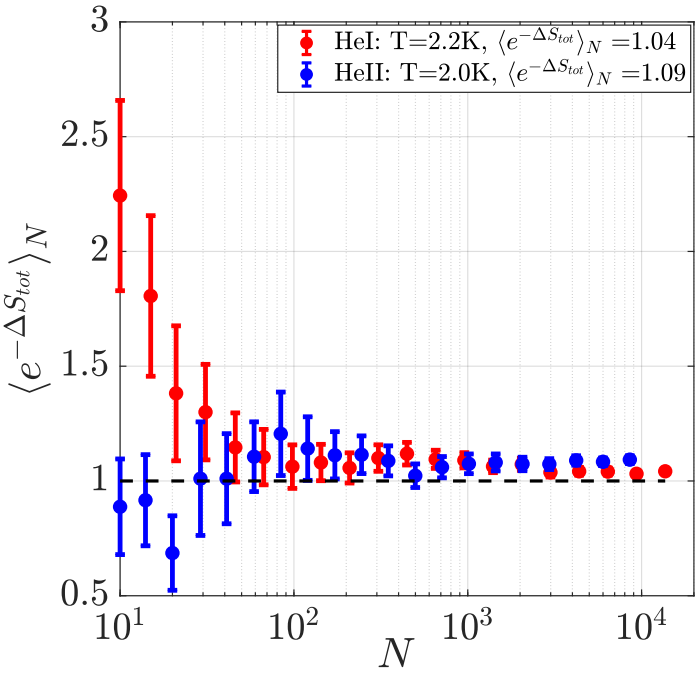

Figure VI.26: Evolution of $\langle e^{-\Delta S_{tot}} \rangle_N$ with respect to independent number of trajectories N in HeI and HeII showing the validity of integral fluctuation theorem

VI.5 Conclusion

In this chapter, we have used an alternative approach of the Fokker-Planck equation to describe the turbulent cascade in the SHREK experiment. Overall, 38 different data sets are studied. In a first step, we verified some Markovian properties and found that the Markov property is fulfilled for the SHREK experimental data. The drift and diffusion coefficients of the Fokker-Planck equation are measured. The procedure to estimate the drift ($D^{(1)}$) and diffusion ($D^{(2)}$) coefficients from the experimental data is explained in detail. We found that the precise estimation of drift and diffusion coefficients is ensured only if the Taylor microscale or Einstein-Markov length is larger than the hot-wire spatial length. This is typically true for the SHREK experimental data. The behavior of drift and diffusion coefficients with respect to scale $\frac{r}{\lambda}$ and velocity increment u_r is explored. We found that the drift coefficient is linear with respect to u_r, whereas the diffusion coefficient is parabolic with respect to u_r. Accordingly, the parametrization of $D^{(1)}$ and $D^{(2)}$ in terms of parameters d_{11}, d_{20}, d_{21} and d_{22} is performed to study their dependence on scales and Reynolds number for different flow configurations of the von Kármán flow.

To check the validity of the estimated drift and diffusion coefficients, the reconstruction of PDFs of velocity increments is performed. We found that the agreement between reconstructed and experimental PDF is very good as a result of scale independent optimization. We found that a scale dependent optimization may help to get a more precise estimate of drift and diffusion coefficients. The validity of integral fluctuation theorem in the SHREK experimental data is addressed. It is found that the IFT is valid for all configurations of the SHREK experiment with a positive mean total production of entropy in the turbulent cascade. The validity of IFT also ensured that the estimated drift and diffusion coefficients for the SHREK experiment are accurate. Based on the validity of IFT and successful reconstruction of PDFs of velocity increments with $d_{21} = 0$ we concluded that the contribution of d_{21} is very negligible and hence we can model the diffusion coefficient with using only d_{20} and d_{22} without any loss of accuracy.

We showed the interpretation of drift and diffusion coefficients linked with the K41 and K62

model. We found that $|d_{11}|$ increases linearly towards small scales for all types of flows. A convergence of parameter $|d_{11}|$ to a value of 0.5 is observed irrespective of the flow configuration which is in agreement with the past studies. We established a power law $|d_{11}| = \mathcal{P}_1\left(\frac{r}{\lambda}\right)^{-\gamma}$ and found that $\gamma \approx 1.0$ holds universally for types of von Kármán flows which is in agreement with the K41 and K62 model. The dependence of parameter d_{11} on Re_λ is found to be universal with $\mathcal{P}_1 \approx 1.0$. We found that d_{20} is dominant at large scale and decreases linearly towards small scales. We found that the dependence of d_{20} on scale is very weak. We also found that d_{20} decreases with increase in Re_λ. Thus, for an infinite Re_λ limit we may expect a vanishing d_{20} in agreement with the K41 and K62 model.

We showed that the K62 intermittency parameter μ is linked with the multiplicative noise d_{22} given by the relation $d_{22} = \frac{\mu}{18r}$. Therefore, d_{22} in FPE expresses the intermittent features of the turbulent cascade. We found that d_{22} increases linearly towards small scales for all flow configurations. We established a power law $d_{22} = \mathcal{P}_2\left(\frac{r}{\lambda}\right)^{-\beta}$ and found that $\beta \approx 0.5 - 0.8$ for all types of flows. We found that d_{22} decreases with increase in Re_λ at a fixed scale for all flow configurations. We also showed that $\mathcal{P}_2$ decreases with increase in Re_λ. Thus, d_{22} suggests the damping of multiplicative noise with an increase in Re_λ. The findings of d_{22} are strongly supported by μ which also tends to decrease with Re_λ, which shows the consistency of two different approaches of FPE and ESS. The dependence of these parameters d_{22} and μ on Re_λ is found to be not universal. In fact, it depends on the type of flow configuration of the von Kármán flow. For the infinite Re_λ limit, the parameters d_{22} and μ collectively show a tendency of going towards zero. This suggests that the K41 model may be valid for infinite Re_λ limit where no intermittency corrections are expected.

The application of FPE and IFT is addressed in superfluid. From the FPE, the same non intermittent contribution (d_{11}) is found for HeI and HeII turbulent flows. We found that the additive noise is more in HeII than in HeI whereas the multiplicative noise is more in HeI than in HeII. The decreasing trend of intermittency parameter d_{22} is coherent with the decrease of K62 intermittency parameter μ in HeII as compared to HeI. IFT is found to be less satisfactory in HeII than in HeI with the error of 9% and 4% respectively. Overall, the statistical investigation of superfluid turbulent flow suggests that the interplay of energy cascade and intermittency in the inertial range is similar to the classical fluids.

VII CONCLUSION AND PERSPECTIVES

In the context of this thesis, a detailed experimental research is performed to explore the phenomenon of intermittency in turbulent flows using classical liquid helium (T = 2.2 - 2.4K) at possibly the highest Reynolds numbers ever achieved in the laboratory. We have used the experimental technique of hot-wire anemometry to measure the velocity of turbulent flows. During this thesis, we have fabricated many hot-wires in collaboration with Jean-Paul Moro with our contribution towards the planning and installation of these hot-wires in various experiments. Typically, we have fabricated hot-wires of $l_w \approx 300\mu m$ and $d_w = 1.27\mu m$ with the present technique. As these hot-wires are very fragile we have seen that they are very likely exposed to the risk of breaking. Nevertheless, we gradually improved the hot-wire fabrication technique and now we are able to make the hot-wires of $l_w \approx 100\mu m$ and $d_w = 0.5\mu m$ with the new technique. But, unfortunately, these hot-wires broke either during installation or the cool-down process. Overall, we have gradually progressed in order to reduce the spatial dimensions of the hot-wire.

To obtain an accurate hot-wire calibration we have designed a cryostat called HECAL. We have modified the instrumentation in the HECAL facility to perform a precise moving/flying hot-wire calibration. For the first time, a successful hot-wire calibration is obtained in the HECAL facility in normal helium. So far, in the HECAL facility we have not fully understood the reason behind the inadequacy of the hot-wire calibration in superfluid. This is the first time that we have succeeded in installing a pre-calibrated hot-wire from the HECAL facility in the ECOUTURB experiment. Overall, the HECAL facility is now fully operational to perform the hot-wire calibration in HeI so that the pre-calibrated hot-wire can be used in other installations.

In this thesis, we have studied two different types of cryogenic turbulent flows, viz. jet flows and von Kármán flows using the HEJET and SHREK facilities respectively. The HEJET is a small scale facility whereas the SHREK is a large scale facility. Based on the previous HEJET experiments performed by Duri [2012] we identified that a possible source of jet instability is associated with the old centrifugal pump which was not well adapted to the piping circuit of the HEJET facility. Thus, at the beginning of this thesis we decided to upgrade the HEJET facility by designing a new centrifugal pump which is well adapted to the HEJET circuit and, thereby eliminating one of the reasons of instability of the jet. A successful characterization of this newly designed centrifugal pump in the HEJET facility is performed in both HeI and HeII, which shows that it works very well with the HEJET piping circuit, with an estimated maximum pump efficiency of 32%. We understood that with the use of new turbine we have certainly increased the efficiency of the centrifugal pump but we have not resolved the problem of jet instability. We had limited hot-wire measurements in the HEJET experiment because most of the times the hot-wires were broken during the cool-down process. We realized that we have not recovered the measurements performed by Duri [2012] in the HEJET facility. In fact, in this thesis we have operated the HEJET facility at high turbine frequencies (at least 4.5 times higher than in Duri [2012]) which was never been explored before. In addition, we have used the hot-wire in CCA mode with high overheating instead of CTA used by Duri [2012]. Altogether, we believe that the jet instability mainly occurs because of the confinement of the jet flow in the experimental chamber.

We have extensively studied the von Kármán flows by performing numerous SHREK experiments. We showed that in the SHREK facility we can generate very high Re_λ ($\approx$ 1000 - 13000) turbulent flows which has never been achieved in the laboratory experiment. We noticed that a large inertial range is present in the power spectral density of the hot-wire signal. But, on the other hand, it is less evident (smaller than expected) from the compensated third order structure function. We believe that the inadequacy to notice a rigorous asymptotic plateau in the compensated third order structure function even at very high Re_λ in the SHREK experi-

ment is related to the lack of homogeneity as the hot-wire is installed quite close to the wall of the von Kármán cell. Nevertheless, we have verified the scaling laws of turbulent flows at high Reynolds number flows in the SHREK experiment. An extensive study of the phenomenon of intermittency in the inertial range is performed over a wide range of Reynolds numbers. We have witnessed an universal slope ≈ -0.1 of the flatness of PDFs of velocity increments with respect to scales. We found that with an increase in Reynolds number the scaling exponents ζ_p of the structure functions shows some convergence towards K41 model. In other words, we found that with increase in Reynolds number the K62 intermittency parameter μ decreases.

We have studied the Fokker-Planck description of the turbulent cascade, as it does not need any assumption on the power laws in the inertial range. We believe that the failure to apply the Fokker-Planck approach to the turbulent cascade in the HEJET experiment is associated with the inability to satisfy the Markov property which is linked with the jet instability. In the spirit of Fokker-Planck analysis we continued our efforts on the SHREK experimental velocity data. We confirmed the existence of the Markov property in the SHREK experiment. And, we verified that the turbulent cascade can be described by the Fokker-Planck equation. We verified that the integral fluctuation theorem is satisfied in the SHREK experiment owing to the great extent of reproducibility and stability of this experiment. From our experimental investigation of the phenomenon of intermittency at very large Reynolds numbers (up to $Re_\lambda \approx \mathcal{O}(10^4)$) it seems that as the Reynolds number increases we are closer to the predictions of K41.

VII.1 Future works

As turbulent flows studied in this thesis have very high Reynolds number, the dissipation scales ($\approx 30\mu m$) are very small. To this date, we have fabricated the hot-wire of $l_w \approx 100\mu m$ and $d_w = 0.5\mu m$ and we are not sure if we could minimize the spatial dimensions any further. But, it is important to continue these efforts to increase the spatial and temporal resolution of the hot-wire. During some of the HEJET experiments, in parallel with the Pt-Rh hot-wires we have also explored the use of hot-wires made of carbon nanotube yarns. We have seen that these hot-wires are very promising in terms of their spatial resolution ($\approx 15 - 20\mu m$) and robustness at cryogenic temperatures. Therefore, further attempts towards the development of a hot-wire made of carbon nanotube yarns can be continued for their special application in cryogenic turbulent flows.

The first and foremost thing to do in the HEJET facility is to address the issue of jet instability. To do this, the future HEJET experiments may be performed with the nozzle diameter of 3mm which may help to reduce the effects of the lateral jet confinement. The hot-wire may be operated at less overheating in the CCA mode or in the CTA/CVA mode to avoid the significant contribution of its natural convection at high overheating. A better jet stability may be expected while changing the position of the horizontal jet stabilization grid. Therefore, based on the investigation of the jet instability multiple HEJET experiments can be performed to find the best position of the grid. With these modifications, future HEJET experiments may be performed in coming months. After resolving the problem of jet instability it would be interesting to carry out an extensive study of the intermittency along with the application of Fokker-Planck equation while addressing the integral fluctuation theorem in the HEJET experiment. This will allow us to compare the dependence of the drift and diffusion coefficients on the Reynolds number in the SHREK and HEJET experiments.

A much more extensive experimentation is still required to fully understand and confirm the findings of superfluid turbulent flows presented in this thesis. To begin with it is important to perform the similar experimental measurements conducted in this thesis while operating the hot-wire at less overheating in the CCA mode. A deeper understanding of the heat transfer

mechanism in superfluid is required to establish the law of hot-wire calibration in HeII. In the HECAL facility, it is necessary to perform the study towards the successful calibration of the hot-wire in superfluid. Certainly, a further investigation of the phenomenon of intermittency, Fokker-Planck analysis and integral fluctuation theorem in superfluid turbulent flows is needed which may be explored using numerous data sets and multitude of experiments.

In parallel with the Fokker-Planck analysis performed in this thesis, there are also some new studies performed by Fuchs et al. [2020, 2021a] at the University of Oldenburg. They showed that the occurrence of the negative entropy producing cascade trajectories may be linked with singularities in turbulent flows. Fuchs et al. [2021a] have also used an approach based on the instanton theory for the description of turbulent cascade. In the framework of future research, the experiments at cryogenic temperatures will allow to bring an important information related to singularities and instanton theory in the turbulent cascade at very high Reynolds number.

Bibliography

Ali, N., Fuchs, A., Neunaber, I., Peinke, J., and Cal, R. B. (2019). Multi-scale/fractal processes in the wake of a wind turbine array boundary layer. *Journal of Turbulence*, 20(2):93–120.

Anselmet, F., Gagne, Y., Hopfinger, E. J., and Antonia, R. A. (1984). High-order velocity structure functions in turbulent shear flows. *Journal of Fluid Mechanics*, 140:63–89.

Antonia, R., Satyaprakash, B., and Hussain, F. (1982). Statistics of fine-scale velocity in turbulent plane and circular jets. *J. FLUID MECH.*, 119:55–89.

Antonia, R. A., Djenidi, L., Danaila, L., and Tang, S. L. (2017). Small scale turbulence and the finite reynolds number effect. *Physics of Fluids*, 29(2):020715.

Antonia, R. A., Satyaprakash, B. R., and Hussain, A. K. M. F. (1980). Measurements of dissipation rate and some other characteristics of turbulent plane and circular jets. *The Physics of Fluids*, 23(4):695–700.

Antonia, R. A., Tang, S. L., Danaila, L., Djenidi, L., and Zhou, Y. (2019). K41 versus k62: Recent developments. In Zhou, Y., Kimura, M., Peng, G., Lucey, A., and Huang, L., editors, *Fluid-Structure-Sound Interactions and Control*, pages 3–14, Singapore. Springer Singapore.

Antonia, R. A., Zhou, T., and Xu, G. (2000). Second-order temperature and velocity structure functions: Reynolds number dependence. *Physics of Fluids*, 12(6):1509–1517.

Barenghi, C. F., L'vov, V. S., and Roche, P.-E. (2014). Experimental, numerical, and analytical velocity spectra in turbulent quantum fluid. *Proceedings of the National Academy of Sciences*, 111(Supplement 1):4683–4690.

Batchelor, G. K., Townsend, A. A., and Jeffreys, H. (1949). The nature of turbulent motion at large wave-numbers. *Proceedings of the Royal Society of London. Series A. Mathematical and Physical Sciences*, 199(1057):238–255.

Benzi, R., Ciliberto, S., Baudet, C., Chavarria, G. R., and Tripiccione, R. (1993). Extended self-similarity in the dissipation range of fully developed turbulence. *Europhysics Letters (EPL)*, 24(4):275–279.

Berson, A., Poignand, G., Blanc-Benon, P., and Comte-Bellot, G. (2010). Capture of instantaneous temperature in oscillating flows: Use of constant-voltage anemometry to correct the thermal lag of cold wires operated by constant-current anemometry. *Review of Scientific Instruments*, 81(1):015102.

Biferale, L., Khomenko, D., L'vov, V., Pomyalov, A., Procaccia, I., and Sahoo, G. (2018). Turbulent statistics and intermittency enhancement in coflowing superfluid ^{4}He. *Phys. Rev. Fluids*, 3:024605.

Bourgoin, M., Baudet, C., and Kharche, S. (2018). Investigation of the small-scale statistics of turbulence in the modane s1ma wind tunnel. *CEAS Aeronautical Journal*, 9(2):269–281.

Bourgoin, M., Marié, L., Pétrélis, F., Gasquet, C., Guigon, A., Luciani, J.-B., Moulin, M., Namer, F., Burguete, J., Chiffaudel, A., Daviaud, F., Fauve, S., Odier, P., and Pinton, J.-F. (2002). Magnetohydrodynamics measurements in the von kármán sodium experiment. *Physics of Fluids*, 14(9):3046–3058.

Bruun, H. (1995). Hot-wire anemometry : principles and signal analysis.

Bruun, H. H., Farrar, B., and Watson, I. (1989). A swinging arm calibration method for low velocity hot-wire probe calibration. *Experiments in Fluids*, 7(6):400–404.

Burattini, P., Antonia, R. A., and Danaila, L. (2005). Similarity in the far field of a turbulent round jet. *Physics of Fluids*, 17(2):025101.

Cadot, O., Couder, Y., Daerr, A., Douady, S., and Tsinober, A. (1997). Energy injection in closed turbulent flows: Stirring through boundary layers versus inertial stirring. *Phys. Rev. E*, 56:427–433.

Castaing, B. (1997). Turbulence: Statistical approach. In Dubrulle, B., Graner, F., and Sornette, D., editors, *Scale Invariance and Beyond*, pages 225–234, Berlin, Heidelberg. Springer Berlin Heidelberg.

Castaing, B. (2016). *Fonctionnement du fil chaud*. Private communication.

Castaing, B., Gagne, Y., and Hopfinger, E. (1990). Velocity probability density functions of high reynolds number turbulence. *Physica D: Nonlinear Phenomena*, 46(2):177 – 200.

Castaing, B., Gagne, Y., and Marchand, M. (1993). Log-similarity for turbulent flows? *Physica D: Nonlinear Phenomena*, 68(3):387 – 400.

Chabaud, B. (1992). *Etude de la turbulence dans un jet d'hélium gazeux à basse température*. PhD thesis, Université Joseph Fourier.

Champagne, F. H. (1978). The fine-scale structure of the turbulent velocity field. *Journal of Fluid Mechanics*, 86(1):67–108.

Chanal, O. (1998). *Vers les échelles dissipatives dans un jet d'hélium gazeux à basse température*. PhD thesis, Université Joseph Fourier.

Chanal, O., Chabaud, B., Castaing, B., and Hébral, B. (2000). Intermittency in a turbulent low temperature gaseous helium jet. *The European Physical Journal B - Condensed Matter and Complex Systems*, 17(2):309–317.

Chevillard, L., Castaing, B., Arneodo, A., Lévêque, E., Pinton, J.-F., and Roux, S. G. (2012). A phenomenological theory of eulerian and lagrangian velocity fluctuations in turbulent flows. *Comptes Rendus Physique*, 13(9):899 – 928. Structures and statistics of fluid turbulence/Structures et statistiques de la turbulence des fluides.

Chevillard, L., Castaing, B., and Lévêque, E. (2005). On the rapid increase of intermittency in the near-dissipation range of fully developed turbulence. *The European Physical Journal B - Condensed Matter and Complex Systems*, 45(4):561–567.

Chevillard, L., Castaing, B., Lévêque, E., and Arneodo, A. (2006). Unified multifractal description of velocity increments statistics in turbulence: Intermittency and skewness. *Physica D: Nonlinear Phenomena*, 218(1):77 – 82.

Claudet, G. (1981). Cooling modes for superconducting magnets. *IEEE Transactions on Magnetics*, 17(5):1749–1756.

Clay (2000). *Millennium problems*. Clay Mathematics Institute: http://www.claymath.org/millennium-problems.

Cleve, J., Greiner, M., Pearson, B. R., and Sreenivasan, K. R. (2004). Intermittency exponent of the turbulent energy cascade. *Phys. Rev. E*, 69:066316.

Comte-Bellot, G. (1976). Hot-wire anemometry. *Annual Review of Fluid Mechanics*, 8(1):209–231.

Comte-Bellot, G. and Sarma, G. R. (2001). Constant voltage anemometer practice in supersonic flows. *AIAA Journal*, 39(2):261–270.

Diribarne, P., Bon-Mardion, M., Girard, A., Moro, J. P., Rousset, B., Chilla, F., Salort, J., Braslau, A., Daviaud, F., Dubrulle, B., Gallet, B., Moukharski, I., Saw, E. W., Baudet, C., Gibert, M., Roche, P. E., Rusaouen, E., Golov, A., L'vov, V., and Nazarenko, S. (2021a). On the investigation of properties of superfluid ^{4}he turbulence using a hot-wire signal.

Diribarne, P., Rousset, B., Sergeev, Y. A., Valentin, J., and Roche, P.-E. (2021b). Cooling with a subsonic flow of quantum fluid. *Phys. Rev. B*, 103:144509.

Douady, S., Couder, Y., and Brachet, M. E. (1991). Direct observation of the intermittency of intense vorticity filaments in turbulence. *Phys. Rev. lett.*, 67(8):983–986.

Dryden, H. L., K. A. M. (1929). The measurement of fluctuations of air speed by the hot-wire anemometer. Technical Report 320, National advisory committee for aeronautics.

Duri, D. (2012). *Mise en évidence expérimentale de l'intermittence dans un jet cryogénique turbulent d'hélium normal et superfluide*. PhD thesis, Université de Grenoble.

Durì, D., Baudet, C., Moro, J.-P., Roche, P.-E., and Diribarne, P. (2015). Hot-wire anemometry for superfluid turbulent coflows. *Review of Scientific Instruments*, 86(2):025007.

Fauve, S., Laroche, C., and Castaing, B. (1993). Pressure fluctuations in swirling turbulent flows. *Journal de Physique II*, 3(3):271–278.

Friedrich, R. and Peinke, J. (1997a). Description of a turbulent cascade by a fokker-planck equationl. *Physical Review Letters*, 78(5):863–866.

Friedrich, R. and Peinke, J. (1997b). Statistical properties of a turbulent cascade. *Physica D: Nonlinear Phenomena*, 102(1):147 – 155.

Friedrich, R., Zeller, J., and Peinke, J. (1998). A note on three-point statistics of velocity increments in turbulence. *Europhys. Lett.*, 41(2):153–158.

Frisch, U. (1995). *Turbulence, the Legacy of A.N. Kolmogorov*. Cambridge Univ. Press.

Frisch, U., Sulem, P.-L., and Nelkin, M. (1978). A simple dynamical model of intermittent fully developed turbulence. *Journal of Fluid Mechanics*, 87(4):719–736.

Fuchs, A., Herbert, C., Rolland, J., Wächter, M., Bouchet, F., and Peinke, J. (2021a). Instantons and the path to intermittency in turbulent flows.

Fuchs, A., Kharche, S., Wächter, M., and Peinke, J. (2021b). An open source matlab package to perform basic statistical analysis of turbulence data and other complex systems along with its application to fokker-planck equation and integral fluctuation theorem.

Fuchs, A., Obligado, M., Bourgoin, M., Gibert, M., Mininni, P. D., and Peinke, J. (2021c). The entropy and fluctuation theorems of inertial particles in turbulence.

Fuchs, A., Queirós, S. M. D., Lind, P. G., Girard, A., Bouchet, F., Wächter, M., and Peinke, J. (2020). Small scale structures of turbulence in terms of entropy and fluctuation theorems. *Phys. Rev. Fluids*, 5:034602.

Fuchs, A., Reinke, N., Nickelsen, D., and Peinke, J. (2019). A rigorous entropy law for the turbulent cascade. In Gorokhovski, M. and Godeferd, F. S., editors, *Turbulent Cascades II*, pages 17–25, Cham. Springer International Publishing.

Gervais, P., Baudet, C., and Gagne, Y. (2007). Acoustic Lagrangian velocity measurement in a turbulent air jet. *Experiments in Fluids*, 42(3):371–384.

Guellouz, M. S. and Tavoularis, S. (1995). A simple pendulum technique for the calibration of hot-wire anemometers over low-velocity ranges. *Experiments in Fluids*, 18(3):199–203.

Horn, G. and Thring, M. (1956). Angle of Spread of Free Jets. *Nature*, 178:205–206.

Huang, N. E., Shen, Z., Long, S. R., Wu, M. C., Shih, H. H., Zheng, Q., Yen, N.-C., Tung, C. C., and Liu, H. H. (1998). The empirical mode decomposition and the hilbert spectrum for nonlinear and non-stationary time series analysis. *Proceedings of the Royal Society of London. Series A: Mathematical, Physical and Engineering Sciences*, 454(1971):903–995.

Hultmark, M. and Smits, A. J. (2010). Temperature corrections for constant temperature and constant current hot-wire anemometers. *Measurement Science and Technology*, 21(10):105404.

Hussein, H. J., Capp, S. P., and George, W. K. (1994). Velocity measurements in a high-reynolds-number, momentum-conserving, axisymmetric, turbulent jet. *Journal of Fluid Mechanics*, 258:31–75.

Idelchik, I. E. (1999). *Handbook of hydraulic resistance*. Begell House Inc.

J.-F. Pinton and R. Labbé (1994). Correction to the taylor hypothesis in swirling flows. *J. Phys. II France*, 4(9):1461–1468.

Jiang, F. (1997). Silicon-micromachined flow sensors. *PhD Thesis, California institute of technology*.

Kahalerras, H., Malécot, Y., Gagne, Y., and Castaing, B. (1998). Intermittency and reynolds number. *Physics of Fluids*, 10(4):910–921.

Karman, T. and Howarth, L. (1938). On the statistical theory of isotropic turbulence. *Proceedings of the Royal Society of London. Series A - Mathematical and Physical Sciences*, 164(917):192–215.

King, L. V. and Barnes, H. T. (1914). Xii. on the convection of heat from small cylinders in a stream of fluid: Determination of the convection constants of small platinum wires with applications to hot-wire anemometry. *Philosophical Transactions of the Royal Society of London. Series A, Containing Papers of a Mathematical or Physical Character*, 214(509-522):373–432.

Klewicki, J. C. and Falco, R. E. (1990). On accurately measuring statistics associated with small-scale structure in turbulent boundary layers using hot-wire probes. *Journal of Fluid Mechanics*, 219:119–142.

Knebel, P., K. A. P. J. (2011). Atmospheric wind field conditions generated by active grids. *Exp Fluids*, 51:471–481.

Kolmogorov, A. (1941). The Local Structure of Turbulence in Incompressible Viscous Fluid for Very Large Reynolds' Numbers. *Akademiia Nauk SSSR Doklady*, 30:301–305.

Kolmogorov, A. N. (1941). Dissipation of energy in locally isotropic turbulence. *Akademiia Nauk SSSR Doklady*, 32:16–18.

Kolmogorov, A. N. (1962). A refinement of previous hypotheses concerning the local structure of turbulence in a viscous incompressible fluid at high reynolds number. *Journal of Fluid Mechanics*, 13(1):82–85.

Kuzzay, D., Faranda, D., and Dubrulle, B. (2015). Global vs local energy dissipation: The energy cycle of the turbulent von kármán flow. *Physics of Fluids*, 27(7):075105.

Landau, L. and Lifshitz, E. (1987). *Fluid Mechanics*, volume 6. Institute of Physical Problems, U.S.S.R. Academy of Sciences.

Lee, T. and Budwig, R. (1991). Two improved methods for low-speed hot-wire calibration. *Measurement Science and Technology*, 2(7):643–646.

Lueck, S., Renner, C., Peinke, J., and Friedrich, R. (2006). The markov-einstein coherence length - a new meaning for the taylor length in turbulence. *Physics Letters A*, 359(5):335 – 338.

Lundgren, T. S. (2003). Kolmogorov turbulence by matched asymptotic expansions. *Physics of Fluids*, 15(4):1074–1081.

Malécot, Y., Auriault, C., Kahalerras, H., Gagne, Y., Chanal, O., Chabaud, B., and Castaing, B. (2000). A statistical estimator of turbulence intermittency in physical and numerical experiments. *European Physical Journal B*, 16(3):549–561.

Mandelbrot, B. (1977). Fractals: Form, chance, and dimension. *San Francisco. W. H. Freeman and Company.*

Marcq, P. and Naert, A. (2001). A langevin equation for turbulent velocity increments. *Physics of Fluids*, 13(9):2590–2595.

Maurer, J. and Tabeling, P. (1998). Local investigation of superfluid turbulence. *Europhysics Letters (EPL)*, 43(1):29–34.

Maurer, J., Tabeling, P., and Zocchi, G. (1994). Statistics of turbulence between two counter-rotating disks in low-temperature helium gas. *Europhysics Letters (EPL)*, 26(1):31–36.

Mazellier, N. and Vassilicos, J. C. (2008). The turbulence dissipation constant is not universal because of its universal dependence on large-scale flow topology. *Physics of Fluids*, 20(1):015101.

Mazellier, N. and Vassilicos, J. C. (2010). Turbulence without richardson–kolmogorov cascade. *Physics of Fluids*, 22(7):075101.

Mi, J., Xu, M., and Zhou, T. (2013). Reynolds number influence on statistical behaviors of turbulence in a circular free jet. *Physics of Fluids*, 25(7):075101.

Mohammed-Taifour, A., Weiss, J., Sadeghi, A., Vétel, J., Jondeau, E., and Comte-Bellot, G. (2015). A detailed procedure for measuring turbulent velocity fluctuations using constant-voltage anemometry. *Experiments in Fluids*, 56:174.

Moisy, F. (2000). *Etude expérimentale des fluctuations de vitesse, de température et de pression en turbulence développée*. PhD thesis, Université Paris 6.

Mora, D. O., Muñiz Pladellorens, E., Riera Turró, P., Lagauzere, M., and Obligado, M. (2019). Energy cascades in active-grid-generated turbulent flows. *Phys. Rev. Fluids*, 4:104601.

Mordant, N. (2008). Experimental high reynolds number turbulence with an active grid. *American Journal of Physics*, 76(12):1092–1098.

Moro, J.-P. (2010). Cea patent. (3045835).

N. Mordant, J.-F. Pinton, and F. Chillà (1997). Characterization of turbulence in a closed flow. *J. Phys. II France*, 7(11):1729–1742.

Naert, A., Friedrich, R., and Peinke, J. (1997). Fokker-planck equation for the energy cascade in turbulence. *Physical Review E*, 56(6):6719–6722.

Nawroth, A. P., Peinke, J., Kleinhans, D., and Friedrich, R. (2007). Improved estimation of fokker-planck equations through optimization. *Physical Review E*, 76(5):056102.

Nickelsen, D. (2014). *Markov processes in thermodynamics and turbulence*. PhD thesis, University of Oldenburg.

Nickelsen, D. (2017). Master equation for she–leveque scaling and its classification in terms of other markov models of developed turbulence. *Journal of Statistical Mechanics: Theory and Experiment*, 2017(7):073209.

Nickelsen, D. and Engel, A. (2013). Probing small-scale intermittency with a fluctuation theorem. *Physical Review Letters*, 110(21):214501.

Noullez, A., WALLACE, G., LEMPERT, W., MILES, R. B., and FRISCH, U. (1997). Transverse velocity increments in turbulent flow using the relief technique. *Journal of Fluid Mechanics*, 339:287–307.

Novikov, E.A., S. R. (1964). Intermittency of turbulence and spectrum of !uctuations in energy dissipation. *Izv. Akad. Nauk Ser. Geophys.*, 3:408.

Ozahi, E., Özdinç Çarpınlıoğlu, M., and Gündoğdu, M. Y. (2010). Simple methods for low speed calibration of hot-wire anemometers. *Flow Measurement and Instrumentation*, 21(2):166 – 170.

Ozkan, M. (2019). Rotating-arm method for low speed calibration of hot-wire probes in water applications. *Measurement*, 145:453 – 459.

Panchapakesan, N. R. and Lumley, J. L. (1993). Turbulence measurements in axisymmetric jets of air and helium. part 1. air jet. *Journal of Fluid Mechanics*, 246:197–223.

Paranthoen, P., Petit, C., and Lecordier, J. C. (1982). The effect of the thermal prong—wire interaction on the response of a cold wire in gaseous flows (air, argon and helium). *Journal of Fluid Mechanics*, 124:457–473.

Peinke, J., Tabar, M. R. R., and Wächter, M. (2019). The fokker-planck approach to complex spatiotemporal disordered systems. *Annual Review of Condensed Matter Physics*, 10:107–132.

Pietropinto, S., Poulain, C., Baudet, C., Castaing, B., Chabaud, B., Gagne, Y., Hébral, B., Ladam, Y., Lebrun, P., Pirotte, O., and Roche, P. (2003). Superconducting instrumentation for high reynolds turbulence experiments with low temperature gaseous helium. *Physica C: Superconductivity*, 386:512–516. Proceedings of the topical conference of the International Cryogenic Materials Conference (ICMC 2002). Superconductors for Practical Applications.

Pietropinto, S. S., Baudet, C., Castaing, B., Chabaud, B., Gagne, Y., Hébral, B., Ladam, Y., Lebrun, P., Pirotte, O., Poulain, C., and Roche, P.-E. (2002). Low temperature gaseous helium and very high turbulence experiments. In *19th International Cryogenic Engineering Conference*, page xxx, grenoble, France.

Pope, S. B. (2001). Turbulent flows.

Praskovsky, A. and Oncley, S. (1997). Comprehensive measurements of the intermittency exponent in high reynolds number turbulent flows. *Fluid Dynamics Research*, 21(5):331 – 358.

Rajaratnam, N. (1976). Chapter 8 confined jets. 5:148 – 183.

Ravelet, F. (2005). *Bifurcations globales hydrodynamiques et magnetohydrodynamiques dans un ecoulement de von Karman turbulent*. PhD thesis, École doctorale de l'École Polytechnique.

Ravelet, F., Chiffaudel, A., and Daviaud, F. (2008). Supercritical transition to turbulence in an inertially-driven von karman closed flow.

Reinke, N., Fuchs, A., Nickelsen, D., and Peinke, J. (2018). On universal features of the turbulent cascade in terms of non-equilibrium thermodynamics. *Journal of Fluid Mechanics*, 848:117–153.

Renner, C., Peinke, J., and Friedrich, R. (2001). Experimental indications for markov properties of small-scale turbulence. *Journal of Fluid Mechanics*, 433:383–409.

Renner, C., Peinke, J., Friedrich, R., Chanal, O., and Chabaud, B. (2002). Universality of small scale turbulence. *Physical Review Letters*, 89(12):124502.

Richardson, L. F. (1922). Weather prediction by numerical process. by lewis f. richardson. cambridge university press. *Quarterly Journal of the Royal Meteorological Society*.

Rilling, G., Flandrin, P., and Goncalves, P. (2005). Empirical mode decomposition, fractional gaussian noise and hurst exponent estimation. 4:iv/489–iv/492 Vol. 4.

Risken, H. (1989). *The Fokker-Planck Equation*. Springer.

Rohsenow, W. M., H. J. P. C. Y. I. (1998). *Handbook of heat transfer*. New York: McGraw-Hill.

Rousset, B., Bonnay, P., Diribarne, P., Girard, A., Poncet, J. M., Herbert, E., Salort, J., Baudet, C., Castaing, B., Chevillard, L., Daviaud, F., Dubrulle, B., Gagne, Y., Gibert, M., Hébral, B., Lehner, T., Roche, P.-E., Saint-Michel, B., and Bon Mardion, M. (2014). Superfluid high reynolds von kármán experiment. *Review of Scientific Instruments*, 85(10):103908.

Russo, G. P. (2011). 3 - hot wire anemometer. In Russo, G. P., editor, *Aerodynamic Measurements*, pages 67 – 98. Woodhead Publishing.

Sadeghi, H., Lavoie, P., and Pollard, A. (2018). Effects of finite hot-wire spatial resolution on turbulence statistics and velocity spectra in a round turbulent free jet. *Experiments in Fluids*, 59(3):40.

Saint-Michel, B. (2013). *L'ecoulement de von Karman comme paradigme de la physique statistique hors de l'equilibre*. PhD thesis, L'Université Pierre et Marie Curie, Sorbonne Universités.

Saint-Michel, B., Herbert, E., Salort, J., Baudet, C., Bon Mardion, M., Bonnay, P., Bourgoin, M., Castaing, B., Chevillard, L., Daviaud, F., Diribarne, P., Dubrulle, B., Gagne, Y., Gibert, M., Girard, A., Hébral, B., Lehner, T., and Rousset, B. (2014). Probing quantum and classical turbulence analogy in von kármán liquid helium, nitrogen, and water experiments. *Physics of Fluids*, 26(12):125109.

Salort, J. (2011). *Turbulence quantique versus classique*. PhD thesis, Université de Grenoble.

Salort, J., Baudet, C., Castaing, B., Chabaud, B., Daviaud, F., Didelot, T., Diribarne, P., Dubrulle, B., Gagne, Y., Gauthier, F., Girard, A., Hébral, B., Rousset, B., Thibault, P., and Roche, P.-E. (2010). Turbulent velocity spectra in superfluid flows. *Physics of Fluids*, 22(12):125102.

Salort, J., Chabaud, B., Lévêque, E., and Roche, P.-E. (2012). Energy cascade and the four-fifths law in superfluid turbulence. *EPL (Europhysics Letters)*, 97(3):34006.

Salort, J., Rusaouën, E., Robert, L., du Puits, R., Loesch, A., Pirotte, O., Roche, P.-E., Castaing, B., and Chillà, F. (2018). A local sensor for joint temperature and velocity measurements in turbulent flows. *Review of Scientific Instruments*, 89(1):015005.

Sarma, G. (1993). Analysis of a constant voltage anemometer circuit. pages 731–736.

Sarma, G. R. (1998). Transfer function analysis of the constant voltage anemometer. *Review of Scientific Instruments*, 69(6):2385–2391.

Sarma, G. R. and Lankes, R. W. (1999). Automated constant voltage anemometer with in situ measurements of overheat and time constant of the hot wire. *Review of Scientific Instruments*, 70(5):2384–2386.

Sattarzadeh, S. S., Kalpakli, A., and Örlü, R. (2013). Hot-wire calibration at low velocities: Revisiting the vortex shedding method. *Advances in Mechanical Engineering*, 5:241726.

Saw, E.-W., Debue, P., Kuzzay, D., Daviaud, F., and Dubrulle, B. (2018). On the universality of anomalous scaling exponents of structure functions in turbulent flows. *Journal of Fluid Mechanics*, 837:657–669.

Seifert, U. (2005). Entropy production along a stochastic trajectory and an integral fluctuation theorem. *Physical Review Letters*, 95(4):040602.

Seifert, U. (2008). Stochastic thermodynamics: principles and perspectives. *The European Physical Journal B*, 64(3-4):423–431.

Seifert, U. (2012). Stochastic thermodynamics, fluctuation theorems and molecular machines. *Reports on Progress in Physics*, 75(12):126001.

She, Z.-S. and Leveque, E. (1994). Universal scaling laws in fully developed turbulence. *Phys. Rev. Lett.*, 72:336–339.

Shukla, V. and Pandit, R. (2016). Multiscaling in superfluid turbulence: A shell-model study. *Phys. Rev. E*, 94:043101.

Sreenivasan, K. R. (1995). On the universality of the kolmogorov constant. *Physics of Fluids*, 7(11):2778–2784.

Sreenivasan, K. R. and Antonia, R. A. (1997). The phenomenology of small-scale turbulence. *Annual Review of Fluid Mechanics*, 29(1):435–472.

Sreenivasan, K. R. and Schumacher, J. (2010). Lagrangian views on turbulent mixing of passive scalars. *Philosophical Transactions of the Royal Society A: Mathematical, Physical and Engineering Sciences*, 368(1916):1561–1577.

Stresing, R., Kleinhans, D., R., F., and Peinke, J. (2011). Different methods to estimate the einstein-markov coherence length in turbulence. *PHYSICAL REVIEW E*, 83(4):046319.

Tabeling, P. and Willaime, H. (2002). Transition at dissipative scales in large-reynolds-number turbulence. *Phys. Rev. E*, 65:066301.

Tabeling, P., Zocchi, G., Belin, F., Maurer, J., and Willaime, H. (1996). Probability density functions, skewness, and flatness in large reynolds number turbulence. *Phys. Rev. E*, 53:1613–1621.

Tang, S. L., Antonia, R. A., Djenidi, L., Danaila, L., and Zhou, Y. (2017). Finite reynolds number effect on the scaling range behaviour of turbulent longitudinal velocity structure functions. *Journal of Fluid Mechanics*, 820:341–369.

Taylor, G. I. (1935). Statistical theory of turbulenc. *Proceedings of the Royal Society A: Mathematical, Physical and Engineering Sciences*, 151(873):421–444.

Taylor, G. I. (1938). The spectrum of turbulence. *Proceedings of the Royal Society of London. Series A, Mathematical and Physical Sciences*, pages 476–490.

Tennekes, H., L. J. (1972). A first course in turbulence.

Tisza, L. (1938). The λ-transition explained. *Nature*, 141.

Vallikivi, M. and Smits, A. J. (2014). Fabrication and characterization of a novel nanoscale thermal anemometry probe. *Journal of Microelectromechanical Systems*, 23(4):899–907.

Van Atta, C. W. and Antonia, R. A. (1980). Reynolds number dependence of skewness and flatness factors of turbulent velocity derivatives. *The Physics of Fluids*, 23(2):252–257.

Van Kampen, N. (2007). Chapter viii - the fokker–planck equation. In VAN KAMPEN, N., editor, *Stochastic Processes in Physics and Chemistry (Third Edition)*, North-Holland Personal Library, pages 193–218. Elsevier, Amsterdam, third edition edition.

Van Sciver, S., Holmes, D., Huang, X., and Weisend, J. (1991). He ii flowmetering. *Cryogenics*, 31(2):75–86.

Van Sciver, S. W. (2012). *Helium Cryogenics*. Springer, New York, NY.

Vassilicos, J. C. (2015). Dissipation in turbulent flows. *Annual Review of Fluid Mechanics*, 47(1):95–114.

Voropayev, S. I., Sanchez, X., Nath, C., Webb, S., and Fernando, H. J. S. (2011). Evolution of a confined turbulent jet in a long cylindrical cavity: Homogeneous fluids. *Physics of Fluids*, 23(11):115106.

Wygnanski, I. and Fiedler, H. (1969). Some measurements in the self-preserving jet. *Journal of Fluid Mechanics*, 38(3):577–612.

Zocchi, G., Tabeling, P., Maurer, J., and Willaime, H. (1994). Measurement of the scaling of the dissipation at high reynolds numbers. *Phys. Rev. E*, 50:3693–3700.